COMMUNICATIONS

Dear readers,

This issue of the Communications – Scientific Letters of the University of Zilina is mainly devoted to materials engineering.

Utility parameters of machines and equipment increase in majority of technical disciplines; in parallel with that there is demand on reduction of their mass. Development in the field of construction materials directs thus to another increasing of strength characteristics, brittle damage resistance, improvement of surface properties, technological properties, etc.

Trend growth of all technical discipline is dependent on development of construction materials. The prestige experimental workplaces of universities and research institutions, both national and international, deal with material research.

The editorial board addressed the institutions whose activities on the material research are significant. Let me thank all of them (Charles University Prague, SVUM, a. s., Prague, University of Defence, Brno, VSB – Technical University of Ostrava, Slovak University of Technology of Trnava, Technical University of Kosice, University of Zilina) who contributed to the Communications – Scientific Letters of the University of Zilina, No. 4, 2010.

Otakar Bokuvka

Z. Trojanova – P. Lukac *

DEFORMATION MECHANISMS OPERATING DURING PLASTIC FLOW OF AN AZ63 MAGNESIUM ALLOY STUDIED BY THE STRESS RELAXATION TECHNIQUE

Magnesium alloy AZ63 (Mg−6Al−3Zn) was deformed at temperatures between room temperature and 300 °C. Stress relaxation tests were performed in order to reveal features of the thermally activated dislocation mechanism. Internal and effective components of the applied stress were estimated. Very high values of the internal stress estimated at lower temperatures decrease rapidly with increasing deformation temperature. The apparent activation volume decreases with increasing effective stress. The values of the activation volume as well as the activation enthalpy indicate that the main thermally activated process is most probably the glide of dislocations in non−compact planes. Non-monotonous temperature dependence of the flow stress was observed. Post relaxation effect was detected. Strain ageing effects are explained by the dynamic solute-dislocation interaction.

Key words: Magnesium alloy; Stress relaxation; Thermally activated dislocation motion; Dynamic strain ageing

1. Introduction

Most used commercial magnesium alloys of an AZ series exhibit a relatively high specific strength (the strength/density ratio) at room temperature but poor mechanical properties at elevated temperatures [1–4]. These alloys exhibit universally the hexagonal close packed structure with the limited number of slip systems in the basal plane. It strongly influences the ductility of such alloys at lower temperatures. The ductility increases at elevated temperatures due to possibility of the activation of non-basal slip systems.

During plastic deformation in a certain range of temperature and strain rate, different micro-mechanisms may play an important role. The analysis of deformation microstructures has shown that one should consider dislocation-based mechanisms in order to explain the deformation behaviour. It is widely accepted that the resolved shear stress, τ, and necessary for dislocation motion in the slip plane can be divided into two components:

$$\tau = \tau_i + \tau^*, \tag{1}$$

where τ_i is the (internal) athermal contribution to the stress, resulting from long-range internal stresses impeding the plastic flow and the effective shear stress, τ^*, acts on dislocations during their thermally activated dislocation motion. The mean velocity of dislocations, v, is connected with the plastic shear strain rate by the Orowan equation:

$$\dot{\gamma} = \rho_m\, bv. \tag{2}$$

In polycrystalline materials, the resolved shear stress, τ, and its components are related to the applied stress, σ, and its corresponding components by the Taylor orientation factor ψ: $\sigma = \psi\tau$. A simple relation between the resolved shear strain rate and strain rate is $\gamma = \psi\varepsilon$, then the flow stress

$$\sigma = \sigma_i + \sigma^*. \tag{3}$$

The internal stress component σ_i is done as

$$\sigma_i = \alpha G b \rho_t^{1/2}, \tag{4}$$

where G is the shear modulus, α is a constant describing interaction between dislocations, b is the Burgers vector of dislocations, and ρ_t is the total dislocation density. The effective stress component, σ^*, is defined by the Arrhenius equation (5). The plastic strain rate, $\dot{\varepsilon}$, for a single thermally activated process can be expressed as:

$$\dot{\varepsilon} = \dot{\varepsilon}_0 \exp\left[-\frac{\Delta G(\sigma^*)}{kT}\right], \tag{5}$$

where $\dot{\varepsilon}_0$ is a pre-exponential factor containing the mobile dislocation density, the average area covered by the dislocations in each activation process, the dislocation Burgers vector, the vibration frequency of the dislocation line, and the geometric factor. T is the absolute temperature and k is the Boltzmann constant. $\Delta G(\sigma^*)$ is the change in the Gibbs free enthalpy depending on the effective stress $\sigma^* = \sigma - \sigma_i$ and its simple form is

$$\Delta G(\sigma^*) = \Delta G_0 - V\sigma^* = \Delta G_0 - V(\sigma - \sigma_i). \tag{6}$$

* **Z. Trojanova, P. Lukac**
Department of Physics of Materials, Faculty Mathematics and Physics, Charles University, Prague, Czech Republic,
E-mail: ztrojan@met.mff.cuni.cz

Here ΔG_0 is the Gibbs free enthalpy necessary for overcoming a short-range obstacle without stress and $V = bdL$ is the activation volume where d is the obstacle width and L is the mean length of dislocation segments between obstacles. It should be mentioned that L may depend on the stress acting on dislocation segments.

The aim of the present work is to investigate deformation behaviour of Mg−6Al−1Zn alloy at different temperatures and to reveal the mechanisms responsible for plastic deformation of the alloy at elevated temperatures.

2. Experimental procedure

Magnesium alloy AZ63 (the nominal composition Mg−6Al−1Zn), in wt. %, was gravity cast. Samples were deformed in compression in an INSTRON 5882 machine at a constant cross head-speed giving an initial strain rate of 2.8×10^{-5} s^{-1} over a temperature range of 23 to 300 °C. Sequential stress relaxation (SR) tests were performed at increasing stress along a stress-strain curve. Duration of the SR was 300 s. Components of the applied stress (σ_i , σ^*) were estimated using Li's method [5, 6]. The SR curves were fitted to a power law function in the form:

$$\sigma - \sigma_i = \left[a(m-1)\right]^{\frac{1}{1-m}}(t+t_0)^{\frac{1}{1-m}}, \tag{7}$$

where a, t_0, and m are fitting parameters.

The stress relaxation technique has been demonstrated to be a useful experimental method for estimating the activation volume and hence for determining thermally activated process(es). In a stress relaxation test, the specimen is deformed to a certain stress σ_0 and then the machine is stopped and the stress is allowed to relax. The stress decreases with time t. The specimen can be again reloaded and deformed to a higher stress and the stress relaxation test may be repeated. The time derivative $\dot\sigma = \mathrm{d}\sigma/\mathrm{d}t$ is the stress relaxation rate and $\sigma = \sigma(t)$ is the flow stress at time t during the SR. Stress relaxation tests are very often analysed under the assumption that the stress relaxation rate is proportional to the strain rate $\dot\varepsilon$ according to [7]:

$$\dot\varepsilon = -\dot\sigma/M \tag{8}$$

where M is the combined modulus of the specimen machine set.

Combining (5), (6) and (8), we have

$$-\dot\sigma = M\dot\varepsilon_0 \exp\left[-\frac{\Delta G_0 - V\sigma^*}{kT}\right]. \tag{9}$$

Taking the logarithm of this equation we get

$$\ln(-\dot\sigma) = \ln(M\dot\varepsilon_0) - \frac{\Delta G_0}{kT} + \frac{V\sigma^*}{kT}. \tag{10}$$

The stress decrease with time during the SR can be described by the well known Feltham equation [8]:

$$\Delta\sigma(t) = \sigma(0) - \sigma(t) = \alpha\ln(\beta t+1), \tag{11}$$

where $\sigma(0) \equiv \sigma_0$ is the stress at the beginning of the stress relaxation at time $t = 0$,

$$\alpha = \frac{kT}{V}, \tag{12}$$

$$\beta = \frac{M\dot\varepsilon_0 V}{kT}\exp\left[-\frac{\Delta G_0 - V\sigma^*(0)}{kT}\right] = \frac{M\dot\varepsilon(0)}{\alpha}, \tag{13}$$

where $\dot\varepsilon(0)$ is the plastic strain rate at the beginning of the relaxation.

3. Results and discussion

3.1 Internal stress

Parts of the true stress−true strain curves measured at various temperatures are introduced in Fig. 1. Full points (depicted as σ_{ap}) indicate the stresses at which the SR tests were performed. Figs 1a-1e demonstrate the development of the internal stress σ_i with temperature. While the internal stress is at ambient temperature and 50 °C a substantial contribution to the applied stress σ_{ap}. The effective stress component σ^* forms at lower temperature small contribution to the applied stress (Fig. 1a.b) but it increases with increasing temperature and at 300 °C is higher then the internal stress (Fig. 1e). The internal stress depends on the dislocation density, i.e. $\sigma_i \propto \rho^{½}$. A decrease of the internal stress indicates a decrease of the dislocation density. In the case when the internal stress is approximately constant or slightly decreasing with strain (see Fig. 1c), some equilibrium between multiplication and annihilation of dislocations may be considered. The decrease of the dislocation density with temperature is also visible from Fig. 2, where the temperature dependences of the ratio σ_i/σ_{ap} are shown. It should be noted that the values were estimated from SR test performed at $\varepsilon \sim 0.01$. The internal stress of several magnesium alloys was studied by Milicka et al. [9] in creep experiments. They

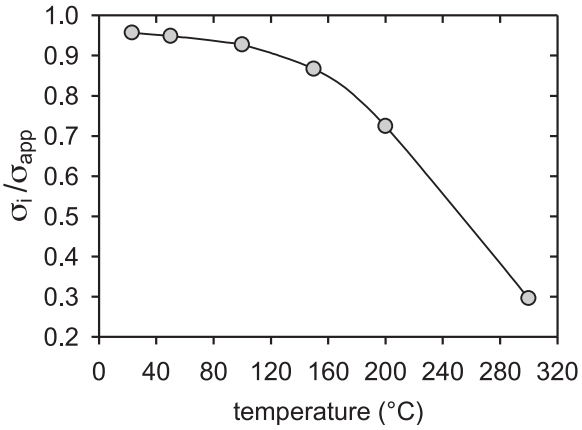

Fig. 2. Variation of the internal/applied stress ratio (obtained at the strain of about 1%) with temperature.

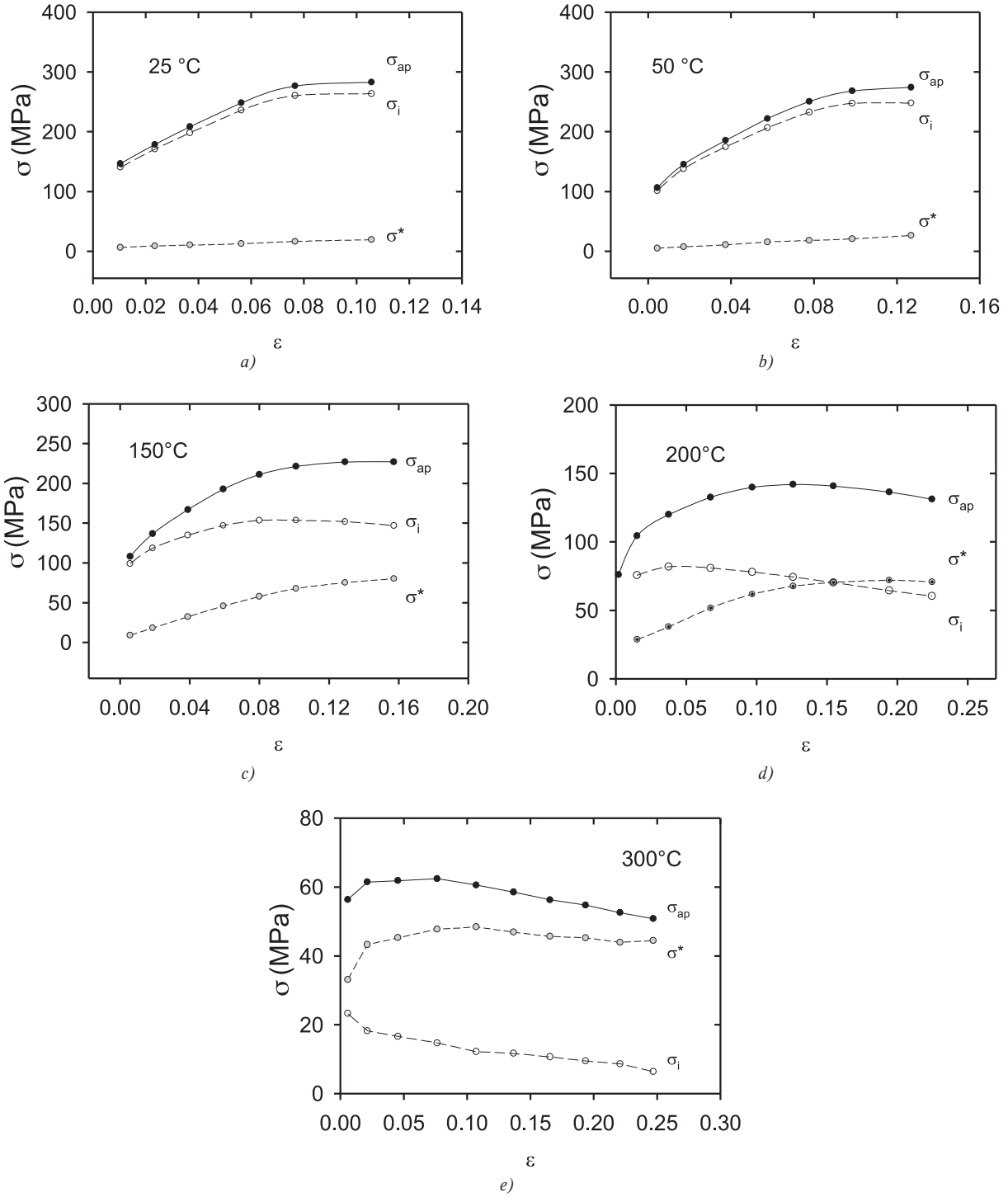

Fig. 1. Parts of the true stress–true strain curves obtained at various temperatures. The points of σap on the curves indicate the stresses at which the SR tests were performed: a) 25 °C, b) 50 °C, c) 150 °C, d) 200 °C, e) 300 °C.

found that the internal stress σi reflects the creep resistance of the material. Experimental internal stresses determined in creep well correspond to those determined in SR tests under comparable testing conditions.

3.2 Thermal activation

The activation volume was estimated using Eq. (11). The values of the activation volume (as usual divided by b^3) estimated at four temperatures are introduced in Fig. 3. Four discrete decreasing curves were observed.

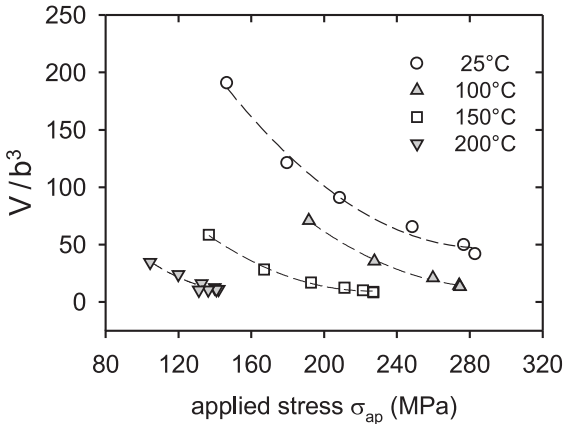

Fig. 3. Plot of the apparent activation volume (in b^3) against the applied stress σ_{ap} estimated at four temperatures.

The dislocation (true) activation volume V_d is obtained by the following equation:

$$V_d = \left(\frac{\partial \Delta G}{\partial \tau^*}\right)_{\tau,s} = kT\left(\frac{\partial \ln(\dot{\gamma}/\dot{\gamma}_0)}{\partial \tau^*}\right)_{\tau,s}, \quad (14)$$

where the subscripts T and s indicate that both the temperature and the dislocation microstructure (especially the mobile dislocation density) have to be constant during the test. Equation (14) is usually used for the activation volume estimation in tests with changes in strain rate (or machine speed). The $\dot{\gamma}_0$ term is essentially structure-dependent and can be expressed as

$$\dot{\gamma}_0 = \rho_m b \frac{A}{\ell_c} v_D \frac{b}{\ell_c}. \quad (15)$$

where A is the mean area swept by the dislocation segment per successful thermally activated event, $A = V/b$, v_D is the Debye frequency and ℓ_c is the critical dislocation length for the thermally activated process to occur. In the stress relaxation experiments of polycrystals, it is only possible to record the variation of the applied stress, σ_{ap}, associated with the change in plastic strain rate (stress relaxation rate) and to determine an apparent activation volume, V_{app}, considering the mobile dislocation density and the internal stress as constant. The apparent activation volume, V_{app}, estimated in experiments with polycrystals is proportional to the dislocation activation volume as $V_{app} = (1/\psi)V_d$. Apparent (experimental) activation volumes estimated for various temperatures are plotted against the thermal stress σ* in Fig. 4. All values appear to lie on one line, "master curve". Kocks et al. [10] suggested an empirical relation between the Gibbs enthalpy ΔG and the effective stress σ* in the following form:

$$\Delta G = \Delta G_0 \left[1 - \left(\frac{\sigma^*}{\sigma_0^*}\right)^p\right]^q, \quad (16)$$

where ΔG_0 and σ_0^* are Gibbs enthalpy and the effective stress at 0 K. From Eqs. (5) and (16) it follows:

$$\sigma^* = \sigma_0^* \left[1 - \left(\frac{kT}{\Delta G_0} \ln \frac{\dot{\varepsilon}_0}{\dot{\varepsilon}}\right)^{1/q}\right]^{1/p}, \quad (17)$$

where p and q are phenomenological parameters reflecting the shape of a resistance profile. The possible ranges of values p and q are limited by the conditions $0 < p \leq 1$ and $1 \leq q \leq 2$. Ono [11, 12], suggested that Eq. (17) with $p = 1/2$, $q = 3/2$ describes a barrier shape profile that fits many predicted barrier shapes. Equation (17) can be rewritten

$$\dot{\varepsilon} = \dot{\varepsilon}_0 \exp\left[-\frac{\Delta G_0}{kT}\left(1 - \left(\frac{\sigma^*}{\sigma_0^*}\right)^p\right)^q\right] \quad (18)$$

and for the activation volume one obtains:

$$V = kT\frac{\partial \ln \dot{\varepsilon}/\dot{\varepsilon}_0}{\partial \sigma^*} = \frac{\Delta G_0 pq}{\sigma_0^*}\left[1 - \left(\frac{\sigma^*}{\sigma_0^*}\right)^p\right]^{q-1}\left(\frac{\sigma^*}{\sigma_0^*}\right)^{p-1}. \quad (19)$$

The values of the activation volume should lie at the curve given by Eq. (19). The fit of the experimental values (taken from Fig. 4) of Eq. (19) gives for the activation enthalpy $\Delta G_0 = 0.95 \pm \pm 0.05$ eV. (see Fig. 4). Similar values of the activation enthalpy were estimated for other magnesium alloys [14, 15]. Using binominal expansion in Eq. (19), the activation volume should depends on the effective stress as $V_{app} \propto (\sigma^*)^{-n}$. Generally, the values of the power exponent found in the literature vary from -0.5 to -1 [10].

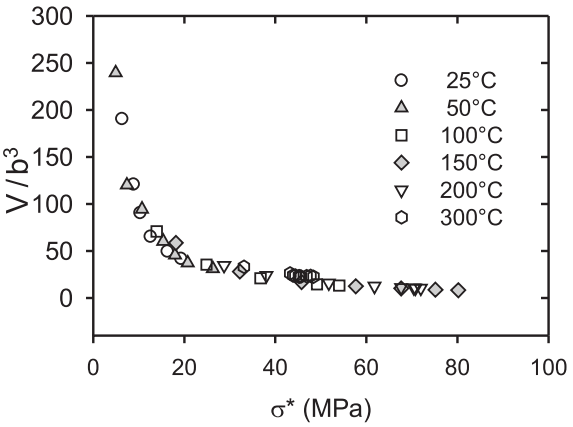

Fig. 4. Plot of the apparent activation volume (in b^3) against the thermal stress σ estimated for various deformation temperatures*

The activation enthalpy $\Delta H = \Delta G - T\Delta S$ (ΔS is the entropy) is done by

$$\Delta H = -TV_d \frac{\partial \tau^*}{\partial T}. \quad (20)$$

For polycrystals, we can measure experimentally $\partial\sigma/\partial T$. Substituting from (14) into (20) it follows for the activation enthalpy

$$\Delta H = T \cdot V_{app}\left(\frac{\partial \sigma}{\partial \tau^*}\right)\left(\frac{\partial \sigma}{\partial T}\right)\left(\frac{\partial \tau^*}{\partial \sigma}\right) = -TV_{app}\left(\frac{\partial \sigma}{\partial T}\right). \qquad (21)$$

The activation enthalpy calculated according to (21) for 150 °C gives (0.96 ± 0.05) eV. Activation energies for high temperature creep of polycrystalline magnesium were measured originally by McG. Tegart [16] for various temperatures and stresses. He estimated that the activation energy is from room temperature up to $0.6T_m$ (T_m is the melting point in K) more less independent of temperature and slightly dependent on the applied stress. It was found for higher stresses to be ~ 1 eV. Similar values were found for pure magnesium at 400 K by Milicka et al. [17] and Vagarali and Langdon [18] and for Mg−0.8% Al [19].

The values of the activation volume and the activation enthalpy may help to identify thermally activated processes considering some of the common short−range barriers to dislocation motion [13]. The dislocation–dislocation interaction mechanism has an activation volume ranging from about $10^2 - 10^4\ b^3$, with the activation volume and enthalpy varying with strain. A rapid decrease in the internal stress with temperature (see Figs. 1d and 1e) indicates that softening is connected with dynamic recovery.

Magnesium alloys, with hcp structure, deform on many possible glide systems with dislocations of Burgers vector $\langle a \rangle = 1/3\ [11\bar{2}0]$ in basal, prismatic, and first-order pyramidal planes and with dislocations of Burgers vector $\langle c + a \rangle = 1/3\ [11\bar{2}3]$ in first- and second-order pyramidal planes. The main deformation mode in magnesium is basal slip of $\langle a \rangle$ dislocations. The secondary conservative slip may be realised by the $\langle a \rangle$ dislocations on prismatic and pyramidal planes of the first order. Couret and Caillard [20, 21] studied by TEM prismatic glide in magnesium in a wide temperature interval. They showed that screw dislocations with the Burgers vector $1/3\ [11\bar{2}0]$ are able to glide on prismatic planes and their mobility is much lower than the mobility of edge dislocations. The deformation is controlled by thermally activated glide of those screw dislocation segments. A single controlling mechanism was identified as the Friedel-Escaig cross slip mechanism. This mechanism assumes dissociated dislocations on compact planes, like (0001), that joint together along a critical length L_r producing double kinks on non-compact planes. The activation volume is proportional to the critical length between two kinks. Amadieh et al. [22] found for the activation volume of the Friedel-Escaig mechanism a value of 70 b^3. Prismatic slip was also observed by Koike and Ohyama [23] in deformed AZ61 sheets The activity of the $\langle a \rangle$ dislocations in prismatic planes is possible when the critical resolved shear stress ratio of prismatic to basal slip exhibits values 1.5-2. It is realised at elevated temperatures and also at lower temperatures for a special texture of samples. The activation of the prismatic slip and subsequent annihilation of dislocation segments with opposite sign are probably the main reason for the observed internal stress decrease. The double cross slip may be a thermally activated process controlling the dislocation velocity. Beside this mechanism, the thermally activated glide of $\langle c + a \rangle$ dislocations should be taken into account. Mathis et al. [24] studied the evolution of non-basal dislocations as a function of temperature in magnesium by X-ray diffraction. They found a majority of $\langle a \rangle$ dislocations in the as-cast state. During plastic deformation in tension the $\langle a \rangle$ -type dislocations remain dominant, however, the dislocation density increased by about a factor of three up to about 100 °C. At higher temperatures the fraction of $\langle c + a \rangle$ -type dislocations increased at the cost of $\langle a \rangle$ -type dislocations and the increase of the dislocation density is strongly reduced. The internal stress acting on the dislocations is determined by the details of the internal structure at that moment and it is independent of the applied stress. The stress that changes when the applied stress is changed is only the effective stress. The internal stresses during plastic deformation of this alloy can be considered as the sum of stresses resulting from various dislocation arrangements and obstacles existing in the deformed material [9, 25]. The solute atoms do not influence the moving dislocations at higher temperatures. However, at higher temperatures the solute atoms my diffuse to the staking fault and influence double cross slip from basal to non-basal planes.

3.3 Strain ageing

From the temperature dependence of the yield stress, introduced in Fig. 5, some local maximum between 50 and 100 °C is obvious. This maximum is a consequence of the dynamic strain ageing. It is also manifested at the stress strain curve by the so called post relaxation effect. When the internal stress as well as the dislocation density are constant than the deformation process continues at the same stress as at the beginning of the SR test. On the stress strain curve shown in Fig. 6 stress increase after SR test is obvious. The flow stress after the stress relaxation, σ_1, is higher than the flow stress at the beginning of the relaxation. The values of $\Delta\sigma = \sigma_1 - \sigma_0$ are plotted against strain for two temperatures of 25 and 50 °C in Fig. 7. For other temperatures the post relaxation effect was not observed. From Fig. 7 it is to see that the strain dependence of $\Delta\sigma$ has some maximum at a certain strain.

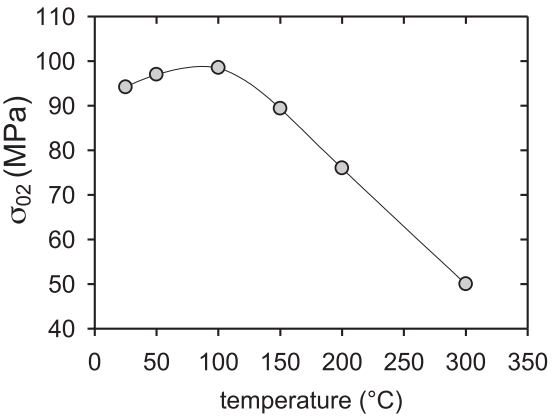

Fig. 5. Temperature dependence of the yield stress.

In an alloy the flow stress may be consider as a sum of two additive contributions:

$$\sigma = \sigma_f + \sigma_d, \qquad (22)$$

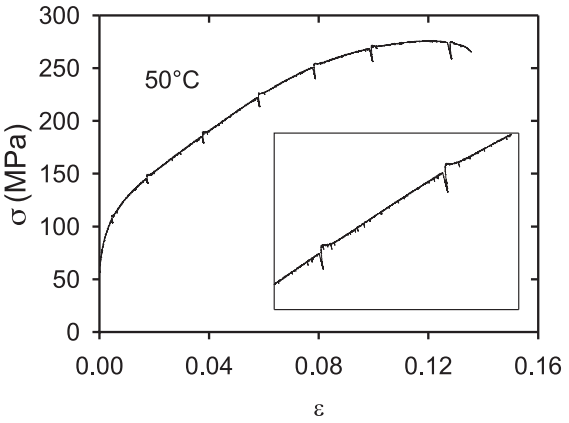

Fig. 6. The stress-strain curve obtained at 50 °C. An increase of the stress after the stress relaxation test is from the insert well visible.

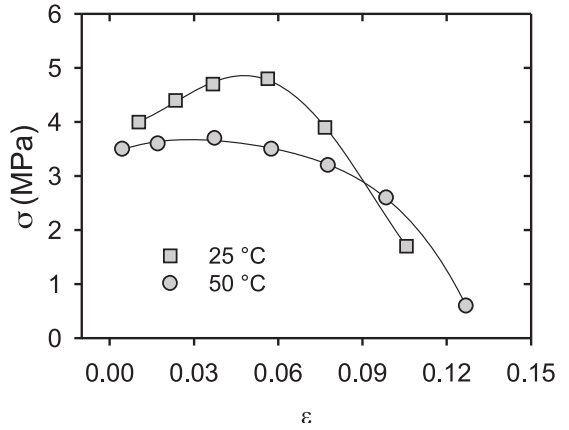

Fig. 7. The stress increase Δσ depending on the strain estimated for 25 and 50 °C.

with σ_f relating to a friction imposed by the solutes-dislocation interaction σ_d relating to the dislocation-dislocation interaction. Hong [26, 27] suggested that the stress σ_f could be described by the following equation:

$$\sigma_f = \alpha_1 GB\delta c \exp\left(-\frac{(T-T_0)^2}{B}\right) \tag{23}$$

where α_1 is a constant, δ is the atomic size misfit parameter, c is the solute concentration and B is the width of the distribution about the temperature T_0 where the maximum of solute-dislocation interaction force occurs. The critical dislocation velocity V_c at which the maximum force occurs can be expressed as:

$$V_c = \alpha_2 \frac{kT_0D_0}{Gb\delta\Omega}\exp\left(-\frac{Q_D}{kT}\right) \tag{24}$$

where α_2 is a constant and D_0 is the diffusion constant for solute atoms, Ω is the atomic volume and Q_D is the activation energy for diffusion of solute atoms in magnesium matrix. The critical strain rate at which the maximum interaction stress occurs can be predicted using the following equation:

$$\dot{\varepsilon}_c = \rho_m b \frac{\pi(1-\nu)kT_0D_0}{(1+\nu)Gb\delta\Omega}\exp\left(-\frac{Q_D}{kT}\right), \tag{25}$$

where ν is the Poisson ratio, ρ_m is the mobile dislocation density. From Eq. (23) it can be seen that the friction force due to solute atoms interaction with moving dislocations exists only in a certain temperature interval depending on solute atoms type. This friction force (stress) is added to the temperature dependence of the yield stress resulting to a local maximum in the temperature dependence of the yield stress. Such local maximum in the temperature dependence is demonstrated in Fig. 5. Similar local maximum was observed in the case of ZE41 alloy [28], AZ91 alloy [29] of binary alloy Mg-0.7Nd [30].

According to Malygin [31] and Rubiolo and Bozzano [32] solute atoms diffuse to dislocations arrested at local obstacles for waiting time t_w. The concentration of solute atoms at dislocation lines as a function of the waiting time $c(t_w)$ is done by the function

$$c = c_m\left[1-\exp\left(-\frac{c_0}{c_m}(\alpha_n D t_w/b^2)\right)^{2/(n+2)}\right], \tag{26}$$

where

$$\alpha_n = n(n+2)\pi^{(n+2)/2}(W_b/kT). \tag{27}$$

c_0 is the average concentration of impurities in the crystal and c_m is the limiting value of impurities on the dislocations. W_B is the binding energy of solute atoms to dislocations. The value of n depends on the details of interaction between solute atom and dislocations. The exponent in eq. (26) $r = 2/(n+2)$ is typically 2/3 and 1/3 for bulk and pipe diffusion, respectively. [33].

The stress increment $\Delta\sigma$ after SR due to solute atoms segregation may be also expressed for longer time by the following equation

$$\Delta\sigma(t, \varepsilon, T) = \Delta\sigma_m(\varepsilon,T)\,\{1-\exp[-(t/t_c)^p]\}, \tag{28}$$

where $\Delta\sigma_m(\varepsilon,T)$ is the stress increment for $t\to\infty$ and it depends on the binding energy between solute atoms and dislocations. (It increases with increasing solute atom concentration and with decreasing temperature.) t_c is a characteristic time which depends on the strain as $t_c \sim \varepsilon^{-k}$. [34]. Solute atoms locking dislocations cause the stress increase after stress relaxation, which depends on strain and on temperature. An increase in the flow stress is needed to move the dislocations after stress relaxation. It is reasonably to assume that $\Delta\sigma$ is proportional to the number of impurities on dislocation lines.

4. Conclusions

The stress relaxation tests were performed during compression experiments at various temperatures with the aim to reveal the main features of the plastic deformation mechanisms. The complex analysis of the stress relaxation curves showed:

- the internal stress decreases with increasing deformation temperature;
- the values of the apparent activation volumes are in the order of tens to hundreds b^3;
- the activation volume depends on the thermal stress so that all values lie at the master curve $V_{app} \propto (\sigma^*)^n$;
- the estimated activation energy indicates that the main thermally activated process is very probably the glide of dislocations in the non-compact planes,
- mobile solute atoms are the reason for the dynamic strain ageing manifested by the post relaxation effect and the local maximum in the temperature dependence of the yield stress.

Acknowledgement. The authors dedicate this paper to Prof. Ing. Otakar Bokuvka, PhD on the occasion his 65th birthday. This work is a part of the research plan 1M2560471601 "Eco-center for Applied Research of Non-ferrous Metals" that is financed by the Ministry of Education, Youth and Sports of the Czech Republic. This work was also supported by the Grant Agency of the Academy of Sciences of the Czech Republic under Grant IAA201120902.

References

[1] POLMEAR, I. J.: *Magnesium alloys,* Light Alloys (Fourth Edition), 2005, 237.
[2] AVEDESIAN, M. M., BAKER, H. (Eds.): *Magnesium and Magnesium Alloys*, ASM Specialty Handbook, ASM International, Materials Park, OH, 1999.
[3] ROBERTS, C. R.: *Magnesium and Its Alloys,* John Wiley & Sons 1960.
[4] MORDIKE, B. L.: *J. JILM* 51, 2001, 2.
[5] LI, J. C. M.: *Canad. J. Appl. Phys.* 45, 1967 493.
[6] DE BATIST, R., CALLENS, A.: *Phys. Stat. Sol.* (a) 21, (1974) 591–595.
[7] DOTSENKO, V.I.: *Phys. Stat. Sol.* (b) 93, 1979, 11.
[8] FELTHAM, P.: *Phys. Stat. Sol.* 3, 1943, 1340.
[9] MILICKA, K., TROJANOVA, Z., LUKAC, P.: *Mater. Sci. Eng.* A 462. 2007. 215..
[10] KOCKS, U. F., ARGON, A. S., ALBY, M. F.: *Progr. Mater. Sci.* 19. 1975. 1.
[11] ONO, K.: J. *Appl. Phys.* 39. 1968. 1803.
[12] KAPOOR, R., WADEKAR, S. L., CHAKRAVARTTY, J. K.: *Mater. Sci. Engn.* A 328, 2002, 324.
[13] EVANS, A.G., RAWLINGS, R. D.: *Phys. Stat. Sol.* 34, 1969, 9.
[14] TROJANOVA, Z., LUKAC. P., KAINER, K. U.: *Advanced Engn. Mater.* 9, 2007, 370.
[15] TROJANOVA, Z., LUKAC, P.: *Inter. J. of Mater*. Research 100, 2009, 270.
[16] MCG. TEGART, W. J.: *Acta Metall.* 9, 1961, 614.
[17] MILICKA, K., CADEK, J., RYS, P.: *Acta Metall.* 18, 1970, 1071.
[18] VAGARALI, S. S., LANGDON, T.G.: *Acta Metall.* 29, 1982, 1969-1982.
[19] VAGARALI, S. S., LANGDON, T.G.: *Acta Metall.* 30, 1982, 1157.
[20] COURET, A., CAILLARD, D.: *Acta metall.* 33 (1985) 1447.
[21] COURET, A., CAILLARD, D.: *Acta metall.* 33 (1985) 1455.
[22] AMADIEH, A., MITCHELL, J., DORN, J. E.: *Trans. AIME* 233, 1965, 1130.
[23] KOIKE, J., OHYAMA, R.: *Acta Mater.* 53, 2005, 1963.
[24] MATHIS, K., NYILAS, K., AXT, A., DRAGOMIR-CERNATESCU, I., UNGAR, T., LUKAC, P.: *Acta Mater.* 52, 2004, 2889.
[25] TROJANOVA, Z., LUKAC, P., MILICKA, K., SZARAZ, Z.: *Mater. Sci. Eng.* A 387–389, 2004, 80.
[26] HONG, S. I.: *Mater. Sci. Eng.* A110, 1989, 125.
[27] HONG, S. I.: *Mater. Sci. Eng.* 91, 1987, 137.
[28] TROJANOVA, Z., LUKAC, P.: *Kovove Mater.* 43, 2005, 73.
[29] TROJANOVA, Z., LUKAC, P., GABOR, P.: *Kovove Mater.* 39, 2001, 368.
[30] TROJANOVA. Z., LUKAC. P.: In: Magnesium Alloys and their Applications 8, Ed. K.U. Kainer, DGM 2009, Willey VCH Weinheim, 785–802.
[31] MALYGIN, G. A.: *Phys. Stat. Sol.* (a) 1982, 72, 493.
[32] RUBIOLO, G. H., BOZZANO, P. B.: *Mater. Trans. JIM* 36. 1995, 1124.
[33] BALIK, J., LUKAC, P.: *Kovove Mater.* 36, 1998, 3.
[16] LUBENETS, S. V., STARTSEV, V. I., FOMENKO, L.S.: *Czech. J. Phys.* B 36, 1986, 493.

Pavel Lukac – Zuzanka Trojanova *

MECHANICAL PROPERTIES AND STRAIN HARDENING BEHAVIOUR OF MAGNESIUM ALLOYS AND COMPOSITES

Selected magnesium alloys and composites with magnesium alloy matrix were deformed at temperatures between room temperature and 300 °C at constant strain rate. The testing temperature influences significantly the deformation behaviour of the al/loys. The flow stress decreases with increasing temperature. The work hardening rate decreases with stress (strain) and temperature. Above about 200 °C, a dynamic balance between hardening and softening is observed. Stress relaxation tests were performed to identify thermally activated dislocation motion. The main thermally activated process is very probably the glide of dislocation in non-basal planes. The internal component of the applied stress decreases significantly with increasing temperature.

1. Introduction

Magnesium alloys, the lightest structural metallic materials, have been considered for many applications including automotive and other transport industries. Most commercial magnesium alloys exhibit a relatively high specific strength (the strength/density ratio), comparable with moderate strength aluminium alloys, and high specific stiffness at room temperature. However, the magnesium alloys possess poor mechanical properties at temperatures above about 150 °C. There are many possibilities how to increase the strength of a metallic material. The mechanical properties of magnesium alloys may be influenced by one or more of the well known strengthening mechanisms – solid solution hardening, precipitation strengthening, dispersion hardening, grain-size refinement. The shape and nature of precipitates and dispersoids have a significant effect on the microstructure, which controls the material behaviour. The addition of ceramic or graphite reinforcements – fibres and/or particles – into magnesium alloys can significantly improve their physical, mechanical and damping behaviour [1]. It is obvious that research on magnesium alloys focusing on mechanical properties has attained an increasing interest during last decades.

The mechanical properties of magnesium alloys were investigated using specimens prepared by different production processes. One of the common casting methods is squeeze casting. During squeeze casting, the molten metal is poured to a preheated die and then the upper half closes the die under press. The advantage of squeeze casting is a low porosity. Wrought magnesium alloys are very often produced by hot rolling and extrusion. Over the last decade, severe plastic deformation (SPD) techniques were used to prepare ultrafine-grained materials [2]. Among these, equal channel angular pressing (ECAP) refines the grain structure of materials to submicrometer level and the material shape does not change. Recent results have shown that processing of some magnesium alloys by ECAP introduces a superplastic capability. The wrought alloys exhibit texture that influences the mechanical properties. There is a difference in the deformation behaviour if a specimen is deformed in tension or in compression and/or the mechanical properties are different if specimens are deformed in different direction.

The deformation behaviour of magnesium alloys and magnesium-based composites were investigated over a wide temperature range – very often between room temperature and 300 – 400 °C. At higher temperatures, dynamic recovery or dynamic recrystallisation may influence the deformation behaviour. Investigations of the effect of temperature on the flow behaviour are important for applications and/or for estimation of suitable forming conditions. In order to understand the flow behaviour of a material, it is important not only to estimate the experimental values – the characteristic of deformation – but also to determine dislocation mechanisms during deformation.

The aim of the present paper is to give an overview on the deformation behaviour of some magnesium alloys at different temperatures and to describe dislocation mechanisms that control the behaviour. Stress relaxation tests will be used in order to describe possible dislocation mechanisms during deformation of alloys prepared by different processing techniques.

2. Stress relaxation

It is widely accepted that the stress necessary for the dislocation motion in polycrystals can be divided into two components [3]

* **Pavel Lukac, Zuzanka Trojanova**
Department of Physics of Materials, Faculty of Mathematics and Physics, Charles University, Praque, Czech Republic,
E-mail: lukac@met.mff.cuni.cz

$$\sigma = \sigma_i + \sigma^*, \quad (1)$$

Here σ_i is the internal (athermal) stress, resulting from long-range stresses impeding the plastic flow. Contribution of dislocation to this internal stress component may be expressed as

$$\sigma_i = \alpha_1 G b \rho_t^{½}. \quad (2)$$

Here G is the shear modulus, α_1 is a constant describing interaction between dislocations, b is the Burgers vector of dislocations and ρ_t is the total dislocation density. The effective stress σ^* acts on dislocations during their thermally activated motion when they overcome short range obstacles.

In a stress relaxation (SR) test, the specimen is deformed to a certain stress σ_0 and then the testing machine is stopped and the stress is allowed to relax [4]. The stress decreases with time t. The specimen can be again reloaded to a higher stress (load) and the SR test may be repeated. The stress decrease with time during the SR test can be described by the following equation [5]

$$\Delta\sigma(t) = \sigma(0) - \sigma(t) = \alpha \ln(\beta t + 1) \quad (3)$$

where $\sigma(0) \equiv \sigma_0$ is the stress at the beginning of the stress relaxation at time $t = 0$, β is a constant and

$$\alpha = \frac{kT}{V}. \quad (4)$$

Here $V = bdL$ is the activation volume where b is the Burgers vector, d is the obstacle width and L of the mean length of dislocation segments between obstacles.

The stress relaxation technique has been demonstrated to be a useful method for estimating the activation volume and the both stress components. The components of the applied stress can be estimated using the method of *Li* [6, 7]. The stress relaxation curve should be fitted to the power law function in the following form

$$\sigma - \sigma_i = [a(m-1)]^{\frac{1}{1-m}} (t + t_0)^{\frac{1}{1-m}} \quad (5)$$

where a, t_0 and m are fitting parameters (m can also be determined from strain rate change experiments). This relation was derived based on dislocation dynamics (a power law relation between dislocation density and stress) assuming that both the internal stress and the density of mobile dislocations are constant during the SR.

3. Experimental procedure

In this paper we will focus our selection on magnesium alloys prepared by cast, squeeze casting, hot rolling and equal channel angular pressing. Samples were deformed in tension and compression in an INSTRON testing machine at a constant cross-head speed giving an initial strain rate of 6.7×10^{-5} s^{-1} over a temperature range of 23 to 300 °C. In some cases, sequential stress relaxation tests were performed along a stress-strain curve. Duration of the SR was 300 s.

4. Results

The true stress–true strain curves obtained in tension for the cast AZ31 (Mg-3Al-1Zn) alloy at different temperature are shown in Fig. 1. It can be seen that the flow stress decreases with increasing testing temperature. At a temperature of 300 °C, the flow stress is practically independent of strain, no significant strain hardening is observed. The result indicates that dynamic recovery occurs. Similar flow curves were obtained for the AX41 (Mg-4Al-1Ca) alloy deformed in tension as shown in Fig. 2 [8]. The true stress–true strain curves obtained for compression tests for the AJ51 (Mg-5Al-1Sr) alloy at various temperatures are shown in Fig. 3 [8]. The true stress-true strain curves for the AZ31 sheets with the tensile axis parallel (P) and perpendicular (T) to the rolling direction obtained at various temperatures are shown in Fig. 4 [9]. It is possible to conclude for the presented results that a high strain hardening is observed at low temperatures, below about 200 °C. At temperatures higher than about 200–250 °C, the flow stress is low and practically independent of strain. A dynamic balance between hardening and softening occurs. It can also be seen that the strength-

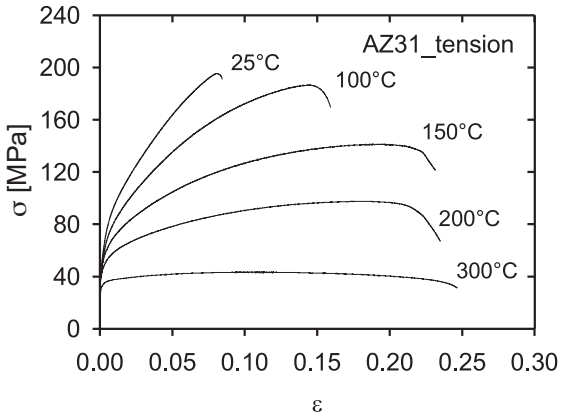

Fig. 1 The true stress–true strain curves of AZ31 measured at different temperatures

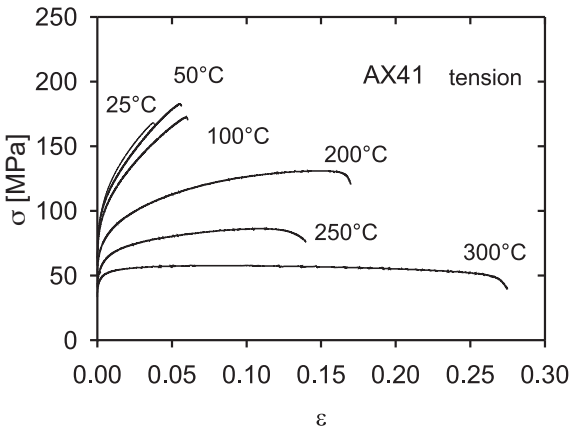

Fig. 2 The true stress-true strain curves of AX41 obtained at various temperatures

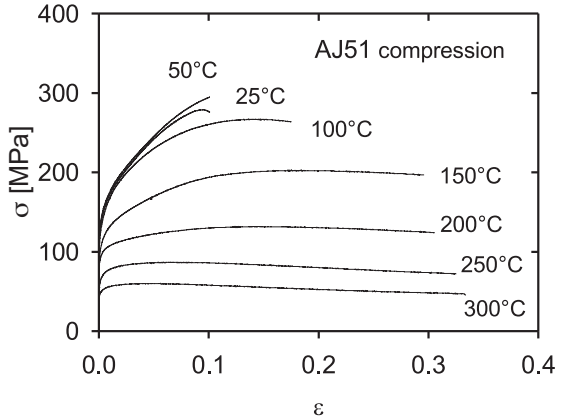

Fig. 3 The true stress-true strain curves of AJ51 measured in compression at various temperatures

ening effect of Zn, as third element, is higher than hardening of Ca and Sr.

An example of the influence of a processing method on the deformation behaviour is shown in Fig. 5 [10]. The heat-treated samples of cast AZ91 (Mg-9Al-1Zn-0.2Mn) were ECAP processed in a right-angled channel via route C. The number of passes was 1, 4 and 8. The total strain rate intensity was 1.15, 4.6. Tensile tests were carried out in a MTS machine at a constant strain rate of 5×10^{-4} s^{-1} and in the temperature range from 20 °C to 300 °C. Figure 5 shows the true stress-true strain curves of both as cast and ECAP processed AZ91 samples at different temperatures. The

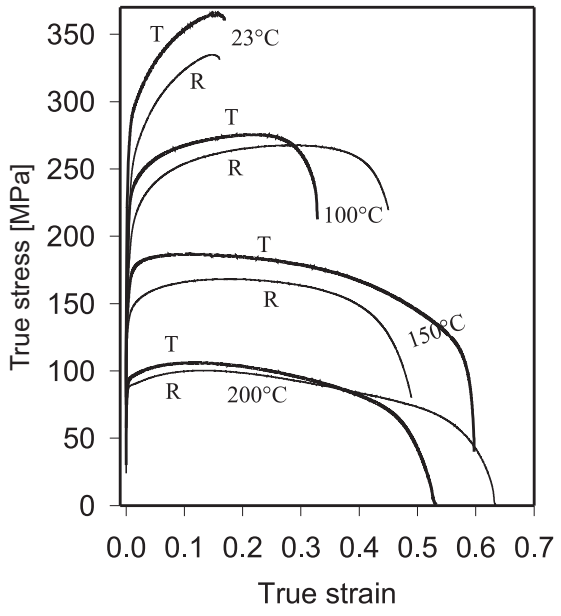

Fig. 4 The true stress-true strain curves of AZ31 sheets measured in tension at various temperatures; the tensile axis was parallel (P) or perpendicular (T) to the rolling direction

values of the yield stress at temperatures below 150 °C for samples after ECAP are higher than those for the cast samples. On the other hand, the yield stress values of samples after ECAP deformed at temeratures above 150 °C are lower than those for the cast samples as shown in Fig. 6 [10]. Processing by ECAP leads to grain refinement. The grain size of the samples after ECAP processing is about 100 nm; much lower than in as-cast samples. An increase of both the yield stress and maximum flow stress of the samples after ECAP deformed at room temperature is caused by the refinement in grain size. The lower values of the yield stress (and the maximum flow stress) of the samples after ECAP pressing measured at 200 and 300 °C in comparison with those of the unpressed material indicate some recovery process(es). Rapid grain boundary diffusion is expected at these temperatures. The elongations to failure of the AZ91 alloy after ECAP pressing are much higher than those of the unpressed alloys.

Considerable improvement of the mechanical properties of magnesium alloys can be achieved by addition of ceramic or graphite

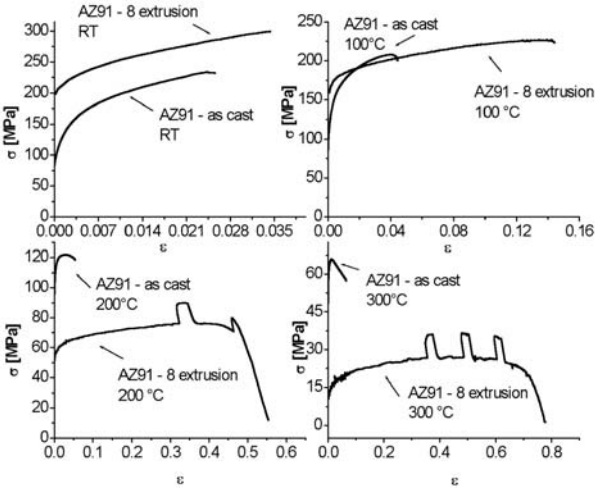

Fig. 5 The true stress-true strain curves measured at different temperatures for cast AZ91 alloy and AZ91 alloy after ECAP processing

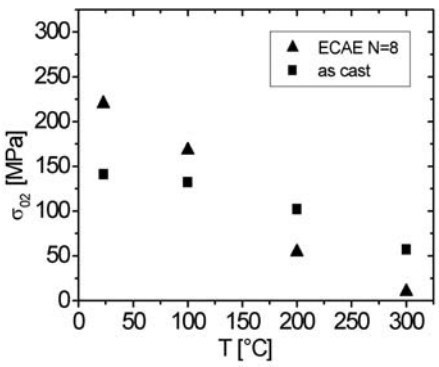

Fig. 6 Temperature dependence of the yield stress of cast AZ91 samples and after ECAP processing

fibres (or particles). Commercial AX41 alloy was reinforced with short fibres of Sigrafil C40 with a mean diameter of 7 μm and a mean length of about 100 μm. Preform of short fibres exhibited a planar isotropic fibre distribution. Metal matrix composites with a fibre volume fraction of 17 vol. % were prepared by squeeze casting. Two kinds of composite samples were investigated in compression tests. The planes of planar randomly distributed fibres were parallel (hereafter referred as Sigrafil_I) and perpendicular (hereafter referred as Sigrafil_II) to the longitudinal axis of the sample (identical to loading direction). Samples were deformed at an initial strain rate of $8.3 \cdot 10^{-5}$ s^{-1} over the temperature range from room temperature up to 300 °C. The temperature in the furnace was kept with an accuracy of ± 2°C.

Figure 7 [11] shows the true stress-true strain curves for AX41+Sigrafil_II deformed at different temperatures. It can be seen that the flow stress decreases with increasing testing temperature. At and above 200 °C, the work hardening rate is decreasing with strain and temperature. Similar deformation behaviour was observed for AX41+Sigrafil_I [11]. Some dynamic recovery occurs. The

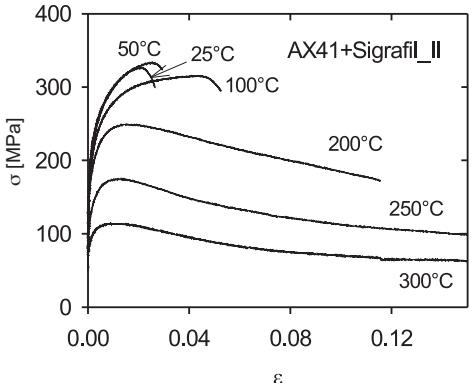

Fig. 7 The true stress-true strain curves of AX41+Sigrafil II deformed at different temperatures; the planes of planar distributes graphite fibres were perpendicular to the tensile axis.

temperature variations of the yield stress, σ_{02}, and maximum stress, σ_{max}, are shown in Fig. 8a for AX41+ Sigrafil_I and in Fig 8b for AX41+Sigrafil_II. A rapid decrease of both the stresses with increasing testing temperature for AX41+Sigrafil_I is obvious whereas the yield stress of AX41+Sigrafil_II decreases very slowly with temperature up to about 200 °C and then a rapid decrease is observed. It is necessary to note the differences in the values of σ_{02} and σ_{max} for the composites with different orientation of the planar fibre distribution to the loading direction.

It is expected that new promising materials may be produced when nanosized ceramic particles are added and distributed in Mg matrices with fine or ultrafine grains. Materials used in this review were ultrafine-grained Mg (hereafter UFG-Mg), UFG-Mg reinforced with 3 vol.% of graphite, and Mg with a mean grain size of about 20 μm (hereafter μ-Mg) reinforces with either 3 vol.% of Al_2O_3 (alumina) or 3 vol.% of ZrO_2 (zirconia) nanoparticles (with a mean grain of 14 nm). Tensile tests were performed in an Instron testing machine at temperatures between 20 and 300 °C at a constant crosshead speed giving an initial strain rate of 6.2×10^{-5} s^{-1}. Uniaxial compression tests were carried out at a constant crosshead speed giving an initial strain rate of 1.4×10^{-4} s^{-1}.

The temperature dependences of the yield stress and maximum stress obtained for UFG-Mg and UFG-Mg+3 vol.% of graphite (200 nm) are presented in Figs. 9 and 10, respectively. Specimens of microcrystalline magnesium reinforced with ZrO_2 and Al_2O_3 nanoparticles were deformed in tension [12]. At temperatures above 100 °C, the work hardening rate is close to zero; a dynamic balance between hardening and softening. The flow stresses for μ-Mg+3n-Al_2O_3 are higher than those for μ-Mg+3n-ZrO_2 at the same testing temperature. Figure 11 shows the temperature variation of the yield stress for microcrystalline Mg reinforced with zirconia and alumina nanoparticles. The difference in the yield stress between both materials deformed at room temperature is about 100 MPa, whereas the differences in the yield stress values at and above 200°C are small. On the other hand, the elongations to failure of μ-Mg+3n-ZrO_2 are higher than those of μ-Mg+3n-Al_2O_3. Similar dependences of

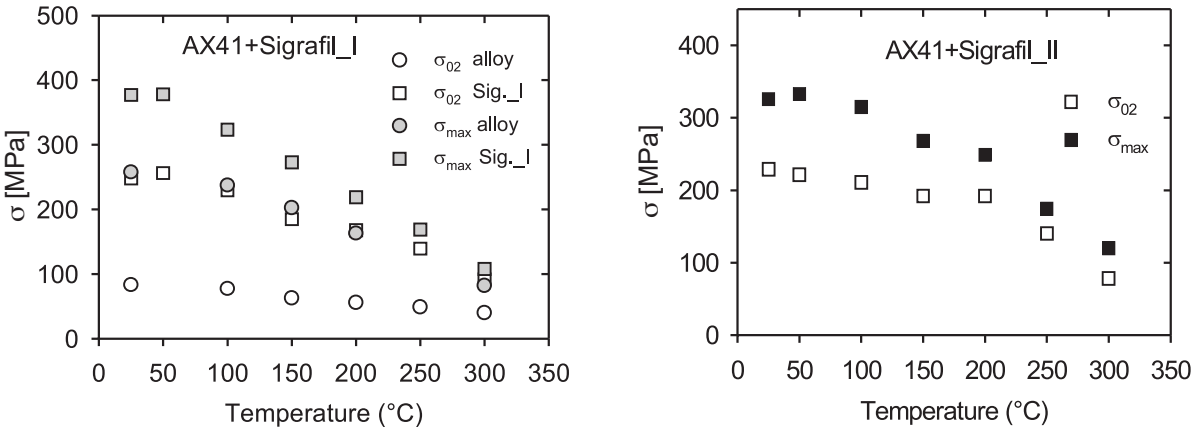

Fig. 8 Temperature variation of the yield stress and maximum stress of (a) AX41+Sigrafil I (the planes of graphite fibres were parallel to the tensile axis) and (b) AX41+Sigrafil II

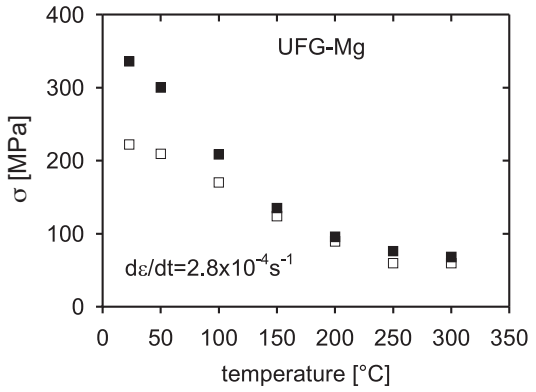

Fig. 9 Temperature dependence of the yield stress and maximum stress of ultrafine-grained magnesium.

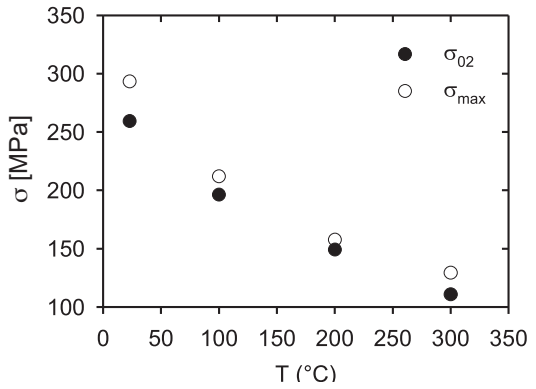

Fig. 10 Temperature dependence of the yield stress and maximum stress of ultrafine-grained magnesium reinforced with 3 vol.% of graphite particles (200 nm)

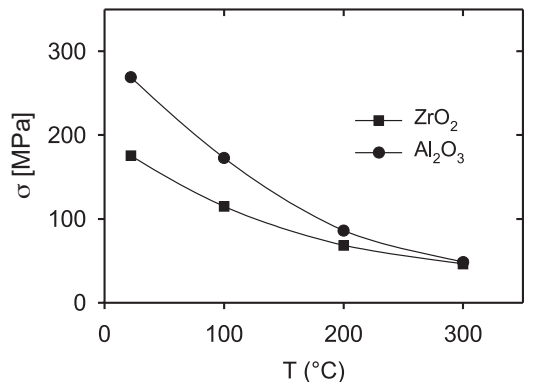

Fig. 11 Temperature dependence of the yield stress of microcrystalline magnesium reinforced with 3 vol.% of ZrO_2 and 3 vol.% of Al_2O_3

the yield stress on the testing temperature were observed for μ-Mg and in μ-Mg+1n-Al_2O_3 [12]. Note the high values of yield stress for magnesium reinforced with 3 vol.% of nanoparticles.

5. Discussion

The deformation behaviors of magnesium alloys and magnesium-based composites are significantly influenced by testing temperature. In order to estimate the deformation mechanisms, the understanding of the effects of deformation temperature and strain on the stress flow is necessitated. It has been found that any restoration processes affect the shape of the true stress-true strain curves. It is expected that both components of the flow stress are a function of strain and temperature.

Analysis of stress relaxation tests indicates that recovery process and dislocation motion are thermally activated processes. The both stress components were determined at different temperatures. Figure 12 [8] shows a part of true stress-true strain curve for AX41 alloy deformed in compression at room temperature. The points indicate the stresses at which the SR tests were performed. The internal stress and the effective stress components are also depicted. It is obvious that the internal stress is a substantial contribution to the applied stress. Similar dependences were obtained e.g. for AJ51

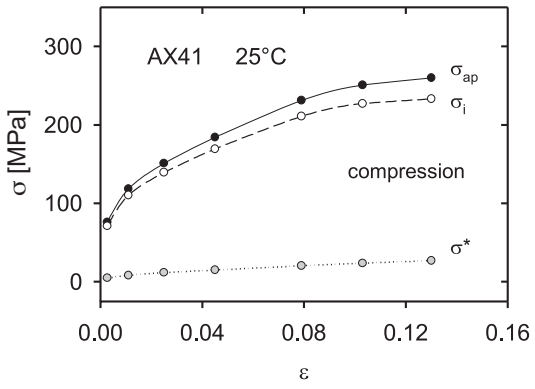

Fig. 12 A part of the true stress-true strain curve of AX41 deformed in compression at room temperature. The points on the curve indicate the stresses at which the SR tests were performed. The both components of the applied stress are shown as a function of strain

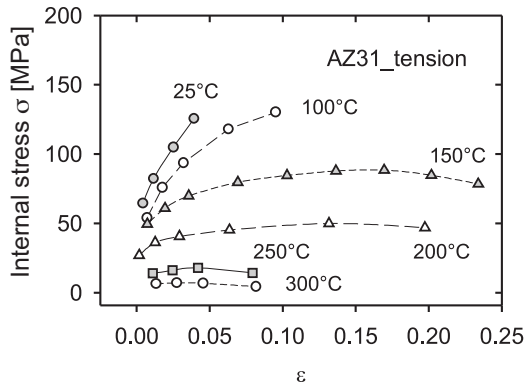

Fig. 13 The internal stress of AZ31 as a function of strain at different testing temperatures

and AZ31. The value of the internal stress depends on the testing temperatures. The values of the internal stress for AZ31 alloy samples are plotted against strain in Fig. 13. A decrease in the internal stress component with increasing test temperature can be seen. It is well-known that the stored dislocations contribute to the strain hardening. Therefore, the observed decrease in the internal stress with temperature indicates a decrease in the total dislocation density – see Eq. (2). The moving dislocations can cross slip and after cross slip they cannot be only stored. They may annihilate, which causes the decrease in the dislocation density. At higher temperatures, the moving dislocations can also climb. The activity of cross slip and climb increases with increasing temperature. This means that the total dislocation density decreases with increasing temperature. It has been reported [8] that the internal stress/applied stress ratio decreases significantly with increasing temperature independent of the deformation mode (the values of the ratio for compression deformation are practically the same as for tension).

The apparent activation volume estimated using Eq. (8) depends on the applied stress and testing temperature. Apparent (experimental) activation volume estimate in experiments with polycrystals is proportional to the dislocation activation volume, V_d, as

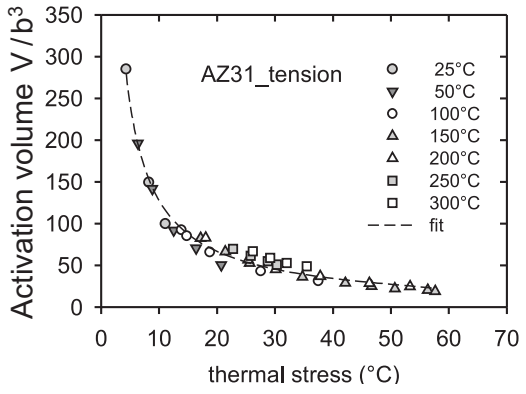

Fig. 14 Activation volume plotted against the thermal stress estimated at various testing temperatures

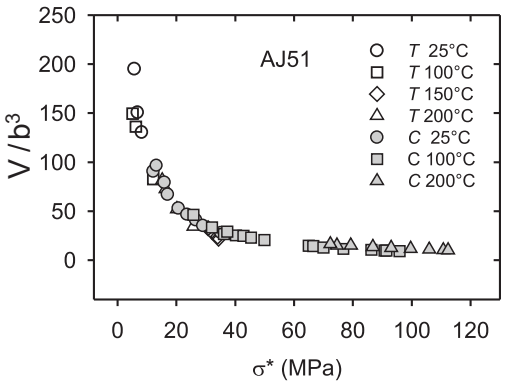

Fig. 15 Activation volume plotted against the thermal stress for AJ51 estimated at different deformation temperatures in compression and tension

$V = (1/\Psi)V_d$, where Ψ is the Taylor factor. Usually, the values of activation volume are given in b^3, which allows their comparison with processes responsible for the thermally activate dislocation motion. The apparent activation volume for AZ31 alloy is a function of the effective stress independently of the testing temperature as shown in Fig. 14. Apparent activation volumes for AJ51 and AJ91 alloys estimated for four deformation temperatures in tensile (T) and compression (C) tests are plotted against the effective (thermal) stress in Figs. 15 and 16 [8]. All values appear to lie on one line, "master curve". In order to analyse the dependences, we will assume an empirical relation between the Gibbs enthalpy ΔG and the effective stress, σ^*, suggested by Kocks et al. [13] in the following form:

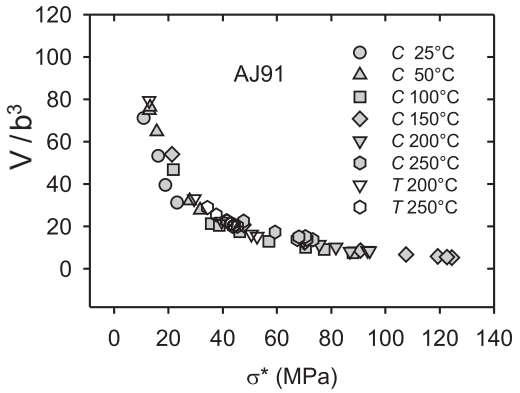

Fig. 16 Activation volume plotted against the thermal stress for AJ91 estimated at different deformation temperatures in compression and tension

$$\Delta G = \Delta G_0 \left[1 - \left(\frac{\sigma^*}{\sigma_0^*}\right)^p\right]^q \tag{6}$$

where ΔG_0 and σ_0^* are Gibbs enthalpy at zero stress and the effective stress at 0 K. It follows:

$$\sigma^* = \sigma_0^* \left[1 - \left(\frac{kT}{\Delta G_0} \ln \frac{\dot{\varepsilon}_0}{\dot{\varepsilon}}\right)^{1/q}\right]^{1/p} \tag{7}$$

where p and q in Eqs. (6) and (7) are phenomenological parameters reflecting the shape of a obstacle profile k is the Boltzmann constant, T is the absolute temperature, $\dot{\varepsilon}$ is the strain rate and $\dot{\varepsilon}_0$ is a pre-exponential factor. The possible ranges of values p and q are limited by the conditions $0 < p \leq 1$ and $1 \leq q \leq 2$. Ono [14], suggested that Eq. (17) with $p = 1/2$, $q = 3/2$ describes a barrier shape profile that fits many predicted barrier shapes. Equation (7) can be rewritten

$$\dot{\varepsilon} = \dot{\varepsilon}_0 \exp\left[-\frac{\Delta G_0}{kT}\left(1 - \left(\frac{\sigma^*}{\sigma_0^*}\right)^p\right)^q\right]. \tag{8}$$

The dependence of the activation volume on the effective stress can be expressed as

$$V = kT\frac{\partial \ln \dot{\varepsilon}/\dot{\varepsilon}_0}{\partial \sigma^*} = \frac{\Delta G_0 pq}{\sigma_0^*}\left[1 - \left(\frac{\sigma^*}{\sigma_0^*}\right)^p\right]^{q-1}\left(\frac{\sigma^*}{\sigma_0^*}\right)^{p-1}. \tag{9}$$

The values of the activation volume should lie at the curve given by Eq. (9). The fit of the experimental values of Eq. (9) – see Figs. (15) and (16) – gives for the activation enthalpy $\Delta G_0 = 0.95 \pm 0.05$ eV for AJ51 and $\Delta G_0 = 1.00 \pm 0.05$ eV for AJ91. Similar values of the activation enthalpy were estimated for all alloy studied.

The values of the activation volume and the activation enthalpy may help to identify thermally activated process considering some of the common short range barriers to dislocation motion [15]. We should consider that a rapid decrease in the internal stress with increasing temperature indicates that observed softening during deformation is connected with dynamic recovery.

It is well-known that the main deformation mode in magnesium and magnesium alloys with hcp structure is basal glide system with dislocations of the Burgers vector $\langle a \rangle = 1/3\ [11\bar{2}0]$. The secondary conservative slip may be realised by the $\langle a \rangle$ dislocations on prismatic and pyramidal of the first order. Couret and Caillard [16, 17] using TEM showed that the screw dislocations with the Burgers vector of $1/3\ [11\bar{2}0]$ in magnesium are able to glide on prismatic planes and their mobility is much lower than the mobility of edge dislocations. They concluded that the deformation behaviour of magnesium over a wide temperature range is controlled by thermally activated glide of those screw dislocation segments. A single controlling mechanism was identified as the Friedel-Escaig cross slip mechanism. This mechanism assumes dissociated dislocations on compact planes, like (0001), that joint together along a critical length L_r producing double kinks on non-compact planes. Therefore, the activation volume is proportional to the critical length between two kinks. Amadieh et al. [18] found for the activation volume of the Friedel–Escaig mechanism a value of 70 b^3. Prismatic slip was also observed by Koike and Ohyama [19] in deformed AZ61 sheets. The activation of the prismatic slip and subsequent annihilation of the dislocation segments with the opposite sign are probably the main reason for the observed internal stress decrease. The double cross slip may be a thermally activated process controlling the dislocation velocity.

The number of independent slip systems in the basal plane is only two. Thus, the von Mises requirement for five independent deformation modes to ensure a reasonable deformability of magnesium alloy polycrystals is not fulfilled. Twinning and the activity of non-basal slip is required. From activities of non-basal slip systems, motion of dislocations with $\langle c+a \rangle$ Burgers vector in the second-order pyramidal slip systems is expected. The critical resolved shear stress (CRSS) for non-basal slip systems at room temperature is higher by about a factor 100 than the CRSS for basal slip. The CRSS for non-basal slip decreases rapidly with increasing temperature. It means that the activity of a non-basal slip system increases with increasing temperature. It is worth mentioning that Mathis et al. [20], who studied the evolution of different types of dislocations with temperature in Mg using X-ray diffraction, found that at higher temperatures the fraction of $\langle c+a \rangle$ dislocations increases at a cost of $\langle a \rangle$ dislocations. The total dislocation density decreases with increasing temperature. The glide of $\langle c+a \rangle$ dislocations may affect the deformation behaviour of magnesium alloys.

The shape of the true stress-true strain curves (Figs. 1–4) indicates that the flow stress and strain hardening and softening is influenced by the testing temperature – at temperatures above about 200 °C, the strain hardening is very close to zero. From the dislocation theory point of view, this deformation behaviour may be explained assuming changes in deformation mechanisms. At temperatures below about 200 °C, strain hardening is caused by multiplication and storage of dislocations. Above about 200 °C, there is not only storage of dislocations during straining leading to hardening but also annihilation of dislocations leading to softening. The intensity of the latter is highly dependent on temperature. A dynamic balance between hardening and softening may take place at higher temperatures. The activity of non-basal slip systems has to play an important role in both hardening and recovery processes in magnesium alloys. The glide of $\langle c+a \rangle$ dislocations may be responsible for an additional work hardening because of the development of several systems of immobile or sessile dislocations. Different reactions between $\langle a \rangle$ basal dislocations and $\langle c+a \rangle$ pyramidal dislocations can occur [21-23]. Glissile (glide) $\langle c+a \rangle$ dislocations can interact with $\langle a \rangle$ dislocations – immobile $\langle c \rangle$ dislocations may arise within the basal plane according to the following reaction:

$$\tfrac{1}{3}\langle 2\bar{1}\bar{1}3\rangle + \tfrac{1}{3}\langle \bar{2}110\rangle \rightarrow \langle 0001\rangle . \qquad (10)$$

Another reaction that employs the basal $\langle a \rangle$ dislocations yields a sessile $\langle c+a \rangle$ dislocation

$$\tfrac{1}{3}\langle 2\bar{1}\bar{1}3\rangle + \tfrac{1}{3}\langle \bar{1}2\bar{1}0\rangle \rightarrow \tfrac{1}{3}\langle 11\bar{2}3\rangle . \qquad (11)$$

Finally, a combination of two glissile $\langle c+a \rangle$ dislocations gives rise to a sessile dislocation of $\langle a \rangle$ type that liess along the intersection of the second order pyramidal planes according to the following reaction:

$$\tfrac{1}{3}\langle 2\bar{1}\bar{1}3\rangle + \tfrac{1}{3}\langle \bar{1}2\bar{1}\bar{3}\rangle \rightarrow \tfrac{1}{3}\langle 11\bar{2}0\rangle . \qquad (12)$$

Different dislocation reactions may produce both sessile and glissile dislocations. Production of sessile dislocations increases the density of the forest dislocations that are obstacles for moving dislocations. Therefore, an increase in the flow stress with straining follows, which is observed in the experiment. On the other hand, screw components of $\langle c+a \rangle$ (and also $\langle a \rangle$) dislocation may move to the parallel slip planes by double cross slip and they can annihilate – the dislocation density decreases, which leads to softening. One has to consider that twins and grain boundaries are also obstacles for moving dislocations in polycrystalline materials. Dislocation pile-ups are formed at the grain boundaries. The stress concentrations at the head of pile-ups contribute to initiations of the activity of the pyramidal slip systems. Another possible source mechanism for $\langle c+a \rangle$ dislocations was proposed by Yoo et al. [24]. The scenario described above can help in understanding the deformation behaviour of magnesium alloy over a wide temperature range.

The increase in the elongation to failure with increasing temperature can be also explained by an increase in the activity of non-basal slip systems.

The addition of the reinforcing phase substantially increases the yield stress of Mg alloys as shown above. Fibres and particles in the matrix act as obstacles for moving dislocations in the slip plane. From figures a significant effect of fibres and/or particles on the yield stress and deformation behaviour at low temperatures (below about 200 °C) and a decreasing effect of the reinforcing phase at higher temperatures can be seen. The main contributions to the yield stress are load transfer and enhanced dislocation density. The analysis – see [25, 26] – showed that the load transfer from matrix to fibres (particles) depends on the reinforcement volume fraction. As to the enhanced dislocation density, important contributions are the density of newly generated dislocations due to thermal stresses and the density of dislocations geometrically necessarily created because of strong strain gradients. It is widely accepted that Orowan strengthening is not significant for metal matrix composites.

6. Conclusions

The mechanical properties and strain hardening effects of magnesium alloys decrease with increasing testing temperature. The increase of the activity of non-basal slip systems with temperature may be responsible for softening. The interactions between dislocations in the non-basal slip system and those in basal slip system cause not only the formation of sessile dislocation leading to hardening but also annihilation of dislocations leading to softening.

Acknowledgements

The authors would like to dedicate this paper to Prof. Ing. Otakar Bokuvka, Ph.D., at the occasion of his 65th birthday. This work was partly supported by the Grant Agency of the Academy of Sciences of the Czech Republic under Grant IAA201120902. A part of this work was financed by the Ministry of Education, Youth and Sports of the Czech Republic under the Research Project 1M2560471601 "Eco-centre for Applied Research of Non-ferrous Metals".

References

[1] MORDIKE, B.L., LUKAC, P.: *Magnesium Technology,* Eds. Fridrich, H. E., Mordike, B. L., Berlin, Springer, 2005.
[2] VALIEV, R. Z., LANGDON, T. G.: *Prog. Mater. Sci.,* No. 51, 2006, 881.
[3] CAILLARD, D., MARTIN, J. L.: *Thermally Activated Mechanisms in Crystal Plasticity,* Amsterdam, Pergamon, 2003.
[4] DOTSENKO, V. I.: *Phys. Stat. Sol.* (b), 93, 1979, 11.
[5] FELTHAM, P.: *Phys. Stat. Sol.* (a), 3, 1963, 1340.
[6] LI, J. C. M.: *Canad. J. Phys.,* 45, 1967, 493.
[7] LI, J. C. M.: *Scripta Metall.,* 15, 1981, 935.
[8] TROJANOVA, Z., LUKAC, P.: *Int. J. Mater. Res.,* 100, 2009, 270.
[9] BALIK, J., LUKAC, P., BOHLEN, J., KAINER, K. U.: *Kovove mater.,* No. 45, 2007, 135.
[10] MATHIS, K., MUSSI, A., TROJANOVA, Z., LUKAC, P., RAUCH, E.: *Kovove mater.,* No. 41, 2003, 293.
[11] TROJANOVA, Z., LUKAC, P.: *Int. J. Mater. Res.,* 100, 2009, 399.
[12] LUKAC, P., TROJANOVA, Z.: *Introduction to Nanotechnology,* Eds. Dusza, J., Drageva, I., Sofia, Herom Press, 2006.
[13] KOCKS, U. F., ARGON, A. S., ASHBY, M. F.: *Prog. Mater. Sci.,* 19, 1975, 1.
[14] ONO, K.: *J. Appl. Phys.,* 39, 1968, 1803.
[15] EVANS, A. G., RAWLINGS, R. D.: *Phys. Stat. Sol.* (a), 34, 1969, 9.
[16] COURET, A., CAILLARD, D.: *Acta Metall.*, 33, 1985, 1447.
[17] COURET, A., CAILLARD, D.: *Acta Metall.*, 33, 1985, 1455.
[18] AMADIEH, A., MITCHELL, J., DORN, J.E.: *Trans. AIME*, 233, 1965, 1130.
[19] KOIKE, J., OHYAMA, R.: *Acta Mater.*, 53, 2005, 1963.
[20] MATHIS, K., NYILAS, K., AXT, A., DRAGOMIR-CERMATESCU, I., UNGAR, T., LUKAC, P.: *Acta Mater.,* 52, 2004, 2889.
[21] LUKAC, P.: *Czech. J. Phys.,* 31, 1981, 135.
[22] LUKAC, P.: *Czech. J. Phys.*, 35, 1985, 275.
[23] LUKAC, P., MATHIS, K.: *Kovove mater.,* No. 40, 2002, 281.
[24] YOO, M. H., AGNEW, S. R., MORRIS, J. R., HO, K. M.: *Mater. Sci. Eng. A,* 321, 2001, 87.
[25] LUKAC, P., TROJANOVA, Z.: *Communications - Scientific Letters of the University of Zilina,* Vol. 11, No. 1, 2009, 5.
[26] TROJANOVA, Z., SZARAZ, Z, GARTNEROVA, V.: *Communications - Scientific Letters of the University of Zilina,* Vol. 11, No. 1, 2009, 10.

K. Bartova – M. Domankova – J. Janovec *

INFLUENCE OF SECONDARY PHASE PRECIPITATION ON RESISTANCE TO INTERGRANULAR CORROSION OF AISI 316L AUSTENITIC STAINLESS STEEL

The AISI 316L steel after cold working of 40% and subsequent annealing at 750°C for 1, 2, 5, 10, 50, or 100 h was investigated. For the microstructure characterization the light microscopy and the transmission electron microscopy were used. To determine the sensitivity to intergranular corrosion the test was performed according to ASTM A 262, practice A. The transition between non-sensitised and sensitised states was found to be between 1 and 2 h of annealing. Sigma, laves and chi phases were identified in all the analyzed conditions. $M_{23}C_6$ was found to start to precipitate between 5 and 10 h of annealing. Sigma, chi, and $M_{23}C_6$ precipitated mainly along the grain boundaries. Laves precipitated mainly inside the grains, and after 50 h of annealing also intergranularly. Time dependent changes in the average metal composition of particular phases were considered as negligible.

Key words: austenitic stainless steel, intergranular corrosion, secondary phase precipitation, transmission electron microscopy

1 Introduction

Austenitic stainless steels (ASS) are frequently used as construction materials of various components in chemical, petrochemical, pharmaceutical and nuclear power industries, because of their excellent corrosion resistance and good mechanical properties at elevated temperatures [1–4]. However, properties of these steels depend strongly on structural, compositional, and morphological characteristics of the grain boundaries, e.g. on the state of intergranular precipitation [5–7].

On heat treatment, welding or service, the unstabilized ASS can be sensitised if isothermally exposed at temperatures 500–800°C or slowly cooled through this temperature range [1, 4, 8, 9]. The sensitisation resulting from microstructural changes can cause intergranular corrosion of unstabilized ASS. The microstructural changes evoking the sensitisation reside mostly in the precipitation of secondary chromium-rich phases (e.g. $M_{23}C_6$, sigma, chi) along the grain boundaries followed by the formation of chromium-depleted zones with chromium content below 12 wt% [10].

Sigma, as a typical phase occurring in the 316L steel, precipitates at temperatures between 550–900°C on grain boundaries, especially on triple points, incoherent twin boundaries and intergranular inclusions [11]. The sigma precipitation has a very slow kinetics, so the formation of precipitates can take hundreds to thousands of hours. Cold work (CW) accelerates its precipitation particularly if also recrystallization occurs on subsequent annealing [11]. Chi is mostly a minor phase and it was found in the AISI 316L steel at temperatures about 750 °C [7]. The formation of this phase can be observed mainly on the grain boundaries, incoherent twin boundaries, coherent twin boundaries and on dislocations within the matrix. Owing to its ability to dissolve carbon and also to its easier nucleation, the chi precipitation, when it occurs, precedes the sigma formation. The chi nucleation is also accelerated by cold work [11]. Laves of the Fe_2Mo type was found in AISI 316 steels with the bulk Mo content between 2–3 wt.% after long-term annealing. It is often a minor phase precipitating intragranularly in the form of equiaxed particles, with occasional occurrence at the grain boundaries [11].

The degree of sensitisation is influenced by many factors, e.g. bulk composition of the steel, grain size, plastic deformation, time-temperature exposure [1, 2, 4, 7]. The influence of time-temperature exposure on the steel sensitisation can be derived from time-temperature-sensitisation (TTS) diagram. In the diagram, each condition characterized by time and temperature of annealing is assigned to the sensitised or the non-sensitised areas separated by typical C-curve. The nose of this curve defines the critical temperature with the minimal time for sensitisation.

In the present work the AISI 316L steel was investigated. The aim of the study resides in the determination of relationships between the steel thermal-deformation history, its resistance to intergranular corrosion, and the state of precipitation. The attention was paid to the characterization of type, metal composition, amount, and distribution of secondary phase particles.

* **K. Bartova[1], M. Domankova[2], J. Janovec[3]**
[1] Institute of Materials Science, Faculty of Materials Science and Technology in Trnava,
[2] Slovak University of Technology in Bratislava, Slovakia, E-mail.: katarina.bartova@stuba.sk

2. Experimental procedure

The chemical composition of the investigated AISI 316L steel is given in Table 1. In the first step, the steel was solution annealed for 1h at 1100 °C. Immediately after the solution annealing, the steel was water quenched to eliminate the formation of new precipitates. In the second step, cold working of the steel sheets was applied at ambient temperature with the deformation of 40 % toward the original sheet thickness. The final step of the sample treatment resided in the isothermal annealing performed at 750 °C for 1, 2, 5, 10, 50 and 100 h.

The samples for the light microscopy were polished up to fine diamond finish (~1μm) and then electrolytically etched for 10–30 s (in dependence on the sample sensitisation) using 10 % oxalic acid at the current density 1 $A.cm^{-2.}$ The metallographic sections were observed by a light microscope NEOPHOT 32 equipped with CCD camera. The samples were tested to determine the sensitivity to intergranular corrosion according to ASTM A 262, practice A (Oxalic Acid Etch Test). In the corrosion test, the same etching procedure as described above for preparing metallographic samples was used, except for the etching time taking 90 s. The following criterion was applied to classify the sensitivity of the etched microstructures to the intergranular corrosion:

- the step structure, when the grain boundaries are not attacked by corrosion,
- the dual structure, when the grains are not completely surrounded by deeply etched boundaries,
- the ditch structure, when at least one grain is completely surrounded by deeply etched boundaries.

The samples showing step or dual structures were considered to be non-sensitised, whereas the samples exhibiting the ditch structure were classified as sensitised [12].

For the identification of secondary phases the transmission electron microscopy (TEM) of extraction carbon replicas was utilised. TEM observations were performed using a JEOL 200 CX microscope operated at 200 kV. It was equipped with an energy dispersive

X-ray spectrometer (EDX). The samples for TEM were prepared as follows:

- etching of the mechanically polished surfaces for 2–3 min with etchant consisting of 10 ml H_2SO_4, 10 ml HNO_3, 20 ml HF and 50 ml H_2O,
- coating of the surfaces with a thin layer of carbon,
- removing the carbon film from the samples in 8 % solution of HCl in ethanol.

At least ten EDX analyses per secondary phase were performed for each condition. At the evaluation of EDX spectra the standardless method for thin specimens was used.

The phase equilibria were calculated for the system corresponding to the investigated steel in the temperature range 500–1500 °C by ThermoCalc software [13] using the database STEEL17 formulated by Kroupa et al. [14]. In the calculation procedure the total Gibbs energy of the system consisting of contributions of individual phases is minimized at constant temperature and pressure. The particular phases were modelled as a sum of the reference level of Gibbs energy, entropy term, excess Gibbs energy, and magnetic term (if plausible the magnetic ordering). In the calculations, the elements Fe, C, Si, Mn, Cr, Mo and Ni were considered, and the phases liquid, delta-ferrite (b.c.c.), austenite (f.c.c.), laves (h.c.p.), M_6C (f.c.c.), $M_{23}C_6$ (f.c.c.), sigma (tetragonal) and chi (b.c.c.) were taken into account.

3. Results

The microstructures of the investigated steels after the solution annealing are composed of polyhedral austenitic grains containing twins (Fig. 1a). After cold working the grains are prevailingly acicular and contain shear bands (Fig. 1b). No precipitates were observed at the grain boundaries of both solution annealed and cold worked conditions. Black discrete areas randomly distributed across the microstructure of the cold worked condition are probably etching artefacts.

TTS diagram for the AISI 316L steel after 40% cold working is illustrated in Fig. 2a. Circles represent experimental results after oxalic acid etch test for the conditions annealed at 750 °C. The solid circles represent sensitised conditions showing the ditch structure. The condition 750 °C/1 h exhibiting the dual structure is illustrated by the empty circle. The microstructures corresponding to conditions 750 °C/1 h and 750 °C/5 h are documented in Figs. 2b and 2c, respectively.

On annealing, secondary phases were observed to start to precipitate on the grain boundaries and in the grain interior. The phases identified are summarized in Table 2. Figs. 3a and 3b show the microstructures of the investigated steel after annealing at 750 °C for 1 h and 2 h, respectively. $M_{23}C_6$ (Fig. 4), chi (Fig. 5) and sigma (Fig. 6) were identified on grain boundaries. Moreover, the particles of laves (Fig. 7) were evidenced. In Figs. 4–7 both the analysed particles and the corresponding diffraction patterns are documented. Average metal compositions of identified secondary phases in the analysed conditions can be seen in Table 3.

Chemical composition of the investigated steel — Table 1

Steel	Contents of elements in wt.%										
	C	N	Si	Mn	P	S	Cr	Ni	Mo	Ti	Fe
AISI 316L	0.021	0.019	0.62	1.10	0.0027	0.004	17.47	12.20	2.10	-	bal.

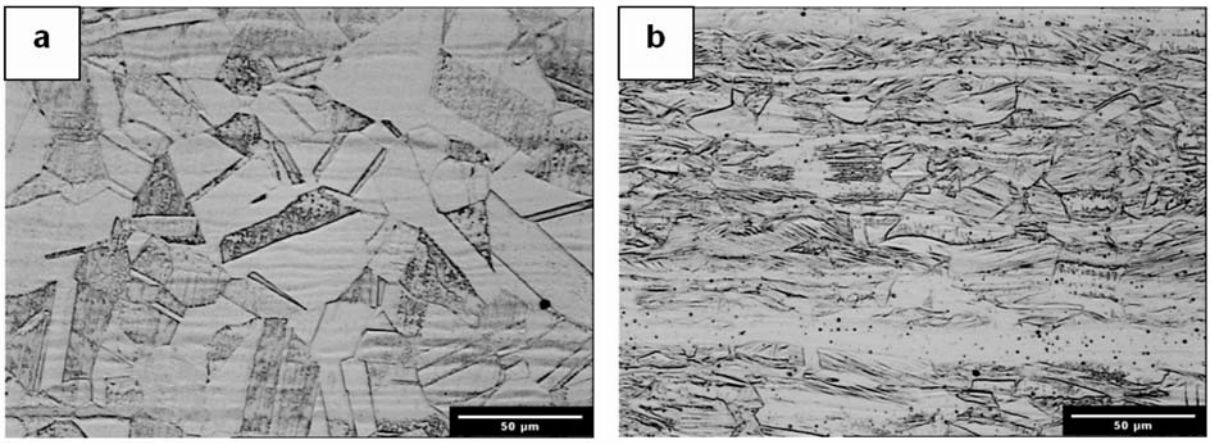

Fig. 1 Microstructures of the investigated steel after solution annealing (a) and subsequent 40 % cold work (b)

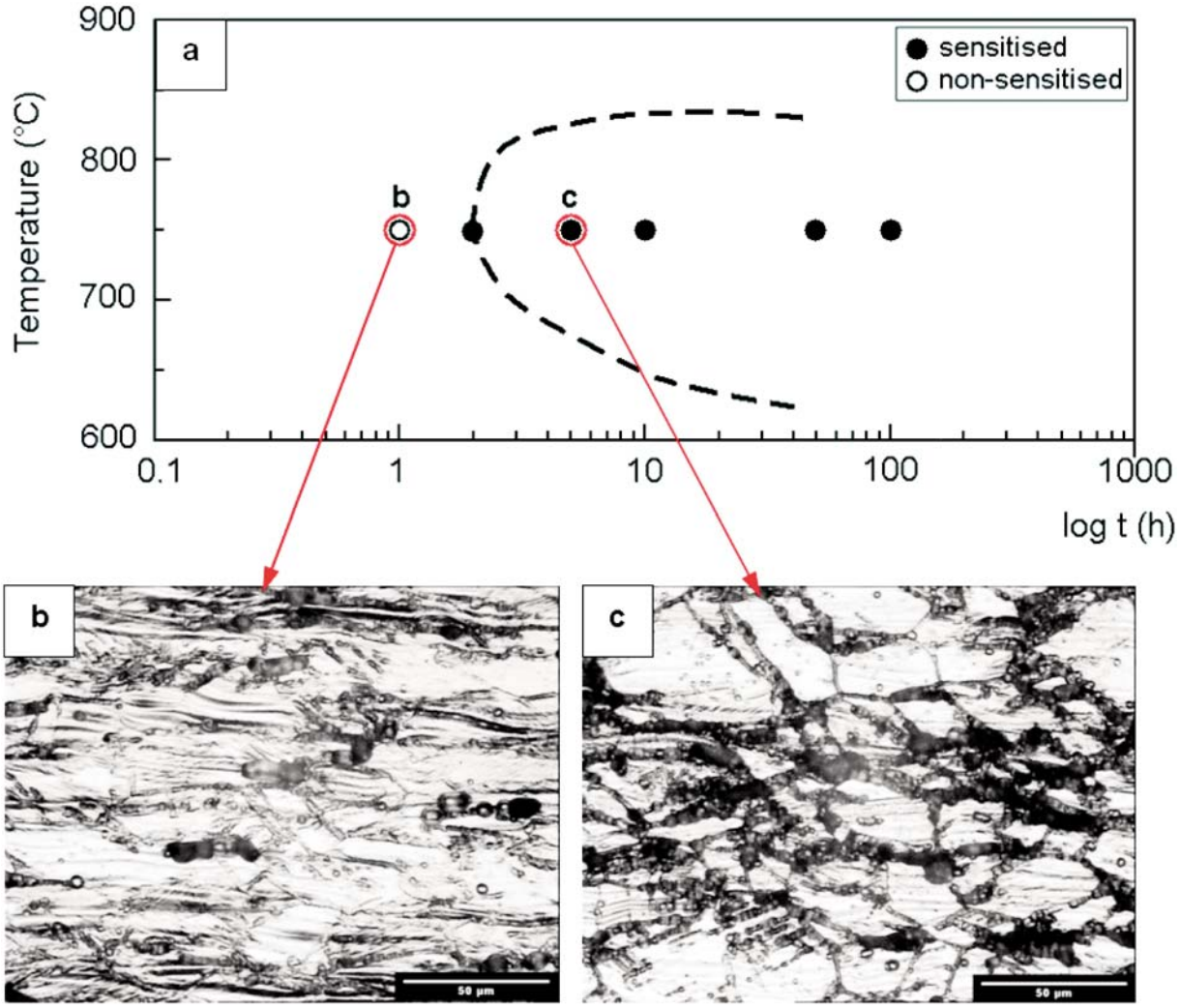

Fig. 2 TTS diagram for the AISI 316L steel after 40% cold working (the circles represent experimental results after oxalic acid etch test for conditions annealed at 750 °C) (a), the microstructure of condition 750 °C/1 h – dual structure (b), the microstructure of condition 750 °C/5 h – ditch structure (c)

Experimentally identified secondary phases in the investigated steel after 40% cold working and subsequent annealing at 750°C. Occurrence of a phase is denoted with symbol "X" Table 2

Annealing time (h)	Secondary phases			
	Sigma	Laves	Chi	$M_{23}C_6$
2	X	X	X	-
5	X	X	X	-
10	X	X	X	X
50	X	X	X	X
100	X	X	X	X

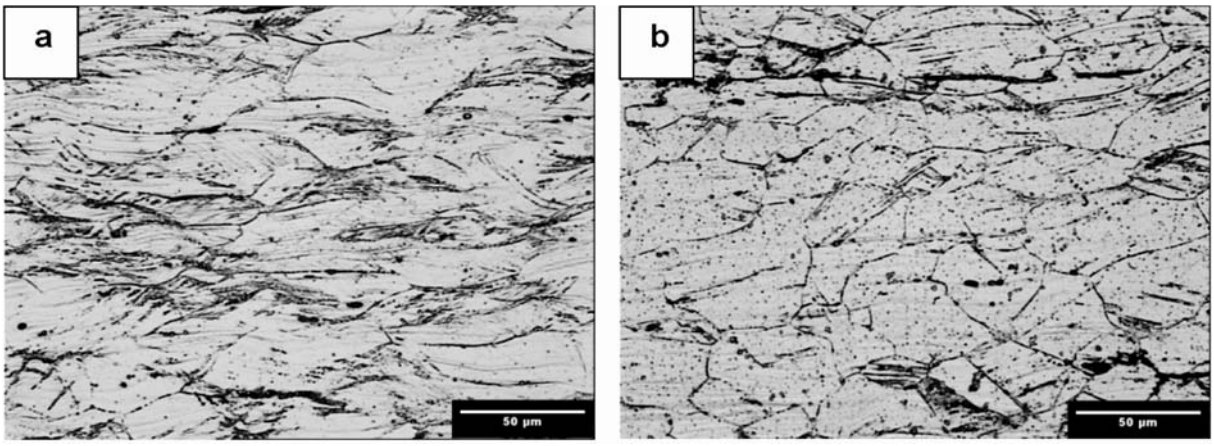

Fig. 3 Microstructures of the investigated steel after annealing at 750 °C/1 h (a), 750 °C/2 h (b)

Metal compositions of identified secondary phases in conditions annealed at 750 °C. Table 3
Average metal compositions of particular phases regardless of condition are highlighted (italic + bolt)

Secondary phases	Annealing time (h)	Mass contents of elements in %				
		Cr	Fe	Mo	Ni	Si
Sigma	2	33.0 ± 1.3	51.2 ± 2.6	10.6 ± 2.6	4.0 ± 0.6	1.3 ± 0.4
	5	32.9 ± 3.9	46.4 ± 4.8	12.9 ± 3.2	5.7 ± 2.7	2.0 ± 2.0
	10	32.7 ± 3.2	48.0 ± 4.8	11.9 ± 4.4	5.1 ± 2.5	2.3 ± 2.7
	50	31.9 ± 2.5	47.8 ± 1.1	13.5 ± 2.7	5.0 ± 0.6	1.9 ± 0.6
	100	32.7 ± 2.2	49.4 ± 2.8	11.3 ± 3.0	5.2 ± 1.2	1.5 ± 0.9
Average metal composition of sigma		32.6 ± 0.9	48.6 ± 3.6	12.0 ± 2.3	5.0 ± 1.2	1.8 ± 0.8
Laves	2	14.4 ± 4.2	28.6 ± 6.5	49.0 ± 8.3	3.8 ± 2.1	4.2 ± 4.0
	5	12.4 ± 5.5	24.7 ± 6.6	51.5 ± 7.0	5.8 ± 4.1	5.6 ± 5.5
	10	11.7 ± 3.6	27.1 ± 9.0	49.6 ± 9.5	4.8 ± 4.6	6.7 ± 5.7
	50	9.7 ± 1.4	25.9 ± 2.5	51.0 ± 2.9	5.0 ± 1.1	8.4 ± 4.4
	100	10.1 ± 1.7	29.5 ± 1.3	49.5 ± 2.0	5.1 ± 1.5	5.9 ± 2.7
Average metal composition of laves		11.7 ± 3.5	27.2 ± 3.3	50.1 ± 2.1	4.9 ± 1.4	6.2 ± 3.1
Chi	2	21.5 ± 4.3	39.1 ± 4.0	33.2 ± 7.3	3.4 ± 1.9	2.7 ± 1.2
	5	25.6 ± 1.0	44.3 ± 2.9	23.7 ± 3.0	4.1 ± 1.2	2.5 ± 0.2
	10	24.3 ± 4.4	43.4 ± 5.7	26.0 ± 5.6	4.1 ± 1.6	2.2 ± 1.8
	50	23.3 ± 1.8	41.6 ± 2.3	27.0 ± 2.5	4.6 ± 0.7	3.5 ± 1.4
	100	22.4 ± 3.3	45.1 ± 5.0	25.2 ± 5.8	4.7 ± 0.9	2.5 ± 2.2
Average metal composition of chi		23.4 ± 3.1	42.7 ± 4.3	27.0 ± 7.1	4.2 ± 0.9	2.7 ± 1.0

Secondary phases	Annealing time (h)	Mass contents of elements in %				
		Cr	Fe	Mo	Ni	Si
$M_{23}C_6$	10	65.9 ± 0.9	15.0 ± 0.2	16.0 ± 0.9	2.9 ± 0.2	0.3 ± 0.0
	50	66.6 ± 5.5	13.7 ± 2.6	16.0 ± 4.5	3.2 ± 1.1	0.6 ± 1.0
	100	68.6 ± 2.3	13.6 ± 0.4	13.7 ± 2.0	3.5 ± 0.4	0.7 ± 0.3
Average metal composition of $M_{23}C_6$		67.0 ± 1.5	14.1 ± 1.0	15.2 ± 1.4	3.2 ± 0.3	0.5 ± 0.3

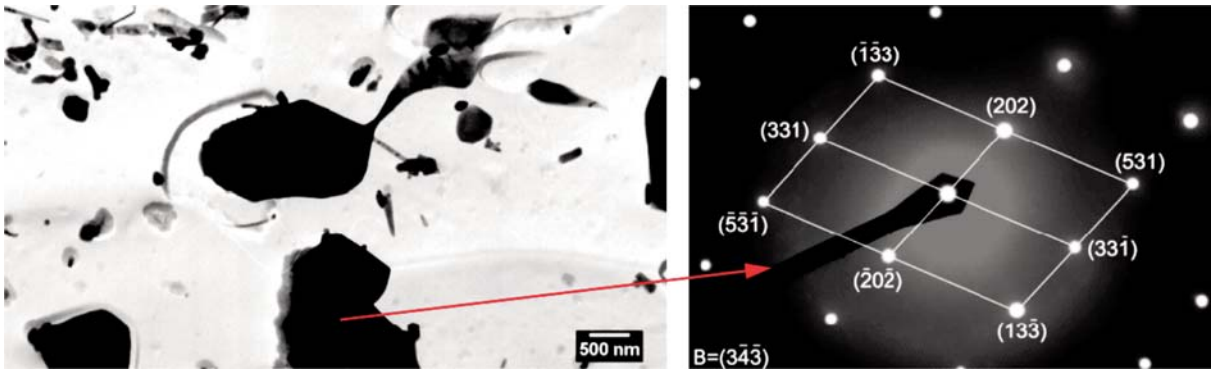

Fig. 4 Particle identified as M23C6 in the condition 750°C/100 h (a), diffraction pattern corresponding to the marked particle (b), TEM of carbon extraction replicas

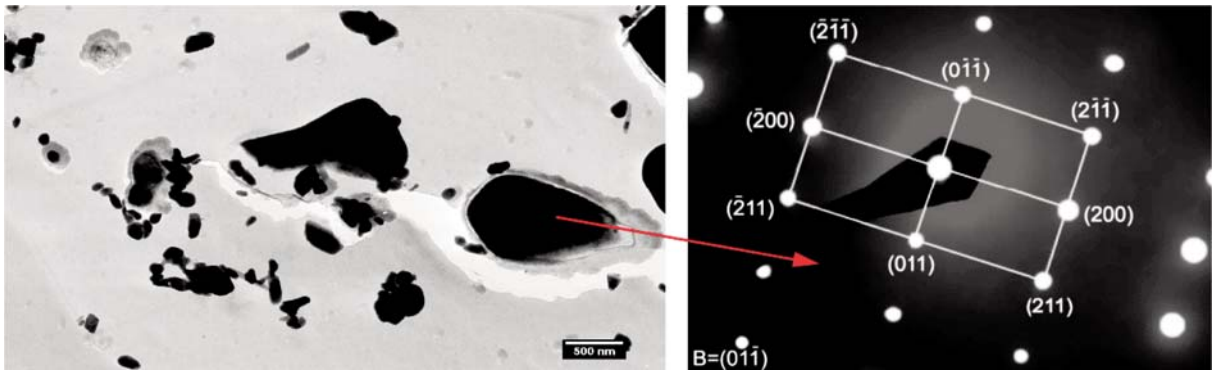

Fig. 5 Particle identified as chi in the condition 750°C/100 h (a), diffraction pattern corresponding to the marked particle (b), TEM of carbon extraction replicas

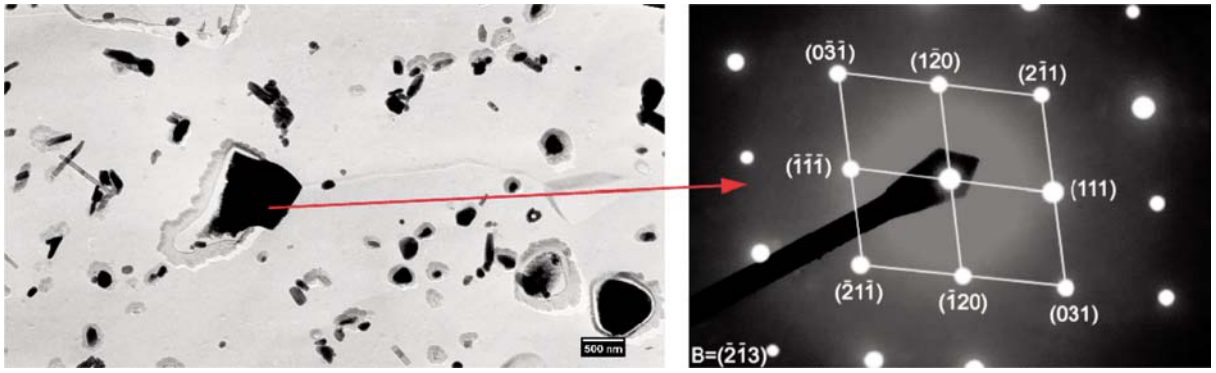

Fig. 6 Particle identified as sigma in the condition 750 °C / 100 h (a), diffraction pattern corresponding to the marked particle (b), TEM of carbon extraction replicas

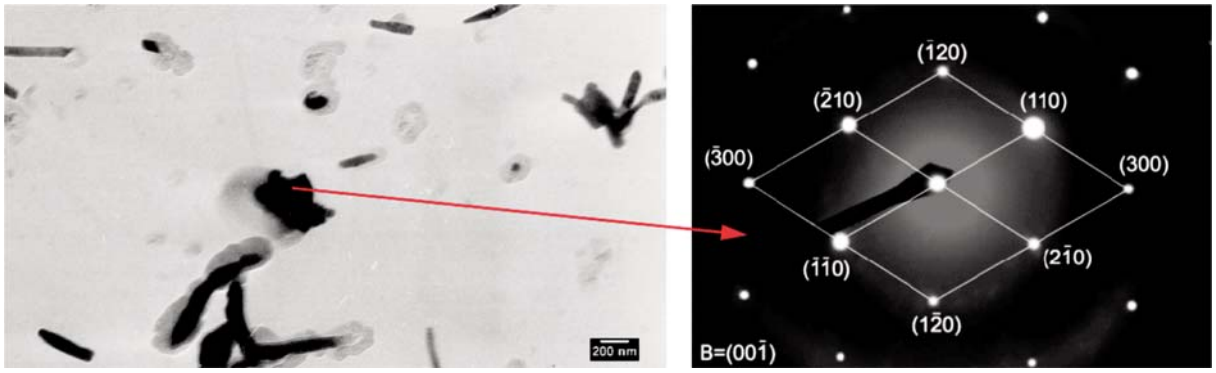

Fig. 7 Particle identified as laves in the condition 750°C/100 h (a), diffraction pattern corresponding to the marked particle (b), TEM of carbon extraction replicas

The experimental characterization of secondary phases was done for the sensitised conditions only. The results of the thermodynamic calculations performed for the temperature range 500–1500 °C are shown in Table 4. According to the prediction, $M_{23}C_6$ is the only secondary phase in equilibrium with austenite at 750 °C.

Phase equilibria predicted for the system corresponding to the investigated AISI 316L steel using ThermoCalc software — Table 4

Temperature range [°C]	Secondary phases predicted to be in equilibrium with austenite
500 – 657	$M_{23}C_6$ + M_6C + sigma
658 – 744	$M_{23}C_6$ + sigma
745 – 849	$M_{23}C_6$
850 – 1500	-

4. Discussion

Two important transitions between the analysed conditions of the AISI 316L steel were found as a result of the current study.

The transition between non-sensitised and sensitised states was determined between 1 and 2 h of annealing at 750 °C according to the corrosion test ASTM A 262, practice A (Fig. 2). During the annealing for 1 h (Fig. 3a) only small changes appear in the microstructure compared to the original 40% CW condition (Fig. 1b). In spite of the "acicular" microstructures documented in Figs. 1b and 3a, the microstructure of the condition annealed for 2 h (Fig. 3b) contains also polyhedral grains surrounded with intergranular particles both features typical for recrystallization. Thus, it is probable that the sensitisation starts between 1 and 2 h of annealing due to a progress in the microstructure recovery and recrystallization.

The another important transition observed between 5 and 10 h of annealing concerns the number of identified secondary phases in the analysed conditions (Table 2). In general, the amount of secondary phase particles in the microstructure was found to increase with increasing the annealing time [7, 8, 11]. Sigma, laves and chi phases were identified in all conditions analysed. The precipitation of $M_{23}C_6$ started however between 5–10 h of annealing. This transition did not influence the steel resistance to intergranular corrosion (Fig. 2), because of a small amount of $M_{23}C_6$ particles in the low-carbon steel (Table 1) and the presence of chromium also in earlier precipitated intermetallic phases (Table 3).

Sigma, chi, and $M_{23}C_6$ were found to precipitate mainly along the grain boundaries. On the other hand, laves precipitated in the grain interior in the form of fine mostly longitudinal particles (Fig. 7). This is in agreement with findings of Padilha and Rios [11]. After 50 h of annealing laves was also found on the grain boundaries in the form of massive particles.

Thermodynamic predictions of phase equilibria for the system corresponding to the AISI 316L steel showed partial agreement with the experimental results. According to the prediction, $M_{23}C_6$ is the only secondary phase co-existing with austenite in equilibrium at 750 °C (Table 4). It shows that sigma, chi, and laves identified experimentally are probably stable phases on annealing for shorter times. In the investigated steel the equilibrium at 750 °C is expected to be reached after annealing for times evidently exceeding 100 h. Then, the amount of the equilibrium $M_{23}C_6$ should increase at the expense of the non-equilibrium intermetallic phases.

The annealing time was not found to influence significantly average values of the metal composition of identified phases. This made possible to calculate the average metal compositions for particular phases regardless of the condition (Table 3). The biggest standard deviations were determined for laves, because the analysed particles of this phase were of smallest dimensions.

5. Conclusions

In the present work the influence of secondary phase precipitation on the resistance to intergranular corrosion of the 40 % cold work AISI 316L steel annealed at 750 °C for 1, 2, 5, 10, 50, and 100 h was investigated. Based on the experimental results the main findings can be summarized as follows:

1. The transition between non-sensitised and sensitised states was found to be between 1 and 2 h of annealing.
2. Sigma, laves, and chi were identified in all the analyzed conditions although they were not predicted to be equilibrium phases at 750 °C. $M_{23}C_6$, predicted to be in equilibrium with austenite at 750 °C, started to precipitate between 5 and 10 h of annealing.
3. Particles of sigma, chi, and $M_{23}C_6$ were observed mainly along the grain boundaries. Laves formed fine mostly longitudinal particles in the grain interior. After 50h of annealing this phase was also observed on the grain boundaries in the form of massive particles.
4. The annealing time was found to influence the average metal composition of the identified secondary phases slightly only.

Acknowledgement

The authors wish to thank to the Grant Agency of the Ministry of Education of the Slovak Republic and the Slovak Academy of Sciences (VEGA) for financial support under the contract No. 1/0126/08.

References

[1] PARVATHAVARTHINI, N, DAYAL, R.K.: Influence of Chemical Composition, Prior Deformation and Prolonged Thermal Aging on the Sensitization Characteristics of Austenitic Stainless Steels, *Journal of Nuclear Materials* 305, 2002, pp. 209–219.
[2] PARVATHAVARTHINI, N, DAYAL, R.K, GNANAMOORTHY, J.B.: Influence of Prior Deformation on Sensitization of AISI Type 316LN Stainless Steel, *Journal of Nuclear Materials* 208, 1994, pp. 209–219.
[3] MAGULA, V, LIAO, J, IKEUCHI, K, KURODA, T, KIKUCHI, Y, MATSUDA, F. New Aspects of Sensitization Behaviour in Recent 316 Type Austenitic Stainless Steels, *Trans. JWRI,* Vol. 25, 1996, pp. 49–58.
[4] ZAHUMENSKY, P, TULEJA, S, ORSZAGOVA, J, JANOVEC, J, SILADIOVA, V.: Corrosion Resistance of 18Cr-12Ni-2,5Mo Steel Annealed at 500-1050°C, *Corrosion Science 41,* 1999, pp. 1305–1322.
[5] DOMANKOVA, M, MAREK P, MORAVCIK, R.: Effect of Annealing at 650°C on Precipitation in Chosen Austenitic Stainless Steels, *Acta Metallurgica Slovaca,* 13, 2007, pp. 52–60.
[6] MAREK, P, DOMANKOVA, M.: Influence of 40% Deformation on Sensitisation Characteristic of 316 and 316L Austenitic Stainless Steels, *Acta Metallurgica Slovaca*, 13, 2007, 61–67.
[7] VACH, M., KUNIKOVA, T., DOMANKOVA, M., SVEC, P., CAPLOVIC, L., GOGOLA, P., JANOVEC J.: Evolution of Secondary Phases in Austenitic Stainless Steels During Long-term Exposures at 600, 650, and 800°C, *Materials Characterization 59*, 2008, 1792–1798.
[8] WASNIK, D.N, DEY, G.K, KAIN, V, SAMAJDAR, I.: Precipitation Stages in a 316L Austenitic Stainless Steel, *Scripta Materialia*, 49, 2003, p. 135–141.
[9] AYDOGDU, G.H, AYDINOL, M.K.: Determination of Susceptibility to Intergranular Corrosion and Electrochemical Reactivation Behaviour of AISI 316L Type Stainless Steel, *Corrosion Science 48*, 2006, 3565–3583
[10] RAMIREZ, L.M, ALMANZA, E, MURR, L.E.: Effect of Uniaxial Deformation to 50% on the Sensitization Process in 316 Stainless Steel, *Materials Characterization 53*, 2004, 79–82
[11] PADILHA, A.F, RIOS, P.R.: Decomposition of Austenite in Austenitic Stainless Steels, *ISIJ International*, Vol. 42, 2002, No. 4, pp. 330–332.
[12] ASM Handbook Vol. 13A Corrosion: Fundamentals, Testing and Protection. *ASM International,* 2003, pp. 266-267.
[13] LUKAS, H.L., FRIES, S.G., SUNDMAN, B.: Computational Thermodynamics. The Calphad Method. *Cambridge University Press,* 2007.
[14] KROUPA, A.: *Personal Communication.*

Jan Michel – Marian Bursak *

THE INFLUENCE OF STRAIN RATE ON THE PLASTICITY OF STEEL SHEETS

The paper analyses the influence of strain rate on the behaviour of un-alloyed steels with Re 210–550 MPa in the deformation process. It presents and analyses the results of the influence of the strain rates ranging from 10^{-3} to 2.5 . 10^{2} s^{-1} on the yield point, tensile strength, elongation and reduction of area. It analyses the non-homogeneity of development of plastic deformation from both, the macroscopic and microscopic points of view, as well as the influence of the strain rate on the development of plastic deformation. Since the intensity of the influence of the strain rate on the properties of materials depends on their internal structure, the tested steels are divided into three groups based on their yield point and yield point of tensile strength ratio.

1. Introduction

The strain rate is an external factor, which significantly influences the limit state of a material, its behaviour in the forming process, as well as on the resulting properties of the formed products [1, 2, 3, 4, 11]. The influence of strain rate on the strength characteristics (yield point, tensile strength) are described using parametric equations [2, 5, 12]. However, the sensitiveness of a material on the strain rate is a function of the material structure, and it can generally be stated that the "more homogeneous" structure, the higher its sensitiveness to the strain rate [6, 7]. In general, it applies that increased strain rate results in increased strength characteristics of materials, while the yield point grows more intensively than the tensile strength [6, 13]. As a result, increased strain rate resulted in an increased of R_e/R_m ratio, and for certain materials at critical strain rate is ratio $R_e/R_m \geq 1$, whereas are created conditions of local loss of plastic deformation This fact significantly influences the formability (in particular pressability) of materials as a result of localization of plastic deformation to "suitable" places.

Plastic deformation is characterized by the fact that its development is markedly non-homogeneous. The non-homogeneity degree is a function of internal and external factors. The internal material microstructure (number and structure of phases, grain size, and structure type) is the internal factor. Increased grain size and number of phases result in significantly increased non-homogeneity of plastic deformation. The temperature, the strain rate and the stress state are crucial external factors [4, 8].

The influence of the strain rate on the development of plastic deformation should be assessed in terms of the deformed body. From the macroscopic point of view, an increased strain rate results in an increased non-homogeneity of deformation of the body as a whole. From the microscopic and submicroscopic points of view, the situation is opposite [8]. However, it applies that an increased degree of plastic deformation results in an increased degree of non-homogeneity.

Increasing the strain rate in forming semiproducts or products is one of the ways of intensification of production. Therefore, an attention is paid to the study of the influence of the strain rate on the behaviour of material in the deformation process, but also on the methodology of evaluation of formability at increased strain rates (including impact ones) [9, 10].

The sensitivity of materials to the strain rate in the forming process is, as mentioned earlier, a material function, and, therefore, it is useful to analyse this sensitivity especially for new materials intended for cold forming. This is necessary in order to determine the limit state, as well as the properties of the final product. The aim of the paper is to extend the pieces of knowledge and to point out certain problems occurring during forming at increased rates (up to impact loads).

2. Experimental material and procedure

Experimental program related to influence of strain rate on plastic characteristics of steel sheets were realized on steel sheets produced by cold forming process. Steel sheets marked as E280G and H340LAD were cold rolled at thickness of 1 mm and next were hot rolled at the final thickness of 8 mm. Microstructure of tested steels is ferrite-pearlite. From steel sheets were taken samples

* **Jan Michel, Marian Bursak**
Department of Material Science, Faculty of Metallurgy, Technical University of Kosice, Slovakia,
E-mail: marian.bursak@tuke.sk

in rolling direction which were for used for tensile test. The main characteristics of tested steels (carbon content, grain size d, and microalloying elements) are shown in Tab. 1

The basic criteria for assessment of the formability of materials obtained during the tensile test including the yield point R_e, the tensile strength R_m, the elongation A, the R_e/R_m ratio.

The presented test result were obtained on the INSTRON tensile testing machine with the loading rate up to 1000 mm/min, as well as on an instrumented pendulum impact testing machine with the loading rate of up to approx. 5 m/s and on a drop tester. By a suitable combination of the loading rate (v) and the deformed length of test bars (L_0), strain rates $\dot{\varepsilon} = v/L_0$ ranging between 10^{-4} and 10^{3} s^{-1} could be obtained.

The influence of the strain rate on the development of plastic deformation was observed from the macroscopic and microscopic points of view. The influence of the strain rate on the development of deformation was observed on test bars, whose measured length was divided into 1 mm divisions. Such prepared test bars were gradually loaded to a certain strain degree (from approx. 5 to 30%). After each strain degree, the distance between individual divisions was measured. The test bars were loaded statically (10^{-3} s^{-1}) and dynamically (10^{2} s^{-1}). The mean non-homogeneity was evaluated, $M = \frac{\sum_{1}^{n} U_x \cdot m}{n}$ where n is the number of elements of the statistic population. The other quantities result from Fig. 8. For evaluation of micro non-homogeneity of plastic deformation, a similar procedure as for evaluation of macro non-homogeneity was used. A metallographic sample was prepared on the test bar stem, and a grid with the mesh size of 0.05 × 0.05 mm was created using a microhardness tester in the area of 1 × 0.5 mm. The mean strain ε was measured on the length of 1 mm, and also on each division at individual strain degrees from 5 to 35%.

3. Influence of the strain rate on the basic mechanical properties

The influence of the strain rate on the basic mechanical properties of the tested steel C4 is shown in Fig. 1, which indicates that increased strain rate results in increased strength properties, while the intensity of growth of R_e is higher than that of R_m. The dependence of the strength properties on the strain rate for unalloyed high-grade steels in the interval from 10^{-3} to 10^{3} s^{-1} was described using parametric equations (1), (2), mostly in the shape presented in [2, 5, 7],

$$R_{e\dot{\varepsilon}} = R_{e\dot{\varepsilon}_0} + A \cdot \ln(\dot{\varepsilon}/\dot{\varepsilon}_0) \quad (1)$$

$$R_{m\dot{\varepsilon}} = R_{m\dot{\varepsilon}_0} + B \cdot \ln(\dot{\varepsilon}/\dot{\varepsilon}_0) \quad (2)$$

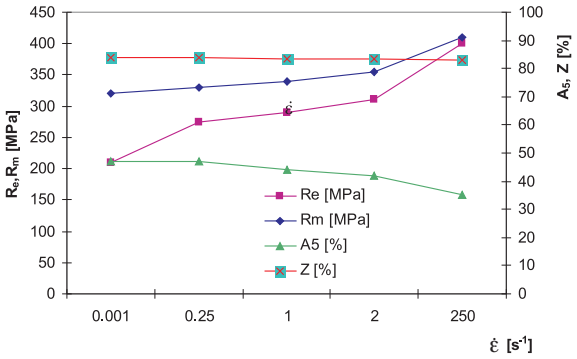

Fig. 1 Influence of the strain rate $\dot{\varepsilon}$ on mechanical properties of steel C4

where R_e, R_m are the yield point and the tensile strength at the respective strain rate $\dot{\varepsilon}$, and $R_{e\dot{\varepsilon}_0}$, $R_{m\dot{\varepsilon}_0}$ are the yield point and the tensile strength at the static strain rate (10^{-3} s^{-1}). The A and B parameters are material constants characterizing the sensitivity of the material to the strain rate. Fig. 2 shows the influence of the strain rate on the increment of the yield point ΔR_e of steel C33 after various heat treatments. The as-quenched steel has the lowest sensitivity to $\dot{\varepsilon}$, because the martensitic structure has the greatest number of obstructions to dislocation movement, and the as-nor-

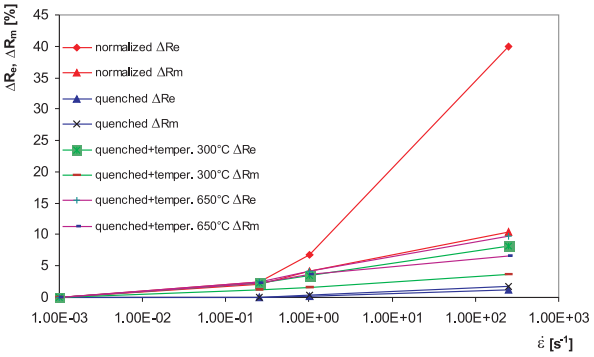

Fig. 2 Influence of the strain rate $\dot{\varepsilon}$ on the increment of strength properties ΔR_e, or ΔR_m, after heat treatment, compared with the initial state ($\dot{\varepsilon} = 10^{-3}$ s^{-1}) of steel C33, after various heat treatments

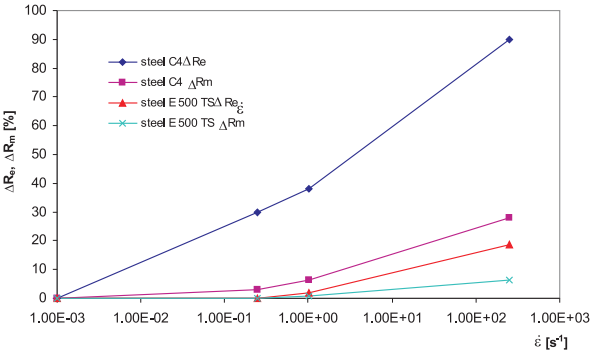

Fig. 3 Influence of the strain rate $\dot{\varepsilon}$ on the increment of strength properties ΔR_e, or ΔR_m, compared with the initial state at $\dot{\varepsilon} = 10^{-3}$ s^{-1} for various steel grades.

Mechanical properties of tested steels at characteristic strain rates. Table 1.

Tested steel	Characteristics	$\dot{\varepsilon}$ s^{-1}			
		10^{-3}	2.5 . 10^{-1}	1	2.5 . 10^{2}
C4 C<0.04% d = 0.031 mm	R_e [MPa] R_e/R_m A_5 [%]	210 0.65 47	275 0.8 46	290 0.83 44	400 0.93 35
E280G C<0.04% d = 0.009 mm	R_e [MPa] R_e/R_m A_5 [%]	295 0.70 30	340 0.79 27	350 0.80 25	459 0.9 22
H340LAD Nb,V<0.1% d = 0.008 mm	R_e [MPa] R_e/R_m A_5 [%]	350 0.81 26	380 0.79 26	430 0.82 26	540 0.94 24
C10 C<0.10% d = 0.022 mm	R_e [MPa] R_e/R_m A_5 [%]	280 0.63 41	340 0.74 40	360 0.78 40	490 0.94 40
C28 C<0.28% d = 0.015 mm	R_e [MPa] R_e/R_m A_5 [%]	370 0.68 30	410 0.74 30	420 0.75 31	540 0.90 33
C33 C<0.33% d = 0.012 mm	R_e [MPa] R_e/R_m A_5 [%]	440 0.62 27	451 0.62 26	470 0.63 26	630 0.80 27
C33 quenched	R_e [MPa] R_e/R_m	1910 0.81	1910 0.81	1910 0.83	1935 0.81
C33 quenched +temp. 300°C	R_e [MPa] R_e/R_m	1480 0.92	1525 0.95	1540 0.95	1600 1.0
C33 quenched +temp. 550°C	R_e [MPa] R_e/R_m	820 0.90	840 0.90	845 0.90	900 0.90
X350M C<0.1% Nb,V d = 0.010 mm	R_e [MPa] R_e/R_m A_5 [%]	380 0.79 34	420 0.80 34	440 0.83 31	590 0.1 30
X420M C<0.1% Nb,V d = 0.0062 mm	R_e [MPa] R_e/R_m A_5 [%]	430 0.75 30	485 0.79 30	500 0.8 30	610 0.87 30
X500M C<0.1% Nb,V d = 0.0037 mm	R_e [MPa] R_e/R_m A_5 [%]	550 0.86 28	550 0.86 28	550 0.86 28	640 0.88 28
X560M C<0.11% Nb,V d = 0.009 mm	R_e [MPa] R_e/R_m A_5 [%]	570 0.87 28	570 0.87 28	570 0.87 28	650 0.89 28
S315MC C<0.05% Nb,V d = 0.007 mm	R_e [MPa] R_e/R_m A_5 [%]	390 0.82 38	420 0.82 38	440 0.82 38	570 0.9 37
S460MC C<0.07% Nb d = 0.006 mm	R_e [MPa] R_e/R_m A_5 [%]	537 0.86 30	550 0.86 30	592 0.86 30	700 0.87 29
E500TS C<0.08% Nb,Ti d = 0.0056 mm	R_e [MPa] R_e/R_m A_5 [%]	540 0.84 39	540 0.84 39	550 0.85 39.5	640 0.94 40

malized steel has the highest sensitivity. Similarly, Fig. 3 documents the influence of $\dot{\varepsilon}$ on ΔR_e and ΔR_m of steels C4 and E500TS with different grain sizes. The grain boundaries are insuperable obstructions to dislocation movement, therefore the finer grain the more obstructions, and the steel is less sensitive to the strain rate $\dot{\varepsilon}$.

In terms of assessment of formability, the R_e/R_m ratio is the most important criterion. Table 1 shows ratio R_e/R_m of the tested steels at four testing conditions (static – 10^{-3} s^{-1}, two quasi-static $-2.5 \cdot 10^{-1}$ and 1 s^{-1} and dynamic $2.5 \cdot 10^2$ s^{-1}) strain rates.

Based on the R_e/R_m ratio at the static tensile test, the tested steels can be divided into three groups: steels with $R_e < 300$ MPa and $R_e/R_m < 0.7$, steels with $R_e > 300$ MPa and $R_e/R_m > 0.7$, and the third group is formed by steels with $R_e > 500$ MPa and $R_e/R_m > 0.8$.

The tests results shown in Tab.1, obtained on various steel grades, confirm that an increased strain rate results in an increased R_e/R_m ratio and the intensity of this increase is a material function. The fewer obstructions to dislocation movement in a material, the more marked intensity of the influence of $\dot{\varepsilon}$. Fig. 4 shows an example how the grain size influences the R_e/R_m ratio at various strain rates.

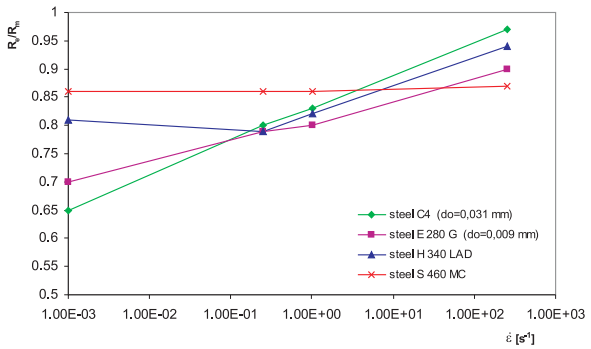

Fig. 4 Influence of the strain rate $\dot{\varepsilon}$ on R_e/R_m for various steel grades.

The analysis of the results of strength properties (R_e, R_m) obtained from tensile test shows that tested steels in strain rates ranging of 10^{-3} to $2.5 \cdot 10^2$ s^{-1} shows the R_e/R_m ratio < 1 and in terms of the macro-volume, up to this strain rate the plastic stability can be maintained up to the strain value corresponding to R_m. The critical value $\dot{\varepsilon}_{cr}$, at the ratio R_e/R_m will equal 1, is influenced by the internal material structure and it can generally be stated that the higher R_e, which is considered to be a macroscopic characteristic of the steel structure, the higher $\dot{\varepsilon}_{cr}$. As proven by the tests made on high-grade unalloyed steels with Re from 210 to 350 MPa (E280G, H340LAD), $\dot{\varepsilon}_{cr}$ is in the interval from 10^2 to 3.10^2 s^{-1}.

4. Influence of the strain rate on the homogeneity of plastic deformation

The elongation (A) and the reduction of area (Z) are the macroscopic characteristics of the plasticity of steel. Fig. 5 shows the graphic relationships $\dot{\varepsilon}$ – A and $\dot{\varepsilon}$ – Z. Tab. 1 shows the values of these quantities at the characteristic strain rates. In terms of the influence of the strain rate in the interval from 10^{-3} to $2.5 \cdot 10^2$ s^{-1} on the above-mentioned characteristics, the tested steels can be classified under the group of steels where the elongation decreases with the growing strain rate, and under the group where the elongation does not change, or even grows. A decrease in the elongation with a growing $\dot{\varepsilon}$ is only shown by steels with $R_e < 300$ MPa after exceeding $R_e/R_m > 0.82$. Steels with a higher yield point

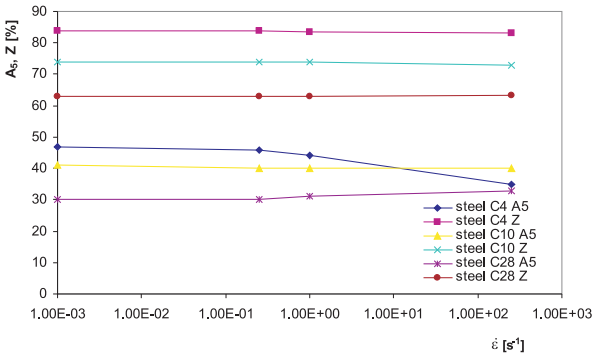

Fig. 5 Influence of the strain rate $\dot{\varepsilon}$ on the elongation A_5 and the reduction of area Z of various tested steel grades

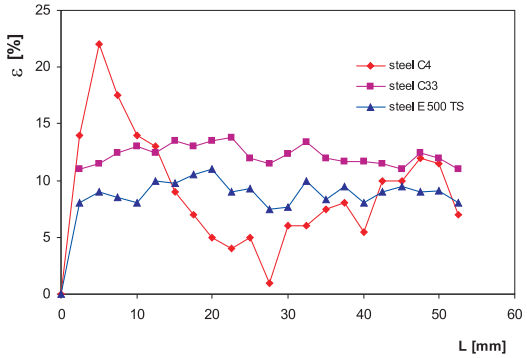

Fig. 6 Distribution of plastic deformation along the test bar at impact loading 10^2 s−1

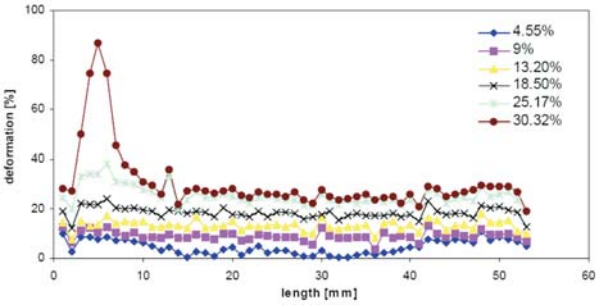

Fig. 7 Distribution of deformation long the test bar at various total strain degrees and impact loading 10^2 s−1 of steel 315MC

maintain or even increase their elongation at $R_e/R_m > 0.82$, too. The non-homogeneity of distribution of deformation along the test bar is influenced, besides the R_e/R_m ratio, also by the $R_m - R_e$ difference. At a little difference, a very non-homogeneous distribution of deformation along the test bar, and hence a decreased elongation, can take place. This assumption is confirmed by Fig. 6, which shows the distribution of deformation along the test bar at the strain rate of 10^2 s^{-1} for steel C4, for which $R_m - R_e = 10$ MPa, steel C33, for which this difference is 160 MPa, and for steel E500TS, where this difference is 100 MPa. Fig. 7 documents the results of measuring the strain distribution along the test bars made of steel S315MC at individual degrees of total strain and dynamic loading. The results of the influence of the strain rate on the criteria of macro non-homogeneity M of the tested steels are presented in Fig. 9. The results show that the non-homogenous strain distribution along the test bar increases with an increased strain degree. The influence of the strain rate on the strain distribution along the test bar depends on the properties of steel. If R_e/R_m approaches to 1 at a given strain rate, then the non-homogeneity of strain distribution along the test bar significantly increases (see Fig. 6, steel C4). If $R_e/R_m < 1$ (0.82 to 0.9), the strain rate favourably influences the strain distribution along the test bar (Fig. 6 and Fig. 9).

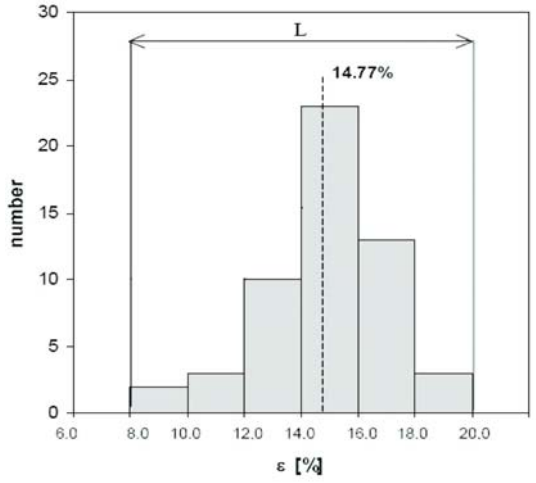

Fig. 8 Histogram of strain distribution at the mean strain ε = 14.77% of steel 315MC at the strain rate of 10^{-3} s^{-1}

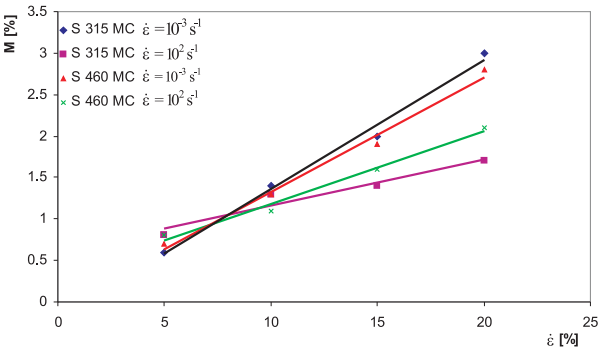

Fig. 9 Relationship between the mean macro non-homogeneity M and the mean strain degree in a micro-area (1x0.5 mm) ε at the strain rates of 10^{-3} and 10^2 s^{-1} of selected steels

The results of the influence of the strain rate on the criteria for micro non-homogeneity of M and L are presented in Fig. 10 and Fig. 11. L is the range of the statistic population (Fig. 8). The results confirms that the micro non-homogeneity increases with an increasing strain degree.

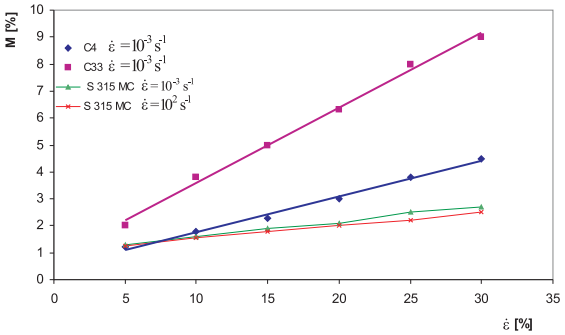

Fig. 10 Relationship between the mean micro non-homogeneity M and the mean strain degree in a micro-area (1x0.5 mm) ε at the strain rates of 10^{-3} and 10^2 s^{-1} of selected steels

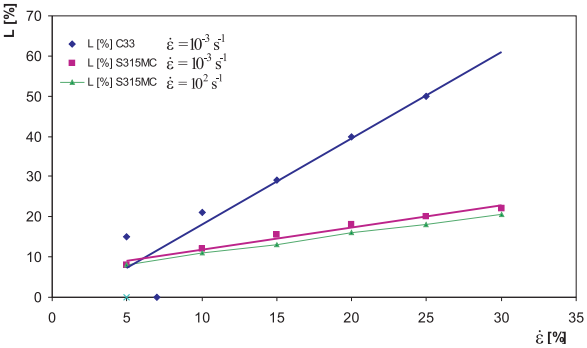

Fig. 11 Relationship between the range of the statistic population L and the mean strain degree in a micro-area ε at the strain rates of 10^{-3} and 10^2 s^{-1}

The results of evaluation of non-homogeneity of plastic deformation show that in the interval of these strain rates from 10^{-3} to 10^2 s^{-1} the non-homogeneity slightly decreases or does not change with an increasing strain rate of the tested steels. This means that forming these steels at higher rates practically does not influence the properties of these products.

The intensity of increase in the non-homogeneity of plastic deformation with an increasing strain degree is a function of the structure, as shown by the results. The degree of non-homogeneity of the steel C33 with the ferrite and pearlite structure is as many as three-times higher than that of steel C4 with the ferrite

structure. It results from Fig. 9–11 that these relationships can be described using the formulae $M = a + k_1 \cdot \varepsilon$, $L = b + k_2 \cdot \varepsilon$ (k_1 and k_2 are material constants). Here it also applies that the less obstructions to dislocation movement in steel, the more non-homogeneous its deformation process, but this deformation process is practically not influenced by the increase in the strain rate.

5. Conclusions

The aim of the paper was to assess the influence of the strain rate in the interval from 10^{-3} to $2.5 \cdot 10^{2}$ s^{-1} on the mechanical properties, with regard to the plasticity of un-alloyed high-grade steels with the yield point from 210 to 550 MPa. Based on the analysis of experimental results obtained from a long time and literature knowledge, the following can be stated:

- The resistance of materials to plastic deformation increases with an increasing strain rate, which increases the strength properties of the tested steels and the yield point to tensile strength ratio R_e/R_m.
- The intensity of increase in R_e/R_m with an increasing strain rate is a function of the internal material microstructure. R_e. The intensity of increase in R_e/R_m with an increasing strain rate is the highest at steels with $R_e < 300$ MPa, lower at steels with $R_e < 500$ MPa, and slight at steels with $R_e > 500$ MPa
- The influence of the strain rate on the plasticity (elongation and reduction of area) values is based on R_e/R_m. Only steels with $R_e < 300$ MPa show a decreased elongation in the observed strain rate interval, from the strain rate where $R_e/R_m > 0.82$. Steels with a higher yield point maintain or increase their elongation.
- The non-homogeneity of plastic deformation increases with an increasing strain degree. The intensity of macro and micro non-homogeneity is a function of the internal material microstructure. An increasing strain rate slightly decreases the micro non-homogeneity of plastic deformation.

Acknowledgemet: This work has been supported by APVV Agency under No. APVV-0326-07

References

[1] PUSKAR, A.: *Medzne stavy materialov a sucasti* [Limit States of Materials and Components], Veda Bratislava, 1989 (in Slovak).
[2] MICHEL, J.: *Materialove inzinierstvo* [Materials Engineering], 3/1996, p. 22 (in Slovak).
[3] BURSAK, M., MICHEL, J., STABA, J.: *Materialove inzinierstvo* [Materials Engineering], 14/2007, 3, 195 (in Slovak).
[4] ELFMARK, J.: *Plasticita kovu,* [Metal Plasticity], VSB Ostrava, 1984 (in Czech).
[5] MICHEL, J., MAMUZIC, I., BURSAK, M.: *Metalurgija* [Metallurgy], 35/1996, 2, p. 69 (in English).
[6] MICHEL, J., MIHALIKOVA, M.: *Vplyv vybranych faktorov na vlastnosti konstrukcnych oceli* [Effect of Selected Factors on the Properties of Structural Steels], Letna skola unavy : Zilina : Oscadnica, 2008 (in Slovak).
[7] MICHEL, J., CIZMAROVA, E., ORUZINSKA, S.: *Kovove materialy* [Metallic Materials], 37/1999, 3, p. 191 (in Slovak).
[8] CIZMAROVA, E., MICHEL, J.: *Acta Metallurgica Slovaca,* 9/2003, p. 90. (in English).
[9] BURSAK, M., MAMUZIC, I.: *Metalurgija* [Metallurgy], 46/2007, 1, p. 37 (in English).
[10] JANOVEC, J., ZIEGELHEIM, J.: *Rust uzitnych vlastnosti u tenkych automobilovych plechu* [Enhancement of Utility Properties on Thin Automotive Sheets], In: Technologie ´99, STU Bratislava, 1999, p. 319 (in Czech).
[11] ZHU YUNTIAN, LONGDON TERENCE: In: *Materials Science and Engineering,* A409 (205), 234
[12] NIECHAJIVICZ,A., TOBOTA, A.: In *Arcivives of Civil Mechanical Engineering,* Vol. VIII., No.2, (2008), 129
[13] MISHRA, A. at all.: In: *Acta Materialia* 56, (2008), 2770.

Milan Zmindak – Daniel Riecky – Josef Soukup *

FAILURE OF COMPOSITES WITH SHORT FIBERS

Strength-based failure criteria are commonly used with the finite element method (FEM) to predict failure events in composite structures. The laminate analogy is very useful for the calculation of the strength of composite materials with short fibers. The prediction of the laminate strength is carried out by evaluating the stress state within each layer of the laminate based on the classical lamination theory. In this paper FEM is used as a tool to predict the laminate strength. Failure criteria are used to calculate a failure index (FI) from the computed stresses and user-supplied material strengths. The micromechanical analysis has been carried out using computer package MATLAB and numerical simulation has been executed by using a commercially available ANSYS code.

Keywords: composite structures, short fibers -reinforced composites, failure criteria, failure index

1. Introduction

Specifically fiber-reinforced composites are one of the most widely used man-made composite materials; they are constituted by reinforcing fibers embedded in a matrix material.

The strength of the uniaxially oriented fibrous structures strongly depends on the length of reinforcing fibers in case of short fibers composites. The fiber and matrix properties, fiber aspect ratio and volume fraction as well as their orientation distribution strongly influence the mechanical response of these materials. Due to the complexity of their microstructure, damage in short fiber composites is extremely difficult to assess numerically or experimentally. Damage involves several types of local degradation processes such as matrix microcracking, fiber/matrix debonding leading to fiber pullout and breakage, etc. These damage mechanisms can occur successively or simultaneously and thus reduce the overall properties of the composite.

Modelling can play an important role in the analysis and design of fiber-reinforced composite materials. Their mechanical properties and possible failure modes can be predicted early during the design stage using effective modeling techniques such, as FEM, boundary element method, a fast boundary element method, meshfree and meshless method, etc. [6, 8]. Recent developments in commercial FEA packages allow the designer to make the detailed analysis of composites.

In a laminate, stresses in the individual layers with different orientations are generally different. Therefore, some of the layers probably reach their limiting stresses before the other remaining layers and they fail first. This is generally referred to as first-ply failure [1, 9]. A fiber-reinforced laminate may or may not be able to carry loads except during the failure initiation, depending on the nature of the first failure. There are two factors contributing to this behaviour. First, the constituent materials are brittle in nature and do not tolerate local failures. The second factor is a large difference in stiffness and strength between the two principal material directions in a layer.

This paper pertains to the micromechanical analysis of composite materials with short fibers. The micromechanical analysis takes into account the nature of the constituents and their distribution. It can be used to evaluate the overall properties of composites. Failure criteria are used to calculate a failure index (FI) from the computed stresses and user-supplied material strengths. The micromechanical analysis has been carried out using computer package MATLAB. FEM is used as a tool to predict the laminate strength based on the classical lamination theory [3]. Numerical simulation has been prepared by using a commercially available ANSYS code.

2. Micromechanics of composite material with short fibers

The basic building block of a composite structure is a unidirectional continuous fiber-reinforced lamina. Placed at various angles of several unidirectional laminae we get a general composite structure. The classical laminate theory is the most commonly used theory for analysing composites with randomly – oriented short fibers [7, 10]. The laminates with the orientation of angles

* **Milan Zmindak[1], Daniel Riecky[1], Josef Soukup[2]**
[1] Department of Applied Mechanics, Faculty of Mechanical Engineering, University of Zilina, Slovakia, Email: Milan.Zmindak@fstroj.uniza.sk
[2] Department of Machinery and Mechanics, Faculty of Production Technology and Management, Jan Evangelista Purkyne University in Usti nad Labem,

[0/±45/90] and [0/±60] are particularly very suitable for practical applications. In order to predict the strength of this type of composite, it is best to use the maximum strain criterion and then the strength of a composite with randomly-oriented short fibers can be determined by using the properties of unidirectionally reinforced composites with short fibers.

Transverse shear stresses are important in failure investigation of composite laminates, primarily because they cause delamination. The longitudinal and transverse modules of these composites can be expressed by Halphin Tsai equations [7]

$$E_1 = E^{(m)}\frac{1+\frac{l}{d}\zeta_E\eta_L\xi}{1-\eta_L\xi} \qquad E_2 = E^{(m)}\frac{1+\zeta_E\eta_T\xi}{1-\eta_T\xi}$$

$$G_{12} = G^{(m)}\frac{1+\zeta_E\eta_G\xi}{1-\eta_G\xi} \qquad v_{12} = v^{(m)}\frac{1+\zeta_E\eta_v\xi}{1-\eta_v\xi} \tag{1}$$

where

$$\eta_L = \frac{\frac{E^{(f)}}{E^{(m)}}-1}{\frac{E^{(f)}}{E^{(m)}}+\zeta_E\frac{1}{d}} \qquad \eta_T = \frac{\frac{E^{(f)}}{E^{(m)}}-1}{\frac{E^{(f)}}{E^{(m)}}+\zeta_E}$$

$$\eta_G = \frac{\frac{G^{(f)}}{G^{(m)}}-1}{\frac{G^{(f)}}{G^{(m)}}+\zeta_E} \qquad \eta_v = \frac{\frac{v^{(f)}}{v^{(m)}}-1}{\frac{v^{(f)}}{v^{(m)}}+\zeta_E} \tag{2}$$

while the superscripts (m) and (f) refer to matrix and fiber, respectively, ζ_E is a reinforcing factor. It depends on the geometry of the fiber in a composite, the packing arrangement of the fibers and its loading conditions. It ranges in value between 1 and 2. However, only when a reliable experimental value of the E_2 is available for a composite, the factor ζ_E can be derived and then applied to predict the E_2 for a range of fiber-volume ratios of the same composite.

A random microstructure results in transversely isotropic properties on a meso-scale level. A simple alternative is to assume that the random microstructure is well-approximated by a periodic microstructure model (Fig.1) [9]. Periodic microstructure mechanics exploits the geometric periodicity of the system in order to simplify mechanical field variables, such as stress, strain, and stiffness. In general, there is a correlation between all of these terms and the position inside the representative volume element (RVE) [11].

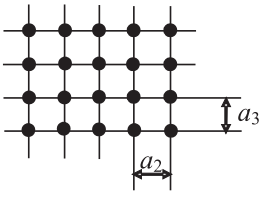

Fig. 1 A periodic microstructure model, square array of fibers.

A simpler alternative is to assume that the random microstructure is well approximated by the hexagonal microstructure displayed in Fig. 2.

The elastic properties of a homogenized material can be computed by [2], i.e. the longitudinal and transversal Young's moduli E_1 and E_2, the longitudinal and transversal Poisson's ratios v_{12} and v_{21} and the longitudinal shear modulus G_{12}, as follows

$$E_1 = C_{11} - 2C_{12}^2/(C_{22}+C_{33})$$

$$v_{12} = C_{12}/(C_{22}+C_{33}) \tag{3}$$

$$E_2 = (C_{11}(C_{22}+C_{33}) - 2C_{12}^2)(C_{22}-C_{33})/(C_{11}C_{22}-C_{12}^2)$$

$$C_{12} = C_{66}$$

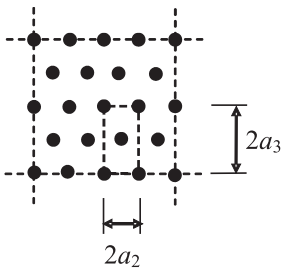

Fig. 2 A hexagonal microstructure model

In order to evaluate the elastic matrix C of a composite, the RVE (fig. 3) is subjected to an average strain.

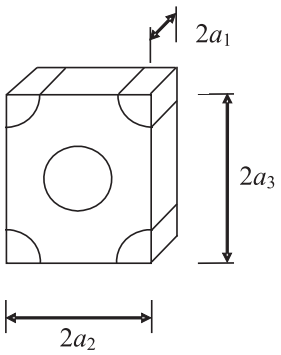

Fig. 3 Representative volume element (RVE)

Then the volume average of the strain in the RVE equals to the applied strain

$$\bar{\varepsilon}_{ij} = \frac{1}{V}\int_V \varepsilon_{ij}dV\,. \tag{4}$$

The components of the tensor C are determined by solving three elastic models of the RVE with its parameters (a_1, a_2, a_3) subjected to the boundary conditions (BC). The unit strain applied to the boundary results in a complex state of stress in the RVE.

Subsequently, the volume average of stress in the RVE equals the required components of the elastic matrix as follows

$$C_{ij} = \bar{\sigma}_i = \frac{1}{V}\int_V \sigma_i dV\,. \tag{5}$$

The coefficients in C are specified by setting a different problem for each column of C. Then the components C_{ij} are determined in three steps:

1. For the components C_{i1} $(i = 1, 2, 3)$, the strain is applied to stretch the RVE in the fiber direction x_1

$$\varepsilon_1^0 = 1,$$

$$\varepsilon_2^0 = \varepsilon_3^0 = \gamma_4^0 = \gamma_5^0 = \gamma_6^0 = 0 \tag{6}$$

and the applied BC are

$$u_1(a_1, x_2, x_3) = a_1,\ u_2(x_1, a_2, x_3) = 0,\ u_3(x_1, x_2, a_3) = 0,$$

$$u_1(0, x_2, x_3) = 0,\ u_2(x_1, 0, x_3) = 0,\ u_3(x_1, x_2, 0) = 0, \tag{7}$$

The coefficients C_{i1} are specified by using the expression

$$C_{i1} = \bar{\sigma}_i\,. \tag{8}$$

2. For the components C_{i2} $(i = 1, 2, 3)$, the strain is applied to stretch the RVE in the direction x_2.

$$\varepsilon_2^0 = 1,$$

$$\varepsilon_1^0 = \varepsilon_3^0 = \gamma_4^0 = \gamma_5^0 = \gamma_6^0 = 0 \tag{9}$$

and the applied BC are

$$u_1(a_1, x_2, x_3) = 0,\ u_2(x_1, a_2, x_3) = a_2,\ u_3(x_1, x_2, a_3) = 0,$$

$$u_1(0, x_2, x_3) = 0,\ u_2(x_1, 0, x_3) = 0,\ u_3(x_1, x_2, 0) = 0, \tag{10}$$

Again, the coefficients C_{i2} are specified by using

$$C_{i2} = \bar{\sigma}_i\,. \tag{11}$$

3. For the components C_{i3} $(i = 1, 2, 3)$, the following strain is applied to stretch the RVE in the direction x_3.

$$\varepsilon_3^0 = 1,$$

$$\varepsilon_1^0 = \varepsilon_2^0 = \gamma_4^0 = \gamma_5^0 = \gamma_6^0 = 0 \tag{12}$$

and applied BC are

$$u_1(a_1, x_2, x_3) = 0,\ u_2(x_1, a_2, x_3) = 0,\ u_3(x_1, x_2, a_3) = a_3,$$

$$u_1(0, x_2, x_3) = 0,\ u_2(x_1, 0, x_3) = 0,\ u_3(x_1, x_2, 0) = 0, \tag{13}$$

Equally, the coefficients C_{i3} are specified by using

$$C_{i3} = \bar{\sigma}_i\,. \tag{14}$$

The coefficient C_{44} can be determined as follows

$$C_{44} = \frac{1}{2}(C_{22} - C_{33})\,. \tag{15}$$

The fiber-volume fraction is expressed as

$$v_f = \frac{\pi}{\sqrt{3}}\left(\frac{d^2}{2a^2}\right). \tag{16}$$

3. Failure criteria for fiber-reinforced orthotropic layers

The strength of unidirectional fibers composite materials depends on the direction of fibers on a macroscopic scale. Composite layers are much stronger in the fibers direction than in the direction perpendicular to their fibers. For loads that are primarily parallel to the fibers, either in tension or compression, the material strength is generally determined by the failure of the fibers. For loads transverse to the fibers, failure is controlled by the failure of the much weaker matrix material. The strength of a composite layer in any other direction is based on various failure criteria [4]. Failure criteria for unidirectional fiber composites used in this paper assume a state of plane stress and are therefore only applicable to thin laminates. New 3D criteria for thick composites are derived in [12].

3.1 Maximum stress and maximum strain criteria

The basic assumption in predicting the failure of fiber-reinforced layers using the maximum stress and maximum strain criteria is the same as for any other isotropic material. Failure is assumed when the maximum stress along the fiber or transverse to the fiber directions exceeds the strengths in tension or compression.

The failure surface is defined as

$$\begin{aligned} &\sigma_1 < X_t, \quad \sigma_2 < Y_t && \text{for} \quad \sigma_1, \sigma_2 > 0 \\ &\sigma_1 > -X_c, \quad \sigma_2 > -Y_c && \text{for} \quad \sigma_1, \sigma_2 < 0 \\ &|\tau_{12}| < S \end{aligned} \tag{17}$$

where X and Y represent the ultimate strengths along and transverse to the fiber directions respectively, indexes $_t$ and $_c$ refer to tension and compression, respectively, S is the ultimate in-plane shear strength of a specimen under pure shear loading.

Similarly, the maximum strain criterion states that failure occurs when one of the following inequalities is violated

$$\begin{aligned} &\varepsilon_1 < \frac{X_t}{E_1}, \quad \varepsilon_2 < \frac{Y_t}{E_2}, \quad \varepsilon_1, \varepsilon_2 > 0 \\ &\varepsilon_1 > -\frac{X_c}{E_1}, \quad \varepsilon_2 > -\frac{Y_c}{E_2}, \quad \varepsilon_1, \varepsilon_2 < 0 \end{aligned} \tag{18}$$

$$|\gamma_{12}| < \frac{S}{G_{12}}$$

3.2 Tsai-Wu criterion

A more general form of the failure criterion for orthotropic materials under plane stress is expressed as [7]

$$F_{01}\sigma_1 + F_{11}\sigma_1^2 + 2F_{12}\sigma_1\sigma_2 + F_{02}\sigma_2 + \\ + F_{22}\sigma_2^2 + F_{44}\tau_{12}^2 < 1 \quad (19)$$

where

$$F_{01} = \frac{1}{X_t} - \frac{1}{X_c},\ F_{11} = \frac{1}{X_t X_c},\ F_{02} = \frac{1}{Y_t} - \frac{1}{Y_c},\ F_{22} = \frac{1}{Y_t Y_c},$$

$$F_{12} = -\frac{1}{2}\frac{1}{\sqrt{X_t X_c Y_t Y_c}},\ F_{44} = \frac{1}{S^2}.$$

The failure criterion for an orthotropic material under a strain is expressed as

$$G_{01}\varepsilon_1 + G_{11}\varepsilon_1^2 + G_{12}\varepsilon_1\varepsilon_2 + G_{02}\varepsilon_2 + \\ + G_{22}\varepsilon_2^2 + G_{44}\gamma_{12}^2 < 1 \quad (20)$$

where

$$G_{01} = F_{01}E_{11} + F_{02}E_{12},\ G_{02} = F_{02}E_{22} + F_{01}E_{12},$$

$$G_{11} = F_{11}E_{11}^2 + F_{22}E_{12}^2 + F_{12}E_{11}E_{12},$$

$$G_{22} = F_{22}E_{22}^2 + F_{11}E_{12}^2 + F_{12}E_{22}E_{12},$$

$$G_{12} = 2E_{12}(F_{11}E_{11} + F_{22}E_{22}) + 2F_1(E_{12}^2 + E_{11}E_{22}),$$

$$G_{44} = F_{44}E_{44}^2.$$

When $F_{12} = \frac{-1}{2X_t^2}$, the Tsai-Wu criterion is reduced to the Tsai-Hill criterion, and when $F_{12} = \frac{-1}{2X_t X_c}$ the Tsai-Wu criterion is reduced to the Hoffman criterion [7].

These failure criteria are used to calculate a failure index (FI) from the computed stresses and user-supplied material strengths. The failure index as a response of quantity is used for several FEM packages and it is defined as

$$I_F = \frac{stress}{strenght}. \quad (21)$$

Failure criteria predict the first occurrence of failure in one of the laminate layers. A value less than 1 denotes no failure and failure is predicted when $I_F \geq 1$. The strength ratio is the inverse of the failure index.

It is important to distinguish between the fiber failure (FF) and the inter-fiber failure (IFF). In the case of shear plane stress, the IFF criteria discriminates three different modes [1]. The IFF Mode *A* is when perpendicular transversal cracks appear in the lamina under transverse tensile stress with or without in-plane shear stress. The IFF Mode *B* denotes perpendicular transversal cracks, but in this case they appear under in-plane shear stress with small transverse compression stress. The IFF Mode *C* indicates the start of oblique cracks when the material is under significant transversal compression.

The FF and the three IFF modes yield separate failure indices. The failure index for FF is defined as

$$I_{FF} = \begin{cases} \sigma_1/X_t & if \quad \sigma_1 > 0 \\ \sigma_1/X_c & if \quad \sigma_1 < 0 \end{cases}. \quad (22)$$

For IFF with positive transverse stress, Mode A is active. The failure index in this case is defined as

$$I_{IFF,A} = \sqrt{\left(\frac{\tau_{12}}{S}\right)^2 + \left(1 - p_{6t}\frac{Y_t}{S}\right)^2\left(\frac{\sigma_2}{Y_t}\right)^2} + p_{6t}\frac{\sigma_2}{S} \\ \text{if} \quad \sigma_2 \geq 0, \quad (23)$$

where $p_{6t} = 0.3$.

Under negative transverse stress, either Mode *B* or Mode *C* is active, depending on the relationship between in-plane shear stress and transversal shear stress. The failure indices are defined as

$$I_{IFF,B} = \frac{1}{S}\left[\sqrt{\tau_{12}^2 + (p_{6c}\sigma_2)^2} + p_{6c}\sigma_2\right], \quad \text{if} \begin{cases} \sigma_2 < 0 \\ \left|\frac{\sigma_2}{\tau_{12}}\right| \leq \frac{F_{2A}}{F_{6A}} \end{cases} \quad (24)$$

$$I_{IFF,C} = -\frac{Y_c}{\sigma_2}\left[\sqrt{\left(\frac{\tau_{12}^2}{2(1+p_{2c})S}\right)^2 + \left(\frac{Y_c}{\sigma_2}\right)^2}\right], \ if \begin{cases} \sigma_2 < 0 \\ \left|\frac{\sigma_2}{\tau_{12}}\right| \geq \frac{F_{2A}}{F_{6A}} \end{cases} \quad (25)$$

where $p_{6c} = 0.2$.

The limit between Mode *B* and Mode *C* is defined by the relation F_{2A}/F_{6A}, where

$$F_{2A} = \frac{S}{2p_{6c}}\left[\sqrt{1 + 2p_{6c}\frac{Y_c}{S}} - 1\right], \quad (26)$$

$$F_{6A} = S\sqrt{1 + 2p_{2c}},\ p_{2c} = p_{6c}\frac{F_{2A}}{S}. \quad (27)$$

4. Numerical examples

Example 1:

In this example, a composite with randomly oriented fibers is assumed with its material characteristics for the fibers: $E_f = 210$ GPa,

$v_f = 0.3$ and for the matrix $E_m = 31$ GPa, $v_m = 0.15$. The geometrical characteristics of the fibers are $L = 6$ cm, $d = 0.75$ mm.

The material characteristics of the composite material given for a variable amount of fibers are shown in Tab. 1, including their Young's modulus E and Poisson's ratio .

Material characteristics Tab.1

	Halphin Tsai		Periodic micro-structure model		Classical laminate theory	
	30 kg/m^3	60 kg/m^3	30 kg/m^3	60 kg/m^3	30 kg/m^3	60 kg/m^3
E Young's modulus [GPa]	31.644	31.795	31.239	31.426	331.470	31.960
Poisson's ratio	0.151	0.151	0.150	0.151	0.1470	0.1480

For the given amount of fibers of 30kg/m^3 and 60kg/m^3, there are only minor differences in the material characteristics regardless of the method used, whether the Halphin Tsai method, the periodic microstructure model or the classical laminate theory. The correlation between the modulus of elasticity and the fibers volume fraction is given in Fig. 4.

The modules of elasticity – the first-ply E_{1FAIL}, the second-ply E_{2FAIL} and the ultimate failure E_{3FAIL} in a fictitious laminate [0/45/-45/90]S are used instead of these in a composite with short fibers. The values calculated using the classical laminate theory are given in Tab. 2.

Modules of elasticity Tab. 2

	30kg/m^3	60kg/m^3
E_{1FAIL} [GPa]	31.47	31.96
E_{2FAIL} [GPa]	23.66	24.10
E_{3FAIL} [GPa]	15.75	16.02

The main characteristic essentially changed is the strength of a composite with short fibers. In the absence of more accurate information, the average and characteristic value of an equivalent flexural tensile strength for steel wire fibers can be calculated as follows [5]

$$R_{e_{m,150}} = \frac{180 W_f \lambda_f d_f^{1/3}}{180C + W_f \lambda_f d_f^{1/3}} \tag{28}$$

with $C = 20$ for hooked-end steel fibers under the trade name of Dramix, where W_f is the fiber content (in kg/m^3), d_f is the diameter of steel fibers, and λ_f is the ratio between the length and the diameter of steel fibers. The flexural tensile strength $f_{fctm,eq}$ and characteristic flexural tensile strength $f_{fctk,eq}$ for fibers are given as (Tab. 3)

$$f_{fctm,eq} = \frac{R_{e_{m,150}} f_{fctm,eq}}{100}, f_{fctk,eq} = 0.7 f_{fctm,eq}\,. \tag{29}$$

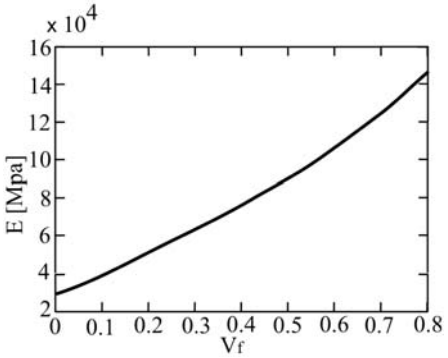

Fig.4. The correlation between the modulus of elasticity and the fiber volume fraction

Flexural tensile strengths Tab. 3

	30 kg/m^3	30 kg/m^3 RC80/60-BN	60 kg/m^3	60 kg/m^3 ZC30/.50
$f_{fctm,eq}$ [MPa]	2.448	2.26	3.519	3.40
$f_{fctk,eq}$ [MPa]	1.714	1.83	2.463	2.40

Example 2:

In this example, failure indices were determined. In this case the laminate consists of four layers [30/60/90/0] made from the uniform material AS4D/9110 [11] with the uniform thickness. The dimensions and the boundary conditions are described in Fig. 5.

The model is obtained by using the ANSYS input command sequence and the element SHELL99. Following the generation of model material strengths, the failure indices were calculated. The strength constants of AS4D/9110 material are: $F_{1t} = 1830$ MPa, $F_{1c} = -1096$ MPa, $F_{2t} = 57$ MPa, $F_{2c} = -228$ MPa, $c_6 = -1$, $c_5 = -1$, $c_4 = -1$.

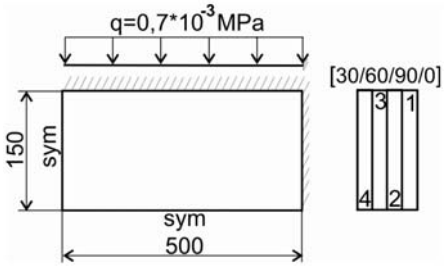

Fig. 5 Loads and the geometry of the laminate and the numbering of its layers

The results are summarized in Tab.4, where $I_{F,MAX\ S}$ is the maximum stress failure index and $I_{F,TW}$ is the Tsai-Wu failure index. As can be seen from the given results, the maximum FI's are in layer 1. The distribution of failure indices is given in Fig. 9. In the following two layers the maximum FI's occurred in the

Failure indices Tab. 4

No. Lamina	$I_{F,MAX\,S}$				$I_{F,TW}$			
	Max.	Node	Min.	Node	Max	Node	Min.	Node
1.	1.29e-2	1	3.32e-7	212	9.52e-3	519	−5.64e-5	202
2.	7.64e-3	4	1.23e-7	212	5.79e-3	4	−3.63e-5	202
3.	3.56e-3	1	0.50e-7	262	1.33e-3	4	−1.92e-4	24
4.	3.22e-6	202	0.35e-9	6627	0.1e-12	202	0.34e-18	467

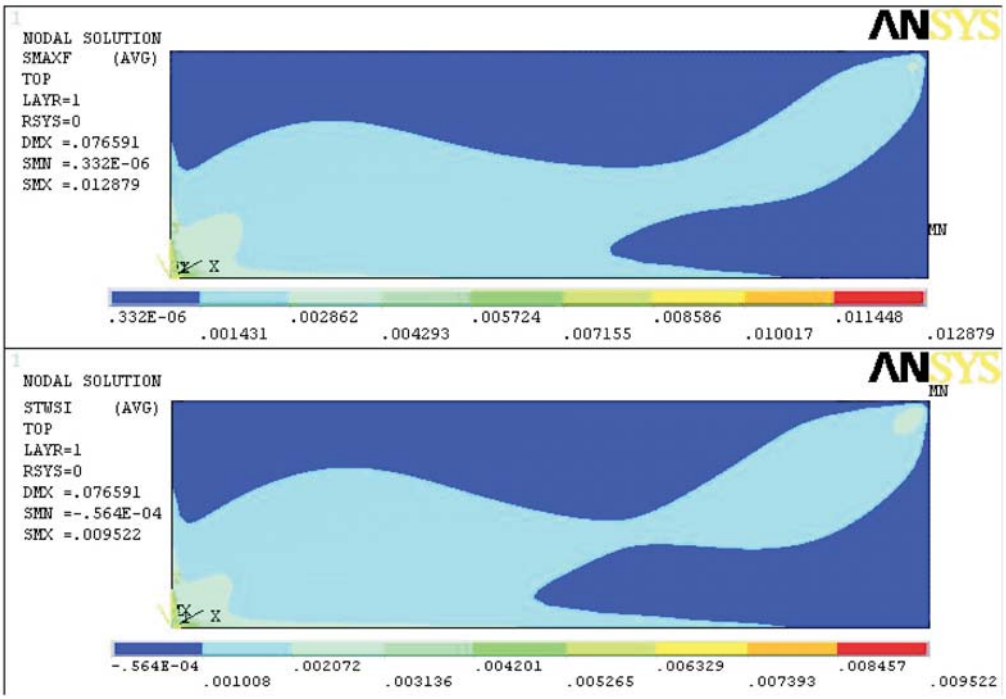

Fig. 9 The distribution of failure indices $I_{F,MAX\,S}$, $I_{F,TW}$ in the first lamina

middle of the laminate. Moreover, the distribution of the FI's in layer 4 is different, the FI values are the smallest and their locations changed. The minimum values occurred in the corner of the laminate where it is fixed.

5. Conclusion

Some calculation methods for the calculation of the modulus of elasticity and the strength of randomly reinforced composite materials are derived in the first example. There are no significant differences in the modulus of elasticity when using the Halphin Tsai method, the periodic microstructure model or the classical laminate theory. The main characteristic that changed essentially is the strength of a composite with short fibers. In the second example failure criteria are presented using failure index. The maximum failure index was calculated using the maximum stress criterion. A laminate plate from AS4D/9110 material was used and the maximum stress failure index $I_{F,MAXS}$ and the Tsai-Wu failure index $I_{F,TW}$ were computed.

Acknowledgements

The authors gratefully acknowledge the support by the Slovak Science and Technology Assistance Agency registered under number APVV-0169-07, the Slovak Grant Agency VEGA 1/0657/09, and the Czech Science Foundation (Project-No GA CR 101/07/0946).

References

[1] ALTENBACH, H., ALTENBACH, J., KISSING. W.: *Structural Analysis of Laminate and Sandwich Beams and Plates*. Lublin, 2001.

[2] BARBERO, E. J.: *Finite Element Analysis of Composite Materials.* In: CRC Press : Taylor & Francis Group, 2008.

[3] CARRERA, E.: T*heories and Finite Elements for Multi-layered Plates and Shells.* In: Arch. Comput. Meth. Engng. 10 (3), 2003, pp. 215–296.

[4] DAVILA, C. G., CAMANHO, P. P., ROSE, CH. A.: *Failure Criteria for FRP Laminates.* In: J. of Composite Materials, Vol. 39, No. 4, 2005, pp. 323–345.

[5] DRAMIX Guideline: *Design of Concrete Structures.* No. 4, 1995.

[6] KOMPIS, V., ZMINDAK, M., MURCINKOVA, Z.: *Trefftz Radial Basis Functions.* Proc. of Leuven Symposium on Applied Mechanics in Engineering (LSAME.08) : Part I : Proc. of Trefftz 08, 5th International Workshop on Trefftz Methods, Leuven, 2008.

[7] LAS, V.: *Mechanics of Composite Materials (in Czech),* West Bohemia University, 2008.

[8] LIU, Y. J., NASHIMURA, N., OTANI, Y., TAKAHASHI, T., CHEN, X. L., MUNAKATA, H.: A Fast Boundary Element Method for Analysis of Fiber – Reinforced Composites Based on a Rigid-Inclusion Model, In: *Journal of Applied Mechanics,* Vol.72, 2005, pp.115–128.

[9] LUCIANO, R., BARBERO, E. J.: Formulas for the Stiffness of Composites with Periodic Microstructure. In: *Int. J. of Solids and Structures,* 31 (21), 1995, pp. 2933-2944.

[10] MALLICK, P. K.: Fiber-Reinforced Composites: Materials. In: *Manufacturing and Design,* CRC Press, Taylor & Francis, 2007.

[11] QU, J., CHEREKAOIU, M.: *Fundamentals of Micromechanics of Solids.* John Wiley & Sons : Hoboken ; New Jersey, 2006.

[12] STAMBLEWSKI, CH., SANKAR, B.V., ZENKERT, D.: Analysis of Three-Dimensional Quadratic Failure Criteria for Thick Composites using the Direct Micromechanics Method, In: *Journal of Composite Materials,* Vol. 42, No. 7, 2008.

Jan Kohout – Vojtech Hruby *

MUTUAL RECIPROCAL INTERCONNECTION OF RELATIONS DESCRIBING CREEP, YIELD STRESS AND STRESS RELAXATION

The steady-state creep rate increases with testing temperature according to the Arrhenius law and its increase with applied stress is usually described by the power law. Simple multiplication of these two laws leads to the dependence of steady-state creep rate on both the variables. Apparent activation energy and stress sensitivity parameter perform in the combined law as constants but most measurements show their dependence on some of the variables. An equation respecting these experimental facts and simultaneously also based on the Arrhenius equation and the power law is derived and verified using some published results of creep tests. It can be presented geometrically by hyperbolic paraboloid. Resulting from this equation, the dependence of yield stress on temperature and strain rate and also an equation describing the relaxation curves are deduced.

1. Introduction

The steady-state creep rate $\dot{\varepsilon}$ at a given applied stress σ increases with temperature T according to the Arrhenius equation (e.g. Cadek [1])

$$\dot{\varepsilon} \propto \exp\left(-\frac{Q_a}{RT}\right) \quad \text{where} \quad Q_a = \left.\frac{\partial \ln \dot{\varepsilon}}{\partial(-1/RT)}\right|_{\sigma = const.} \tag{1}$$

is the apparent activation energy of creep and R is the universal gas constant. The increase of the creep rate at a given temperature with applied stress is mostly described by the power law

$$\dot{\varepsilon} \propto \sigma^{n} \quad \text{where} \quad n = \left.\frac{\partial \ln \dot{\varepsilon}}{\partial \ln \sigma}\right|_{T = const.} \tag{2}$$

is the stress sensitivity parameter (see Garofalo [2]). Combining Eqs (1) and (2), an equation

$$\dot{\varepsilon}(\sigma, T) = C\left(\frac{\sigma}{G}\right)^{n} \exp\left(-\frac{Q_a}{RT}\right) \tag{3}$$

is obtained describing the dependence of creep rate on both the variables determining experimental conditions (e.g. Cadek [1], Sherby [3]). The main role of elasticity modulus in shear G is to avoid the problems with physical units in the case when n is not equal to integer.

The values of apparent activation energy and of stress sensitivity parameter are implicitly assumed to be constant but nearly all the results of creep tests show that the apparent activation energy depends on applied stress and the stress sensitivity parameter depends on temperature. The solution of these contradictions is the main aim of the present paper.

During several last decades the main attention was paid to physical approach: various creep mechanisms were described by means of many different models. Each of the models leads to certain integer value of stress sensitivity parameter in the range from 1 to 7 (see e.g. Cadek [1]). The results of creep experiments lead to real values of this parameter sometimes substantially overreaching the value of 10. The approach presented in this paper is fully phenomenological but without any limitation of the stress sensitivity parameter value.

2. New relation for steady-state creep rate

Apparent activation energy Q_a is defined for constant applied stress and stress sensitivity parameter n is defined for constant temperature, see Eqs (1) and (2). Therefore, dependences $Q_a = Q_a(\sigma)$ and $n = n(T)$ can be considered. Considering Eqs (1) and (2), the creep rate can be concurrently expressed in the following two ways

$$\dot{\varepsilon}(\sigma, T) = A(\sigma)\exp\left[-\frac{Q_a(\sigma)}{RT}\right] \text{ and } \dot{\varepsilon}(\sigma, T) = B(T)\sigma^{n(T)} \tag{4}$$

because the factor of proportionality A can be dependent (at least principally) on applied stress and the factor of proportionality B can be dependent on temperature. But both relations (4) should be equivalent in principle. To derive the common equation, the values $\sigma = 1$ (MPa) and/or $T \to \infty$ are introducing, for which Eqs (4) turn substantially simpler [4]

$$\dot{\varepsilon}(1, T) = A(1)\exp\left[-\frac{Q_a(1)}{RT}\right] = B(T)$$

$$\dot{\varepsilon}(\sigma, \infty) = A(\sigma) = B(\infty)\sigma^{n(\infty)} \tag{5}$$

* **Jan Kohout[1], Vojtech Hruby[2]**
[1] Department of Mathematics and Physics, Faculty of Military Technology, University of Defence, Brno, Czech Republic, E-mail: jan.kohout@unob.cz
[2] Department of Mechanical Engineering, Faculty of Military Technology, University of Defence, Brno, Czech Republic

$$\dot{\varepsilon}(1,\infty) = A(1) = B(\infty)$$

Using new declarations (and taking into account negative values of p)

$$Q_a(1) = E\ln\sigma_0,\ n(\infty) = p = -\frac{E}{RT_0},$$

$$\text{and}\ \ \frac{B(\infty)}{\sigma^{n(\infty)}} = \dot{\varepsilon}_0 \qquad (6)$$

the apparent activation energy as well as the stress sensitivity parameter can be expressed as

$$Q_a(\sigma) = E\ln\frac{\sigma_0}{\sigma},\ \text{and}\ \ n(T) = \frac{E}{R}\left(\frac{1}{T} - \frac{1}{T_0}\right) \qquad (7)$$

and the form of the searched dependence is

$$\dot{\varepsilon}(\sigma,T) = \dot{\varepsilon}_0\left(\frac{\sigma_0}{\sigma}\right)^{E/RT_0}\exp\left(-\frac{E}{RT}\ln\frac{\sigma_0}{\sigma}\right) \equiv \dot{\varepsilon}_0\left(\frac{\sigma_0}{\sigma}\right)^{\frac{E}{R}\left(\frac{1}{T}-\frac{1}{T_0}\right)} \qquad (8)$$

Eq. (7) explains the meaning of parameter E: it represents apparent activation energy for applied stress $\sigma = \sigma_0/e$ ($e = 2.7182818...$ is the base of natural logarithms).

3. Geometrical explication of final equation and its parameters

Logarithmic form of Eq. (8)

$$\ln\dot{\varepsilon}(\sigma,T) = \frac{E}{R}\left(\frac{1}{T} - \frac{1}{T_0}\right)\cdot(\ln\sigma - \ln\sigma_0) + \ln\dot{\varepsilon}_0 \qquad (9)$$

obtains in coordinates

$$x = \frac{1}{T},\ x_0 = \frac{1}{T_0},\ y = \ln\sigma,\ y_0 = \ln\sigma_0,$$

$$z = \ln\dot{\varepsilon},\ \text{and}\ \ z_0 = \ln\dot{\varepsilon}_0 \qquad (10)$$

a simple form

$$z(x,y) = a(x - x_0)(y - y_0) + z_0,\ \text{where}\ a = E/R \qquad (11)$$

which represents the equation of hyperbolic paraboloid with the origin in point (x_0, y_0, z_0). This fact explains the meaning of parameters T_0, σ_0 and $\dot{\varepsilon}_0$. The equation of hyperbolic paraboloid (11) written for (0,0,0) origin

$$z(x,y) = axy \qquad (12)$$

differs from the most usual form

$$x^2 - y^2 = bz,\ \text{where}\ \ b = 2/a \qquad (13)$$

because the paraboloids (12) and (13) are turned one to the other by 45° round the z-axis.

Analyzing Eq. (8) it can be said:

1. For the temperature $T = T_0$ the creep rate is independent of applied stress (arbitrary number raised to 0 is equal to 1). Therefore the curves $\dot{\varepsilon} = f(T)$ for various applied stresses intersect in one point and its coordinates are T_0, $\dot{\varepsilon}_0$. In the $1/T - \ln\dot{\varepsilon}$ fit these curves are represented by straight lines with the slope equal to the ratio Q_a/R, see Eq. (1).
2. For the applied stress $\sigma = \sigma_0$ the creep rate is independent of temperature (1 raised to arbitrary number is equal to 1). Therefore the curves $\dot{\varepsilon} = f(\sigma)$ for various temperatures intersect in one point with coordinates σ_0, $\dot{\varepsilon}_0$. In the $\ln\sigma - \ln\dot{\varepsilon}$ fit these curves are represented by straight lines with slope equal to stress sensitivity parameter n, see Eq. (2).

Representation of the curves $\dot{\varepsilon} = f(T)$ and $\dot{\varepsilon} = f(\sigma)$ by straight lines in the fits $1/T - \ln\dot{\varepsilon}$ and $\ln\sigma - \ln\dot{\varepsilon}$ follows directly from the fact that Eq. (8) describes hyperbolic paraboloid in coordinates (10). Depicting of Eq. (8) not only in 3D by hyperbolic paraboloid but also in 2D by families of straight lines if coordinates (10) are used, defines unambiguously the geometrical meaning of parameters T_0, σ_0 and $\dot{\varepsilon}_0$ as well as the meaning of the fourth parameter $E = Q_a(\sigma_0/e)$ describing in fact the scale factor of the third axis with respect to the first two axes. It is the greatest advantage of Eq. (8) that for the complete description of steady-state creep rate dependence on temperature and applied stress only four parameters are enough. Obversely, the disadvantage of using parameters T_0, σ_0, $\dot{\varepsilon}_0$ and E is low accuracy of their determination on the base of regression of experimental creep data using regression function (8) because the values of these parameters are far from the regions of testing temperatures, applied stresses and creep rates covering usual experimental conditions.

4. Verification of new equation

The derived equation (8) was verified using the test results of Sklenicka et al. [5, 6] obtained by studying creep of P91 steel. The experimental results and the fit using regression equation (8) are given in Fig. 1 (dependence on applied stress for various temperatures) and in Fig. 2 (dependence on temperature for various applied stresses, see *converse* reciprocal temperature axis on top of figure). In Fig. 2 only a part of results is plotted – only when a certain stress was applied at least at two temperatures.

Averages and standard deviations of regression parameters together with *standard* index of determination r^2 and *corrected* index of determination r^2_{corr} are presented in Table 1.

The points of intersection of straight lines are (1478 MPa, 10.8 s^{-1}) for Fig. 1 and (1270 K, 10.8 s^{-1}) for Fig. 2. Parameter E represents the apparent activation energy for the applied stress $\sigma = \sigma_0/e = 544$ MPa. Because the values of regression parameters are substantially higher than typical values of strain rates, applied stresses, and temperatures, their determination cannot be very accurate in principle, see the values of standard deviations in Table 1 (but in spite of quite high values of standard deviations – relatively to the averages of regression parameters – the fit of experimental data is very successful which coincides with high values of the indexes of determination). The other consequence of this fact is that the values of regression parameters can hardly be interpreted

as certain important quantities directly connected with the test material. Maybe only temperature T_0 (which is here 1270 K ≈ 1000 °C) could be interpreted as a very rough approximation of limit temperature at which the microstructure of test material changes by phase transformation.

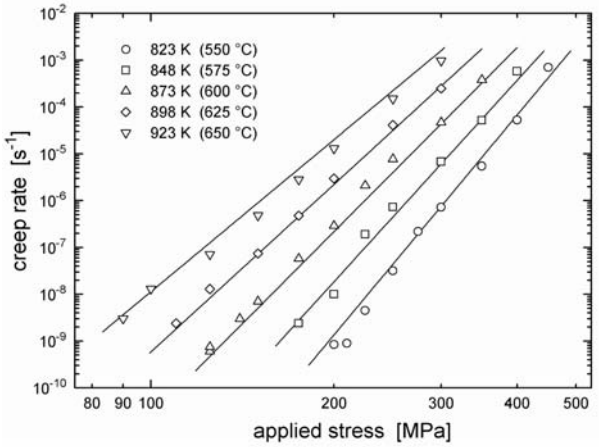

Fig. 1 Dependence of steady-state creep rate of P91 steel on applied stress for the given temperatures (Sklenicka et al. [5, 6]) and its regression using Eq. (8).

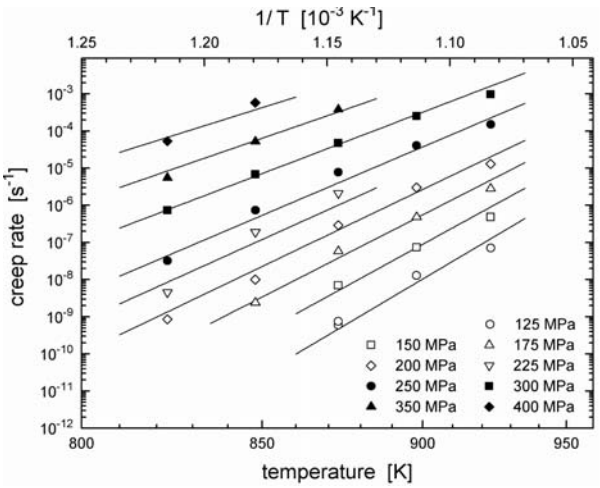

Fig. 2 Dependence of steady-state creep rate of P91 steel on temperature for the given applied stresses (Sklenicka et al. [5, 6]) and its regression using Eq. (8).

Regression parameters and indexes of determination Table 1

$\dot{\varepsilon}_0$ [s^{-1}]	E [kJ/mol]	σ_0 [MPa]	T_0 [K]	r^2 [1]	r^2_{corr} [1]
10.8±3.0	303±36	1478±329	1270±66	0.990026	0.989217

Changing slopes in both figures mean that the stress sensitivity parameter is quite strongly dependent on temperature and that the apparent activation energy is quite strongly dependent on applied stress. The values of stress sensitivity parameter are not even approximately equal to an integer and they reach sometimes even 15 or more. It seems that the *classical* approach based on assumption of different particular mechanisms of creep deformation, represented by small integer constant values of the stress sensitivity parameter independent of temperature, should be modified and temperature dependence of this parameter should be considered, e.g. according to Eq. (7).

5. Low temperature phenomena

Eq. (10) can be also a starting point for the description of the dependence of yield stress on temperature and strain rate as well as for the description of stress relaxation curves, in both cases at temperatures lower than the usual temperatures of creep behaviour of studied material are. Only two following modifications are useful to do:

1. For both these phenomena often connected with substantially lower temperatures than creep it can be considered that $T_0 \to \infty$ (i.e. $p = 0$), which simplifies the description.
2. For lower temperatures the internal stress is necessary to introduce in the relation for applied stress which, on the other hand, a little complicates the description, i.e.

$$\sigma = \sigma_G\left[\varepsilon, G(T)\right] + \sigma_{ef}\left(T, \dot{\varepsilon}\right) \tag{14}$$

where σ_G is the internal stress connected with long-range obstacles and σ_{ef} is the effective stress connected with short-range obstacles of dislocation motion. The internal stress is nearly temperature-independent but it strongly depends on the development of dislocation structure, i.e. on the level of plastic deformation. On the other hand, short-range obstacles can be overcome with the assistance of thermal fluctuations and, therefore, the effective stress is strongly dependent on temperature and strain rate.

5.1 Yield stress

One of the most important stress values of test material is yield stress σ_y, i.e. the loading stress at which first substantial motion of dislocations appears and, in fact, plastic deformation starts to develop ($\varepsilon \approx 0$, $\sigma_G \approx$ const.). Respecting both the low-temperature features mentioned above, the relation

$$\sigma_y(T, \dot{\varepsilon}) = \sigma_G + \sigma_0 \exp\left(-\frac{RT}{E}\ln\frac{\dot{\varepsilon}_0}{\dot{\varepsilon}}\right) \equiv \sigma_G + \sigma_0\left(\frac{\dot{\varepsilon}}{\dot{\varepsilon}_0}\right)^{RT/E} \tag{15}$$

for the description of yield stress dependence on temperature and strain rate can be written. Its validity can be verified by experimental results of Vlach et al. [7] studying the dependence of yield stress on temperature and strain rate for Cr-Mo steel used for pressure vessels. The yield stress was measured in the temperature range −196 to +20 °C, i.e. 77 to 293 K, and the strain rate range 0.0014 to 11 s^{-1}. Experimental points and fitting curves drawn in Fig. 3 show that the description of the dependence by Eq. (15) is very successful.

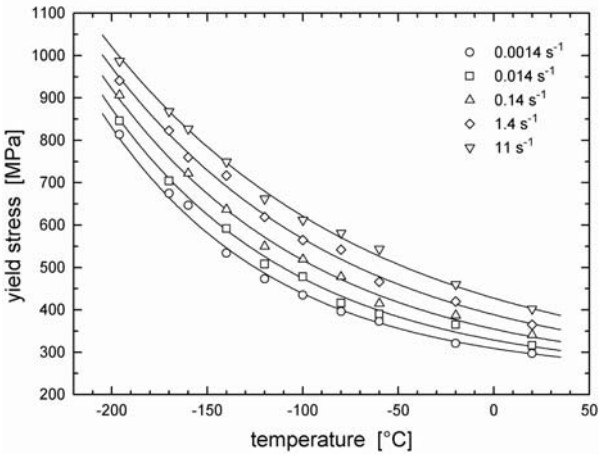

Fig. 3 Dependence of yield stress of Cr-Mo steel on temperature for the given strain rates (Vlach et al. [7]) and its regression using Eq. (15).

Another verification of Eq. (15) can be made using the experimental results of yield stress measurements of low-carbon steel published by Meyers [8]. The measurements were made in the temperature range 195 to 713 K, i.e. −78 to +440 °C, and in the strain rate range 10^{-3} to 10^{5} s^{-1}. For the verification, only the range 1 to 10^{3} s^{-1} was chosen, in which the measurements were made over the whole temperature range given above. Experimental results and their fit are drawn in Fig. 4. Also in this case the description of the dependence by Eq. (15) is very successful.

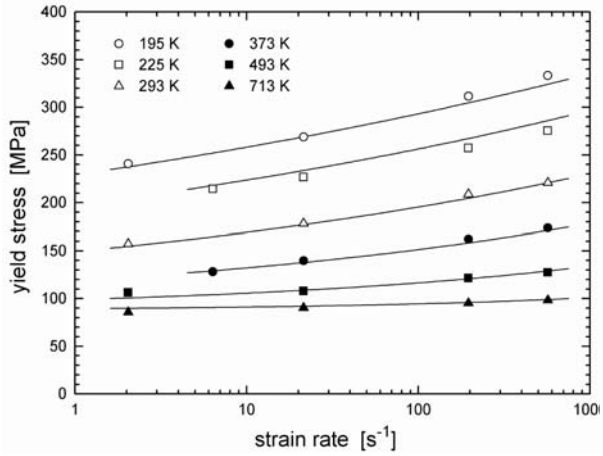

Fig. 4 Dependence of yield stress of low-carbon steel on strain rate for the given temperatures (Meyers [8]) and its regression using Eq. (15).

Both Fig. 3 and Fig. 4 testify to the validity of Eq. (15), which was obtained on the basis of the newly derived Eq. (8).

5.2 Stress relaxation

The basis of the stress relaxation description consists in the proportionality between the strain rate and the rate of stress decrease

$$\dot{\varepsilon} = -\frac{\dot{\sigma}}{M} \tag{16}$$

where M is modulus of elasticity of the system formed by a test bar and a testing device. Introducing this relation into Eq. (8), substituting $p = 0$ and considering effective stress σ ef instead of applied stress σ, a differential equation

$$-\frac{d\sigma}{M} = \dot{\varepsilon}_0 \left(\frac{\sigma - \sigma_G}{\sigma_0}\right)^{E/RT} dt \tag{17}$$

is obtained, which can be solved by direct integration. Its solution is

$$\sigma(t) = \sigma_G + \frac{\sigma(0) - \sigma_G}{(\alpha t + 1)^m} \tag{18}$$

where σ(0) is the initial value of stress (for $t = 0$) and parameters α and m are temperature-dependent and they substitute the following more complicated expressions

$$\alpha(T) = \frac{M\dot{\varepsilon}_0}{m(T)\sigma_0}\left[\frac{\sigma_0}{\sigma(0) - \sigma_G}\right]^{-1/m(T)} \quad \text{and}$$

$$m(T) = \frac{RT}{E - RT} \tag{19}$$

Eq. (18) is formally equivalent to the equation

$$\sigma(t) = \sigma_G + K(t + a)^{-m} \tag{20}$$

derived by Li [9] using considerations different from the considerations applied in this paper. Moreover, no further specifications of parameters K and a were given and no connection between parameter m and temperature was described by Li [9].

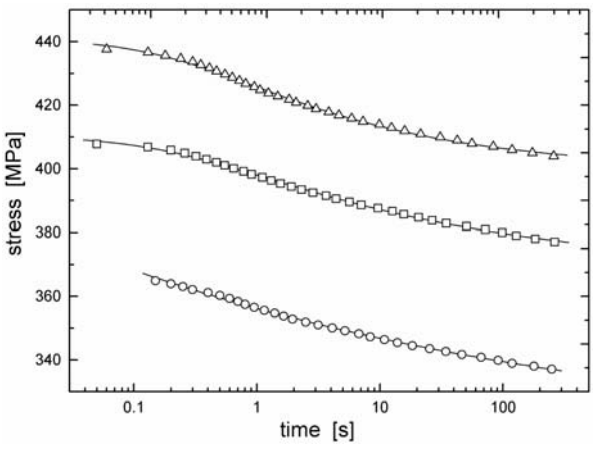

Fig. 5 Results of relaxation measurements of ferritic nodular cast iron (Kohout [10]) and its regression using Eq. (18).

To verify Eq. (18), the relaxation curves of ferritic nodular cast iron determined by the author [10] were used, see Fig. 5. This figure (as well as all the previous figures) shows very good agreement between measured points and fitting curves.

The relaxation of many other metallic materials was studied with the same result: Eq. (18) provides for a better fit of experimental data than all the other equations used for this purpose.

6. Discussion

Eqs (8), (15), and (18) describe phenomena connected with creep, yield stress, and stress relaxation using common parameters $\dot{\varepsilon}_0$, σ_0, E and T_0 or σ_G. In the case of creep temperature T_0 plays a significant role while internal stress σ_G can be mostly neglected with respect to effective stress σ_{ef}. On the other hand, in yield stress effects and during stress relaxation nonzero internal stress σ_G should be considered while the term $1/T_0$ disappears considering $T_0 \to \infty$. Naturally, parameters $\dot{\varepsilon}_0$, σ_0 and E are common for all studied phenomena and their values can be determined by studying some of these phenomena. Then in the case of studying another phenomenon from those mentioned, the values of common parameters can be used e.g. for rough estimation or forecast of behaviour of studied material during the other phenomenon. An example is given by Kohout [10]: to determine the dependence of yield stress on temperature and strain rate it is sufficient to determine only strain rate dependence. The temperature dependence can be estimated on the basis of the value of parameter E determined from exponent m of the stress relaxation curves, see Eqs (15), (18) and (19). In the last resort only one test bar can be sufficient for a rough estimation of the temperature and strain rate dependence of yield stress, see [10].

7. Conclusions

1. Although using only four regression parameters, the newly derived relation describes the dependence of steady-state creep rate on temperature and applied stress better than the classically used Sherby relation does.
2. The newly derived relation respects a certain dependence of activation energy on applied stress and of the stress sensitivity parameter on temperature.
3. Based on the newly derived relation, the dependence of yield stress on temperature and strain rate can be deduced, which provides for a very good fit of experimental results.
4. Also the equation describing the relaxation curves better than the usually used equations do can be deduced from the newly derived relation.
5. Although being phenomenological, the presented consistent description of creep, yield stress, and relaxation issuing from the same base enables to study these phenomena commonly, using common set of parameters. The values of these parameters determined during studying one of these phenomena can be used in the description or prediction of the other phenomena.

Acknowledgement

The work presented in this paper has been supported by the Ministry of Defence of the Czech Republic (Research Plan No. MO0FVT0000404).

References

[1] CADEK, J.: *Creep in Metallic Materials,* Prague : Academia & Amsterdam : Elsevier, 1988.
[2] GAROFALO, F.: *Fundamentals of Creep and Creep Rupture in Metals,* New York : Macmillan, 1965.
[3] SHERBY, O.D.: *Acta Met.,* 1962, vol. 10, p. 135.
[4] KOHOUT, J.: New Description of Steady-state Creep Rate, Yield Stress, Stress Relaxation and their Interrelation, *Materials Structure & Micromechanics of Fracture IV (Materials Science Forum)*, 2005, vol. 482, pp. 319–322.
[5] SKLENICKA, V., KUCHAROVA, K., DLOUHY, A., KREJCI, J.: In: *Materials for Advanced Power Engineering, Part I* (ed. Coutsouradis, D.), Dordrecht : Kluwer Academic Publishers, 1994, p. 435.
[6] SKLENICKA, V., KUCHAROVA, K., KLOC, L.: In: *Materials for Advanced Power Engineering 1998, Part I* (eds Lecomte-Beckers, J. et al.), Julich : Forschungszentrum Julich, 1998, p. 233.
[7] VLACH, B., HOLZMANN, M., MAN, J.: *Zvaranie* [Welding], 2/1986, vol. 35, p. 35, ISSN 0044-5525 (in Czech).
[8] MEYERS, M.A.: *Dynamic Behavior of Metals,* New York : Wiley, 1994.
[9] LI, J.C.M.: *Canadian Journal of Physics,* 1967, Vol. 45, p. 493.
[10] KOHOUT, J.: Prediction of Temperature and Strain Rate Dependence of Yield Stress Using Test of One Bar at Room Temperature *(in Czech), Materials Engineering,* Vol. 4, 1997, pp. 1–9, ISSN 1335-0803.

Marian Bursak – Jan Michel *

DEEP-DRAWING AND FATIGUE PROPERTIES OF ADVANCED STEEL SHEET STRIPES

Analysis of the deep drawing and fatigue properties is given in this contribution for two advanced micro alloyed sheet steel grades with Yield strength values R_e = 246 and 382 MPa, respectively. The 2 mm thick steel sheets were hot dip zinc coated. The deep drawing properties were evaluated by tensile testing and by the Erichsen test at different strain rates. For fatigue testing the symmetric bending test was applied. Results showed favorable deep drawing properties of these steel sheets assigned for heavy duty parts in automotive industry. Steel grade with R_e = 246 MPa had elongation $A_{80} > 32\%$, n = 0.21, Erichsen number I_E = 12.5 mm and the steel with R_e = 382 MPa had $A_{80} > 24$ %, n = 0.17 and I_E = 12.4 mm. The tested values showed some growth in dependence on the strain rate up to the press tool velocity about 0.1 m.s^{-1} and at higher strain rates they decreased. The fatigue limit in bending was about 0.6.R_e. The zinc coating on the sheet surface remains complete up to the final fracture of the test piece.

1. Introduction

Zinc coated deep-drawing sheet is marketable in many industrial applications including first of all automotive industry. The barrier effect of zinc protects steel against corrosion in several environments [1, 2]. A light weight design, required mainly nowadays, is possible only with the application of higher strength steel, with maintained plastic properties, the latter essential for steel used in automotive industry. It can be obtained by the use of micro alloyed steel sheet, with micro alloying (under < 0.15%) applied together with controlled cooling rolling (thermo-mechanical treatment). For the increase of strength, grain refinement and precipitation strengthening is used. The grain refinement has a beneficial effect on plastic properties too, and it can offset the adverse effect of precipitation hardening [3, 4, 5]. Micro alloyed steel sheet has finer grain than usual steel sheet and that is why the criteria for plastic formability of the sheet are to be modified.

In this contribution the deep-drawing and fatigue properties of selected zinc coated steel sheet are analyzed. The increase of productivity in current press lines is sought in the increase of the pressing speed at first. It means the increase of the strain rate. Higher strain rate results higher resistance of the material to plastic deformation, and changes in the deformation process of the material [5, 6, 7]. As references show, up to a certain value of the strain rate the plastic deformation properties of the material do not change significantly, or the plasticity can even grow slightly [7,8]. The intensity by which the strain rate can influence the plastic properties is strongly material dependent [4, 5].

The critical degradation mechanisms influencing the life of an automobile part are the fatigue and corrosion. Cyclic loading is frequently the main factor of surface damage and, on the other hand, surface damages can decrease fatigue properties significantly.

The aim of this contribution is the analysis of plasticity for selected deep drawing zinc coated micro alloyed steel sheet and the evaluation of the influence of strain rate on the analyzed properties, as well as to determine the fatigue properties and to monitor the behavior of the zinc layer during forming and fatigue life.

2. Experimental material and methods

Experimental test pieces were made from 2 mm thick stripes made of micro alloyed cold rolled steel which was hot zinc coated after rolling. The steel was grade H220YD (C < 0.01%, Al > 0.01%, Ti < 0.012%, Nb < 0.022%) and H380LAD (C < 0.15%, Al < < 0.01%, Ti < 0.015%, Nb < 0.09%). The grade H220YD has actually a ferritic microstructure with the mean grain size of 0.016 mm (Fig. 1) and the grade H380LAD has ferrite with the mean grain size of 0.0056 mm with a small amount of pearlite (Fig. 2). Cut outs were made from the sheet and flat test pieces oriented in the direction of rolling were machined for tensile testing. The same was applied for the deep drawing Erichsen tests and fatigue tests in bending.

For static tensile tests a universal test machine INSTRON 1185 was used and this machine was used retooled with an Erichsen test fixture for the deep drawing tests in the press tool velocity interval from $3.3.10^{-3}$ m.s^{-1} to 1.10^{-3} m.s^{-1}. Deep drawing tests with ram speed of up to 2.5 m.s^{-1} were made in a drop weight tester. The fatigue properties of the steel sheet were tested in bending with symmetrical fatigue cycles at 35 Hz for the limit $N_C = 10^7$.

* **Marian Bursak, Jan Michel**
Department of Material Science, Technical University of Kosice, Slovakia, E-mail: marian.bursak @tuke.sk

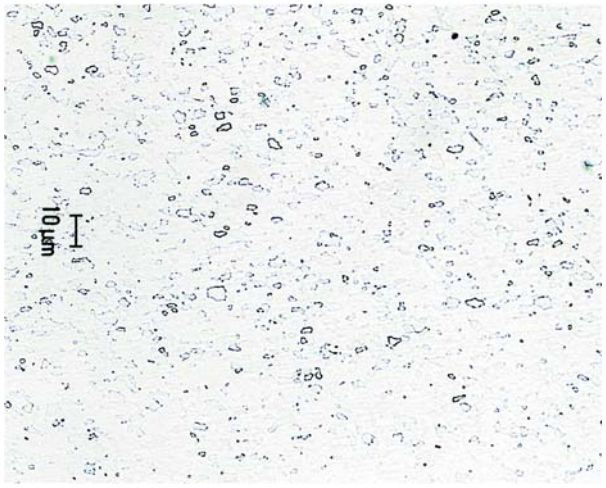

Fig. 1 Microstructure of steel sheet H220YD

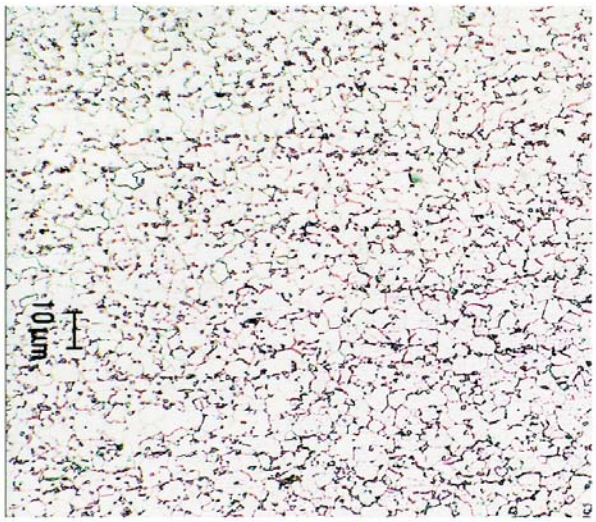

Fig. 2 Microstructure of steel sheet H380LAD

The behavior and integrity of the zinc coating layer was monitored in both macro and microscope.

3. Results and discussion

The tensile test results for the tested 2 mm thick sheet are in Tab. 1.

Mechanical properties of steel sheet Tab. 1.

Steel Grade	$R_{p0,2}$ [MPa]	R_m [MPa]	A_{80} [%]	n	$R_{p0,2}/R_m$	D [MPa]
H220YD	246	371	32.7	0.21	0.66	3590
H380LAD	382	509	24.1	0.17	0.75	5050

As shown in Tab. 1 the steel grade with higher strength (H380LAD) has the measured plasticity values lower (A_{80}, n) compared to the steel grade H220YD. The increased strength of steel grade H380LAD in comparison to grade H220YD is first achieved by the finer grain and precipitation strengthening due to the higher carbon content and micro alloying elements. According to the elongation values A_{80}, deformation strengthening exponent *n*, and the ratio $R_{p0,2}/R_m$ the steel grade H220YD sheet belongs into the group of deep drawing sheet, suitable for deep drawing. Steel grade H380LAD sheet cannot be put into this group for the obtained characteristic values. During plastic deformation for the steel grade H380LAD sheet a higher strengthening modulus D was obtained, tested for the 10% part of the total deformation.

Basic information about the formability of the steel sheet can be obtained by tensile testing. However, the formability of the sheet is influenced by a number of factors arising from the production technology applied [7, 9, 10]. Important characteristics of formability can be obtained by technological tests. Tab. 2 presents the results of deep drawing Erichsen tests (I_E – is the Erichsen number) at different press tool velocities.

Erichsen deep drawing test results for different press tool velocities v Tab. 2.

Steel Grade	v [$m.s^{-1}$]	$3.3.\ 10^{-3}$	$8.34.10^{-3}$	$1.6.10^{-2}$	2.10^{-1}	2.5
H220YD	I_E [mm]	12.5	12.6	13.0	12.7	11.2
H380LAD		12.4	12.5	12.6	12.5	11.5

Erichsen deep drawing test results showed that the indentation depth up to the fracture of the indented cup (I_E) is actually the same for both steel grades used, though they have large differences in elongation A_{80}. This can be caused due to difference in the stress distribution at the Erichsen deep drawing test and during tensile test.

The influence of the strain rate on the I_E values is plotted in Fig. 3. As it can be seen, for the increase of the press tool velocity up to about $v = 0.2$ $m.s^{-1}$ there is a slight growth of the I_E, then there is a slight decrease of the I_E value. For the highest velocity 2.5 $m.s^{-1}$ the obtained value I_E is the lowest. The turning point velocity 0.2 $m.s^{-1}$ marking the start of the I_E value decrease is roughly equivalent to the strain rate 1 s^{-1}. The experiments are in good agreement with data reported in references [6, 7, 8], declaring that up to the strain rate of about 1 s^{-1} there is no significant decrease of steel sheet formability by the increase of the press tool velocity, and in this zone the traditional deep drawing criteria can be applied.

During testing and production by forming due to the heterogeneity of deformation the instant strain rate of a local spot is changing and can be different from the mean value calculated and can be significantly higher. The homogeneity of the plastic deformation is dependent on the microstructure of the steel sheet and

on the applied forming technology [4, 5]. The critical forming velocity depends on these factors, too.

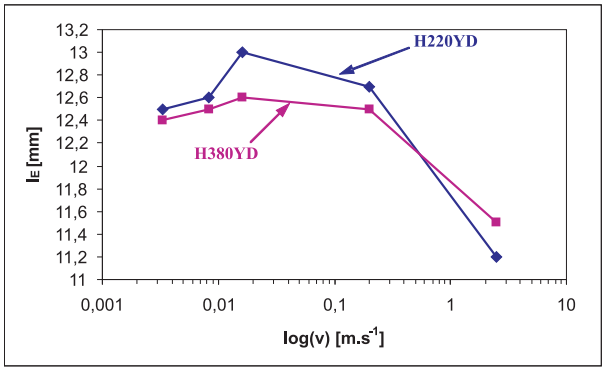

Fig. 3 Influence of pressing tool velocity on Erichsen number I_E for investigated steel

The susceptibility of the material to influences caused by strain rate depends on the internal composition of the material. In generally, the higher homogeneity of the internal structure and the lower amount of barriers to the movement of dislocations causes that material is more sensitive to strain rate [4, 5]. Deep drawing test results show, too, as shown in Fig. 3 that the I_E value for steel grade H380LAD sheet (R_e = 382 MPa) is less susceptible to strain rate than steel grade H220YD sheet (R_e = 246 MPa).

The outstanding decrease of the I_E at impact forming (v = = 2.5 m.s^{-1}) is due to different factors. We suppose that the decisive factor is heterogeneity of the plastic deformation distribution during the forming of the cup at very high strain rates and the deformation is localized in the critical parts of the cup. This can result in a decrease of the total value of plasticity. Changes of the friction between the tool and sheet can have influence, too.

For the service life in the car body the most important properties of pressed steel sheet parts are the resistance against fatigue and corrosion. They are stressed most frequently by alternating forces in bending. In Fig. 4 are plotted the dependences of the fatigue stress σh on the number of cycles to fracture N, for sym-

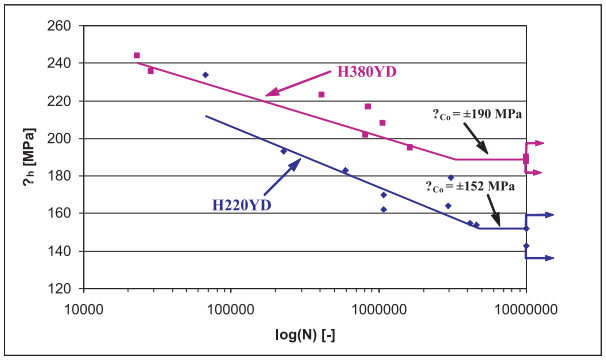

Fig. 4 Wöhler fatigue curves σh -N for tested steel sheets

metric cyclic bending of the tested steel sheet. The final fatigue limit and its rate to the UTS are the determined characteristics showing the quality of the resistance to fatigue. The fatigue limit of the steel grade H220YD in bending was $\sigma_{Co} = \pm 152$ MPa and the rate to UTS was $\sigma_{Co}/R_m = 0.41$. For the steel grade H380LAD it was $\sigma_{Co} = \pm 190$ MPa and $\sigma_{Co}/R_m = 0.37$, respectively. The tested characteristics and the slope of the decreasing Wöhler curve, (Fig. 4) assign both the tested steel grade sheets to ones with a good resistance to fatigue damage.

The increased corrosion resistance of the tested steel sheet is achieved by hot dip zinc coating. Damages of the integrity to the zinc coating layer during forming or service life decrease the corrosion resistance significantly, and can be an initiation spot of damage by fatigue [10, 11]. Macro and microscopic analyses of the tensile test pieces surface layer during tensile testing did neither reveal any damages of the coating nor any loss of cohesion to the steel base. Neither the other tests, the deep drawing Erichsen test and fatigue testing in bending showed damages to the coating. It is documented in Fig. 5 where the fracture surface of the sheet H220YD with the zinc surface layer is shown after cycling with stress equal to the fatigue limit σ_{Co} and life to the limit of 10^7 cycles.

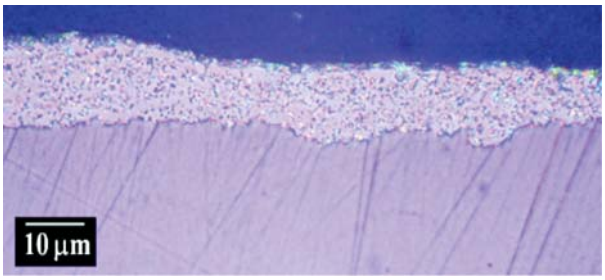

Fig. 5 Fracture of investigated steel H220YD with zinc surface layer after fatigue at σ = 152 MPa, N = 10^7 cycles.

4. Conclusion

Deep drawing and fatigue properties of two advanced deep drawing steel grades with yield points 246 and 382 MPa are analyzed in the contribution. The sheets were hot coated with zinc. The influence of the forming tool velocity on the deep drawing Erichsen test results are evaluated (the depth of the drawn cup at cracking).

The experimental results and discussion showed:

- The tested steel grades with increased strength and fatigue properties obtained by grain refinement and precipitation strengthening manifested very promising plasticity properties. The steel grade with high R_e = 382 MPa, though having a lower elongation at tensile testing A_{80} = 24%, had the Erichsen depth equal to the one for the steel grade with R_e = 246 MPa and A_{80} = 32%. A new approach is necessary to evaluate the deep drawing

properties of these steels if tensile test results are known only (A_{80}, n, R_e/R_m).
- The increase of the press tool velocity during forming (or at the Erichsen test) up to about 0.2 $m.s^{-1}$, which is equal to about 1 s^{-1} strain rate, results in a slight increase of the deep drawing test result. Exceeding this velocity brings a decrease of deep drawing properties; the decrease is more intense for the steel with a lower yield point.
- The zinc surface layer retained integrity and cohesion to the basic steel up to the final fracture of the tested piece by tensile testing, Erichsen deep drawing tests, and fatigue tests.

Acknowledgement

This work has been supported by APVV Agency under No. APVV-0326-07

References

[1] KOCICH, J., TULEJA, S.: *Corrosion and Protection of Steels (in Slovak)*, TU Košice, 1998.
[2] SEVCIKOVA, J.: *Surfaces (in Slovak)*, HF TU Kosice, 2005.
[3] PARILAK, L.: *Structural Fundamentals of Mechanical and Fracture Attributes of Materials (in Slovak)*, Habilitation Thesis, HF TU Kosice, 1998.
[4] CIZMAROVA, E. et al.: *Metalurgija* [Metallurgy], 43/2004, p. 211.
[5] MICHEL, J. et al.: *Kovove materialy* [Metallic Materials], 37, 1999, 191, (in Slovak).
[6] BURSAK, M. et al.: *Metalurgija* [Metallurgy], 46/2007, p. 37.
[7] JANOVEC, J., ZIEGELHEM, J.: *Increase of Use Properties at Vehicle Sheetmetal (in Czech)*, In. Technológia ´99, STU Bratislava, 1999, p. 319.
[8] STABA, J., BURSAK, M.: *Metalurgija* [Metallurgy], 48/2009, p. 167.
[9] HRIVNAK, A., EVIN, E.: *Sheet Compressibility – Compressibility Prediction of Sheet Steel with Advanced Strength Properties (in Slovak)*, Elfa, Kosice, 2004.
[10] SPISAK, E.: *Mathematical Designing and Simulation of Technological Processes for Profiling (in Slovak)*, TYPO Pres, Kosice 2000.
[11] SPISAK, E. et al.: *Production Engineering 1 (in Slovak)*, Kosice, 2003.

Frantisek Novy – Rastislav Mintach – Otakar Bokuvka *

EFFECT OF GALVANIC METALLIZATION, PVD PROCESSES AND THERMAL SPRAYING ON FATIGUE PROPERTIES OF PLAIN STRUCTURAL STEELS IN THE ULTRA-HIGH-CYCLE REGIME

This work presents information about the influence of Ni and ZnFe galvanic metallization on the fatigue properties of S235JRG2 steel and about the TiN physical vapour deposition and WC thermal spraying on the fatigue properties of S355J0 steel in the ultra-high-cycle region of loading ($N = 6\times10^6$ - 10^{10} cycles) obtained at high-frequency fatigue testing ($f \approx 20$ kHz, $T = 20 \pm 3$ °C, $R = -1$). Technical coatings are used in order to modify the properties of the surface that is being covered for protection against corrosion but also in order to increase the hardness and resistance to wear. The Ni coating produced by galvanic metallization favourably influences the corrosion resistance but it introduces tensile stresses into the surface layer which act negatively on fatigue properties. No evidence of improving fatigue lifetime was detected in the case of ZnFe, TiN and WC coatings. In all types of coating the fatigue cracks were initiated on the specimen surface e.g. on the coatings surfaces.

Key words: ultra-high cycle fatigue, fatigue limit, galvanic metallization, thermal spraying, PVD processes.

1. Introduction

Fatigue limit is one of the most important criteria determining the quality of components and structures. More than 90% of all fractures are caused by fatigue in service [1, 2]. Fatigue lifetime is investigated in the low-cycle region of loading ($N_f < 10^4$ - 10^5 cycles), high-cycle region of loading (10^4 - $10^5 < N_f < 2\times10^6$ - 10^7 cycles) and in the ultra-high-cycle region of loading ($10^7 < N_f < 10^{10}$ cycles). In recent ten years, the ultra-high-cycle region of loading ($10^7 < N_f < 10^{10}$ cycles) has been investigated intensively by several research teams. The aim of these experimental studies is to increase the fatigue limit, safety and reliability of components and structures [3].

Conventional fatigue testing machines work in the frequency range from $f \approx 10$ Hz to $f \approx 200$ Hz. The fatigue tests take a lot of time and they are expensive. The fact that fatigue fractures occur after more than $N_f < 10^7$ cycles of loading motivates the researches to use experimental methods working with a high frequency cyclic loading ($f \approx 20$ kHz) [3, 4].

Fatigue cracks most often occur on the surface. Therefore, surface conditions (microstructure, roughness and residual stresses) can have a significant effect on fatigue resistance resulting in the increase of the fatigue resistance [5, 6]. Fatigue strength mostly depends on surface roughness. The reducing of the surface roughness about several-tenfold-percent can improve the fatigue limit about 25–100 % [5].

The use of super-high strength steels is growing rapidly, due to their outstanding characteristics. However most steels do have a fundamental disadvantage namely their resistance to corrosion and wear is often insufficient. The application of non-ferrous metal coating is used in engineering praxis with the aim to renovate the components, to increase the resistance to the effect of aggressive environments, to increase the wear resistance and to produce decorative coating. On the other hand, the coatings deposited by galvanic metallization can cause a decrease of the fatigue limit [8].

Galvanic coating deposited on the surface of the metal in order to protect it from corrosion or to increase resistance to abrasion, usually produces in being covered basic material tensile stresses, which reduce the fatigue resistance. During nickel galvanic metallization, but also during other galvanic treatments, the negative impact of treatment increases with an increase of material strength.

Thermal Spraying (THSP) is a group of processes that deposit molten metallic or non-metallic surfacing materials onto a prepared substrate. All thermal spraying processes introduce a feedstock (usually a powder or wire) into a heating device (combustion or electrical). There the material is heated, blended into the heat plume, and sprayed onto a prepared substrate. The molten particles strike the surface, flatten, and form thin platelets that conform and adhere to the substrate and to one another. As they cool, they build up a lamellar structure to form the desired coating.

Physical vapor deposition (PVD) processes are family of coating processes suitable for depositing corrosion protection and other

* **Frantisek Novy, Rastislav Mintach, Otakar Bokuvka**
Department of Materials Science, Faculty of Mechanical Engineering, University of Zilina, Slovakia, E-mail: frantisek.novy@fstroj.uniza.sk

functional layers onto steels. The TiN or TiCN coatings belong to among of PVD coatings. The PVD coatings are produced by BryCoat's proprietary vacuum deposition technologies utilizing cathodic arc coating technology. The advantage of this environmentally friendly technology is that a wide variety of coating materials can be deposited (metals, alloys and compounds).

The aim of this study is to reveal the influence of Ni and ZnFe coatings deposited by galvanic metallization on the fatigue behaviour of S235JRG2 steel and influence of TiN coating deposited by PVD process and WC coating deposited by THSP process on the fatigue behaviour of S355J0 steel. The results are obtained from fatigue tests in ultra-high-cycle region by the methods of high-frequency loading.

2. Material and experiments

The materials used in experimental study were plain low carbon structural steels, namely the S235JRG2 and S355J0 steel. Chemical composition (in wt. %) and mechanical properties of experimental materials are presented in tables 1 and 2.

Chemical composition and mechanical properties of S235JRG2 steel — Tab. 1.

Chemical composition [wt. %]								
C	Mn	Si	S	P	Cr	Ni	W	B
0.17	0.51	0.12	0.032	0.013	0.07	0.09	0.011	0.0001
Cu	Mo	V	Ti	Al	Sn	N	Pb	As
0.27	0.01	0.001	0.001	0.003	0.001	0.0065	0.002	0.001
Mechanical properties								
R_e [MPa]		R_m [MPa]				A_5 [%]		
340.0		445.6				30.8		

Chemical composition and mechanical properties of S355J0 steel — Tab. 2.

Chemical composition [wt. %]								
C	Mn	Si	S	P	Cr	Ni	W	B
0.17	1.35	0.34	0.019	0.016	0.014	0.017	0.009	0.0002
Cu	Mo	V	Ti	Al	Sn	N	Pb	As
0.045	0.008	0.004	0.021	0.035	0.006	0.0073	0.019	0.005
Mechanical properties								
R_e [MPa]		R_m [MPa]				A_5 [%]		
429.1		557.3				28.6		

Six series of specimens were used for the experimental research. The 1st series represents the specimens made from the basic material of S235JRG2 steel without any coating. The 2nd series was made from the same steel with nickel coating. The microstructure of S235JRG2 steel with Ni coating is shown in Fig. 1. The thickness of Ni layer was about 38 μm. The 3rd series was prepared also from already mentioned S235JRG2 steel with ZnFe coating, the microstructure is shown in Fig. 2. The thickness of ZnFe layer was about 40 μm. The 4th series represented the specimens made from basic material of S355J0 steel without any coating. The 5th series was prepared from the same steel with TiN PVD-coating (Fig. 3) and in 6th series specimens with WC thermal sprayed coating were used (Fig. 4). The thickness of TiN layer was about 4 μm and WC layer about 100 μm.

A light metallographic microscope AXIO Imager A1m was used for metallography analysis. Both experimental steels have ferritic-perlitic fine-grained microstructure. The S355J0 steel was delivered after normalization. The fractography analyses of fracture surfaces were carried out by using scanning electron microscope TESLA BS 340 [9], [10].

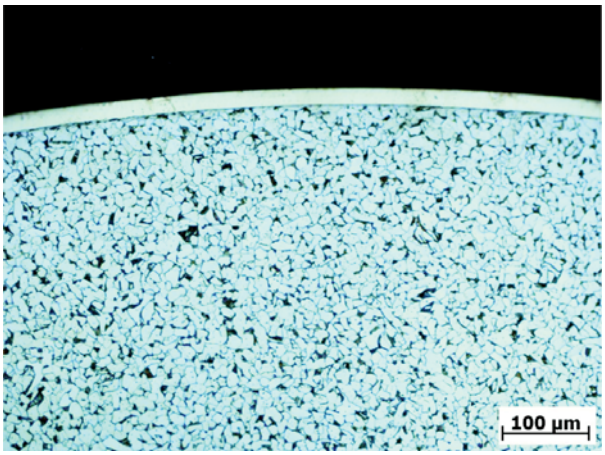

Fig. 1 Microstructure of S235JRG2 steel with Ni coating

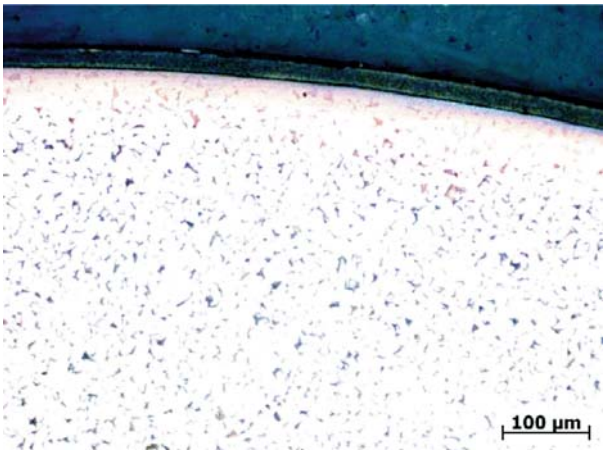

Fig. 2 Microstructure of S235JRG2 steel with ZnFe coating

An ultrasonic resonant high-frequency fatigue machine KAUP-ZU was used for fatigue tests. The experiments were carried out at sinusoidal tension-compression loading with the frequency of 20 kHz. The stress ratio of $R = -1$ was used. The smooth fatigue

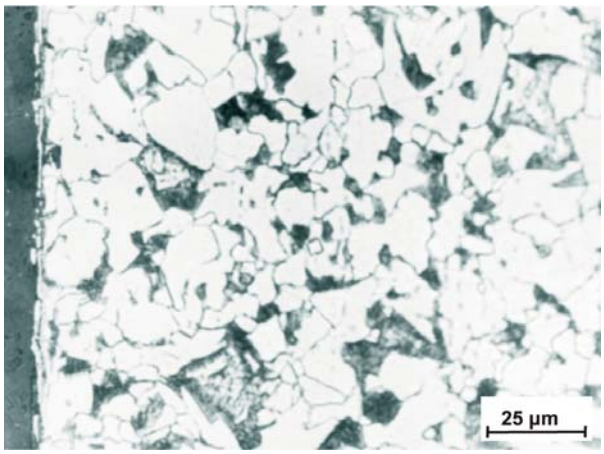

Fig. 3 Microstructure of S355J0 steel with TiN coating

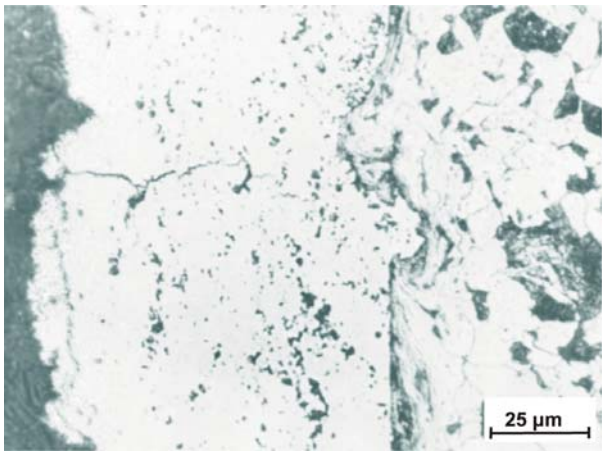

Fig. 4 Microstructure of S355J0 steel with WC coating

specimens with gauge diameter of 4 mm, were prepared according to Puskar's recommendations, so that they fulfil resonance conditions at high frequency fatigue loading. Used testing methods and procedures are described and explained in more detail in [4]. Fatigue tests were performed at the ambient temperature ($T = 20 \pm 3$ °C). Specimens were cooled by distilled water with an anticorrosive inhibitor. The whole specimens were grounded and polished for elimination of surface roughness before the application of coatings.

3. Results and discussion

Results of high frequency fatigue tests obtained on S235JRG2 steel at uniaxial cyclic push-pull loading in the region from $N_f \approx$ $\approx 2.5 \times 10^6$ cycles to $N_f \approx 3 \times 10^{10}$ cycles are presented in the form of S-N curve (dependence of stress amplitude vs. number of cycles) in Fig. 5. The stress amplitude was chosen from the interval σ_a = (260 – 160 MPa). There are represented the fatigue results for specimens from basic material, specimens with Ni and ZnFe coatings. All the specimens were cycled till fracture. It can be seen that the experimental fatigue lifetime continuously decreases from high-cycle to ultra-high-cycle region for all three series of specimens. Decreasing stress amplitude leads to increase of number of cycles to fracture. The fatigue lifetime of basic material is essentially higher than that for the material with Ni coating in the region of higher stress amplitude ($\sigma_a > 200$ MPa) and lower number of cycles to fracture ($N_f < 10^9$ cycles). In this region of stress amplitude the steel with ZnFe coating has approximately the same values of fatigue lifetime as the basic steel. In the ultra-high-cycle region any clear distinction of fatigue lifetime wasn't detected among basic material and steel with Ni and ZnFe coatings.

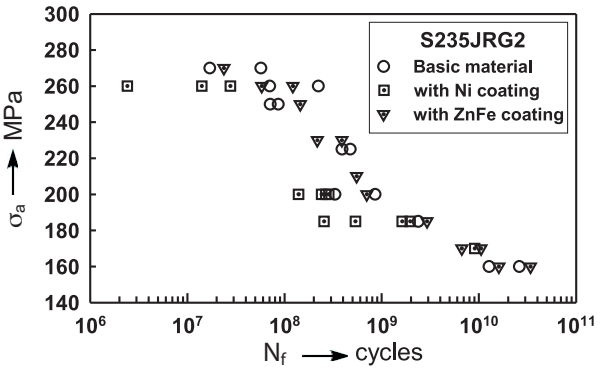

Fig. 5 The S-N dependence of the S235JRG2 steel

Three different types of coating fractures were observed in the case of steel with Ni coating. The fatigue cracks were initiated either from the specimen surface (e.g. from the surface of Ni coating) or from the interface between base material and Ni coating. In the region of high stress amplitude and low cycle region the granular fracture of the coating was detected. The example for the specimen subjected to stress amplitude $\sigma_a = 260$ MPa is shown in Fig. 6. The fatigue lifetime was about $N_f = 1.41 \times 10^7$ cycles. The thickness of Ni layer was 38 µm. The decohesion between the base material and coating (marked with arrows) was often observed.

With decreasing stress amplitude the character of coating damage was changed. The example of fracture surface of the Ni base layer in the case of specimen subjected to stress amplitude $\sigma_a = 200$ MPa is shown in Fig. 7. Fatigue lifetime was $N_f = 2.66 \times 10^8$ cycles. It can be seen that the fatigue fracture of the coating has fine grained character. In the case of stress amplitude lower than 185 MPa the fatigue striations were detected on the fracture surface of Ni coating. The detail of fatigue striation in the Ni coating is shown in Fig. 8 for the specimen subjected to stress amplitude of $\sigma_a = 185$ MPa, $N_f = 1.62 \times 10^9$ cycles. This indicates the localization of high plastic deformation during the fatigue crack growth. The fatigue fracture areas alternated the areas with brittle fracture in the Ni coating. The brittle character of Ni coating and change of fracture mode with decreasing stress amplitude can be the reasons of premature degradation of tested steel with Ni coating.

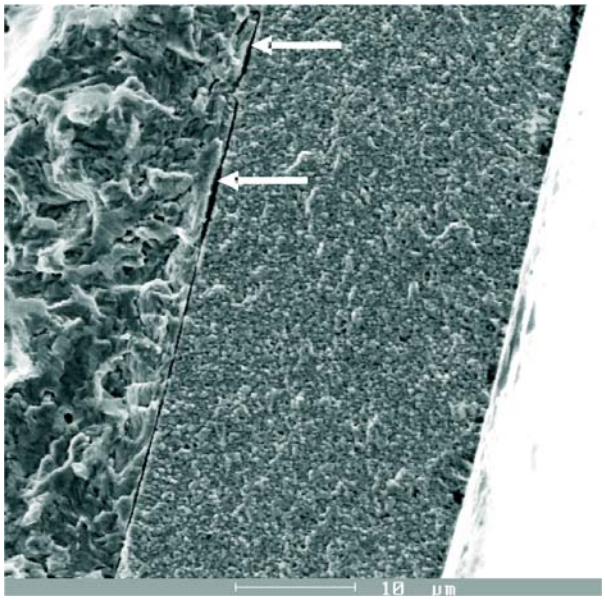

Fig. 6 Granular fracture surface of Ni coating on the S235JRG2 steel, σ_a = 260 MPa, N_f = 1.41×10^7 cycles

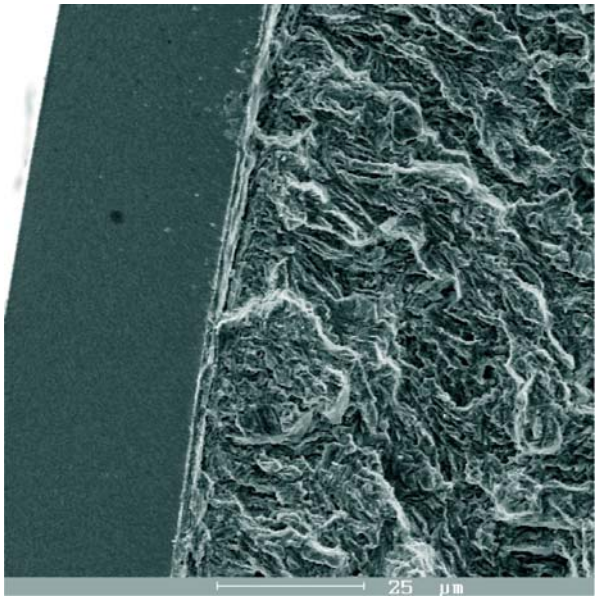

Fig. 7 Fine grain fracture surface of Ni coating, σ_a = 200 MPa, N_f = 2.66×10^8 cycles

In the case of FeZn coating the fatigue cracks were initiated from the coating surface and propagated through this layer to the specimen interior. In whole range of stress amplitudes the ductile damage of FeZn coating was detected. No changes of fracture mode were detected with decreasing stress amplitude. This led to similar fatigue lifetime in the whole range of cyclic loading as in the case of basic material without coating. The example of fracture surface of FeZn coating is shown in Fig. 9 for the specimen subjected to stress amplitude of 260 MPa with fatigue lifetime N_f = 5.82×10^7 cycles. The exact fatigue crack initiation site couldn't be relived because of ductile fracture of FeZn coating which had granular character.

Results of high frequency fatigue tests obtained on S355J0 steel are presented also in the form of S-N curve (Fig. 10). The fatigue data for basic material and for steel with TiN and WC coatings are mutually compared. The S-N curve continuously decreases from high-cycle to ultra-high-cycle region. It can be seen that all

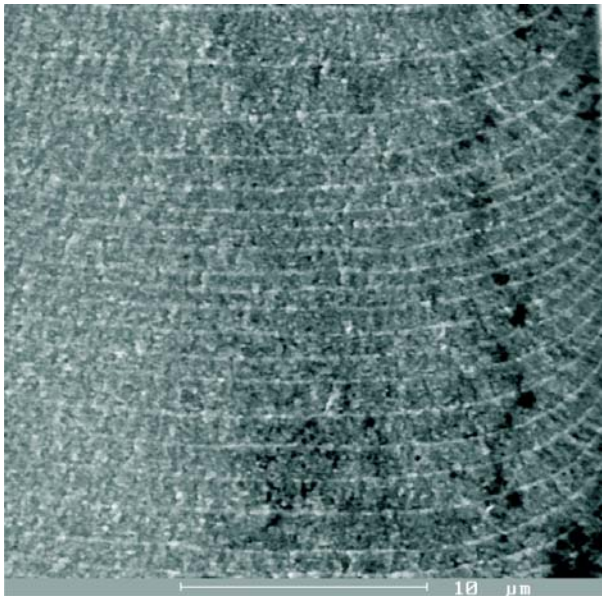

Fig. 8 Detail of fatigue striations on the surface of Ni coating, σ_a = 185 MPa, N_f = 1.62×10^9 cycles

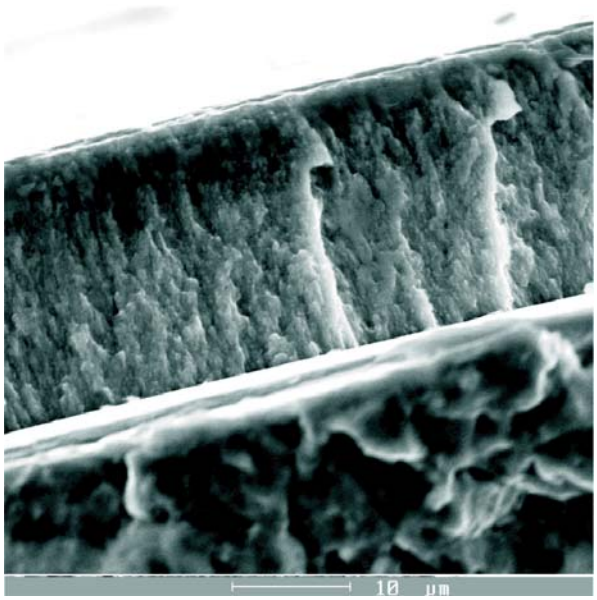

Fig. 9 Ductile damage of FeZn coating, σ_a = 260 MPa, N_f = 5.82×10^7 cycles

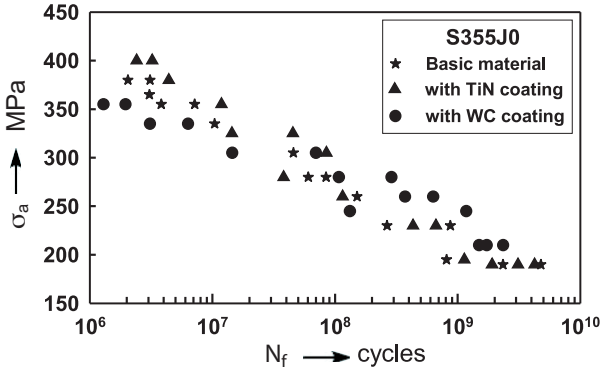

Fig. 10 The S-N dependence of the S355J0 steel

experimental data (for basic steel and steel with coatings also) mutually differ less than 50 MPa in the whole range of stress amplitude. In the region of high stress amplitude the steel with TiN coating has higher fatigue lifetime than that for basic steel and steel with WC coating. With decrease of the stress amplitude this behavior was changed and the lifetime of steel with TiN coating is lower than in the case of basic steel and steel with WC coating. It can be probably explained by high scatter of data due to pores and inhomogenities found in the WC coating. It is hard to say whether or not the TiN and WC coating have positive or negative influence on the fatigue lifetime when compared to basic steel. The fatigue fracture character of the specimens with TiN and WC coatings can be seen in Figs. 11–14.

4. Conclusions

On the basis of this study and the obtained experimental results it was determined that:

- Galvanic Ni coating causes a reduction of fatigue lifetime of the S235JRG2 steel in the low-cycle fatigue region. On the other hand, in the high and ultra-high-cycle fatigue area the influence of galvanic metallization by Ni on the fatigue lifetime is not as strong as in low-cycle fatigue area.
- Galvanic ZnFe coating doesn't influence the fatigue lifetime of the S235JRG2 steel in the whole range of cyclic loading.
- The TiN coating deposited by PVD process and WC coating deposited by thermal spraying have only weak influence of the fatigue lifetime of S355J0 steel.

Acknowledgements

This research has been supported by the Scientific Grant Agency of the Ministry of Education of the Slovak Republic and Slovak Academy of Sciences, grants No. 1/0193/10 and No. 1/0262/10.

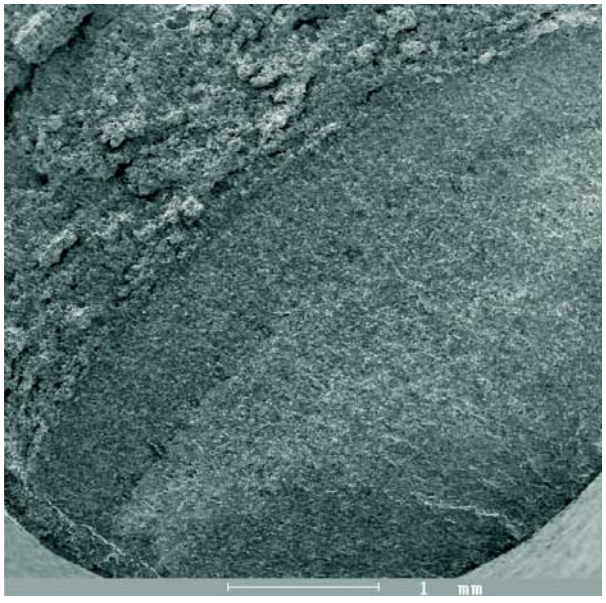

Fig. 11 Fracture surface of S355J0 steel with TiN coating, $\sigma_a = 310$ MPa, $N_f = 9.1\times10^7$ cycles

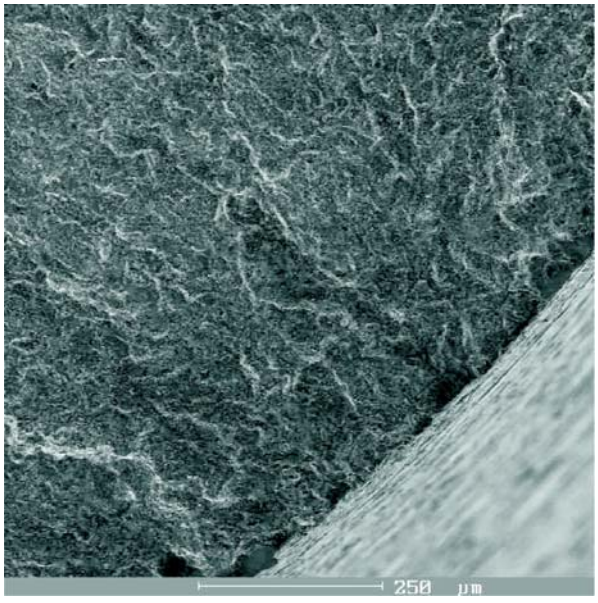

Fig. 12 Detail of fatigue crack initiation site on TiN coating, $\sigma_a = 310$ MPa, $N_f = 9.1\times10^7$ cycles

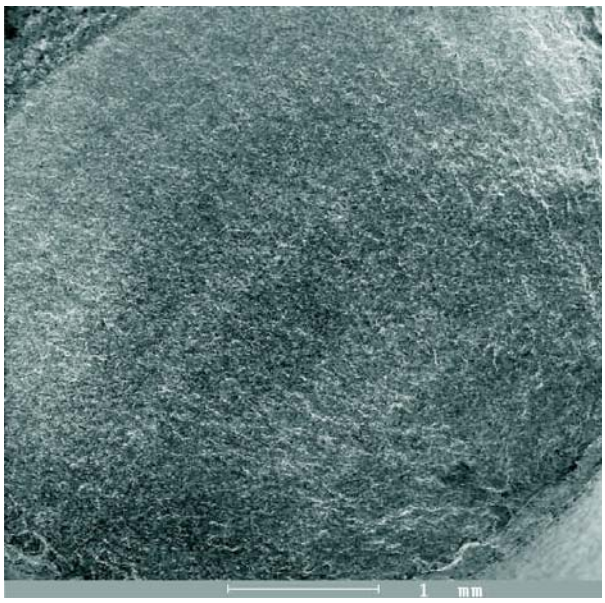

Fig. 13 Fracture surface of S355J0 steel with WC coating, σ_a = 310 MPa, $N_f = 1.5 \times 10^7$ cycles

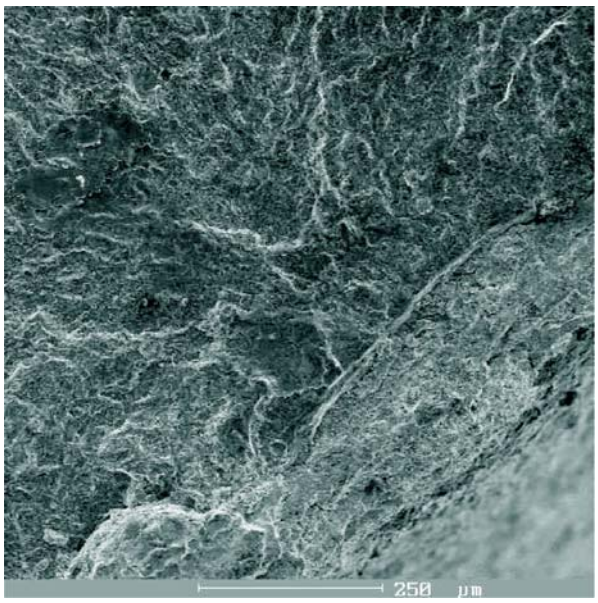

Fig. 14 Detail of fatigue crack initiation site on WC coating, σ_a = 310 MPa, $N_f = 1.5 \times 10^7$ cycles

References

[1] BIDULSKY, R., ACTIS-GRANDE, M., KABATOVA, M., BIDULSKA, J.: *Journal of Materials Science & Technology*. Vol. 25, No. 5, 2009, pp. 607–610.

[2] BOKUVKA, O., NICOLETTO, G., KUNZ, L., PALCEK, P., CHALUPOVA, M.: *Low and High Frequency Fatigue Testing.* EDIS, University of Zilina, 2002.

[3] BATHIAS, C., PARIS, P. C.: *Gigacycle Fatigue in Mechanical Practice.* M. Dekker : New York 2005.

[4] PUSKAR, A.: *The Use of High – Intensity Ultrasonic. Elsevier*, Amsterdam : Oxford : New York 1982.

[5] MURAKAMI, Y.: *Metal Fatigue: Effects of Small Defects and Nonmetalic Inclusions. First edition*, Elsevier Science, 2002.

[6] NOVY, F., KOPAS, P., BOKUVKA, O., CHALUPOVA, M.: *Materials Engineering,* Vol. 10, No. 3, 2003, pp. 67-70.

[7] BURAKOWSKI, T., WIERZCHON, T.: *Surface Engineering of Metals.* WNT Warsaw 1995.

[8] DORAZIL, E., HRSTKA, J.: *Strojirenske materialy a povrchove upravy* [Engineering Materials and Surface Treatments]. VUT Brno, 1985 (in Czech).

[9] PALCEK, P., CHALUPOVA, M.: *Materials Engineering*. Vol. 9, No. 2, 2002, pp. 57–66.

[10] PALCEK, P., CHALUPOVA, M.: *Predikcia zivotnosti strojovych zariadeni* [Endurance Prediction of Machine Devices]. EDIS ZU Zilina, 2000 (in Slovak).

Vaclav Linhart – Dagmar Mikulova – Ivo Cerny *

EFFECT OF INCLUSIONS ON FATIGUE STRENGTH OF HEAT TREATED COMPONENTS

Inclusions significantly affect fatigue properties of quenched and tempered parts. Data about inclusions importance in fatigue crack initiation process were acquired within the framework of a systematical fatigue test programme carried out to verify fatigue properties of CrNiMo(V) steels quenched and tempered to 800 ÷ 1000 MPa strength. A valuable set of fatigue failures from the high lifetime area was acquired.

Microfractographical analysis of these failures enabled to evaluate critically the influence of inclusions, their dimensions, character and morphology on the initiation and propagation of the fatigue cracks in the area of fatigue strength. Comparison of inclusions size "a" according to Murakami with size determined experimentally was made. Limiting influence of small single inclusions in the structure was shown. Initiation of secondary fatigue cracks on inclusions outside of the fracture initiation area was observed. Danger of the fracture initiation after very high lifetime was confirmed.

1. Introduction

Contemporary demands for efficiency and lifetime of plants lead to an increasing amount of heat-treated parts, the strength of which is 800–1000 MPa even in the case of large bulky components. The load-carrying capacity as well as the lifetime of fatigue loaded parts result not only from strength properties, but also from the steel purity and inclusion contents. Modern metallurgical processes of steel production afford new possibilities in this field [1, 2].

The present work follows of our previous experiments [3] and deals with the effect of inclusions on fatigue strength. A sufficiently long lifetime is generally required and thus the data on long-term fatigue properties, characterized by fatigue limit above all, are quite indispensable for the construction of plants.

The basis for assessment of the inclusion effect was obtained during the fatigue tests performed on rods of CrNiMoV and CrMo steels that were cut from large forgings of ship crankshafts and hydraulic cylinders. The tests were of "stair case" type and were aimed at obtaining statistically supported values of the fatigue limit. To evaluate the effect of inclusions, an extensive set of fatigue failures occurring in the specimens having long lifetimes close to the fatigue limit was investigated.

Previous works [4–6] carried out on heat treated steels showed an unfavourable influence of inclusions (e.g. silicates, aluminates) even at their size of 10 μm and this effect became more pronounced with the increasing size of inclusions.

Recent development in fracture mechanics has been connected with some works dealing with the possibilities of a more general evaluation of small inhomogeneities, short cracks, on the fatigue strength. However, the application of fracture mechanics quantities, particularly that of K and ΔK factors to those small areas seems to be rather problematic [7]. To solve this problem, various engineering modifications have been proposed. The modification of El Haddad et al. [8] is well known and describes the dependence of fatigue properties and that of fatigue limit on inhomogeneity size ℓ and on the threshold value of ΔK_{th}

$$\Delta\sigma_{th} = \Delta K_{th}/\sqrt{(\pi(\ell_0 + \ell))} \quad (1)$$

Taking fatigue limit $\Delta\sigma_{th} = 2\ \sigma_C$ and $\ell = 0$, we obtain

$$\ell_0 = (1/\pi)\ (\Delta K_{th}/2\sigma_C)^2 \quad (2)$$

Another modification of relation (1) was made by Lukas and Kunz [9].

Murakami, Endo et al. [10,11] and other authors describe the dependence of fatigue limit σc [MPa] on strength properties of the base material [HV] and on the inclusion area $\underline{a}$ as

$$\sigma_C = \Lambda\ (HV + 120)/(\sqrt{a})^{1/6} \quad (3)$$

* **Vaclav Linhart, Dagmar Mikulova, Ivo Cerny**
SVUM a.s., Praha Czech Republic, E-mail: linhart@svum.cz

Thus, the critical size of inclusion on fatigue limit is

$$a = [\Lambda(HV + 120)/\sigma_C]^{12} \quad (4)$$

where $\underline{a}$ is projected area of the inclusion in the plane perpendicular to the plane of maximum normal stresses. The values of constant Λ are 1.43 for the inclusions situated at the surface and 1.56 in the case of inclusions occurring under the surface.

The assessment of the inclusion effect on fatigue properties by means of $\sqrt{a}$ was accepted also by Bomas et al. [12] and Kunz and Lukas [13] .

2. Effect of inclusions on specimens obtained from the hydraulic cylinder

Forgings of the high capacity press hydraulic cylinders diameter 1580/1060 mm were made of 20NiCrMoV14-6 steel, the chemical composition of which is as follows (weight %): 0.19 C; 0.36 Mn; 1.6 Cr; 3.1 Ni; 0.4 Mo; 0.03 V; 0.016 Al; 0.0059 P; 0.004 S. Statistically processed results of staircase fatigue tension – compression tests ($R = -1$) carried out on specimens of diameter 8.6 mm are given in Table 1. The forgings of the second group (No. 5708, 5709) were substantially heavier than those of the first one (No. 4758, 4759).

Table 1

Forging No.	Strength [MPa]	Fatigue limit σ_C [MPa]		Standard deviation of fatigue limit [MPa]
		P = 50 %	P = 95 %	
4758	801.5	417	386	9.06
4759	789.9	406	332	25.6
5708	874.8	387	262	40.5
5709	859.1	387	363	9.1

It follows from Table 1 that the fatigue limit at the probability level $P = 50\%$ of the forgings with higher strength (Nos. 5708, 5709) is surprisingly lower – *c.* by 10% - than that of the forgings with lower strength (Nos. 4758, 4759).

As expected, the failure occurred in several specimens in the region of high cycle loading close to the fatigue limit. These specimens were examined by microfractographical microanalysis using JEOL JSM 35 scanning microscope.

In most of cases, the initiation centres of fatigue failure, characteristic by typical rosettes of fine gradual defect growth with radial orientation, were found under the fracture surface even at low magnifications (Fig. 1). The second phase of defect growth which led to fatigue failure took place after the spreading out of original rosette up to the rod surface. Microfractographical examination showed that the initiation of fatigue failure occurred at clusters of granular inclusions with an incompact network (Fig. 1). The length of inclusions is 150–300 μm, the dimension of their characteristic area $\underline{a}$ is 6000–46000 μm^2. It follows from the electron microanalysis carried out on CAMEBAX electron microanalyser that the inclusions are complex and contain a high amount of Al,

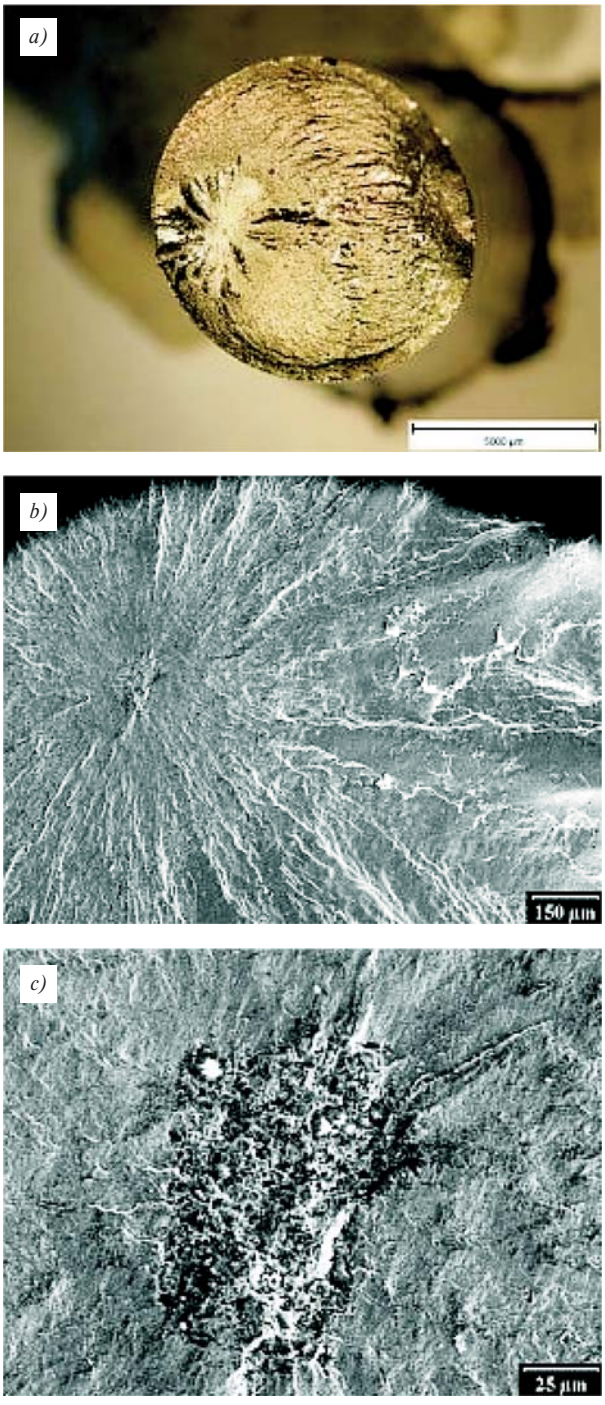

Fig. 1 Initiation fracture rosette under the surface, specimen No. 5708-37 a) macroscopic view, b) microscopic view, c) detail of the cluster

Ca, O and C. They are apparently aluminates ($Al_2 O_3$) and calcium compounds (CaO, $CaCO_3$).

The occurrence of inclusions lead to a substantial increase in statistical scatter of fatigue limit values in the investigated forgings (Table 1). On the other hand, this result is considerably influenced by a random spacing of clusters and, therefore, it may not be generally valid.

The differences in the spacing of initiation rosette occurring on the fracture surface did not cause, surprisingly, any significant changes of fatigue lifetime.

Surfaces are generally more sensitive to the initiation of fatigue fracture than the regions under the surface. It arises from the greater deformation freedom of surface structural regions. The analysis of fracture relief at the specimen surface under which the initiation rosette occurred showed that the cause of latent tendency of surface layers to the initiation were isolated granular inclusions whose length was rather small, up to some tens of μm. It can be expected that in the case of bulky forgings the danger of occurrence of unfavourable inclusion clusters will be quite considerable.

The analysis of the second set of forgings (No.4758, 4759) with higher value of the fatigue limit showed that the fatigue failure initiated, almost without exception, at the specimen surface on groups or smaller clusters of granular inclusions (Figs. 2, 3). These clusters are similar to the larger ones observed in forgings of the first group; their length is 50–150 μm and the area reaches the values between 1000 and 13000 μm^2. However, a considerably larger cluster area (50000 μm^2) was also exceptionally observed; in this case, the determined lifetime was very low (3 – 4.10^5 cycles). The presence of large clusters of inclusions caused in some cases (see Table 1) a greater scatter of fatigue limits whose values were low at the required higher reliability level.

The effect of regions containing sulphide inclusions was found to be quite unimportant in comparison with the influence of granular complex inclusions. For example, fatigue failure initiated at the surface on the group of granular inclusions with the total area a = = 7400 μm^2, but only some weak symptoms of secondary initiation of the fatigue failure were observed at the large sulphide cluster (Fig. 4) with the dimensions 133 × 200 μm (a = 20890 μm^2) occurring inside of the same specimen.

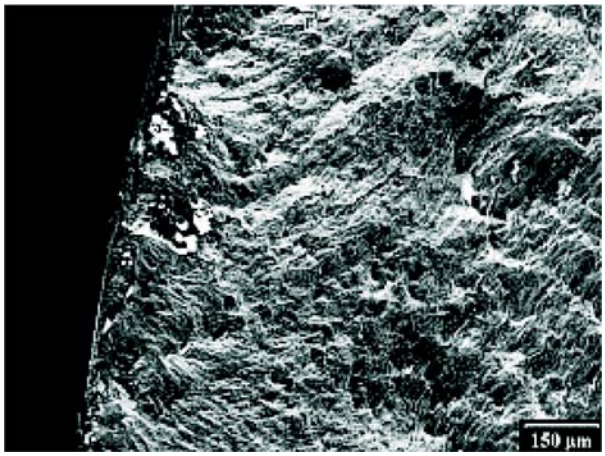

Fig. 2 Group of granular inclusions, specimen No. 759-30

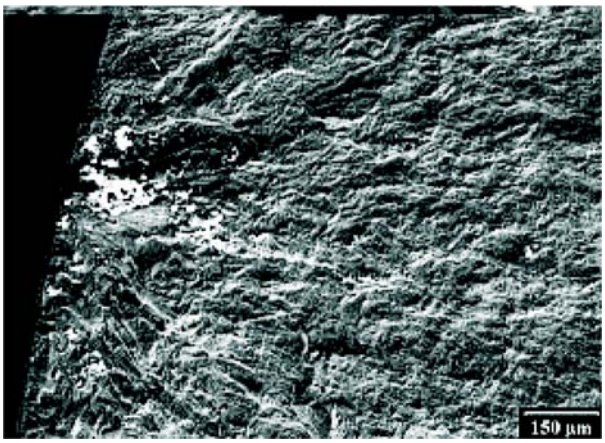

Fig. 3 Cluster of granular inclusions at the initiation area, specimen No. 4759-16

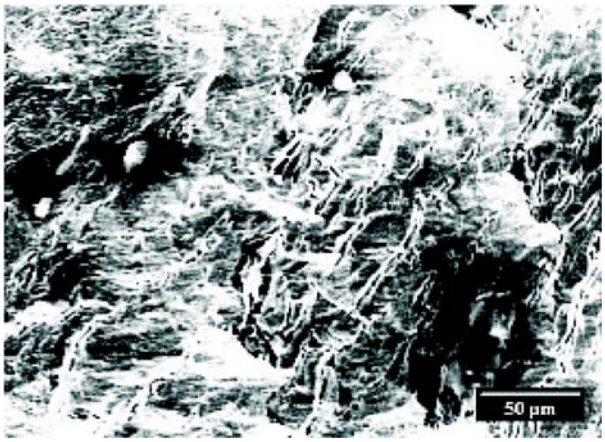

Fig. 4 Cluster of sulphides in fracture surface, specimen No. 4759-16

It was found, similarly to the first group of forgings *that the isolated granular inclusions, the size of which was 15 – 20 μm (Fig. 6), occurring in the coarser tempered bainitic structure (Fig. 5) did not lead to initiation of fatigue failure.* In this case, the fatigue failure did not initiate on inclusions, but inside the basic quenched structure.

We compared our results with the critical sizes of inclusions determined according to the relations (3) and (4) of Murakami et al. – Tab. 2, for the fatigue limit at the probability levels of 50% and 95%. The calculated critical values are close – within one order – to those determined metallographically even though the evaluation according to Eqs. (3) and (4) corresponds rather to the con-

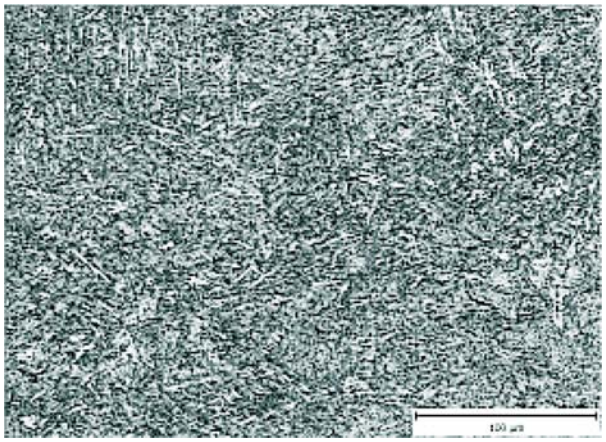

Fig. 5 Fairly coarse tempered bainitic structure

servative approach. This is quite obvious from Fig. 7, where the measured sizes of inclusions at the surface and the calculated values according to relation (4) are given.

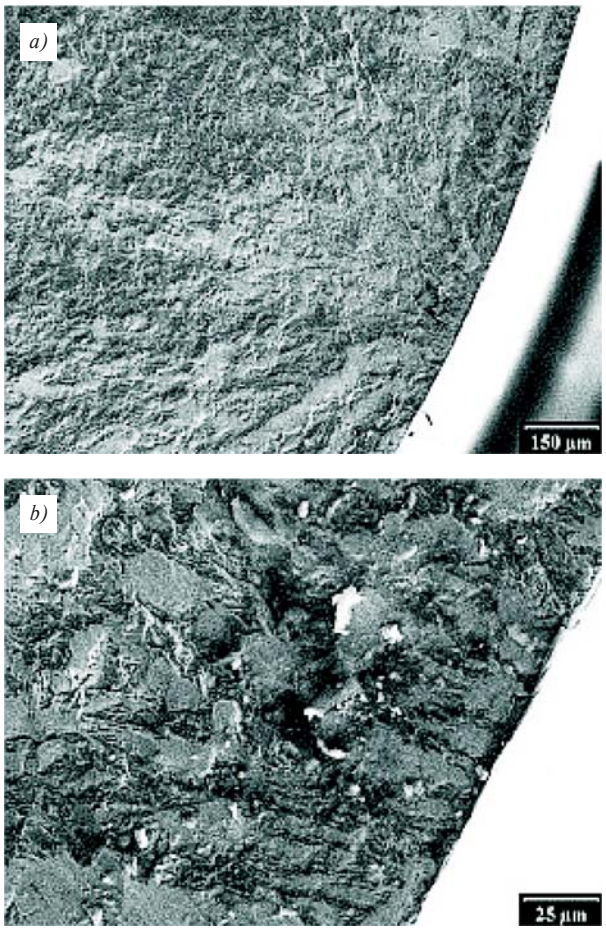

Fig. 6 a), b) Initiation of the fatigue fracture is not practically influenced by isolated granular inclusions, specimen No. 4758-9

Table 2

Forging No.	Surface / Fracture Area S / FA	Critical inclusion size "a" [µm]	
		σ_C (P = 50%) [1)]	σ_C (P = 95%) [1)]
4758	S	59	102
	FA	90.7	309
4759	S	45.1	504.9
	FA	128.1	1431.7
5708	S	150.5	1623.7
	FA	427.6	46128.4
5709	S	129.6	297
	FA	368.2	843.7

Note 1): Specific concrete σ_C values – see Table 1

3. Effect of inclusions in specimens cut from the crankshafts

The massive crankshaft forgings with the journals of 450–460 mm diameter were investigated.

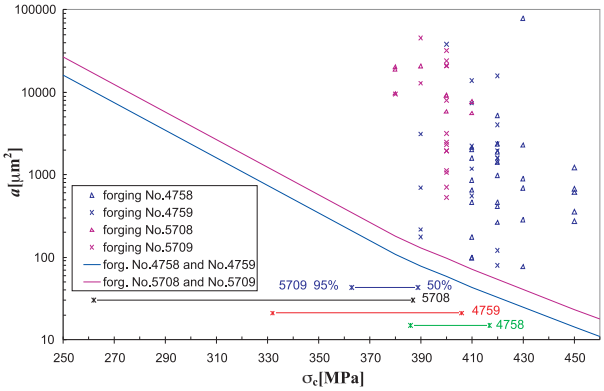

Fig. 7 Comparison of calculated "a" value with the inclusions size determined experimentally

3.1. 50CrMo4 steel crankshafts

The steel of the chemical composition (weight %) 0.51 C; 0.79 Mn; 1.18 Cr; 0.49 Ni; 0.27 Mo; 0.1 V; 0.007 P; 0.001 S and with the micropurity according to standards: A 0 – 0.5; oxides D 1.5 was heat-treated to the strength R_m = 928 MPa and hardness 296 – 320 HV. Resulting tempered structure was characteristic by a needle morphology. Fatigue limit in tension-compression loading ($R = -1$) was determined with the help of staircase fatigue tests. It reaches the value σ_C = 441 MPa at the probability level P = 50% and only 249.5 MPa at the probability level P = 95%.

Macroexamination revealed fatigue failures initiating at the surface in all specimens. Microfractographical investigation showed

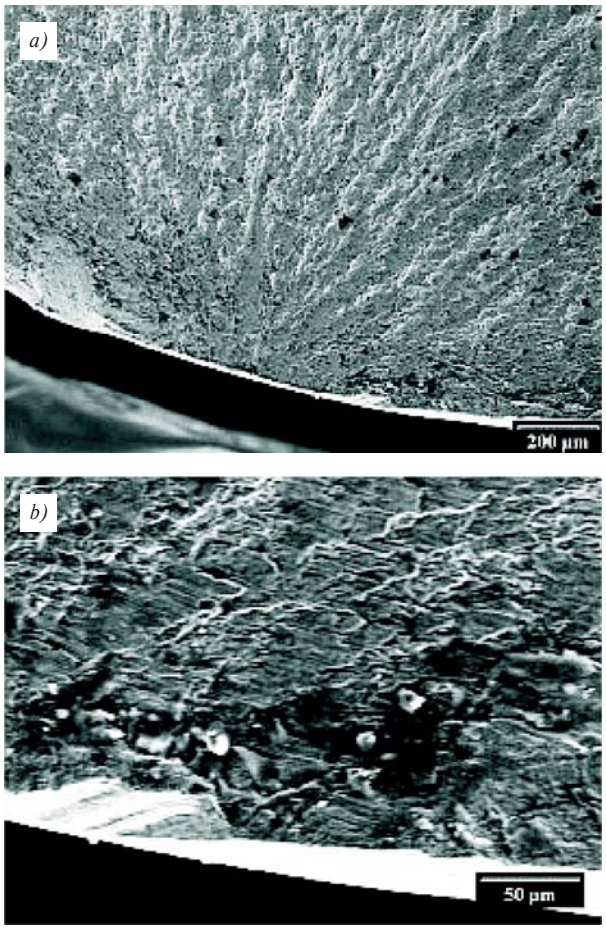

Fig. 8 a), b) Initiation of the fatigue fracture is not influenced by isolated fine granular inclusions, specimen No. P7 cut from the crankshaft

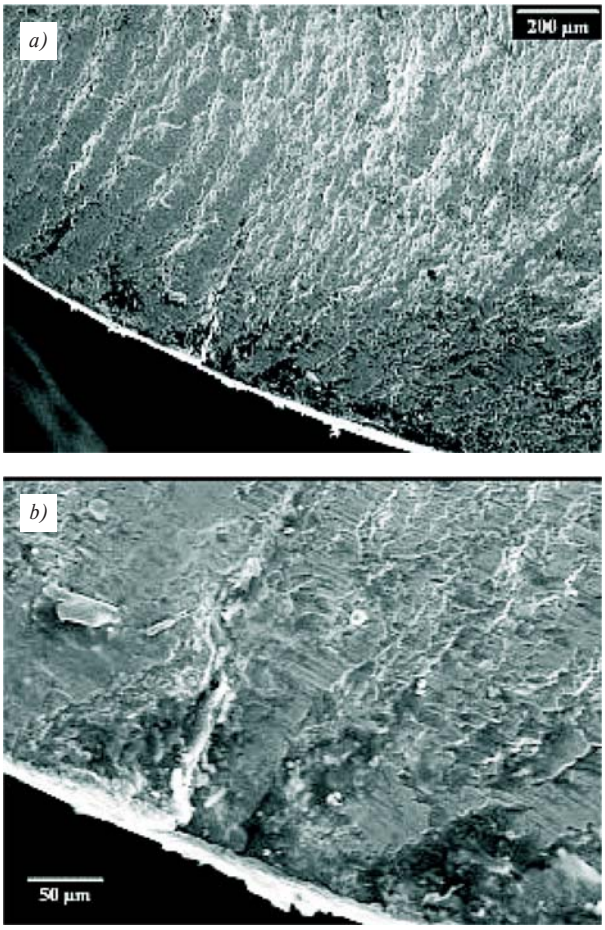

Fig. 9 a), b) Row of fine granular inclusions affected the initiation of fatigue fracture, specimen No. P7 cut from the crankshaft

the occurrence of inclusions (apparently the complex inclusions of aluminates and calcium oxides) in the form of isolated granular particles or groups of the particles. Their typical size is several tens of µm (maximum 100–170 µm) and their area a at the surface reaches several hundreds of µm (max. 3000 µm^2) – see Fig. 8. It is quite apparent even in this case that the initiation centre of fracture lies outside the region of fine particles, it occurs in the structure of the base material. Fatigue relief is not practically influenced by the presence of granular inclusions. This situation was observed in most cases, but, on the other hand, there are also some specimens where the fracture initiated at the group of inclusions (Fig. 9a, b). A considerable scatter of fatigue tests results, particularly of fatigue limit values at the probability level 95%, can be explained in this way.

3.2. 34CrNiMo6 steel crankshafts

The steel of the chemical composition (weight %) 0.36 C; 1.5Cr; 1.45 Ni; 0.21 Mo; 0.0058 Al; 0.0028 P; 0.0067 S; 0.0019 N was heat-treated to the strength σ_c = 961 MPa and hardness 315 HV. The fatigue limit in tension–compression loading ($R = -1$) was determined by staircase fatigue tests again and reached the values σ_C = 390 MPa at the probability level P = 50% and σ_C' = = 355.2 MPa at the probability level P = 95%.

The fatigue failures initiating at the surface were found in all rods. In spite of the fact that the R_m value is close to that of 50CrMo4 steel crankshaft (961 and 928 MPa, respectively), the fatigue limits are different. σ_C = 390 MPa for the present crankshaft and σ_C = 441 MPa for the previous one at 50% probability level. However, at 95% probability level, the situation is opposite: σ_C' = 355.2 MPa and 249.5 MPa, respectively.

The oxide-sulphidic inclusions as well as complexes of granular inclusions containing Al_2O_3 and CaO_2 were found both at surface fatigue initiation sites and at internal sites under the surface. The size of oxide-sulphide inclusions was 70–180 µm, exceptionally up to 900 µm. The size of clusters of granular inclusions was up to 100 µm, sometimes even 1100 µm.

The specimens were loaded uniformly across the whole cross-section during the tension-compression tests. Even in regions located

far from the surface, the formation of secondary initiation cracks on some inclusions was found. It follows from the occurrence of fracture steps diverging from the inclusions. Typical examples of secondary initiation can be seen in Figs. 10 and 11.

According to (4), the critical size of inclusion $a = 271$ μm can be determined for the fatigue limit. This area corresponds to the diameter of 18.6 μm in the case of circular particle and to the size 36.8 × 7.4 μm (ratio 5:1) in the case of prolonged inclusions. Our results suggest that the assessment of the limit inclusion size according to Eq. (4) seems to be very conservative.

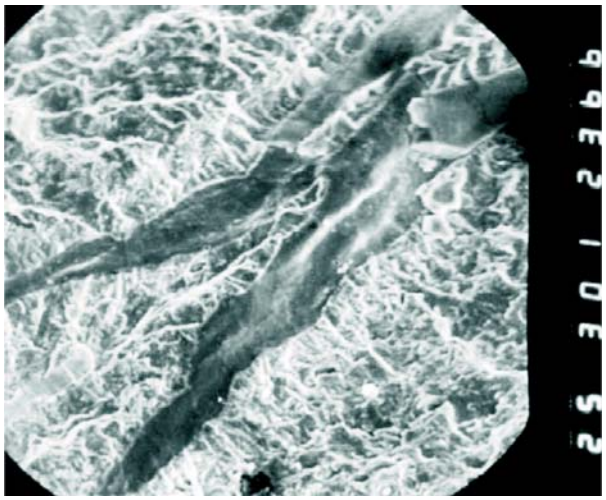

Fig. 10 Secondary initiation cracks at inclusions (sulphide), specimen No. K1 cut from the crankshaft

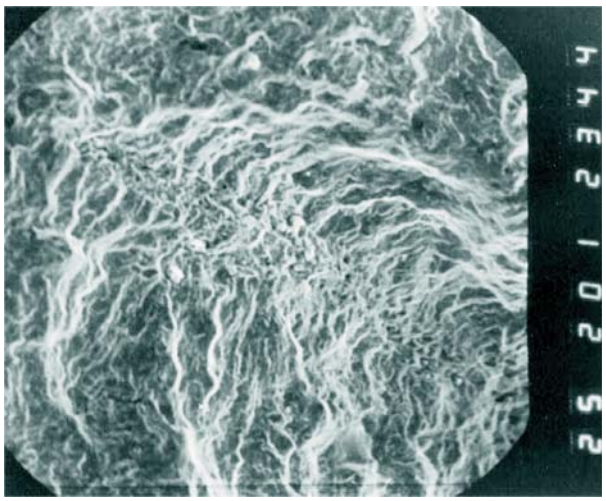

Fig. 11 Secondary initiation cracks at large cluster of granular inclusions, specimen No. K10 cut from the crankshaft

4. Conclusions

In this paper, results of fatigue tests of tension-compression type in the region of fatigue limit performed on the specimens cut from the massive forgings of alloy steels heat-treated to strength $R_m = 800–960$ MPa are described and discussed. The main results can be summarised as follows:

- Inclusions occurring in heat-treated steels cause very often the initiation of the fatigue failure. However, isolated fine granular inclusions (up to 20 μm), which are present particularly in coarser heat-treated structure, have practically no effect on the fracture initiation.
- According to the results obtained from fatigue tests at tension-compression with load amplitudes close to fatigue limit, large clusters of granular inclusions with the length exceeding 100 μm result in initiation of fatigue failure. This effect was often observed even in cases when the inclusions did not occur on the surface as the area most sensitive to fatigue crack initiation, but inside the specimens. In such the cases, initiation area is often connected with distinct circular, radially growing rosette, which, after reaching the surface, causes fast fatigue failure.
- Secondary initiation nuclei, latent up to 10^7 cycles, were formed during the fatigue tests at some large oxide-sulphide inclusions and at clusters consisting of granular complex inclusions located at the surface. They can result in the formation of fatigue failure after very long lifetime (by several orders higher than 10^7 cycles). The internal initiations with the rosettes can have a similar effect.
- The unfavourable effect of inclusions is dependent first of all on their size, the inclusion type being less important. This fact makes the evaluation of their effect simpler.
- Considering more general fracture mechanics approaches of evaluation of inclusions significance, attention was paid first of all to the procedure according to Murakami et al. (Eqs. (3) and (4)), using the projected area a as the characteristic value. The comparison with our results indicates that this procedure can be useful for engineering orientation, but it is rather conservative and overestimates the adverse effect of inclusions.

Acknowledgement

This work was carried out within Research Programme MSM 2579700001 supported by the Ministry of Education, Youth and Sport of the Czech Republic.

References

[1] STRNADEL, B., BUZEK, Z., KUBENA, J.: Problems of Micro-purity of Structural Steels Determined for Demanding Technical Applications (in Czech). *Hutnicke listy,* 2003, 12, 3

[2] BAZAN, J., BUZEK, Z., STRANSKY, K., BUZEK, R.: Increase of Steel Purity Using Secondary Metallurgy Method (in Czech). In: *Hutnicke listy*, 1999, 7–8, 20
[3] LINHART, V., SIGMUNDOVA, J.: Inclusions and their Effect on Fatigue Failure of Heat-treated Parts. In: *Materials Engineering,* 14, 2007, 3, 13
[4] ABE T., FURUYA Y., MATSUOKA S.: Gigacycle Fatigue Properties of 1800 MPa Class Spring Steels. In: *Fatigue & Fracture of Engineering Materials & Structures,* 27, 2004, 2, 159
[5] CUMMINGS, H.N. et al.: *Proceedings of ASTM*, 8, 1958
[6] CUMMINGS, H.N., STULEN, F.B. et al.: *ASM Handbook*, 19, Fatigue and Fracture, ASM International, 1996
[7] LUKAS, P., KUNZ, L.: Small Cracks-nucleation, Growth and Implication to Fatigue Life. In: *International Journal of Fatigue,* 25, 2003, 9, 855
[8] EL HADDAD, M.H., TOPPER, T.H., SMITH, K.N.: Prediction of non Propagating Cracks. In: *Engineering Fracture Mechanics,* 11, 1979, 3, 573
[9] LUKAS, P., KUNZ, L., WEISS, B., STICKLER, R.: Notch Size Effect in Fatigue. In: *Fatigue & Fracture of Engineering Materials & Structures,* 12, 1989, 3, 175
[10] MURAKAMI, Y., ENDO, M.: Effects of Defects, Inclusions and Inhomogeneities on Fatigue Strength. In: *International Journal of Fatigue*, 16, 1994, 3, 163
[11] MURAKAMI, Y., NOMOTO, T., UEDA, T.: Factors Influencing the Mechanism of Prolonged Fatigue Failure in Steel. In: F*atigue & Fracture of Engineering Materials & Structures*, 22, 1999, 7, 580
[12] BOMAS, H., LINKEWITZ, T. MAYR, P.: Application of a Weakest-link Concept to the Fatigue Limit of the Baring Steel SAE 52100 in a bainitic condition. In: *Fatigue & Fracture of Engineering Materials & Structures,* 22, 1999, 9, 733
[13] KUNZ, L., LUKAS, P.: Notch Sensitivity of a Steel for Railway Wheels Plates at High Mean Stress. In: *Materials Engineering*, 10, 2003, 1, 7

Milan Vasko – Bohus Leitner – Milan Saga *

COMPUTATIONAL FATIGUE DAMAGE PREDICTION OF THE LORRY FRAMES UNDER RANDOM EXCITATION

The paper deals with FEM application in the TATRA 815 lorry frame construction fatigue life estimation. Construction of critical nodes from the fatigue damage point of view was found and analyzed. Analysis of the particular traffic state influence on the fatigue damage cumulation will be presented too.

Keywords: computer simulation, random vibrations, finite element method, fatigue life, cumulative damage prediction

1. Introduction

The process of fatigue damage (fatigue life) prediction is generally very complicated and contains a lot of uncertain inputs, e.g. material characteristics, randomness of the service loading etc. Our paper aim is to present the selected results of the computer simulation analysis of fatigue damage lorry frames. This simulation concentrates to:

- the most important aspects which are typical for means of transport working conditions,
- use of the obtained computational models for a working exciting simulation of a virtual lorry construction,
- dynamic analysis of the vehicle critical parts stress under the influence of typical working conditions,
- the fatigue life prediction of the analyzed vehicle most exposed parts.

During the computational simulation of the chosen vehicle (TATRA 815 S1) under the modeled conditions of its service, it was necessary to consider that it is a kind of vehicle whose traffic conditions are determined mainly by the influence of the following aspects:

- roadways and terrain surface undulation,
- traffic velocity.

2. Analyzed Vehicle Characterization

It is known from technical publications and from similar performed analyses of various kinds of transportation vehicles, that the most loaded lorry parts are their bearing members (bearing frames, subsidiary bearing constructions) and axles. They carry the loads occurring at the interaction of the vehicle instantaneous weight influence and roadways surface undulation influence in synergy with chosen traffic velocity.

This is the reason why the presented description is oriented mainly to these construction entities. TATRA 815 S1 lorry undercarriage consists of a frame, a subsidiary frame, front and back hangers composed of axels with wheels, cushioning, own brakes and an axle control operating machinery, control and brakes machinery.

The main vehicle bearing part is formed by a spinal frame to which a subsidiary ladder frame for bodywork assessment, a driving-gear and a sleigh is mounted. The spinal frame consists of particular axle gear-boxes, an additional gear-box, front and back joining piece, front and back bearing tube and transoms. The connection of the mentioned parts is realized by means of flanges and bolted connections.

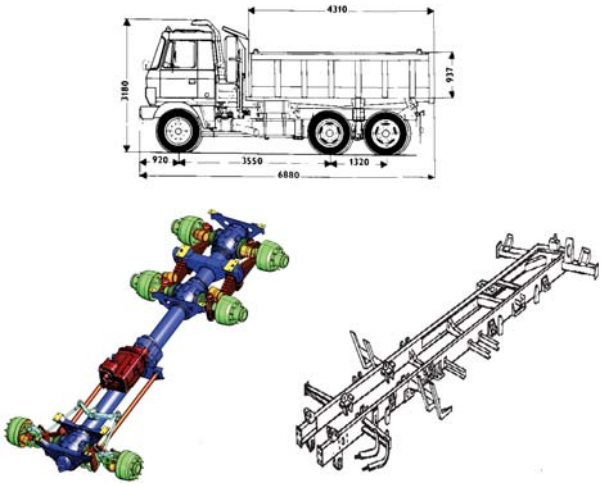

Fig. 1 Three-dimensional model of TATRA 815 S1 lorry undercarriage and subsidiary ladder frame

* **Milan Vasko[1], Bohus Leitner[2], Milan Saga[1]**
[1] KAME, Faculty of Mechanical Engineering, University of Zilina, Slovakia, E-mail: milan.vasko@fstroj.uniza.sk
[2] Faculty of Special Engineering, University of Zilina, Slovakia

The subsidiary ladder frame welded from longitudinal "U" shapes is mounted on the transoms by bolted connections. The "U" shapes are going through all the vehicle length and are interconnected by transoms. A cab, an engine together with a clutch, a sleigh, a reel, bumpers, draw-bar equipment etc. are mounted on transoms, brackets and holders of the subsidiary ladder frame.

3. Computational Vehicle Model

The computational finite element model of the TATRA 815 S1 vehicle was built-up in COSMOS/M program in cooperation with TATRA Koprivnice Company. In general, its applied realization consisted of several consequential phases [9]

- geometry model generation,
- definition of elements, their cross-section constants and material characteristics,
- generation of final element mesh,
- definition of boundary conditions,
- setting of acting load,
- computation and verification of obtained results.

Beam elements of the BEAM3D type, mass elements of the MASS type, axial spring boundary elements of the BOUND type together with damping units were used for generation of the finite-element model of the analyzed TATRA vehicle. The generated model of the TATRA vehicle is presented in Fig. 2.

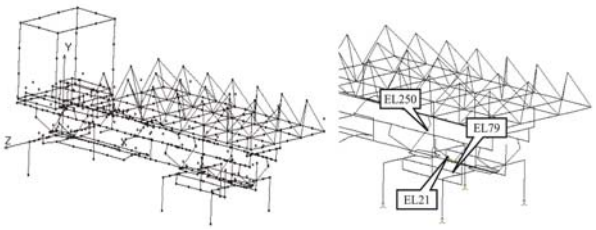

Fig. 2 Finite-element model with definition of chosen vehicle critical parts location

Several elements representing the most exposed parts of the real vehicle construction were determined from the static analysis results – considering a vertical loading character. From these elements, the critical parts from the fatigue life damage accumulation point of view were chosen.

Normal stresses in marginal profile points of elements No. 21, 79 and 250 obtained extreme values as ensued from the graphical representation of performed stress analysis results and from the next performed analyses output files [9]. Particular examined elements can be shortly characterized as follows:

- element 21 – part of the vehicle bearing spinal frame, specifically the back bearing tube, construction material – steel STN 41 1523, shape according to Fig. 3a,
- element 79 – part of the formed thick-walled bridge tube of the right central half-axle, construction material – steel STN 41 1523, tube shape according to Fig. 3b,
- element 250 – the longitudinal truss part of the subsidiary bearing frame, approximately in the middle between both back axles, "U" shape 250×100×7, construction material – steel STN 41 1523, element shape according to Fig. 3c.

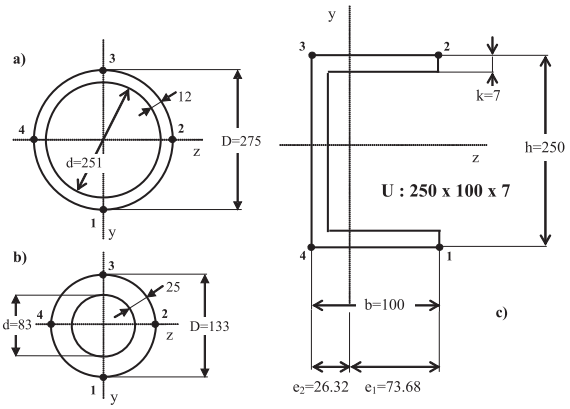

Fig. 3 Cross-sections of the analyzed critical parts

4. Excitation Model

The process of kinematics excitation was considered a cooperation of two basic operating factors:

- road surface quality (5 road surface quality classifications and difficult terrain specifications),
- vehicle velocity (4 reference velocities for each road surface quality).

As the excitation generator were applied behaviors of the section's longitudinal height unevenness for different road and terrain surfaces. The method of their acquiring is particularly described for an example in [1, 7]. The experimental obtaining of the height unevenness behavior is time and financially demanding. Therefore, the additional realizations needed for the left and right track excitation were obtained by application of the autoregression modeling theory [6, 7]. Suggested theoretical equipment allows for describing the examined process by means of identified ARMA model and stochastic processes generation with identical statistical characteristics of 1st and 2nd degree.

The basic process of the road unevenness generation [3, 6, 7]:

- selection of the road sections with regard to data from road database SSC (5 road surface quality classifications),
- experimental measurement of the longitudinal height unevenness behavior so-called middle longitudinal profiles (exact leveling at an interval of 0.25 cm),
- part of the leveling line longitudinal slope and rough unevenness elimination; the random part was extracted, it has a character of a random value of the centered stochastic function and it especially excites the vertical vibration of the vehicle and sig-

nificantly affects the stochastic vibration of the vehicle's parts during the movement,
- application of the autoregression modeling theory for the suitable ARMA model specification and for generation of new statistically adequate realizations of the stochastic height unevenness behavior on the miscellaneous surface quality.

The behavior of the chosen random kinematics excitation functions for road classification 5 and terrain are shown in Fig. 4.

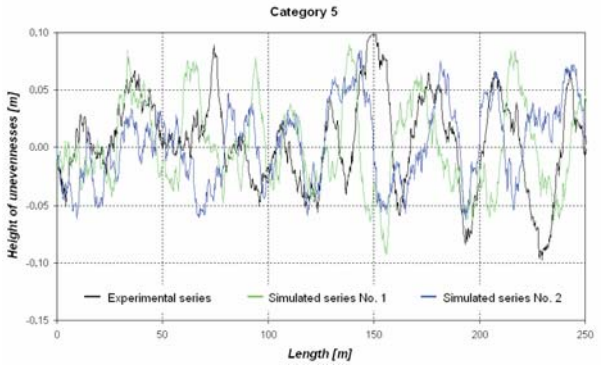

a)

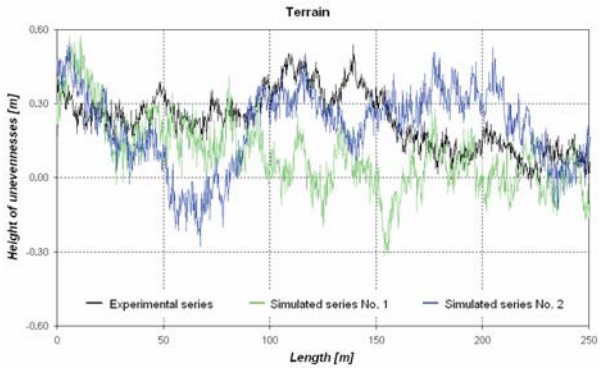

b)

Fig. 4 The random function - $u_{yL}^{(1)}$
a) road classification No. 5, b) terrain

The points where these functions input into the computational model are presented in Fig. 5, where:

v – vehicle speed, [km/h],
L_1 – wheel base No. 1, [m], (see Fig. 5),
L_2 – wheel base No. 2, [m], (see Fig. 5),
$u_{zL}^{(1)}$ – unevenness of the left rail in a vertical direction for the front axle, [m],
$u_{zP}^{(1)}$ – unevenness of the right rail in a vertical direction for the front axle, [m],
$u_{zL}^{(2)}$ – unevenness of the left rail in a vertical direction for the 1st back axle, i.e.

$$u_{zL}^{(2)}(t) = u_{zL}^{(1)}\left(t - \frac{L_1}{v}\right), \text{ [m]},$$

$u_{zP}^{(2)}$ – unevenness of the right rail in a vertical direction for the 1st back axle, i.e.

$$u_{zP}^{(2)}(t) = u_{zP}^{(1)}\left(t - \frac{L_1}{v}\right), \text{ [m]},$$

$u_{zL}^{(3)}$ – unevenness of the left rail in a vertical direction for the 2nd back axle, i.e.

$$u_{zL}^{(3)}(t) = u_{zL}^{(1)}\left(t - \frac{L_2}{v}\right), \text{ [m]},$$

$u_{zP}^{(3)}$ – unevenness of the right rail in a vertical direction for the 2nd back axle, i.e.

$$u_{zP}^{(3)}(t) = u_{zP}^{(1)}\left(t - \frac{L_2}{v}\right). \text{ [m]},$$

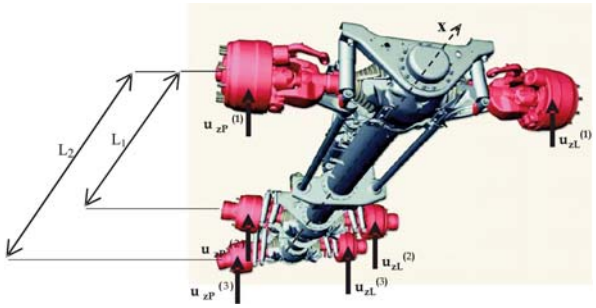

Fig. 5 Identification of the kinematics excitation functions

5. Computational Fatigue Prediction

The vehicle operational reliability, in particular its no-failure operation and lifetime is a dominant property for vehicles as a typical representative of the dynamically stressed complex mechanical constructions. These properties continually gain importance. Obviously it relates to raising of the transport velocity, weight reduction of the construction parts, decreasing of the computational safety constants, development and application of the new construction materials, etc. Various vehicles operational failure cause analyses definitely prove that the fatigue process as a dynamic stress consequence assists in nearly all cases.

During the simulation, the dynamic analysis often ends at the modal-spectral construction properties determination, or at its stochastic oscillation solving only from the rigid body oscillation point of view, as for example vehicle vibration, swinging, rolling etc.

If the potential response acquisition is needed too, the problems related to the size can often occur. This means enormous

requirements for the computer performance and the available operating memory size.

Fatigue life "computation" or rather "estimation" in fact differs from the value achieved during the real machine operation. This is caused mainly by problems related to exact determination of external load characteristic parameters, which affect the construction during operation. Fatigue strength values are not available for specific construction nodes but mainly only for the material samples representing the perfect status, which occurs in real operation conditions only rarely.

Considerations about the problem solution possibilities of the fatigue life estimation can be simply reduced to the four basic tasks:

- *selection of the construction critical locations* that will become the subject of additional analysis,
- *stress determination in the chosen critical locations* and its "post-processing" using the methods suitable for the lifetime estimation,
- design or examination of the used construction material properties on the base of the chosen material characteristics,
- selection of a suitable computational procedure – *theorem of the fatigue damage cumulation* – which effectively joins the material characteristics to the operational stress characteristics. An application result of the suitable fatigue damage cumulation theorem is the lifetime estimation quantified value of the analyzed critical part of the examined construction.

Rajcher's theorem was used for the fatigue damage computations in the identified critical parts of the analyzed vehicle. This theorem defines the fatigue damage in the critical location of the construction part induced per one second and is expressed by the following equation [2, 5]

$$D_s = \frac{\Gamma\left(\frac{w}{2}+1\right)\cdot\left[2\cdot\int_0^{\infty} f^{\frac{2}{w}}\cdot S(f)df\right]^{\frac{w}{2}}}{N_C\cdot\sigma_C^w}, \qquad (1)$$

where:

w – exponent of S/N curve, [-],
σ_C – fatigue limit, [Pa],
N_C – limit number of cycles to failure, [-]
f – frequency, [Hz],
$S(f)$ – spectral power density of the stress loading process, [Pa^2.s],

$\Gamma\left(\frac{w}{2}+1\right)$ – gamma function value, [-].

Time until the next failure can be expressed (in hours) as follows

$$T = \frac{1}{3600\cdot D_s} = \frac{N_C\cdot\sigma_C^w}{3600\cdot f_e\cdot\left(2\cdot s_\sigma^2\right)^{\frac{w}{2}}}\cdot\Gamma\left(\frac{w}{2}+1\right). \qquad (2)$$

It is obvious that all the process can be realized only by means of the computer technique efficient. The approach in practice is that after the import or calculation of the process spectral power density values $S(f)$, the process standard deviation s_σ and process effective frequency f_e of the probability density will be determined.

The practical application of the presented process was realized by the program created in the MATLAB environment. The computational program *fatigue.m* was used at the fatigue life computational estimation of the construction in the selected critical locations under the chosen characteristics of the lorry operating conditions.

In the application the following material parameters defining the fatigue properties were used:

- slope of S/N curve w,
- fatigue limit σ_C,
- limit number of cycle N_C;

which gain the following values for the particular elements:

- for EL 21: $w = 5.8$, $N_C = 3\cdot10^6$, $\sigma_C = 190$ MPa,
- for EL 79: $w = 5.8$, $N_C = 3\cdot10^6$, $\sigma_C = 190$ MPa,
- for EL 250: $w = 5.8$, $N_C = 3\cdot10^6$, $\sigma_C = 240$ MPa.

The value σ_C was during the process corrected according to the stress average value and also according to factors affecting the fatigue limit (shape, size, treatment quality, stress concentration in the score, etc.).

From the influence analysis of the chosen operational condition characteristics it was determined that the impact of the roadway surfaces from the 1st to 4th class on the TATRA vehicle parts fatigue damage level is nearly negligible. Therefore, only a simulated loading process generated only from the stress behavior originating during the vehicle operation on the 5th class roadways and in the terrain was further applied.

On the base of the statistically determined percentage expression of the analyzed vehicle operation particular mode appearance (Tab. 1), the TATRA critical vehicle parts operation stress processes were created as the implication of the operation loads effect evoked by the analyzed lorry operation on the 5th class roadways and in the terrain.

Percentage ratio estimation of the selected vehicle operation modes occurrence — Tab. 1.

	5th class				terrain			
Velocity [km/h]	20	40	60	80	10	20	30	40
Estimation ratio [%]	10	10	10	10	15	20	15	10

Obtained stresses behavior in the particular critical elements of the TATRA vehicle construction were constituted by 40.000 discrete values representing roadway or terrain distance with the overall length of 10 km. The chosen time stress response is presented in Fig. 6.

The influence of the vehicle movement velocity on the resulting level of the middle axle dynamic stress during the drive under

the terrain conditions is presented in Fig. 7. Behaviors of the centered stresses part in the bearing beam middle section at the velocity of 80 km/h on the road segments with different qualities are presented.

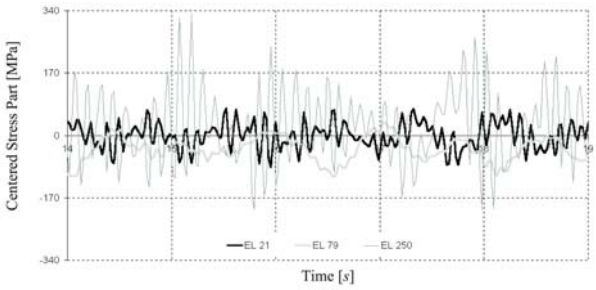

Fig. 6 Time section of the centered stress part behavior at the terrain drive (v = 40 km/h)

The selected power spectral stress density behavior in the analyzed elements under the chosen velocity and specific roadway class are for the illustration displayed in Fig. 8.

These stress PSD behaviors in all three determined critical construction locations were used as inputs for the *fatigue.m* program. The critical vehicle parts lifetime estimations were its output. The obtained fatigue life estimations of the particular critical elements are listed in Tab. 2.

Estimated fatigue life values of the vehicle critical parts during its real operating employment — Tab. 2.

Element	EL 21	EL 79	EL 250a	EL 250b	EL 250c	EL 250d
Lifetime Estimation [h]	27 251	19 095	10 743	11 961	595 720	66 133

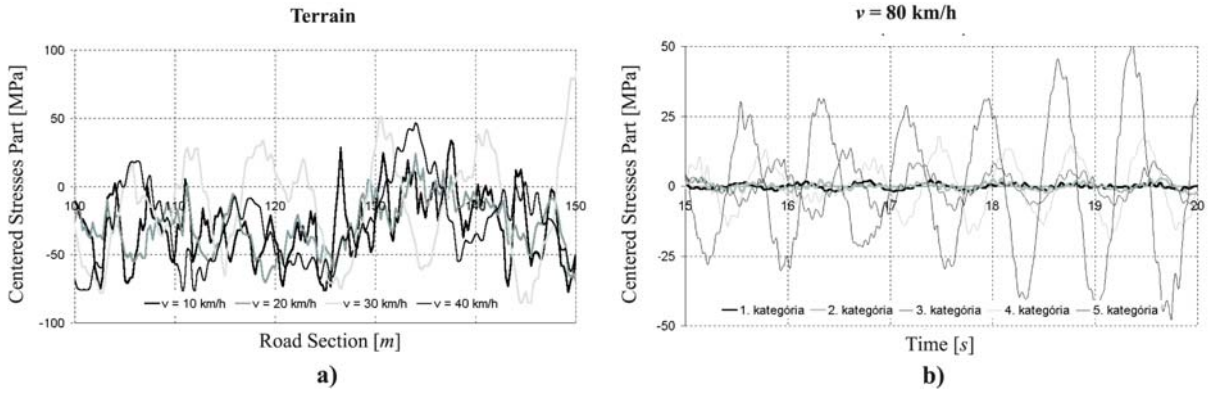

Fig. 7 a) Influence of the surface quality on the centered stresses part in EL 21
b) Influence of the movement velocity on the centered stresses part in EL 79

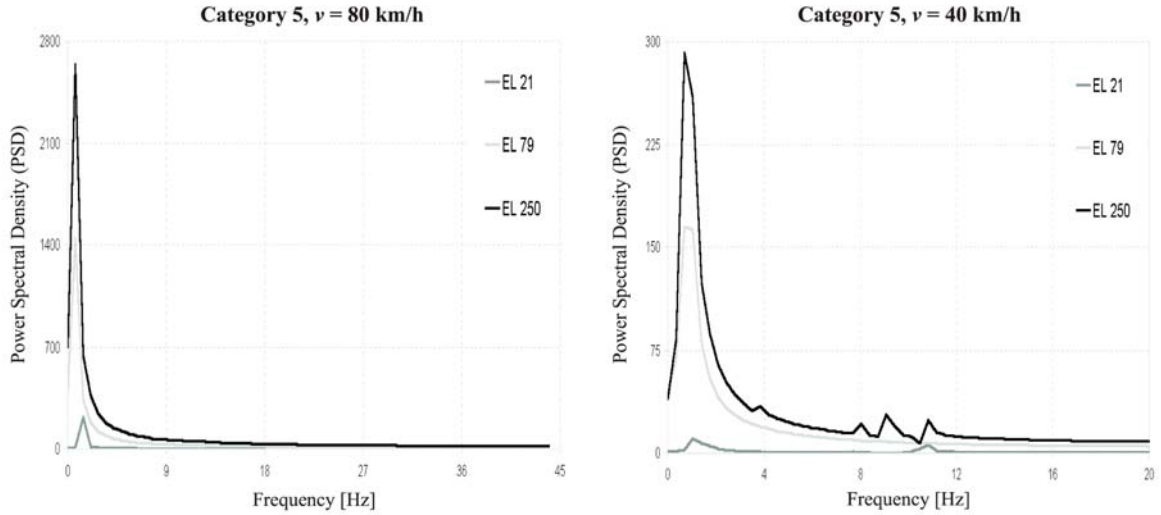

Fig. 8 Stress PSD in the critical elements at the selected surface quality and velocity

On the base of the performed analyses and comparisons it is possible to state that according to the evaluation of the selected operation condition characteristics influence on the dynamic stress level of the transport vehicle construction parts, both examined characteristics of the working transport vehicle (roadway and terrain undulation and operational velocity) have a significant influence on the stress of the vehicle critical parts.

It is obvious that it was not possible to analyze all the actuating characteristics and factors of the typical lorry operating conditions. Therefore, it is necessary to understand the presented paper as a contribution to the solution of the problem related mainly to the operational processes modeling and computer simulation. Behaviors of particular stress parts and their extreme values in the critical points of the vehicle construction are significantly determined by the chosen vehicle operational velocity [4, 6, 8].

6. Conclusion

Performed calculations confirmed that the analyzed TATRA lorry construction was dimensioned sufficiently also from the fatigue damage point of view. The goal of the paper was mainly:

- to present the methodology of the fatigue life prediction based on the modeling of the most important factors of working conditions,
- to show the possibilities of the available software optimal use based on the FEM in order to obtain the results needed to the fatigue life prediction,
- to verify the suggested computational approach on the specified lorry construction.

Acknowledgements

This work has been supported by VEGA grants No. 1/0125/09 and 1/0727/10.

References

[1] CACKO, J., BILY, M., BUKOVECZKY, J.: *Measuring, Evaluation and Simulation of Random Industrial Processes [in Slovak].* In: Veda : Bratislava, SR, 1984.

[2] BALDA, M., SVOBODA, J., FROHLICH, V.: Using Hypotheses for Calculating Fatigue Lives of Parts Exposed to Combined Random Loads. In: *Engineering Mechanics* 2003, pp.12-15, Svratka, 2003.

[3] DECKY, M.: ISO Standards in Evaluation of Straight Surface Road Process [in Slovak]. In: *Anniversary volume Q-2001 Asphalt Roads,* SF ZU, Zilina, 2001.

[4] GERLICI, J., LACK, T.: *Test Benches Computer Control Software Tools Development.* Scientific bulletin, Series C, Vol. XVII, Part II, International Multidisciplinary Conference, 5th edition; North University of Baia Mare : Romania, pp. 181–186, 2003.

[5] RUZICKA, M., HANKE, M., ROST, M.: *Dynamic Strength and Lifetime [in Czech].* CVUT : Praha, 1989.

[6] LEITNER, B.: Modelling and Simulation of Transport Machines Working Conditions by Using of Autoregressive Models. In: *Academic Journal Mechanics, Transport, Communications,* Issue 1/2007, Article No. 0079, VTU Todora Kableskova, Sofia, Bulgaria, pp. 10, www: http://mtc-aj.com/php/welcome.php?lang=gb, 2007.

[7] LEITNER, B.: The Software Support for an Identification of Stochastically Loaded Parts of Mechanically Structures. In: *Applied and Computational Mechanics,* Vol. 1, No. 2, pp. 515–520, Plzen.

[8] SAGA, M., MEDVECKY, M.: Contribution to Machine Frames Optimization Subjected to Fatigue Damage. In: *Machine Design* 2009, pp. 177–182, Novi Sad, 2009.

[9] SAGA, M., VASKO, M.: Stress Sensitivity Analysis of the Beam and Shell Finite Elements. In: *Communications - Scientific Letters of the University of Zilina*, Vol. 11, No. 2, 2009, pp. 5–12.

Ivo Cerny – Dagmar Mikulova – Pavel Novak *

CONDITIONS OF STRESS CORROSION CRACK GROWTH AND RETARDATION IN X70 STEEL IN CARBONATE ENVIRONMENTS

X70 steel has been often used for building of high pressure transit pipelines. In spite of multiple pipeline protection being used, namely insulation and cathodic protection, in complicated soil and environmental conditions, some pipeline sections can be exposed to corrosive environments. Seriousness of stress corrosion cracking (SCC) damage in carbonate environments is being sometimes flouted by some operators. The work was aimed at qualitative and quantitative analyses of SCC process and damage mechanisms under static loading with individual unloading cycles in standard carbonate solution at room and elevated temperatures. SCC growth was demonstrated as well as an importance of stress fluctuations affecting the process.

1. Introduction

A considerable part of Czech gas and oil pipelines have been in service already for many years. In recent years, non-destructive inspections or several high-pressure pipeline crashes indicated a significant amount of stress corrosion cracking (SCC) damage. In this context, research programmes aimed at an investigation of sensitivity of high pressure pipeline steels to SCC and connected damage mechanisms have become important.

Numerous cases of SCC damage to transit pipelines in areas containing alkaline soil and carbonates have been observed not only worldwide. (e.g. [1]), but also in the Czech Republic. An occurrence of carbonates in the soil can be supported by cathodic protection potentials [2]. When an insulation layer is damaged, for instance during pipeline mounting or land up, or in case of cathodic protection dysfunction, SCC damage to pipe external surface can be usually observed [3]. Such a case also occurred in Slovakia near Borsky Mikulas in 1988. After the explosion, the pipe was damaged by 25 m long spiral crack, in parallel with the weld [3].

SCC process usually has three characteristic phases of sigmoidal shape of the time dependence, (i) relatively fast microcrack initiation followed by (ii) quite lengthy microcracks development and formation of the main crack and evetually (iii) SCC growth of the main crack to failure. Previous works in the field of SCC in alkaline environments performed at SVÚM were focused on investigations of the first stage [4]. This paper contains results of a research programme aimed at an investigation of SCC growth of already existing long cracks and at verification, whether and under which conditions such a process occurs and what its mechanisms are.

2. Experiments

Experiments were performed on an X70 steel having been recently often used particularly for building of high-pressure transit pipelines not only in our country, but also in many worldwide regions. Evaluation of reliability and safety of pipelines made of this steel has been recently a matter of numerous extensive research programmes (e.g. [5]).

Specimens were taken from a sheet thermomechanically treated using standard procedures, resulting in a characteristic line type, orientated, ferritic-pearlitic microstructure. Specimens were of a non-standard CT-type (Fig. 1), with an increased length to enable to attach chambers for the corrosive solution (Fig. 2).

Direct current potential drop (DCPD) method with analytical calibration was used to measure a crack length and growth [6, 7]. Potential cables were initially connected in the vicinity of a notch (crack) mouth to get the highest possible sensitivity. The cables were therefore inserted into the chamber – Fig. 2. However, during the long-time tests, the cable attachment in the solution was corroded off. Therefore, later on, potential cables were connected outside the chamber, approximately 20 mm from the notch. This measure resulted in a reduced sensitivity, but made the measurement reliable.

An initial crack was prepared by fatigue pre-cracking in air, at a load frequency of 30 Hz, the asymmetry $R = 0.5$, a load range of 9 kN and 7.5 kN in the first and second stages, respectively. The final crack length was approximately 21.5 mm, the stress intensity factor range at the final stage $\Delta K = 19.5$ MPam$^{1/2}$, i.e. $K_{max} = 39$ MPam$^{1/2}$.

* **Ivo Cerny, Dagmar Mikulova, Pavel Novak**
SVUM a.s., Praque, Czech Republic, E-mail: Ivo.Cerny@seznam.cz

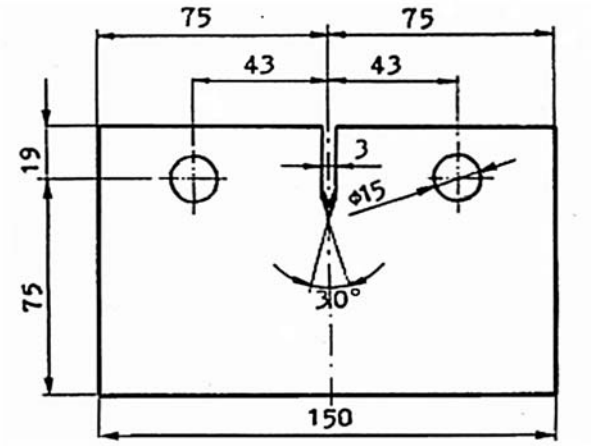

Fig. 1 Non-standard CT specimen used

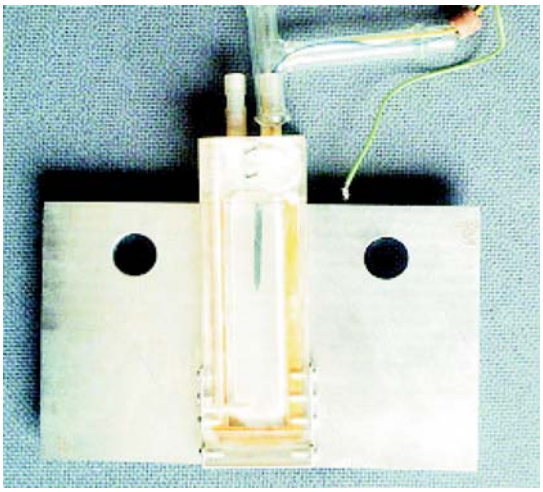

Fig. 2 Actual specimen with chamber for corrosive solution and potential cables

The alkaline corrosive solution simulating real carbonate environments was prepared according to [8], namely mixture of 1-normal sodium carbonate and 1-normal sodium bicarbonate solutions in the ratio of 1:1. Resulting pH was 9.8. SCC experiments were performed at a static load of 36.6 kN, with the resulting K = = 90 MPam$^{1/2}$, that means at rather high loading. The corrosive medium was circulating through the chamber. Three specimens were tested: (i) specimen designated X75 at an elevated temperature of 70 °C, (ii) X76 at room temperature and (iii) X78 at room temperature with a long-time exposure. The elevated temperature had practical reasons: Gas is usually considerably warmed-up when passing through compression stations in transit pipelines.

Due to possible fracture surface passivation in alkaline environments, unloading cycles corresponding to the load asymmetry R = 0.1 started to be applied after some initial stage of the experiments. Unloading cycles also are linked to real conditions, they correspond to pressure fluctuations or pipeline service interruptions.

All the tests were finished after interruption of the static loading stage with individual unloading cycles, with fatigue loading at the same load range (F_{max} = 36.6 kN, R = 0.1), with reduced load frequency f = 0.05 Hz, without interrupting the circulation of the corrosive solution. Eventually, the test programme was completed with a reference test of specimen X77, where the same loading sequence was applied including the final fatigue stage, but without any corrosive environment.

Fracture surfaces, particularly zones following fatigue pre-cracking, where SCC mechanisms were expected, were fractographically analysed using a scanning electron microscope JEOL JSM 35.

3. Experimental results and discussion

3.1. Theoretical DCPD calibration

Analytical calibration was calculated for all the configurations of potential electrodes used. It should be mentioned that potential was measured not only near the crack mouth ($V(a)$), but also a reference potential V_{ref} was recorded to compensate temperature changes and the ratio $V(a)/V_{ref}$ was evaluated [6,7,]. The results are shown in Fig. 3. s

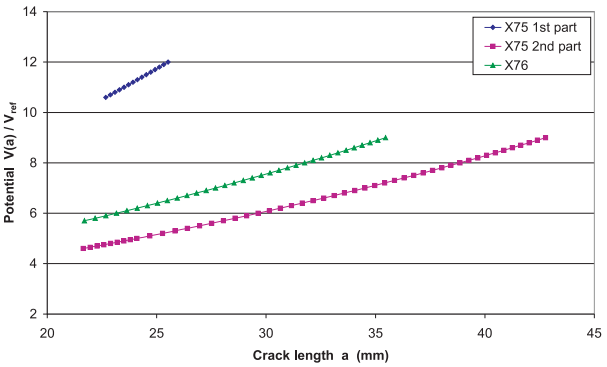

Fig. 3 Analytical calibration curves of the DCPD method used

3.2. Stress corrosion crack growth

Results of DCPD measurement during the SCC test of the specimen X75 *tested at 70 °C* are shown in Fig. 4. The points correspond to individual measurement sequences and represent average values of more than 10 potential measurements. There are two stages in the diagram, which shows as a whole a continuous, not interrupted test. The first stage, initial increase of the potential corresponding to 1 hour exposure, can be an artefact connected or at least affected by temperature balancing. This stage corresponds to the temperature growth of the solution from room temperature to 70 °C. The next 8 hours stage, however, already indicates some initial SCC growth with a saturation effect at the end. Further exposure at these conditions and temperature did not lead to further significant increase of potentials. The total potential increase

$V(a)/V_{ref}$ at the second stage 0.25 is not negligible, it corresponds approximately to more than 0.5 mm crack increment.

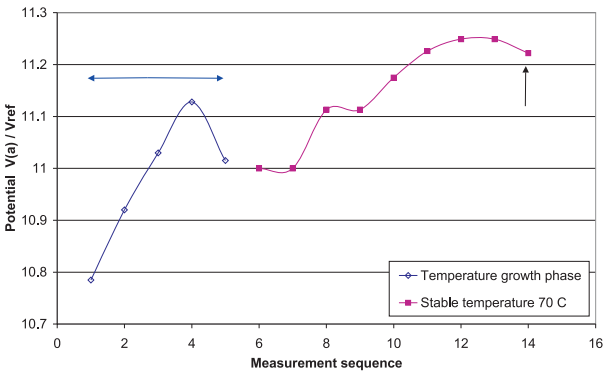

Fig. 4 Potential measurement during SCC test of specimen X75 at 70°C

The results indicate that the characteristic first stage of the SCC process was monitored during the 8–10 hours measurement, namely quite fast crack growth, which is typically followed by a retardation of the process and long-time development phase. The retardation may also be affected by an occurrence of corrosion products near the crack tip resulting in a restricted access of the corrosive medium to the crack front.

The second experiment, carried out on another specimen of the X70 steel designated X76, was performed at *room temperature*. Details of the DCPD measurement at two important phases, namely after starting the corrosive solution input into the chamber and after starting individual unloading cycles, respectively, are shown in Figs. 5 and 6. In the diagrams, individual recorded points connected with a considerable scatter are plotted together with moving average, better indicating changes of the time dependence.

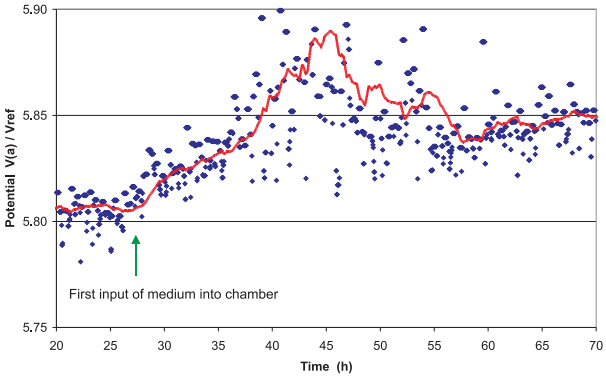

Fig. 5 Potential measurement during SCC test of specimen X76 at room temperature, the phase following the first medium input into chamber

Before the first input of the medium into the chamber, average DCPD values were constant, as expected. However, a distinct increase of the potential values can be seen next 17–18 hours, followed then by saturation and even a slight decrease. It is the same tendency like in the previous test at 70 °C with the difference that at room temperature, the process was approximately two times longer. Almost no changes were then observed until 225 hours of the exposure, when three unloading cycles were gradually applied with the interval of 24 hours. In spite of the scatter, the moving average of potentials shows potential increase after each of the unloading cycle followed by fairly small decrease, the most intensive increase occurring after the first of the three cycles. This effect may be connected with microcracking of a passivation layer being most important after the first cycle, which occurred after a long period with purely constant static load. The effect of the second and third unloading cycles, when the passivation likely was not so strong due to the short time of constant load, just 24 hours, seems not to be so strong. However, the total increase after the three cycles is evident.

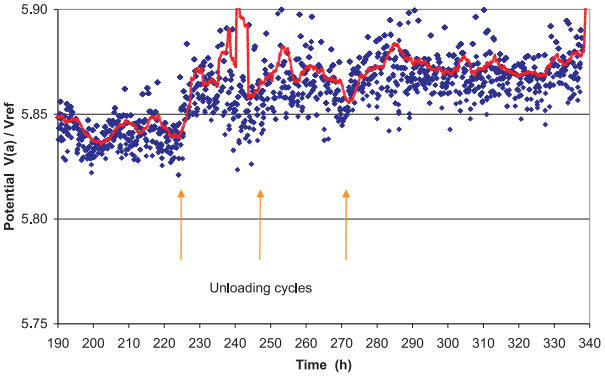

Fig. 6 Potential measurement of specimen X76 at room temperature, the phase with unloading cycles

The last SCC experiment, specimen designated X78, was carried out exactly at the same conditions as the previous one, i.e. at room temperature with the only differences that more than three unloading cycles were applied and the whole experiment was performed for a longer time, almost three times. Unloading cycles were applied manually during weekdays in the morning and late afternoon, starting after 160 hours of exposure in the solution just with a constant static load. Unloading was, however, inter-

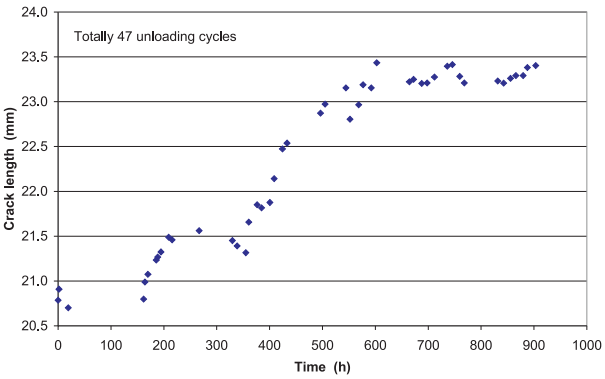

Fig. 7 SCC growth in specimen X78 at room temperature

rupted for the 115 hours period, between 215 and 330 hours of the exposure.

Results are shown in Fig. 7 Each point represents the average value of 20 measurements. In this diagram, the potentials are already recalculated to the actual crack length. This experiment confirmed without doubt what was already indicated during the previous one: an importance of unloading cycles in the SCC growth process at carbonate solution in the X70 steel. On the contrary, when load fluctuation occurred, SCC growth was quite rapid. The results confirm seriousness of SCC growth in carbonate environments in actually operated pipelines, unlike numerous allegations of particularly domestic operators that such the process cannot occur.

Some minor remarks concern two phases of the experiment: (i) the beginning, when the initial crack growth was observed as before (not distinctly recorded in the diagram in Fig. 7), followed by the saturation to 160 hours and (ii) a distinct saturation of the potentials between 215 and 330 hours, when application of unloading cycles was temporarily discontinued. The potential decrease may be caused by increasing contact of fracture surfaces near crack tip due to growth of corrosion products.

3.3. Fractographical analysis

Fracture surfaces of specimens X75 (tested at 70 °C), X76 (tested at room temperature) and X77 (loaded just in laboratory air without corrosive solution) were analysed, with a special attention to the zones of crack growth supported by SCC mechanisms, i.e. in the zones between the end of fatigue precracking and following approximately 0.3–1 mm crack increments.

There are some characteristic features common for both the specimens tested in the corrosive solutions, proving existence of SCC mechanisms: an occurrence of numerous secondary cracks confirming strong branching mechanism typical for SCC processes.

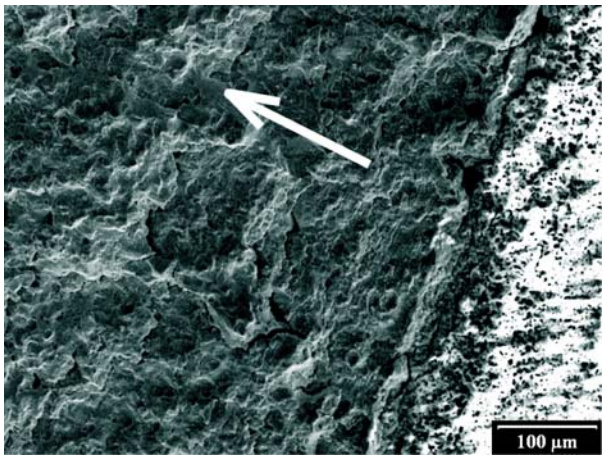

Fig. 8 Example of secondary cracks in region of SCC growth in specimen X75

Fig. 8 represents an example of such secondary cracks in specimen X75. Crack growth direction is indicated by the arrow. The white part of the Figure in the right margin represents the fracture surface of fatigue precracking, strongly corroded during the next exposure in the warm carbonate solution. Numerous deep secondary stress corrosion (SC) cracks can be seen in the boundary line between fatigue precracking and SCC growth. These cracks are mostly parallel to the main crack front. At the distance up to 0.3 mm from the boundary line, further secondary SC cracks, more branched and with more complicated directions can be observed.

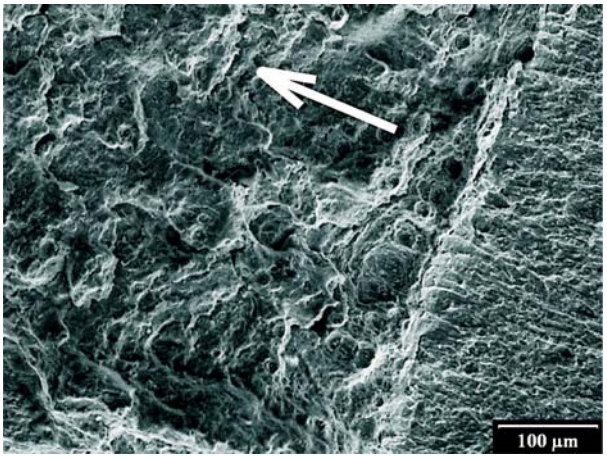

Fig. 9 Secondary cracks in region of SCC growth in specimen X76 (room temperature)

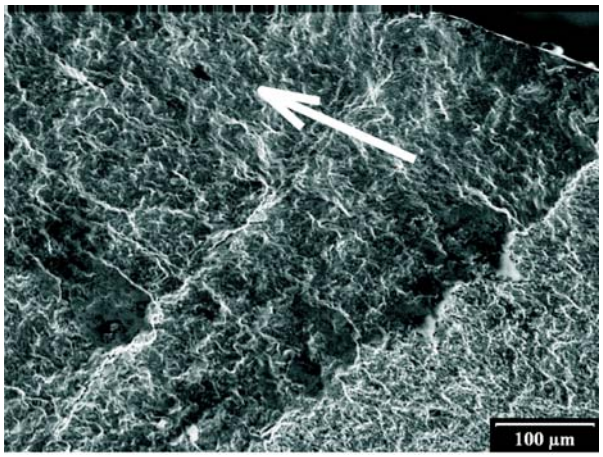

Fig. 10 Fracture surface without secondary SCC cracks in specimen X77 loaded in air

In spite of some common features, fracture surface of specimen X76 tested at room temperature is rather different from X75 – Fig. 9. First of all, no huge corrosion products occurred on the fatigue precracked surface, indicating that surface corrosion at room temperature was suppressed. On the other hand, secondary SC cracks could be observed in a similar way as in Fig. 8 – a zone of secondary cracks parallel to the boundary line and numerous SC cracks with a complicated shape in the region, where crack

growth was supported by SCC mechanisms. On the contrary, the fracture surface of specimen X77, loaded with the same sequence as the previous two specimens, was completely different – Fig. 10. The secondary cracking characteristic for the stress corrosion process could not be observed in this case.

4. Conclusions

The experimental programme was focused on qualitative and quantitative analyses of stress corrosion crack process and damage mechanisms in an X70 steel under static loading with individual unloading cycles, exposed to carbonate solution, at room and elevated (70 °C) temperatures. The most important results can be summarised as follows:

- The results proved without doubt a significant occurrence of SCC growth in the X70 steel in carbonate environments. This result contrasts with numerous allegations of some pipeline operators that there is no danger of SCC process at these conditions.
- An importance of unloading cycles in the SCC growth process in carbonate solution was shown. When the loading was purely static without fluctuations, damaging the passivation layer near the crack tip, SCC growth was saturated after some time and even some decrease of measured potentials could be observed. On the contrary, when load fluctuations were applied, SCC growth was quite rapid. SCC growth seemed to be somewhat more progressive at elevated temperature.
- Fractographical analyses proved an existence of SCC growth mechanisms, showing numerous secondary strongly branched cracks on fracture surface in the region of SCC growth. Such cracks were observed on fracture surfaces of specimens tested in solutions at both room and elevated temperatures.

Acknowledgement

The work was carried out within the project supported by the Czech Ministry of Education, Youth and Sport under grant MSM 2579700001.

References

[1] PARKINS R. N.: Stress Corrosion Cracking of Pipelines – Its Control or Prevention Corrosion, Paper No. 249, *NACE International,* 1996.
[2] LEIS, B.-N., PARKINS, R.-N.: Mechanics and Materials Aspects in Predicting Serviceability Limited by SCC. *Fatigue & Fracture of Eng. Mater.* V. 21, 1998, p. 583–601.
[3] LINHART V., SIGMUNDOVA J., RABL V.: Resistance of Steels Applied in Gas Transmission Pipelines to Stress Corrosion Cracking. Slovgas, Vol. 5, 2008, pp. 12–15 [in Czech].
[4] CERNY I., LINHART V.: An Evaluation of Resistance of Pipeline Steels to Initiation and Early Growth of Stress Corrosion Cracks. *Engng. Fracture Mech.*, Vol. 71, 2004, pp. 913–921.
[5] SHANGHAI RESEARCH INSTITUTE OF MATERIALS (SRIM): *Research on Stress Corrosion Cracking of Engineering Materials.* Power Point presentation, ME08118 project workshop, SVUM Praha, 2008.
[6] CERNY, I.: The Use of DCPD Method for Measurement of Growth of Cracks in Large Components at Normal and Elevated Temperatures. *Engng. Fracture Mech.,* Vol. 71, 2004, pp. 837–848.
[7] CERNY, I.: Measurement of Subcritical Growth of Defects in Large Components of Nuclear Power Plants at Elevated Temperatures. *Int. J. of Pressure Vessels and Piping,* Vol. 78, 11/2001, pp. 893–902.
[8] WANG, Z. F., ATRENS A.: Initiation of Stress Corrosion Cracking for Pipeline Steels in a Carbonate-Bicarbonate Solution, *Metallurgical and Materials Transactions,* Vol. 27A, 1996

Milan Saga – Peter Kopas – Milan Vasko *

SOME COMPUTATIONAL ASPECTS OF VEHICLE SHELL FRAMES OPTIMIZATION SUBJECTED TO FATIGUE LIFE

The paper deals with the implementation of the fatigue damage conditions into structural optimization process. The study considers a shell finite element structural analysis in conjunction with the multiaxial rainflow counting, the fatigue damage prediction and naturally the sizing (element thickness) optimizing design. We will analyze FE models under random excitation in time domain. The presented optimizing approach will be implemented into solution program compiled in Matlab.

Keywords: finite element analysis, optimization algorithm, multiaxial rainflow counting, fatigue damage

1. Introduction

Nowadays it is almost impossible to pick up a journal or conference focused on computational mechanics that doesn't contain some reference to structural optimizing. Although it is possible to design machine parameters by experience it is much better and more effective to predict the basic properties of the new designed structure by using optimizing procedure which is generally based on a series of controlled computing analyses [1].

2. Chosen methods for multiaxial fatigue damage prediction

To calculate the structural mass (or volume) is not a complicated problem but the constrain conditions usually depend on FE analysis, identification of a "damage" critical points and multiaxial fatigue prediction [12]. Let's now focus on the cumulative damage counting by using multiaxial rainflow decomposition of the stress response. It should be noted [4, 12] that the fatigue damage calculation of the machine parts is generally problematic because the results are considerable changed in the principal stresses [2, 5]. Using FE analysis we can get six components of the stress-time function (multiaxial stress) but it is very difficult to obtain an equivalent – uniaxial load spectrum by reason of comparison with applied computational fatigue curve. In our case the rainflow analysis for random stresses known in classic uniaxial form as von Mises or Tresca hypotheses is impossible. It means that the important goal of this part will be to propose some approaches to estimate the high-cycle fatigue damage for multiaxial stresses caused by random vibration analysed structure [7, 11]. Generally we can apply two fundamental approaches for multiaxial rainflow counting:

- Critical Plane Approach (CPA) [11] and
- Integral Approach (IA) [7].

It is well-known that the Wöhler curve (Fig. 1, sometimes called S-2N curve) is basic source of getting information of the material fatigue life. Generally the S-2N curve is statistically evaluated by experimental fatigue curve. This is a graph of the magnitude of a cyclical nominal stress σ_A against the logarithmic scale of cycles to failure $2N_f$. It is advantage to show it in logarithmical or semi logarithmical coordinates.

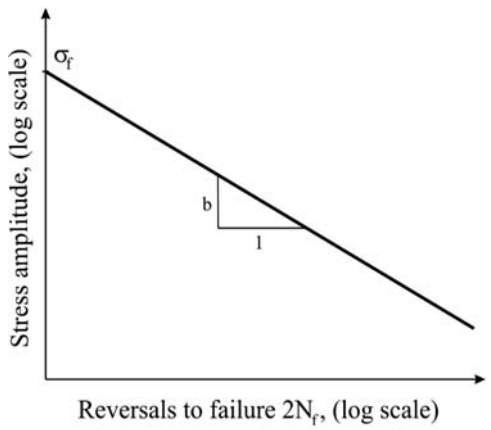

Fig. 1. S-2N curve

The $\sigma_A - 2N_f$ relation can be written as follows

$$\sigma_A = \sigma_f \cdot (2N_f)^b , \tag{1}$$

where σ_f is the fatigue stress coefficient, $2N_f$ is number of cycles to failure, b is fatigue strength exponent and σ_A is stress amplitude

* **Milan Saga, Peter Kopas, Milan Vasko**
Department of Applied Mechanics, Faculty of Mechanical Engineering, University of Zilina, Slovakia, E-mail: milan.saga@fstroj.uniza.sk

to failure. Some researches rewrite the relationship (1) into following form

$$\sigma_A^m \cdot (2N_f) = K \tag{2}$$

where $m = -(1/b)$ and $K = \sigma_f^{(-1/b)} = \sigma_f^m$

Considering the mean stress modified version of the stress amplitude (using Goodman, Soderberg, Geber), eq. 2 can be rewritten as follows

$$\left\{\sigma_A \cdot \left[1 - \left(\frac{\sigma_M}{R_F}\right)^k\right]^{-1}\right\}^m \cdot (2N_f) = K\,. \tag{3}$$

If $k = 1$ and $R_F = R_E$ (yield stress) the Soderberg's model is used, if $k = 1$ and $R_F = R_M$ (strength limit) the Goodman's model is used and if $k = 2$ a $R_F = R_M$ the Geber's model is used. Using the linear Palmgren-Miner law we can calculate fatigue damage for stress amplitude σAi as follows

$$d_i = \frac{1}{2N_{f-i}} = \left\{\frac{\sigma_{Ai}}{\sigma_f} \cdot \left[1 - \left(\frac{\sigma_M}{R_F}\right)^k\right]^{-1}\right\}^m. \tag{4}$$

3. Damage calculation for thin shell finite element using CPA

Let us consider well-known shell finite elements (Kirchhoff's or Mindlin's formulation) [1, 9, 11]. The stiffness parameters depend on material constants and element geometry, mainly on its thickness. At first we have to prepare the stress calculation process. This process is based on the expression of the *j*-th element membrane forces and bending moments (without shear forces) [10, 11], i.e.

$$\begin{aligned}\left[F_{xx}\ \ F_{yy}\ \ F_{xy}\right]_j^T = \boldsymbol{F}_m^j = \int_S \boldsymbol{E}_m^j \cdot \varepsilon_m^j dS_j = \\ = \boldsymbol{E}_m^j \cdot \int_S \boldsymbol{B}_m^j dS_j \cdot \boldsymbol{u}_L^j = t_j \cdot \boldsymbol{D}_j \cdot \boldsymbol{I}_m^j \cdot \boldsymbol{u}_L^j\end{aligned} \tag{5}$$

and

$$\begin{aligned}\left[M_{xx}\ \ M_{yy}\ \ M_{xy}\right]_j^T = \boldsymbol{M}_b^j = \int_S \boldsymbol{E}_b^j \cdot \varepsilon_b^j dS_j = \\ = \boldsymbol{E}_b^j \cdot \int_S \boldsymbol{B}_b^j dS_j \cdot \boldsymbol{u}_L^j = \frac{t_j^3}{12} \cdot \boldsymbol{D}_j \cdot \boldsymbol{I}_b^j \cdot \boldsymbol{u}_L^j\end{aligned}\,. \tag{6}$$

The auxiliary matrices Im and Ib can be calculated only using the numerical approach. Further details about Em, Eb, D, Bm, Bb, uel and t are presented in [10]. The extreme stress values can be expected at the top or at the bottom surface. Generally, it means

$$\begin{bmatrix}\sigma_{mb}\big|_{top} \\ \sigma_{mb}\big|_{bot}\end{bmatrix}^j = \begin{Bmatrix}\sigma_{xx,top} \\ \sigma_{yy,top} \\ \sigma_{xy,top} \\ \sigma_{xx,bot} \\ \sigma_{yy,bot} \\ \sigma_{xy,bot}\end{Bmatrix}^j = \begin{bmatrix} 1/t_j & 0 & 0 & 6/t_j^2 & 0 & 0 \\ 0 & 1/t_j & 0 & 0 & 6/t_j^2 & 0 \\ 0 & 0 & 1/t_j & 0 & 0 & 6/t_j^2 \\ 1/t_j & 0 & 0 & -6/t_j^2 & 0 & 0 \\ 0 & 1/t_j & 0 & 0 & -6/t_j^2 & 0 \\ 0 & 0 & 1/t_j & 0 & 0 & -6/t_j^2 \end{bmatrix} \cdot \begin{Bmatrix}F_{xx} \\ F_{yy} \\ F_{xy} \\ M_{xx} \\ M_{yy} \\ M_{xy}\end{Bmatrix}^j = \begin{bmatrix}A_{t,top} \\ A_{t,bot}\end{bmatrix}^j \cdot \begin{Bmatrix}F_m \\ M_b\end{Bmatrix}^j, \tag{7}$$

or

$$\sigma_{mb\_L}^j = \boldsymbol{C}_L^j \cdot \boldsymbol{f}_L^j\,. \tag{8}$$

Let's build new material and auxiliary matrices

$$\boldsymbol{E}_{mb} = \begin{bmatrix} t_j \cdot \boldsymbol{I}_3 & \boldsymbol{0}_3 \\ \boldsymbol{0}_3 & \dfrac{t_j^3}{12} \cdot \boldsymbol{I}_3 \end{bmatrix} \cdot \begin{Bmatrix}\boldsymbol{D} \\ \boldsymbol{D}\end{Bmatrix}_j = \boldsymbol{D}_t \cdot \boldsymbol{D}_{mb}\,,\ \ \boldsymbol{I}_{mb} = \begin{Bmatrix}\boldsymbol{I}_m^j \\ \boldsymbol{I}_b^j\end{Bmatrix}, \tag{9}$$

where the matrix I_3 is the classical unit matrix. Then (7) can be rewritten as follows

$$\sigma_{j\_mb}\big|_{top} = \boldsymbol{A}_{t,top} \cdot \boldsymbol{E}_{mb} \cdot \boldsymbol{I}_{mb} \cdot \boldsymbol{u}_L^J = \boldsymbol{A}_{t,top} \cdot \boldsymbol{D}_t \cdot \boldsymbol{D}_{mb} \cdot \boldsymbol{I}_{mb} \cdot \boldsymbol{u}_L^J\,, \tag{10a}$$

$$\sigma_{j\_mb}\big|_{bot} = \boldsymbol{A}_{t,bot} \cdot \boldsymbol{E}_{mb} \cdot \boldsymbol{I}_{mb} \cdot \boldsymbol{u}_L^J = \boldsymbol{A}_{t,bot} \cdot \boldsymbol{D}_t \cdot \boldsymbol{D}_{mb} \cdot \boldsymbol{I}_{mb} \cdot \boldsymbol{u}_L^J\,. \tag{10b}$$

Findley hypothesis

Findley has assumed the critical plane as a plane with maximum shear stress, i.e. the fatigue equivalent shear stress can be written as follows [11]

$$\tau_{A\_Fin} = \tau_{\max} + k \cdot \sigma_m\,, \tag{11}$$

where k is Findley's factor whose value for tough metal can be about 0.3. Using von Mises relationship between normal and shear stresses and classical plane stress analysis for top or bottom element surface it is possible to rewrite (9) into the following form

$$\begin{aligned}\sigma_{A\_Fin}^j\big|_{top} = \sqrt{3} \cdot \left\{sign\left(T_2 \cdot \sigma_{j\_mb}\big|_{top}\right) \cdot \left[\left(\sigma_{j\_mb}\big|_{top}\right)^T \cdot T_1 \cdot \right.\right. \\ \left.\left. \cdot \left(\sigma_{j\_mb}\big|_{top}\right)\right]^{-1/2} + k \cdot T_2 \cdot \sigma_{j\_mb}\big|_{top}\right\},\end{aligned} \tag{12a}$$

$$\begin{aligned}\sigma_{A\_Fin}^j\big|_{bot} = \sqrt{3} \cdot \left\{sign\left(T_2 \cdot \sigma_{j\_mb}\big|_{bot}\right) \cdot \left[\left(\sigma_{j\_mb}\big|_{bot}\right)^T \cdot T_1 \cdot \right.\right. \\ \left.\left. \cdot \left(\sigma_{j\_mb}\big|_{bot}\right)\right]^{-1/2} + k \cdot T_2 \cdot \sigma_{j\_mb}\big|_{bot}\right\},\end{aligned} \tag{12b}$$

where

$$T_1 = \begin{bmatrix} 0{,}25 & -0{,}25 & 0 \\ -0{,}25 & 0{,}25 & 0 \\ 0 & 0 & 1 \end{bmatrix} \text{ and } T_2 = \begin{bmatrix}0{,}5 & 0{,}5 & 0\end{bmatrix} \tag{13}$$

The damage calculation can be realised using eq. (4). The presented relationships were applicable for FE analyses. Numerical and experimental tests confirmed that the factor $k = 0.3$ was overstated [4, 11] by the author.

Dang Van hypothesis

Dang Van again assumed the critical plane with shear stress but with difference in factor k, which can be calculated from normal and shear fatigue limit, i.e.

$$\tau_{A\_DV} = \tau_{\max} + k \cdot p_m = \frac{\sigma_1 - \sigma_3}{2} + \frac{\tau_C - \frac{\sigma_C}{2}}{\frac{\sigma_C}{\sqrt{3}}} \cdot \frac{\sigma_1 + \sigma_2 + \sigma_3}{3}, \tag{14}$$

where τ_C is shear (torsional) fatigue limit, σ_C is normal (axial) fatigue limit, σ_1, σ_2, σ_3 are principal stresses. Relationship (11) is possible to use like that

$$\sigma_{A\_DV} = \sqrt{3} \cdot \left[sign\left(\frac{\sigma_1 - \sigma_3}{2}\right) \cdot \frac{\sigma_1 - \sigma_3}{2} + \frac{\tau_C - \frac{\sigma_C}{2}}{\frac{\sigma_C}{\sqrt{3}}} \cdot \frac{\sigma_1 + \sigma_2 + \sigma_3}{3} \right]. \tag{15}$$

Using von Mises hypothesis we can get [4]

$$\frac{\tau_C - \frac{\sigma_C}{2}}{\frac{\sigma_C}{\sqrt{3}}} \approx \frac{\tau_C - \frac{\sqrt{3}\,\tau_C}{2}}{\frac{\sqrt{3}\,\tau_C}{3}} \approx 0{,}232\,. \tag{16}$$

Using the application of the shell stress theory and eqs. 10a, b we can obtain

$$\sigma^j_{A\_DV}\big|_{top} = \sqrt{3} \cdot \left\{ sign\left(T_3 \cdot \sigma_{j\_mb}\big|_{top}\right) \left[\left(\sigma_{j\_mb}\big|_{top}\right)^T \cdot T_1 \cdot \left(\sigma_{j\_mb}\big|_{top}\right) \right]^{-1/2} + 0{,}232 \cdot T_3 \cdot \sigma_{j\_mb}\big|_{top} \right\}, \tag{17a}$$

$$\sigma^j_{A\_DV}\big|_{bot} = \sqrt{3} \cdot \left\{ sign\left(T_3 \cdot \sigma_{j\_mb}\big|_{bot}\right) \cdot \left[\left(\sigma_{j\_mb}\big|_{bot}\right)^T \cdot T_1 \cdot \left(\sigma_{j\_mb}\big|_{bot}\right) \right]^{-1/2} + 0{,}232 \cdot T_3 \cdot \sigma_{j\_mb}\big|_{bot} \right\}. \tag{17b}$$

Relations (12) and (17) present equivalent stresses applicable for rainflow decomposition for both proportional and non-proportional loading. The cumulative damage calculation can be realised using eq. (4) again.

HMH modified hypothesis

Applying von Mises equivalent stress for CPA we can obtain the following relationship

$$\sigma_{A\_HMH} = sign\left[\sigma(\boldsymbol{n}_{CPA})\right] \cdot \sqrt{\sigma(\boldsymbol{n}_{CPA})^2 + 3 \cdot \tau(\boldsymbol{n}_{CPA})^2}\,, \tag{18}$$

or in detail

$$\sigma^j_{A\_HMH}\big|_{top}(\boldsymbol{n}_{CPA}) = sign\left[\sigma^T_{j\_mb}\big|_{top}(\boldsymbol{n}_{CPA}) \cdot T_\sigma \cdot \sigma^T_{j\_mb}\big|_{top}(\boldsymbol{n}_{CPA})\right] \cdot \left[\sigma^T_{j\_mb}\big|_{top}(\boldsymbol{n}_{CPA}) \cdot T_4 \cdot \sigma^T_{j\_mb}\big|_{top}(\boldsymbol{n}_{CPA})\right]^{-1/2} \tag{19a}$$

$$\sigma^j_{A\_HMH}\big|_{bot}(\boldsymbol{n}_{CPA}) = sign\left[\sigma^T_{j\_mb}\big|_{bot}(\boldsymbol{n}_{CPA}) \cdot T_\sigma \cdot \sigma^T_{j\_mb}\big|_{bot}(\boldsymbol{n}_{CPA})\right] \cdot \left[\sigma^T_{j\_mb}\big|_{bot}(\boldsymbol{n}_{CPA}) \cdot T_4 \cdot \sigma^T_{j\_mb}\big|_{bot}(\boldsymbol{n}_{CPA})\right]^{-1/2} \tag{19b}$$

where

$$T_4 = \begin{bmatrix} 1 & -0.5 & 0 \\ -0.5 & 1 & 0 \\ 0 & 0 & 3 \end{bmatrix} \quad \text{and} \quad T_\sigma = \begin{bmatrix} \sigma_x & \tau_{xy} & 0 \\ \tau_{xy} & \sigma_y & 0 \\ 0 & 0 & 0 \end{bmatrix}. \tag{20}$$

In this case it should be noted that computational approach depends on a searching process of a critical plane normal vector $\boldsymbol{n}_{CPA}$. If the rainflow analysis is used it is very important to know the sign of the calculated equivalent stress therefore the sign of this stress is defined by sign of normal component. For searching process was used optimizing tools in Matlab [12] and optimizing problem for cumulative damage function is usually formulated as follows

$$D_{i\_\max}\big|_{HMH} = \max\left[\sum_{j=1}^{mc} d_j(\boldsymbol{n}_{CPA})\right] = = \max\left\{\left\{\frac{\sigma^i_{A\_HMH}\big|_{bot}(\boldsymbol{n}_{CPA})_j}{\sigma_f} \cdot \left[1 - \left(\frac{\sigma^i_{M\_HMH}\big|_{bot}(n_{CPA})_j}{R_f}\right)^k\right]^{-1}\right\}^m\right\} \tag{21}$$

for unknown vector $\boldsymbol{n}_{CPA}$ and stresses on bottom surface. The same computational process can be realised on top element surface.

4. Damage calculation for thin shell finite element using IA

The fundamental idea is to count rainflow cycles on all linear combinations of the stress random vector components [7], i.e.

$$\sigma_{A\_MRF}(t) = c_1 \cdot \sigma_x(t) + c_2 \cdot \sigma_y(t) + c_3 \cdot \sigma_z(t) + + c_4 \cdot \tau_{xy}(t) + c_5 \cdot \tau_{yz}(t) + c_6 \cdot \tau_{zx}(t) \tag{22}$$

on the assumption that the parameters ci belong to a hypersphere $\sum_{i=1}^{n} c_i^2 = 1$. Practically if the stress state is biaxial (e.g. thin shell finite element) the stress components can be written under the form of three dimension vector $\sigma = [\sigma_x, \sigma_y, \tau_{xy}]^T$ and the equivalent stress will be calculated as follows

$$\sigma_{A\_MRF}(t) = c_1 \cdot \sigma_x(t) + c_2 \cdot \sigma_y(t) + c_3 \cdot \tau_{xy}(t) = c \cdot \sigma \tag{23}$$

on condition that $c_1^2 + c_2^2 + c_3^2 = 1$. In the case of shell element we can obtain again the following relationships

$$\sigma^j_{A\_MRF}\big|_{top}(\boldsymbol{c}) = \boldsymbol{c} \cdot \boldsymbol{\sigma}_{j\_mb}\big|_{top}(\boldsymbol{c}) \quad \text{and} \quad \sigma^j_{A\_MRF}\big|_{bot}(\boldsymbol{c}) = \boldsymbol{c} \cdot \boldsymbol{\sigma}_{j\_mb}\big|_{bot}(\boldsymbol{c})\,. \tag{24}$$

Hence the next goal will be to find extreme value of the estimated damage for vector c and *i*-th element, i.e.

$$D_{i\_\max}\big|_{MRF} = \max\left[\sum_{j=1}^{mc} d_j(\boldsymbol{c})\right] = \\ = \max\left\{\left\{\frac{\sigma^i_{A\_MRF}\big|_{bot}(c)_j}{\sigma_f}\cdot\left[1-\left(\frac{\sigma^i_{M\_MRF}\big|_{bot}(c)_j}{R_f}\right)^k\right]^{-1}\right\}^m\right\} \quad (25)$$

where $D_{i\text{-}max}/_{MRF}$ is the maximum value of the cumulative damage for i-th element, $2N_i$ is the number of cycles to failure, mc is the number of cycles after rain-flow decomposition of the stress. Naturally we have to observe the normality condition for c using the following transformation

$$c = \frac{c'}{\sqrt{c'^T \cdot c'}}. \quad (26)$$

The searching process is realized by computational program FAT_MRFA developed in Matlab. Program calculates elements damage from stress response using original optimizing multiaxial rainflow procedure suggested by authors [4, 6, 12].

5. Formulation of the optimizing problem

Nowadays the optimizing problem of the structural mass minimizing subjected to the prescribed fatigue damage is topical [3]. The optimization problem with optimizing variables $\boldsymbol{x}$ (element thicknesses) can be mathematically stated as follows

$$F(x) = \sum_{i=1}^{n} \rho_i \cdot l_i \cdot X_i \rightarrow \min, \quad (27)$$

subjected to

$$D^k_{\max}(x) - D_p \leq 0, \quad k = 1 \ldots \mathrm{m} \quad (28)$$

where n is number of the elements, m is number of the element groups, D_P is the prescribed cumulative damage, D^k_{max} is the calculated extreme value of the cumulative damage for k-th element group. Another formulation can be based on the idea to built-in damage conditions into objective function, i.e.

$$F(x) = \sum_{k=1}^{m}\left[1 - \frac{D_k(x)}{D_P}\right] \rightarrow \min. \quad (29)$$

It is necessary to note that the identification of the extreme element (or node) cumulative damage is generally very time-consuming hence the stress sensitivity or signification analysis plays important role. By reason that the shell structures are in our attention, the signification analysis of the thin shell finite elements will be presented. Theory of this process is in detail published in [11, 12].

6. Optimization of the track maintenance machine frame

Let's realise the optimum design of the chosen parameters of the track maintenance machine VKL 400 (Fig. 2) [11]. The computational model creation, the analysis of the vertical and transversal stochastic vibrations of the model and the process of structural designing for a vehicle speed of 40, 70 and 100 kmph will be presented. The cumulative damage determination and design of the cross sections (thicknesses) of the machine frame will be the gist of the solution.

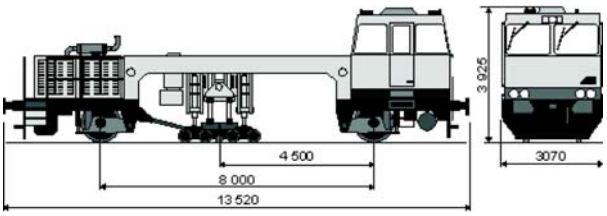

Fig. 2 The basic geometry of the maintenance machine VKL 400

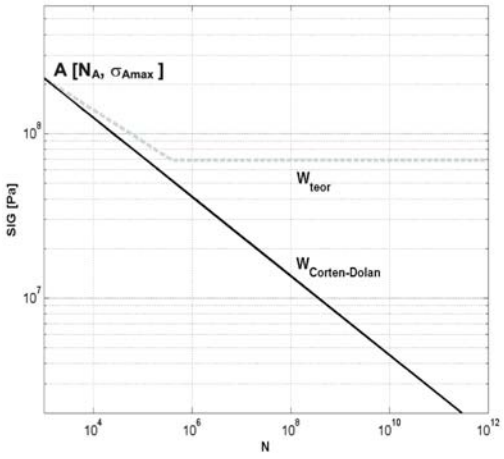

Fig. 3 The "working" S-N curve

Applied material characteristics

The material computational parameters are Young's modulus $E = 2.10^{11}$ Pa, Poisson ratio $\mu = 0.3$, density $\rho = 7800$ kg/m^3, point of $S-N$ curve $NA = 10^3$ cycles, $\sigma_{Amax} = 217$ MPa, Fatigue limit $\sigma_C = 68.7$ MPa, $C-D$ constant $k = 0.8$, exponent of $S-N$ curve $m = 5.2$. Graphical presentation of the "working" Wöhler curve reduced according to Corten-Dolan is in Fig. 3.

Computational model

The computational FE model (Fig. 4) was built-up from a virtual model created in PRO/Engineer (Fig. 5) [11]. The selected values describing physical properties of the computing model were parameterized in order to their arbitrary changes. The goal of parameterization was to achieve the maximum variability of the model which related mainly to verification and debugging of this model and consequently to the optimization process. Additional vehicle parameters were considered as follows: the stiffness of vertical primary spring $k_1 = 360000$ N/m, the damping coefficient for vertical primary spring $b_1 = 16000$ N.s/m, the stiffness of vertical secondary spring $k_2 = 600000$ N/m, damping coefficient for vertical secondary spring $b_2 = 900$ N.s/m.

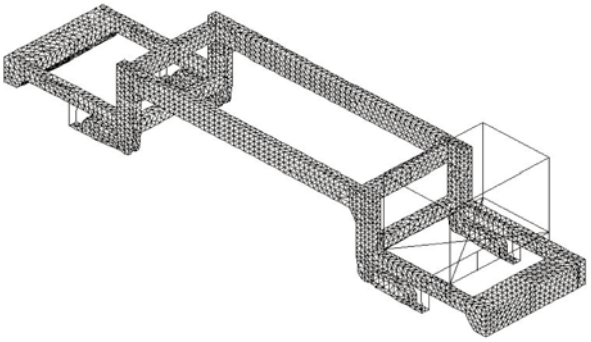

Fig. 4 The finite element model in COSMOS/M

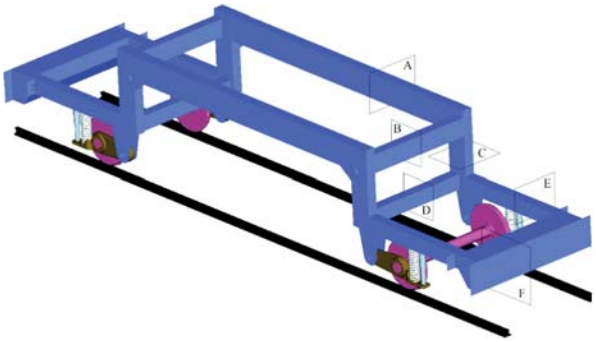

Fig. 5 Model of the analyzed vehicle frame with cross sections identification

Optimizing parameters

The objective function and constrain conditions were defined by equations (1) and (2). Cross-section parameters, i.e. the thickness of the welded frame plates were been parameterized (Fig. 6). Values used on the build of the frame were applied in the initial analysis, of course. The list of these values is presented in Table 1.

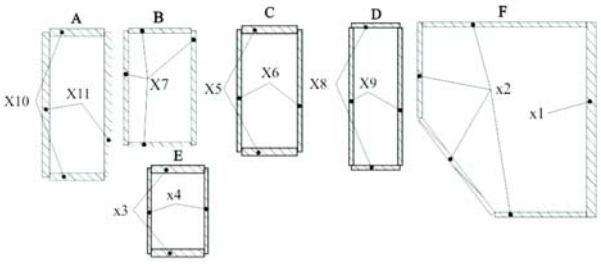

Fig. 6 Variables of the frame cross sections

It should be noted that in each optimizing step the stress response and cumulative damage were calculated for each element group, i.e. for 11 groups. Identification of the damage critical finite

Initial values of design variables Tab. 1.

Variable	X1	X2	X3	X4	X5	X6	X7	X8	X9	X10	X11
Value [mm]	30	20	25	20	35	35	15	25	15	25	25

elements was realised using classical static analysis [8, 11]. The results of this process are presented in Table 2.

Numbers of critical elements Tab. 2.

Variable	X1	X2	X3	X4	X5	X6	X7	X8	X9	X10	X11
Elem. No.	74	802	1753	2433	3420	3639	4007	4655	4939	5117	7252

The optimization problem was defined as follows

- weight minimization of the frame structures,
- regarding boundary condition – maximum value of the fatigue damage $Dp = 0.6$,
- 11 optimization parameters – thicknesses (X1 - X11) .

Optimization variables can gain the discrete values listed in Table 3.

Model of stochastic excitation

The stochastic character of excitation was modelled on the basis of the vertical and transversal track unevenness obtained from the measuring on real track [7, 11]. The behaviour of the chosen random kinematic excitation function is shown in Fig. 8. The points where these functions are input into the computational model are presented in Fig. 7.

Where:

v – vehicle speed,

L – wheel base (8 m),

$u_{yL}^{(1)}$ – unevenness of the left rail in transverse direction for the front axle,

$u_{zL}^{(1)}$ – unevenness of the left rail in vertical direction for the front axle,

$u_{yP}^{(1)}$ – unevenness of the right rail in transverse direction for the front axle,

$u_{zP}^{(1)}$ – unevenness of the right rail in vertical direction for the front axle,

$u_{yL}^{(2)}$ – unevenness of the left rail in transverse direction for the back axle, i.e. $u_{yL}^{(2)}(t) = u_{yL}^{(1)}\left(t - \frac{L}{v}\right)$,

$u_{zL}^{(2)}$ – unevenness of the left rail in vertical direction for the back axle, i.e. $u_{zL}^{(2)}(t) = u_{zL}^{(1)}\left(t - \frac{L}{v}\right)$,

$u_{yP}^{(2)}$ – unevenness of the right rail in transverse direction for the back axle, i.e. $u_{yP}^{(2)}(t) = u_{yP}^{(1)}\left(t - \frac{L}{v}\right)$,

$u_{zP}^{(2)}$ – unevenness of the right rail in vertical direction for the back axle, i.e. $u_{zP}^{(2)}(t) = u_{zP}^{(1)}\left(t - \frac{L}{v}\right)$.

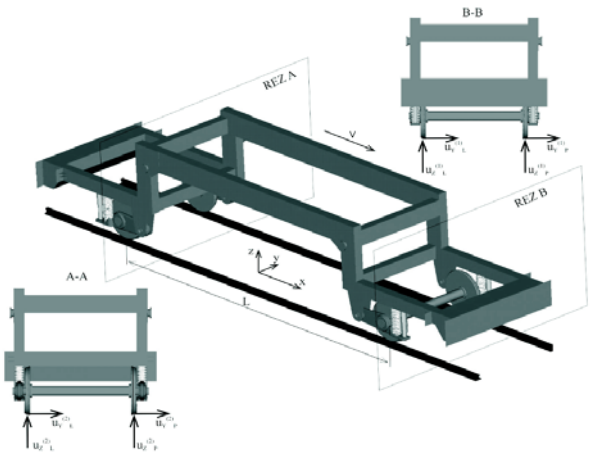

Fig. 7 Identification of the kinematic excitation functions

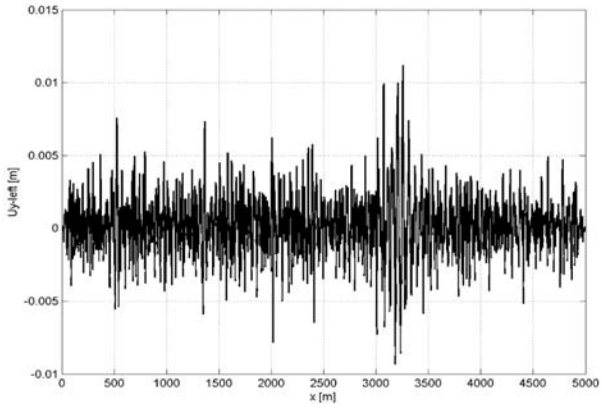

Fig. 8 The random function - $u_{yL}^{(1)}$

Following operating conditions were assumed

- movement 27.000 hours with the velocity of 40kmph,
- movement 18.000 hours with the velocity of 70kmph,
- movement 9.000 hours with the velocity of 100kmph.

Results of the optimizing process

The optimizing process was very time consuming and contained a lot of computational procedures. The main goal – structural weight reduction was reached. Process of the weight reduction is shown in Fig. 9. The calculation of the cumulative damage for non-proportional shell stresses using IA was one of the most complicated parts of the whole analysis [12]. The convergence history of the optimizing process for chosen optimizing variables and corresponding cumulative damages are presented in Fig. 10. It can be seen that the proposed algorithm is effective in view of a number of design variables ($nvar = 11$), i.e. the number of iteration steps was very low. Table 3 contains optimum values of the sheet thicknesses.

Optimum values Tab. 3.

Variable	X1	X2	X3	X4	X5	X6	X7	X8	X9	X10	X11
Value [mm]	10	10	12	14	12	12	12	18	12	12	10

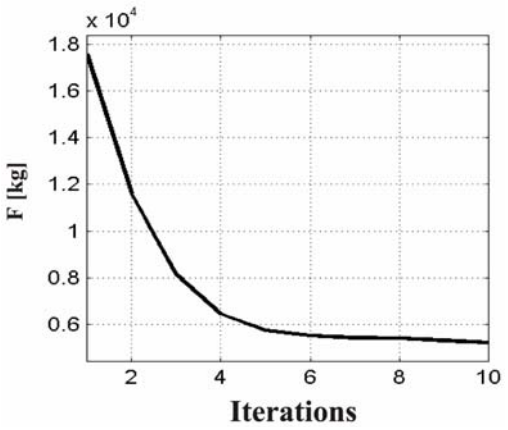

Fig. 9 Reduction of the structural weight

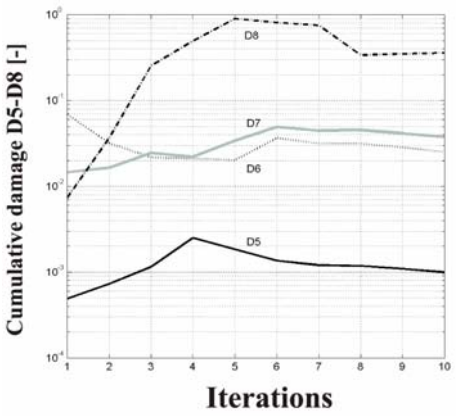

Fig. 10 Convergence history of the cumulative damage for optimizing groups X5 – X8

7. Conclusion

The goal of the paper was to present some multi-axial fatigue damage computational approaches and implementation and application of the chosen structural optimization technique in the case of the thin shell vehicle frames. The used methods were in-built into finite element analysis. The results of numerical studies verify accuracy of the applied optimizing approach in structural designing

with fatigue damage conditions. It is also necessary to remember a general problem of computational mechanics, i.e. time-consuming calculation hence in the authors' opinion the proposed algorithms will be acceptable in technical community.

Acknowledgements

This work has been supported by VEGA grant No. 1/0125/09 and 1/0727/10.

References

[1] BATHE, K. J.: *Finite Element Procedures.* New Persey : Prentice Hall, 1996.
[2] CARPINTERI, A., SPAGNOLI, A., VANTADORI, S.: A Multiaxial Fatigue Criterion for Random Loading, *Special Issue of Fatigue and Fracture of Engineering Materials and Structures,* Vol.26, 6/2003, pp. 515–522.
[3] HAFTKA, R. T., GURDAL, Z., KAMAT, M.: *Elements of Structural Optimizatio*n. Kluwer, Dordrecht, 1990.
[4] KWON, Y. W., BANG, H.: *The Finite Element Method using MATLAB.* CRC Press : University of Minnesota, 1996.
[5] PITOISET, X., PREUMONT, A., KERNILIS, A.: *Tools for a Multiaxial Fatigue Analysis of Structures Submitted to Random Vibrations.* Proc. of European Conference on Spacecraft Structures Materials and Mechanical Testing, Braunschweig, Germany, 1998.
[6] PREUMONT, A., PIEFORT, V.: Predicting Random High Cycle Fatigue Life with Finite Elements. *Journal of Vibration and Acoustics,* 116, 1994, pp. 245–248.
[7] SAGA, M., MEDVECKY, S., KOPECKY, M.: *The Effective Algorithm for Discrete Structural Mass Minimising Subjected to Fatigue Life.* 6th World Congress on Structural and Multidisciplinary Optimization, Rio de Janeiro, Brasil, May 2005, (full paper on CD).
[8] SAGA, M., VASKO M.: Stress Sensitivity Analysis of the Beam and Shell Finite Elements. *Communications – Scientific Letters of the University Zilina*, Vol. 11, No. 2, 2009, pp. 5–12.
[9] SAGA, M., VASKO, M., JANDACKA, J., HOLKOVA, Z.: Contribution to Stress Sensitivity Analysis of the Shell Finite Elements. *Applied and Computational Mechanics,* Vol. II, No. 1, 2008, pp. 113–122.
[10] SAGA, M., VAVRO, J.: Contribution to Non-Proportional Multiaxial Fatigue Analysis by FEM. *Materials Engineering,* Vol. 11, No. 1, 2004, pp. 143–150.
[11] SAGA, M.: Mass Minimising of Truss Structures Subjected to Prescribed Fatigue Life. *Machine Dynamics Problems,* Vol. 28, No. 4, 2004, pp. 101–106.
[12] SAGA, M.: Optimising Techniques for Multiaxial Fatigue Analysis by FEM. *Computational Mechanics,* 2002, Nectiny, 2002, pp. 403–408.

Lenka Skublova – Viktor Skorik – Rastislava Mrazikova – Branislav Hadzima*

CORROSION RESISTANCE OF TI6AL4V TITANIUM ALLOY WITH MODIFIED SURFACES

Corrosion behaviour of biocompatible Ti6Al4V titanium alloy has been investigated by using electrochemical impedance spectroscopy in Hank's physiological solution for two modified states of titanium surface. On the basic of type and shape of Nyquist curves obtained from EIS measurements probable mechanisms of corrosion in a specific corrosion system are assigned.

1. Introduction

Titanium and its alloys are widely used as orthopaedic and dental implants. They belong among the best biocompatible materials due to their passivation characteristics and the stability of the passive films in a biological system [1, 2].

This material has received widespread attention due to its low density, good strength, ductility corrosion resistance and biocompatibility. Titanium alloys have been clinically applied since 1970s when surgical implants were made with high-strength Ti6Al4V alloy. The natural oxide layer on commercially pure titanium is composed of titanium oxide in different oxidation states (TiO_2, Ti_2O_3 and TiO), while for Ti6Al4V alloy, aluminium and vanadium are additionally present in oxidized form (Al_2O_3 or V_2O_5). The passive films on the implant surface act as a barrier against the ion dissolution. Vanadium can alter the kinetics of the enzyme activity associated with the inflammatory response cells [2, 3].

With the degradation process metal ions are released, which accumulate in the tissue around the implant and also enter into the bloodstream. These ions may be responsible for wide range of undesirable effects. Various studies from the retrieved hip implants have established that the local reaction to particulate wear debris initiates the formation of a granulomatous tissue that ultimately invades the bone-implant interface and causes aseptic loosening. The combination of in vivo corrosion and cyclic loading may lead to the fracture of the implant, which is a serious clinical problem [4].

One of the biggest advantages of titanium alloys is their good corrosion resistance. The types of corrosion that have been observed on titanium and its alloys may be classified under the following general headings: general corrosion, crevice corrosion, stress corrosion cracking, anodic breakdown pitting, and galvanic corrosion. General corrosion is characterised by an uniform attack over the entire exposed surface of metal. Titanium alloys are very resistant to almost all salt solution over the pH range of 3 to 11 (pH of the physiological solution is about 7.4 [5]). The corrosion rate values for titanium alloys in variety of salt solution are generally less than 0.03 mm/yr [6].

Titanium is mechanically and chemically suitable for use in orthopedic devices and dental implants, but lacks the bioactivity needed for bonding to bone tissue. Different surface treatments have been developed to improve the bioactivity and osteconductivity of titanium implants [7].

The main goal of presented investigation is evaluation of the corrosion resistance of the Ti6Al4V alloy surface after electroerosion treatment in Hank's solution.

2. Experimental materials and methods

Ti6Al4V alloy belongs to the most commonly used ($\alpha + \beta$) titanium alloys. This type of Ti alloy is used as implant because of its good strength and ductility, being stronger and more resistant than both α or β alloys and has an excellent corrosion resistance in biofluids [3].

Titanium and titanium alloys are nontoxic, well tolerated materials for human body. The implant must have safety stability (20 years) in the body fluid environment that can be in a fact considered as the water solutions of salt [8].

2.1. Material preparation

The medical grade TiAl6V4 titanium alloy made by forging was used for the study. The standardized chemical composition of this alloy is in Tab. 1 [8].

* **Lenka Skublova, Viktor Skorik, Rastislava Mrazikova, Branislav Hadzima**
Department of Materials Engineering, FME, University of Zilina, Slovakia, E-mail: lenka.skublova@fstroj.uniza.sk

Standardized chemical composition (wt %) of Ti6Al4V titanium alloy — Tab. 1

N	C	H	Fe	O	Al	V	Ti
max. 0.05	max. 0.08	max. 0.15	max. 0.4	max. 0.2	5.50 – 6.75	3.50 – 4.50	balance

The specimens were organized into two groups with different modified surface:

- set I – specimens prepared from the basic state of Ti6Al4V alloy,
- set II – specimens prepared of Ti6Al4V alloy with additional electro-erosion surface treatment (at electric discharge of 29 A).

2.2. Microstructure analysis

Microstructural investigation was done by an optical microscope Carl ZEISS AXIO Imager.A1m. The microstructure of Ti6Al4V specimens (Fig.1) is a two-phase structure created by elongated polyedric grains of α phase (bright grains with the average size of about 6.25 μm) and intergranular β phase (dark/gray grains – 5 μm). Detail of the surface profile after electroerosion is in Fig. 2. Average height of the profile at treated surface is about 190 μm.

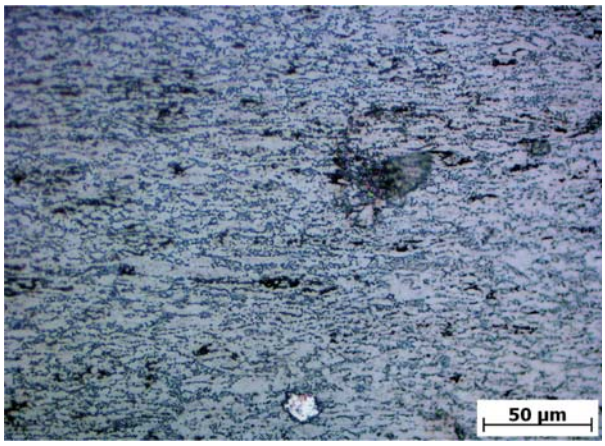

Fig. 1 Microstructure of Ti6Al4V alloy, etched 2 mL HF+8 mL HNO_3 + 90 mL H_2O [9]

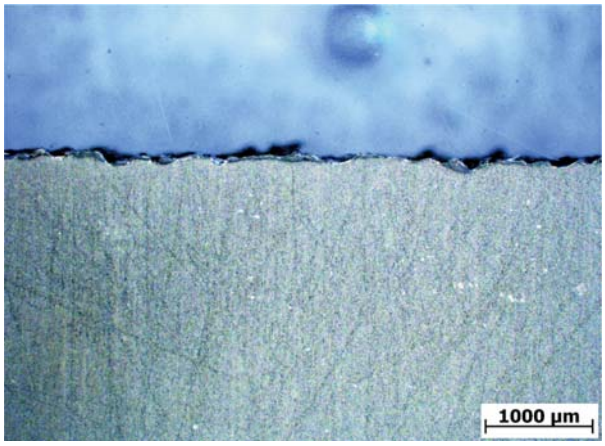

Fig. 2 Profile of electroeroded surface of Ti6Al4V alloy

2.3. Corrosion testing

The electrochemical tests were performed using electrochemical impedance spectroscopy (EIS) in Hank's physiological solution (8 g/L NaCl, 0.4 g/l KCl, 0.14 g/L $CaCl_2$, 0.1 g/L $MgSO_4.7H_2O$, 0.06 g/L KH_2PO_4, 0.05 g/L $NaH_2PO_4.H_2O$ a 1 g/L D – glucose [8]) at human body temperature (37 °C). This method allows establishing the value of polarization resistance of less conductive corrosion systems, for example when a passive layer with good adhesion is created on the metal surface. The polarization resistance R_p is an electrochemical property characterizing the material properties in the certain environment. The higher value of R_p represents better corrosion resistance of the material in corrosion environment. The electrochemical experiments were performed in a conventional three-electrode cell system with a calomel reference electrode and a platinum auxiliary electrode using Voltalab 10 corrosion measuring system with PGZ 100 measuring unit. The scheme of circuit connection and measuring principle is described in detail elsewhere [10].

The times for potential stabilization between the specimen and electrolyte, and the measuring frequencies are presented in Tab. 2. The amplitude of AC voltage was 20 mV. DC voltage component by which the specimen was polarized during testing was set to the measured value of free potential after stabilization.

Selected conditions of EIS measurements — Tab. 2

Exposure time	Measured frequency
5 min.	100 kHz – 5 mHz
1 and 2 h.	100 kHz – 10 mHz
4 h.	100 kHz – 15 mHz
8 and 16 h.	100 kHz – 25 mHz

3. Results

The results of electrochemical impedance spectroscopy measurements as Nyquist diagrams for Ti6Al4V alloy with basic surface and Ti6Al4V alloy with electroeroded surface are in Figs. 3 and 4, respectively.

The procedure and method of polarization resistance calculating from Nyquist plots is described in [11]. The impedance spectrum for TiAl6V4 was fitted by EC-Lab Software V9.32 using equivalent circuit (Fig. 5) [12].

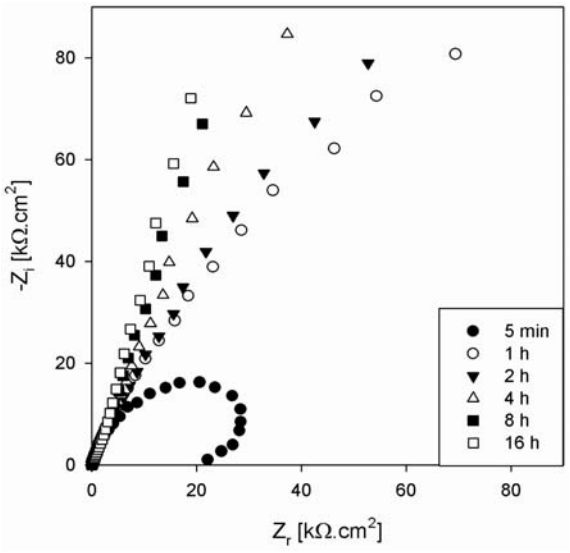

Fig. 3 Nyquist diagrams for basic state of Ti6Al4V alloy

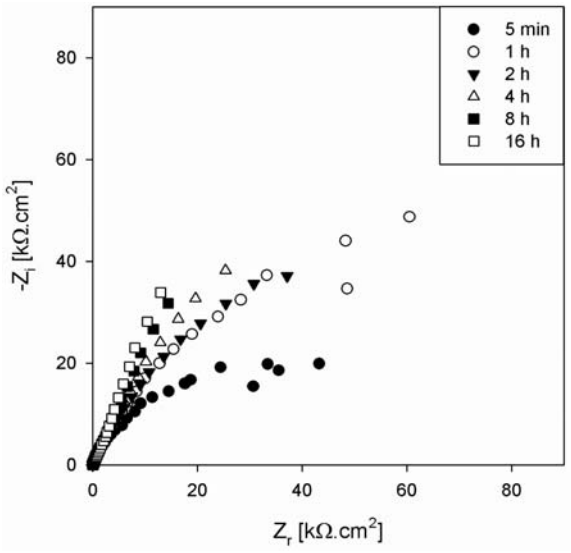

Fig. 4 Nyquist diagrams for electroeroded Ti6Al4V alloy

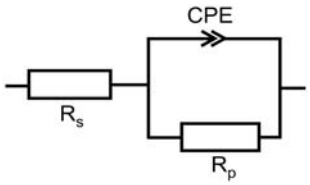

Fig. 5 Equivalent circuit for analysis of Nyquist plots, R_s – resistance of testing solution, R_p – polarization resistance, CPE – constant phase element

The results of the Nyquist plots analysis are in Tab. 3 and Tab. 4 for basic and electroeroded surface of the Ti6Al4V alloy, respectively.

Electrochemical characteristic values for basic state of Ti6Al4V alloy in Hank's solution — Tab. 3

	R_s [Ω.cm^2]	CPE [10^{-6}.F.sn^{-1}]	n	R_p [Ω.cm^2]
5 min	35.43	29.77	0.845	132.141
1 h	29.96	21.26	0.8932	649.731
2 h	30.14	20.19	0.8655	768.760
4 h	30.21	20.19	0.8232	1,014.000
8 h	28.44	19.32	0.8176	1,387.000
16 h	25.09	18.26	0.8177	2,707.000

4. Discussion

The biggest production problem of a total hip replacement is not the way how to make an endoprothesis itself, but to find the best way of its fixation into human body. Nowadays, more methods are used. The endoprothesis with bioactive properties has the best prospect due to interacting between its surface and biological tissue. For example, porous surface of implants leads to tissue ingrowth. The investigation deals with the evaluation the corrosion resistance of the surface that had been treated by electro-erosive discharge. This kind of treatment can provide bioactive properties to the surface, but it also can cause small cracks due to stress that appears on the surface during treating process.

Electrochemical characteristics values for electroeroded Ti6Al4V alloy in Hank's solution — Tab. 4

	R_s [Ω.cm^2]	CPE [10^{-6}.F.sn^{-1}]	n	R_p [Ω.cm^2]
5 min	36.52	44.32	0.7499	195.205
1 h	34.34	37.01	0.7744	392.568
2 h	40.61	32.61	0.7898	276.640
4 h	39.72	33.93	0.7793	408.300
8 h	39.73	32.72	0.7772	633.648
16 h	37.08	31.96	0.7759	1,189.000

The analysis of the measured results shows that the polarization resistance (R_p) of the interface titanium alloy – Hank's solution increases with exposure time (Fig. 6). The values of polarization resistance increase in case of using basic material (black columns in Fig. 6) and material with modified surface (gray columns in Fig. 6) as well. These values increase due to expansion of the passivation film on the surface that appears immediately after the investigated material is immersed into the experimental solution.

Dynamics of polarization resistance increase is affected by changes on the surface that are caused by modification of the surface

during electrochemical erosive discharges. The R_p values of the basic material increase uniformly. In a relatively short time, only 16-hour of exposure, R_p value increases 20-times, which is equal to the increase of the corrosion resistance. The measured values of the basic material surface are considered as reference because the modification of the implant surface is necessary for cell ingrowth. The analysis of curves measured on the electro-erosive modified surface shows that the R_p values in case of electro-eroded material increase during exposure time more slowly than in case of basic material. At the time of exposure from 2 to 4 hours, it even stagnates.

The most likely reason of this polarization resistance behavior is less stability and greater inhomogenity of the passive layer due to the residual stresses on the surface after electro-erosive modification. This modification may also cause extra layer damage by creating cracks. Higher inhomogenity of the passive layer on the electro-eroded material is shown also by lower values of the parameter "*n*" acquired by the analysis of the measured curves. During the 16-hour of exposure there was an increase of R_p values, but compared to the basic material, it was relatively low (the reached value of 1.1 MΩ.cm^2). Corrosion resistance of electro-eroded material decreases by more than half in comparison with the basic material.

The future investigation has to focus on an elimination of the deficiencies caused by surface modification. One possibility is to remove the internal stresses on the surface by heat treatment or chemical, possibly, electrochemical surface treatment.

4. Conclusions

On the basis of electrochemical impedance spectroscopy measurements we concluded the following results:

- The values of polarization resistance of basic and electroeroded material surface increase with the increase of exposure time. The R_p values, in case of the basic material, increase after all exposure time. In the case of electroeroded surface, R_p values increase between exposures of 5 minutes and 1 hour. During 1-4 hours of exposure, the R_p values stagnate and after 8 and 16 hours of exposure time, they increase again.
- Comparison of the R_p values shows that the electroeroded material reaches lower values of polarization resistance. In this case, the residual stresses generated on the surface during and just after the electric discharge reduced not only its mechanical properties, but also corrosion resistance. The polarization resistance of the basic material surface, without modifying the surface, reaches the twofold value (2.7 MΩ.cm^2) compared to electroeroded material surface (1.1 MΩ.cm^2).

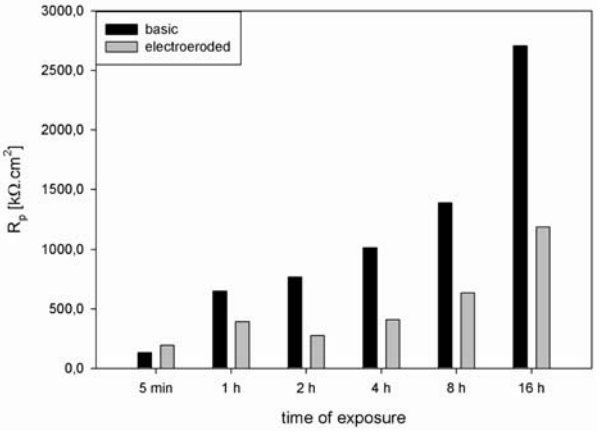

Fig. 6 Influence of exposure time of Ti6Al4V alloy in Hank's solution on polarization resistance for two types of different modified surface

Acknowledgements

This work was supported by the Science and Technology Assistance Agency under Contract No. APVV-LPP-0144-06. This work has been supported by the Scientific Grant Agency of the Ministry of Education and Slovak Academy of Sciences, grant No. 1/0203/08.

References

[1] MIAO, S., WENG, W., LI, Z., CHENG, K., DU, P., SHEN, G., HAN, G.: Electrolytic Deposition of Octacalcium Phosphate/Collagen Composite Coating on Titanium Alloy. In: *J Mater Sci: Mater Med* 20, 2009, pp. 131–134.

[2] THAIR, L., KAMACHI MUDALI, U., RAJAGOPALAN, S., ASOKAMANI, R., RAJ, B.: Surface Characterization of Passive Film Formed on Nitrogen Ion Implanted Ti–6Al–4V and Ti–6Al–7Nb Alloys Using SIMS. In: *Corrosion Science* 45, 2003, pp. 1951–1967.

[3] VASILESCU, E., DROB, P., RADUCANU, D., CINCA, I., MARECI, D., CALDERON MORENO, J.M., POPA, M., VASILESCU, C., MIRZA ROSCA, J.C.: Effect of Thermomechanical Processing on The Corrosion Resistance of Ti6Al4V Alloys in Biofluids. In: *Corrosion Science* 51, 2009, pp. 2885–2896.

[4] PALIWAL, M., ALLAN, D.G., FILIP, P.: Failure Analysis of Three Uncemented Titanium-Alloy Modular Total Hip Stems. In: *Engineering Failure Analysis* 17, 2010, pp. 1230–1238.

[5] NARAYANAN, R., KWON, T.-Y., KIM, K.-H.: Direct Nanocrystalline Hydroxyapatite Formation on Titanium from Ultrasonated Electrochemical Bath at Physiological pH. In: *Materials Science and Engineering:* C 28, 8, 2008, pp. 1265–1270.

[6] SHA, W., MALINOV, S.: *Titanium Alloys: Modelling of Microstructure, Properties and Applications.* Woodhead Publishing, Cambridge, UK, 2009, p. 592.

[7] LOPEZ-HEREDIA, M.A., LEGEAY, G., GAILLARD, C., LAYROLLE, P.: Radio Frequency Plasma Treatments on Titanium for Enhancement of Bioactivity. In: *Acta Biomaterialia* 4, 2008, pp. 1953–1962.
[8] SKUBLOVA, L., HADZIMA, B., BORBAS, L., VITOSOVA, M.: The Influence of Temperature on Corrosion Properties of Titanium and Stainless Steel Biomaterials. In: *Materials Engineering* 15, 2008, No. 4, pp. 18–22.
[9] PETZOW, G.: *Metallographic Etching.* 2nd Edition, ASM International, Ohio, 2001, p. 240.
[10] HADZIMA, B., LIPTAKOVA, T.: *Zaklady elektrochemickej korozie kovov* [Fundamentals of Electrochemical Corrosion of Metals]. 1st ed. EDIS ZU, Zilina, 2008, p. 116 (in Slovak).
[11] HADZIMA, B., SKORIK, V., BORBAS, L., OLAH, L.: Corrosion of Biocompatible AISI316 Stainless Steel in Physiological Solution. In.: *Materials Engineering* 15, 2008, No. 4, pp. 27–30.
[12] ORAZEM, M.E., TRIBOLLET, B.: *Electrochemical Impedance Spectroscopy.* New Jersey: John Willey and sons, USA, 2008, p. 523.

Henrietta Lelovics – Tatiana Liptakova *

RHEOLOGICAL PROPERTIES OF ACRYLIC BONE CEMENT SmartSet® HV

The rheological behaviour of polymethylmethacrylate bone cement SmartSet® HV prepared by hand and vacuum mixing was characterized using an oscillatory rheometer. Complex viscosity, damping factor, loss and storage modulus were measured by dynamic mechanical thermal analysis (DMTA) after several periods of ageing as a function of temperature for a range of 22–70 °C. Time-dependent changes of measured parameters were observed which were partially influenced by the cement preparation method.

1. Introduction

Acrylic bone cements are commonly used in orthopaedric surgery as bone filler and implant fixture agents. They are two-component systems consisting of powdered polymer and liquid monomer which are mixed together to form a dough.

Bone cement was mixed first using a spatula and opened bowl. During this method the person who mixed the cement was exposed to a high level of methylmethacrylate (MMA) vapors which are noxious. Moreover, mixing at atmospheric pressure in an opened bowl caused high degree of porosity of the premix and also of the cured cement. Nowadays, cement is mixed and transferred within the closed mixing barrel under reduced pressure (vacuum), thus there is no human contact with it. Vacuum mixing improves the quality of cement by eliminating the quantity of air bubbles in the cement structure and also reduces the level of monomer fumes discharged into environment [1]. Carefully prepared and cleaned bone canal is filled with the polymerizing cement mass and then the prosthesis is inserted and held in place while the cement solidifies [2]. The solidification is caused by exothermic polymerization of the monomer included in the liquid component. During this process free radicals break the covalent double bonds between the carbons of monomer allowing them to bind to the lengthening polymer chains. The function of cured bone cement in vivo is load and stress distribution by mechanical bonding between the bone and endoprosthesis [3].

During the last years, numbers of investigations attended to rheological properties of bone cements were realized. But no one of them was aimed at time-dependent changes which occur after bone cement ageing concerning cement preparation technology. Because of this reason we focused our attention to these questions and realized mechanical thermal analyses (DMTA) on aged cements which were prepared by different techniques of mixing (hand mixing, vacuum mixing).

2. Background to rheological characterization

A viscoelastic material, as the name implies, exhibits both viscous and elastic properties. These materials change their properties with temperature and time. One way to look at these changes is by measuring the response of the material to deformation by periodic forces (during forced vibration or small-amplitude oscillatory shear) [4]. The response obtained shows that stress and strain are not in phase, the strain delays behind the stress by a phase angle. If the oscillatory shear is sinusoidal, then *shear stress* is equal to

$$\tau(t) = \tau_0 \cdot e^{i\omega t} = \tau_0(\cos\omega t + i \cdot \sin\omega t) \quad (1)$$

where τ_0 – stress amplitude, ω – angular frequency, t – time and $i = \sqrt{-1}$.

Because of the delay *shear strain* is then equal to

$$\gamma(t) = \gamma_0 \cdot e^{i(\omega t - \delta)} = \gamma_0\big(\cos(\omega t - \delta) + i \cdot \sin(\omega t - \delta)\big) \quad (2)$$

where γ_0 – strain amplitude and δ – phase angle.

The *complex shear modulus G** is defined as

$$G^* = \frac{\tau(t)}{\gamma(t)} \quad (3)$$

Using equation (1) and (2), it can be devided into two parts

$$G^* = G' + i \cdot G'' = \frac{\tau_0}{\gamma_0}(\cos\delta + i \cdot \sin\delta) \quad (4)$$

* **Henrietta Lelovics, Tatiana Liptakova**
Department of Materials Engineering, Faculty of Mechanical Engineering, University of Zilina, Slovakia, E-mail: henrietta.lelovics@fstroj.uniza.sk

The first G' is in phase with strain, and the second G'' is out of phase with strain with angle δ. Therefore, two dynamic moduli can be defined as

$$G' = \frac{\tau_0}{\gamma_0}\cos\delta \quad \text{and} \quad G'' = \frac{\tau_0}{\gamma_0}\sin\delta \qquad (5)\,(6)$$

G' is called *storage modulus* and G'' is called *loss modulus*. The G' value is a measure of the deformation energy stored by the sample during the shear process. Thus, it represents the elastic behaviour. G'' value is a measure of the deformation energy used up by the sample during the shear process and therefore it represents the viscous behaviour of the material [5, 6]. From equations (2) – (6) it can be seen that

$$\mathrm{tg}\,\delta = \frac{G''}{G'} \qquad (7)$$

which is also called *damping factor* [7]. It reveals the ratio of the viscous and the elastic portion of the viscoelastic deformation behaviour. Idealelastic behaviour is specified in term of $\delta = 0°$ as $\mathrm{tg}\,\delta = 0$ and the idealviscous behaviour can be expressed by $\delta = 90°$ as $\mathrm{tg}\,\delta = \infty$.

The *complex viscosity* η^* is defined by the equation

$$\eta^* = \frac{\tau(t)}{\dot{\gamma}(t)} \qquad (8)$$

where $\dot{\gamma}$ is *shear rate*. Thus, complex viscosity can be also written as

$$|\eta^*| = \frac{|G^*|}{\omega} \qquad (9)$$

3. Experimental material

As an experimental material acrylic self-curing high viscosity bone cement SmartSet HV® was used. It is suitable for hand and vacuum mixing as well and its quantitative composition is specified below in Table 1.

The powdered component is white coloured and consists mainly of a methylmethacrylate (MMA) and methylacrylate (MA) based polymer. It also contains di-benzoyl peroxide which initiates cement polymerization when the powder and liquid components are premixed and radiopaque agent zirconium dioxide.

The liquid component is colorless and flammable with a distinctive odor. Its major component is the monomer methylmethacrylate (MMA). Hydroquinone is added as a stabilizer preventing premature polymerization which may occur when the liquid is exposed to heat or light. N,N-dimethyl-p-toluidine promotes cement polymerization.

4. Specimen preparation

Cement specimens were prepared by hand and vacuum mixing technique, both with exact timing. For hand mixing a suitable ceramic mixing bowl and spatula were used. The powdered component was poured into a bowl and then liquid component was added. The dough was mixed for 30 seconds very carefully. When the dough was formed there was a need to wait 60 seconds (waiting time) for this type of cement. Then it was taken into hands and kneaded for a few seconds. For vacuum mixing the CEMVAC syringe mixing system was used. After 90 seconds of mixing the syringe system with included cement was transferred into a suitable application gun from where the cement mass was ready to strike out.

After mixing processes the cement was stroked into a metal mould with a length of 50 mm and cross section 2×8 mm where it hardened for about 15 minutes. Then, hardened specimens were removed form the mould and stored on air at 25 °C and at relative humidity of 40–45 % for 3, 6 and 12 months.

5. Experimental methods

Experimental data were obtained by using an oscillatory rheometer Physica MCR301 with a convection heating device CTD 450. In dynamic mechanical thermal analysis (DMTA) under torsion, the physical properties of the samples were measured as a function of the temperature. The magnitude of the oscillating stress was kept as small as possible so that the cements structure was not destroyed or changed during the measurement. The measuring cell CTD 450 enables gradient-free measurement of the material properties according to the standard ASTM D-5279 [8]. The temperature displayed by the sensor corresponds to the actual sample temperature at all times. The main advantage of this measuring method is in simultaneous monitoring of all mentioned parameters, e.g. G', G'', tg δ and η^*.

6. Results and discussion

Our measurements on the oscillatory rheometer Physica MCR301 were performed under constant dynamical mechanical

Quantitative composition of bone cement SmartSet® HV — Tab.1

Bone Cement Powder			Bone Cement Liquid		
MMA/MA copolymer	Di-benzoyl peroxide	Zirconium dioxide	MMA	N,N-dimethyl-p-toluidine	Hydroquinone
84 (%w/w)	1 (%w/w)	15 (%w/w)	97.5 (%w/w)	≤ 2.5 (%w/w)	0.0075 (%w/w)

conditions. Deformation amplitude γ was 0.05% and frequency of oscillation *f* was 1 Hz, which practically isn't exceeded in vivo. The temperature range of measurements was between 25 and 75°C. The lower limit of this interval represents the storage temperature of specimens and the upper interval is under the glass transition temperature of polymethylmethacrylate (PMMA). Heating rate during the measurements was 2 K min^{-1} according to ISO 6721-10 [9].

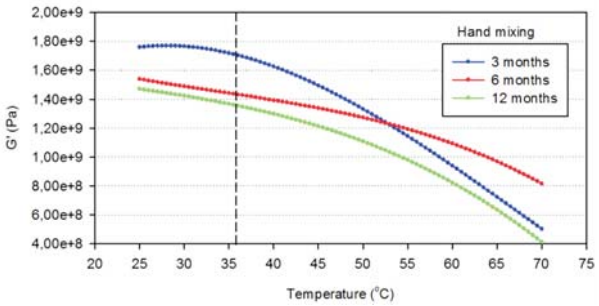

Fig. 1 G′ of hand-mixed samples

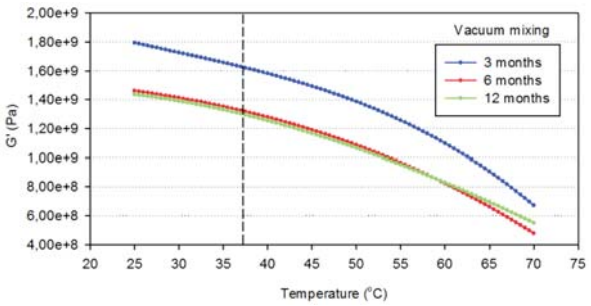

Fig. 2 G′ of vacuum-mixed samples

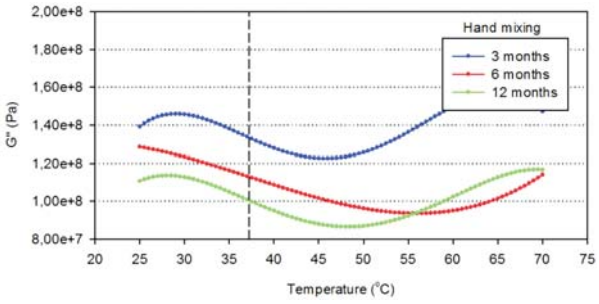

Fig. 3 G″ of hand-mixed samples

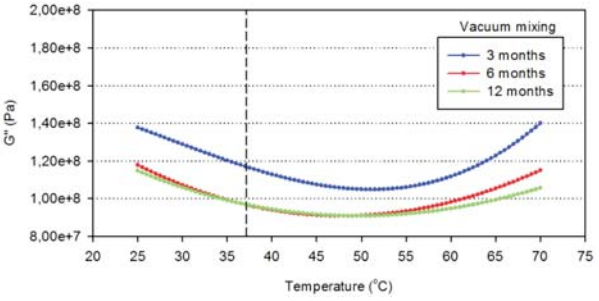

Fig. 4 G″ of vacuum-mixed samples

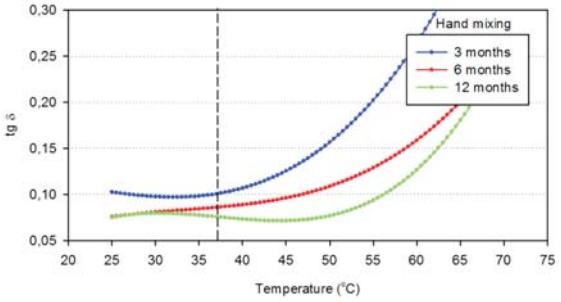

Fig. 5 tg δ of hand-mixed samples

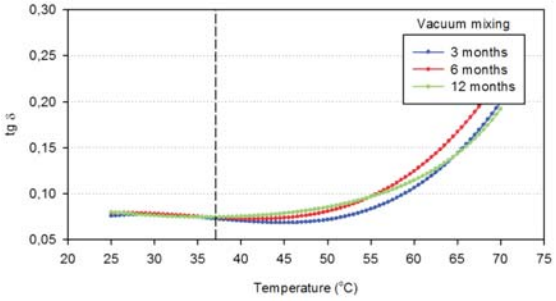

Fig. 6 tg δ of vacuum-mixed samples

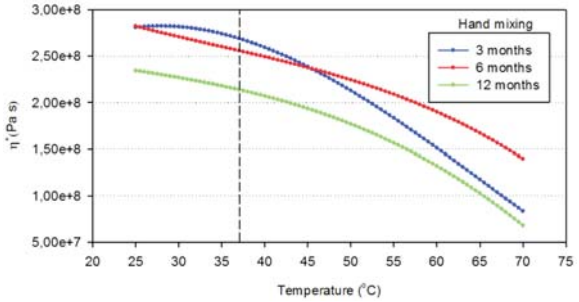

Fig. 7 η of hand-mixed samples*

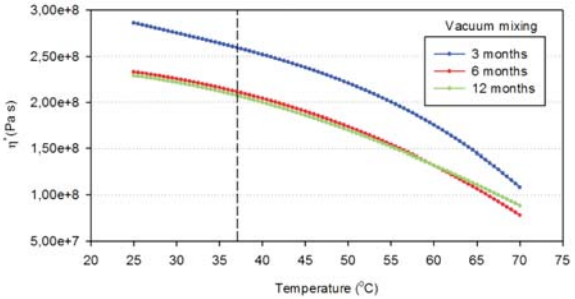

Fig. 8 η of vacuum-mixed samples*

The results of rheological measurements are shown in Figs. 1 – 8. The temperature of 37 °C which corresponds to the body temperature is marked with dashed line.

The results obtained show that after the hardening process of cement it is still subjected to continuous structural changes for both techniques of mixing. Differences in courses of the obtained characteristics mean that the sensitivity of the cements to temperature changes by the time of exposition and vary for each mixing technique. Hand-mixed cements are more sensitive to temperature than the ones mixed in vacuum. This phenomenon springs from the fact that the structure of cements and their properties were influenced by the mixing technique.

During the exposition in given environment (air) the cement was in direct contact with air humidity. For different concentration of water molecules in the air and in the structure of cement gradient controlled diffusion occurred. Diffused molecules of water to bone cement act as plasticizers and influence its physical and mechanical properties [10]. It is commonly known that cement mixing at reduced pressure minimizes the number of ineligible pores in its structure [1]. Thus, the density of cement is higher and free volume between the molecules is lower. Changes in physical and mechanical properties of vacuum-mixed cement are then less influenced by the environment in which the cement is stored, in this case by the diffused molecules of water. This claim is confirmed by relatively unchanged values of parameters for vacuum mixed cements after 6 months of exposition.

Our attention should be further focused on the parameters measured at body temperature, e. g. at 37 °C. After 3 months of exposition the storage modulus G', the loss modulus G'' and also the complex viscosity η^* decreased for both techniques of mixing. This phenomenon could be caused by higher mobility of polymer chains rested in plasticizing effect of diffused water from the surrounding environment. After next 3 months of exposition only small changes were registered for vacuum mixed cements but the changes in hand-mixed ones remained to continue. In term of energy dissipation which is presented by the damping factor tg δ, no changes occurred in vacuum-mixed cements during the monitored period. In other study we also registered time-dependent changes in bone cement tested by indentation measurements of microhardness, elastic modulus and creep.

Described processes are much faster in vivo where bone cement is directly washed with body fluids and for increased temperature as well. Thus, the in vivo behaviour of bone cement forms a comprehensive problem which also includes the bilateral diffusion of molecules of residual monomer and of body fluids. So, the changes occurred in the cement in vivo may originate from different reasons. On the other hand, these changes may be partially influenced by later polymerization of the confined monomer in the structure of cement and by other chemical processes activated e. g. by oxidation. The effect of structural changes on mechanical properties of acrylic bone cement was also shown by Hailey et al. [11]. They showed that the individual storage media and temperatures have significantly different effects on its behaviour.

7. Conclusions

Performed rheological measurements show that in bone cement SmartSet® HV structural changes over the time can be reported. These changes occurred without previous functional loading of the cement when it was stored in a wet environment. The measures of these changes partially depend on the structure of material influenced by a mixing method. Results obtained after different periods of testing were caused by ongoing polymerization, by diffusion of water molecules to structure of the cement as well as by other chemical changes. The mentioned results suggest a need for standardization of storage conditions of acrylic bone cements. Later effect of cyclic stresses in vivo e. g. during walking could influence the mechanical properties of the cement over the time as well and the changes may affect stress distribution in the bone-cement-prosthesis complex.

Acknowledgements

This research has been supported by the Scientific Grant Agency of the Ministry of Education of the Slovak Republic and Slovak Academy of Sciences, grant No. 1/0603/08. This support is gratefully acknowledged.

References

[1] LIPTAKOVA, T., LELOVICS, H., NECAS, L.: Variations of Temperature of Acrylic Bone Cements Prepared by Hand and Vacuum Mixing During their Polymerization. In: *Acta of Bioengineering and Biomechanics*, ISSN 1509-409X, 2009, Vol. 11, No. 3, p. 47–51.

[2] ORR, J.F., DUNNE, N.J., QUINN, J.C.: Shrinkage Stresses in Bone Cement. In: *Biomaterials*. ISSN 0142-9612, 2003, vol. 24, No. 17, pp. 2933–2940.

[3] LELOVICS, H., LIPTAKOVA, T.: Comparison of Surface Temperatures of Acrylic Bone Cements During Polymerization After Different Techniques of Mixing. In: *26th Danubia-Adria Symposium on Experimental Methods in Solid Mechanics.* Leoben, 2009. ISBN 978-3-902544-02-5, pp. 135–136.

[4] FARRAR, D.F., ROSE, J.: Rheological Properties of PMMA Bone Cements During Curing. In: *Biomaterials.* ISSN 0142-9612, 2001, vol. 22, no. 22, pp. 3005–3013.

[5] MEZGER, T.G.: *The Rheology Handbook.* 2nd ed. Hannover: Vincentz Network, 2006. 299 p. ISBN: 3-87870-174-8.

[6] NICHOLAS, M.K.D. et al: Analysis of Rheological Properties of Bone Cements. In: *Journal of Materials Science: Materials in medicine.* ISSN 0957-4530, 2007, Vol. 18, No. 7, pp. 1407–1412.
[7] POSTAWA, P., SZAREK, A.: Analysis of Changes in Bone Cement Damping Factor and its Effect on Bone Load. In: *Journal of Achievements in Materials and Manufacturing Engineering.* ISSN 1734-8412, 2007, Vol. 23, No. 1, pp. 35–38.
[8] ASTM D5279: Standard Test Method for Plastics: Dynamic Mechanical Properties In Torsion, 2008.
[9] ISO 6721: Plastics - Determination of Dynamic Mechanical Properties. 1999.
[10] NOTTROTT, M. et al: Time Dependent Mechanical Properties of Bone Cement. An in Vitro Study Over one Year. In: Journal of Biomedical Materials Research - Applied Biomaterials. ISSN 1552-4973, 2007, Vol. 83, No. 2, pp. 416–421.
[11] HAILEY, J.L., TURNER, I.G., MILES, A.W.: An in Vitro Study of the Effect of Environment and Storage Time on the Fracture Properties of Bone Cement. In: *Clinical Materials.* ISSN 0267-6605, 1994, Vol. 16, No. 4, pp. 211–216.

Zdenek Jonsta – Petr Jonsta – Katerina Konecna – Miriam Gabcova *

PHASE ANALYSIS OF NICKEL SUPERALLOY INCONEL 738 LC

Alloys of INCONEL (hereinafter IN) type play an important role among superalloys, used for the components of aircraft engines, gas turbines and turbo blowers. It is cast material which is alloyed in a complex manner on the Cr-Al-Mo-Ti-Nb-Zr basis.

The presented work made a detailed microstructural analysis of cast nickel superalloy IN 738 LC after heat treatment to the required quality and after long term annealing at the temperature of 850 °C and at dwell of 100, 500, 1000, 5000 and 10 000 hours.

Higher level of alloying of this alloy shows the higher level of a segregation activity. This may lead to high temperature exploitation to the development of microsegregation processes, connected to possible precipitation of carbidic or some variants of intermetallic phases [1]. Several strengthening mechanisms take place here, and a main strengthening is the precipitation strengthening by coherent precipitates of an intermetallic phase Ni_3Al, or $Ni_3(Ti, Al)$ [2].

The objective of the presented microstructural analysis consisted in a more detailed understanding of investigated nickel superalloy from a technical applicability viewpoint.

1. Introduction

High requirements for materials working in extreme conditions create space for the use of nickel based superalloys. Superalloys are suitable for these demanding applications particularly due to the fact that they preserve almost unchanged strength even after long term exposition to the temperatures exceeding 650 °C. The most exacting application of these materials is their use in heat parts of turbines. Important position of superalloys in this area is reflected in the fact that at present they represent more than 50% of mass of advanced aircraft engines. Extensive use of superalloys in turbines, supported by the fact that thermo dynamic efficiency of turbines increases with increasing temperatures at the turbine inlet, became a partial reason for the effort aimed at increase of maximum utility temperature of high alloyed alloys [3, 4].

This increase was enabled namely by two factors. The first factor consists in advanced processing techniques, which improved purity of alloys and thus increased its reliability, and also in mastering of a directional crystallisation technique and subsequently in mastering of technology of single crystalline products manufacture. The second factor consists in development of alloys with higher utility temperature, particularly by alloying with Re, W, Ta and Mo [4].

The submitted paper is oriented on materials engineering investigation of microstructural characteristics of cast nickel superalloy IN 738 LC after heat treatment to the required quality and after long term annealing at the temperature of 850 °C within interval of 100 – 10 000 hours.

2. Material and Experimental Technology

The microstructural analysis was made with the use of samples of the above mentioned nickel superalloy IN 738 LC. The analysis was made on the sample in the initial state after annealing to required quality by the mode 1120 °C/2h/air + 845 °C/24h/air, and subsequently on the samples after long term annealing at the temperature of 850 °C for 100, 500, 1000, 5000 and 10 000 hours. Microstructure was developed by chemical etching and it was documented on light metallographic microscope GX51.

Electron-microscopic investigation of the investigated alloy was made on a scanning electron microscope JEOL JSM-6490LV equipped with an energy dispersive spectral analyser INCA x act. Documentation of microstructure was made in the mode of secondary electrons (SEI) and backscattered electrons (COMPO-material contrast). Individual phases were identified by qualitative X-ray microanalysis. The semiquantitative X-ray microanalysis was made only in the case of particles greater than 1μm when results were not distorted more significantly by X ray signal from the surrounding matrix.

The following Table I contains a chemical composition of the investigated alloy.

For this nickel superalloy additional information about chemical constitution is given – a mean value of an electron vacancy level on the 3d sphere $\bar{N}_V = 2.36$ max. On the basis of this value it is possible to state in conformity with the existing experience that the investigated alloy will probably not show a susceptibility

* **Zdenek Jonsta, Petr Jonsta, Katerina Konecna, Miriam Gabcova**
Department of Materials Engineering, Faculty of Metallurgy and Materials Engineering, VSB-Technical University of Ostrava, Czech Republic,
E-mail: zdenek.jonsta@vsb.cz

Chemical composition of IN 738 LC (wt. %) Table I

C	Cr	Ti	Al	Fe(max)	Nb	Ta	Co	Zr	Ni
0.09 - 0.13	15.7 - 16.3	3.20 - 3.70	3.20 - 3.70	0.35	0.60 - 1.10	1.50 - 2.00	8.00 - 9.00	0.03 - 0.08	rest

to the formation of σ – phase. It was found in practice that σ – phase was formed on the one hand only in a case that $\overline{N}_V > 2.5$ – 2.6, on the other hand in a case when $\overline{N}_V \approx 2.0$ – 2.1.

3. Basic microstructural analysis

The basic microstructure of the sample in an initial state was formed by γ matrix. Particles of γ′ phase were segregated in it. Two stage heat treatment led to the creation of bimodal distribution of this phase. Chemical composition of particles of the γ′ phase with certain variability corresponds to intermetallics $Ni_3(Al, Ti)$. This phase contained also significant quantity of dissolved Ta. Processes of unmixing in the course of crystallisation led to the creation of distinct chemical heterogenities in the final microstructure. Primary carbides of the type MC were segregated in a non homogenous manner in the matrix. They contained variable quantities of strong carbide forming elements, namely tantalum, niobium and titanium. Carbides of the type MC often decorated grain boundaries. Numerous eutectic formations γ + γ′ were segregated in interdendritic spaces. In the areas of eutectics that solidified as the last ones, coarse particles of the phase γ′ were formed. In some cases small shrinkage porosities were present in their vicinity and a phase rich in Zr was also present locally. EDX spectrum showed that it was probably ZrS_x. Titanium carbonitrides were also detected in the proximity of eutectics. No particles of other

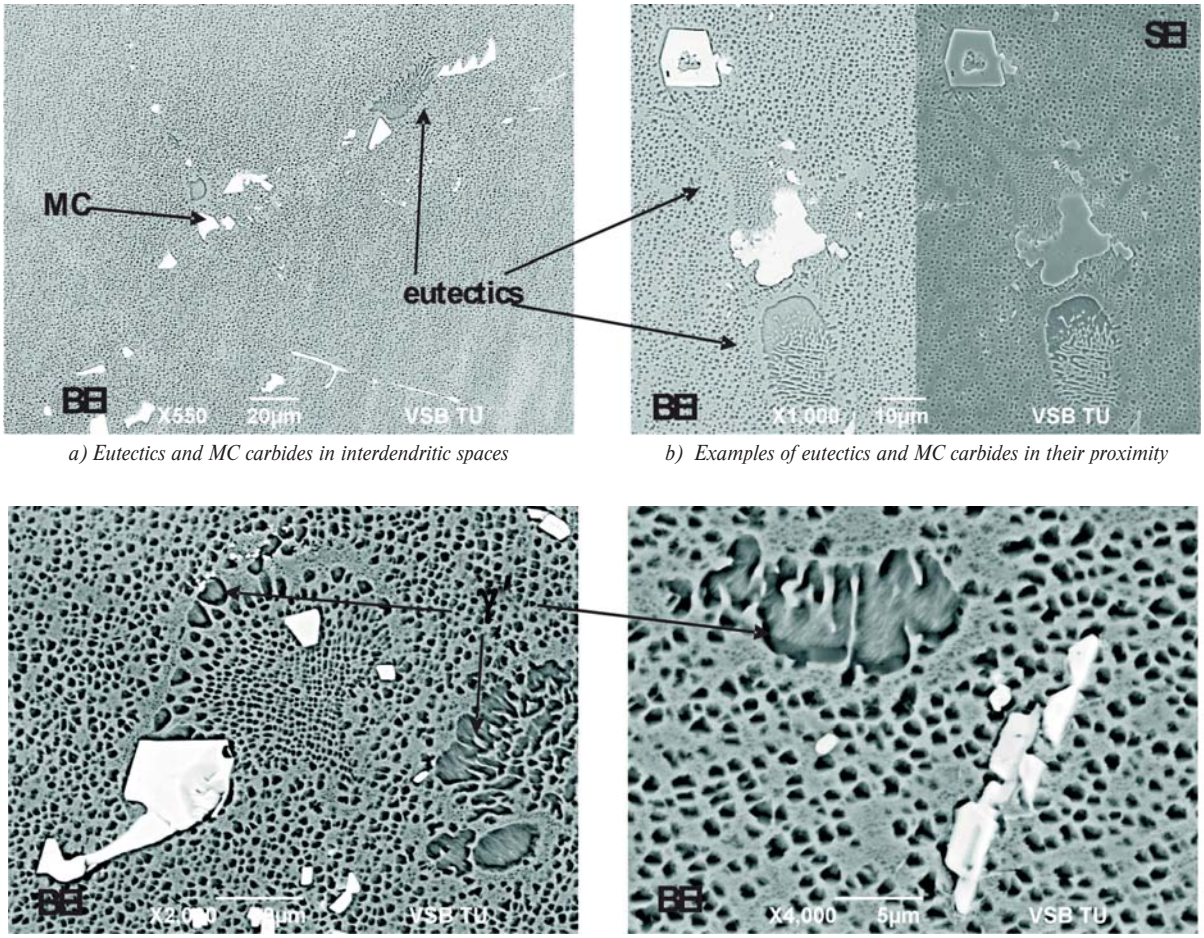

a) Eutectics and MC carbides in interdendritic spaces

b) Examples of eutectics and MC carbides in their proximity

c) Detail of eutectics

d) Detail of coarse particle γ′, particle rich in Zr surrounded by MC carbides

Fig.1 Examples of structure in initial state

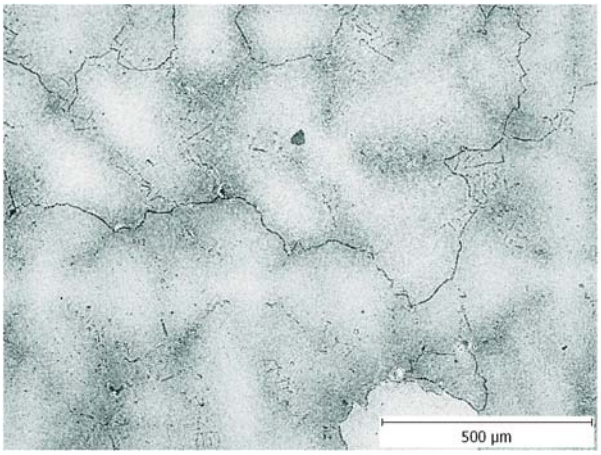

Fig. 2 Microstructure in initial state

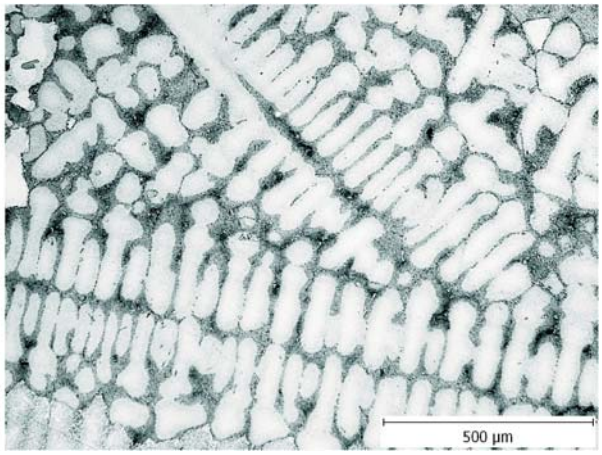

Fig. 3 Microstructure after annealing 850 °C/5000 hours

minority phases with size exceeding approx. 0.5µm were observed. Fig. 1 documents the appropriate microstructure. At visualisation in backscattered electrons (BEI) the white contrast corresponds to primary MC carbides, particles ZrS_x are grey.

It is evident from the next Fig. 2 taken with the use of a light microscope that dendritic structure in the initial state was not very distinct. During subsequent long term exposition at the temperature of 850 °C the bimodal distribution of the phase γ′ in the total volume of the alloy is gradually eliminated [1]. In comparison with the initial state the dendritic structure was very distinct, as it can be seen in Fig. 3, documenting microstructure of the sample after long term annealing at the temperature of 850 °C/5000 hours.

4. Microstructural characteristics after long term annealing

After long term annealing differences were observed in a grain size in interdendritic spaces and inside branches of dendrites. Particles in interdendritic spaces were coarser, inside branches of dendrites were finer. Grain boundaries were decorated with discontinuous mesh of carbides MC and $M_{23}C_6$. It is known that primary carbides in nickel superalloys are unstable. They gradually decompose at high temperatures.

This decomposition is accompanied with the creation of secondary carbides particles $M_{23}C_6$ and phase γ′ [2]. It is evident from photos of microstructures in Figs. 4a, 4b and 5 that the creation of secondary carbides occurs both by degeneration of primary MC carbides, and by precipitation from solution, which contains residual carbon. A rim formed by γ′ phase was gradually formed along carbides on grain boundaries. It was the most distinct in the sample with the longest duration of annealing (10 000 hours). This example is shown in Fig. 6.

Formations of eutectics were more difficult to be discerned with an increasing duration of annealing due to the growth and coarsening of particles of the γ′ phase. Migration of grain boundaries occurred, the boundaries became significantly more toothed, which according to the work [6] is advantageous from the view-

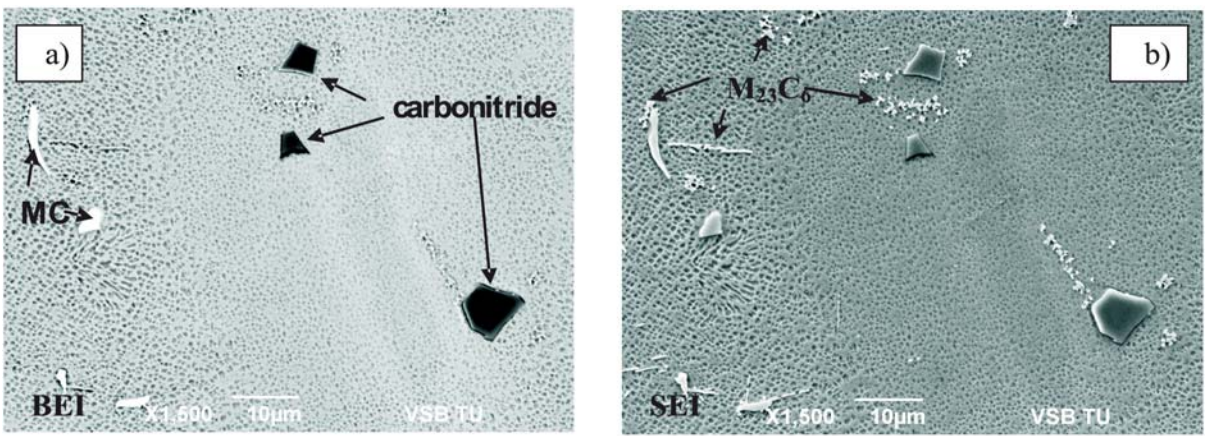

Fig. 4 An example of structure after annealing by regime 500 hours/850 °C

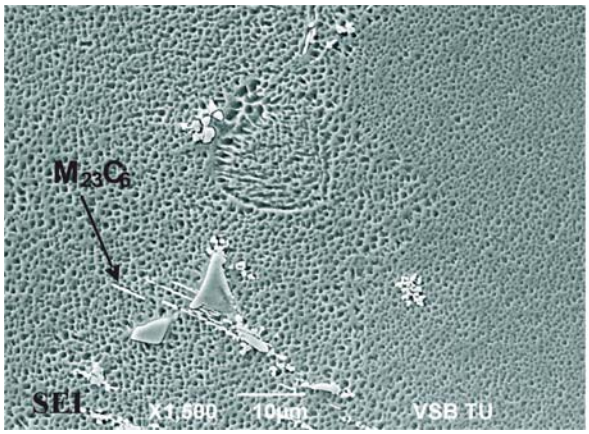

Fig. 5 Precipitation of $M_{23}C_6$ around MC carbides and from γ solution

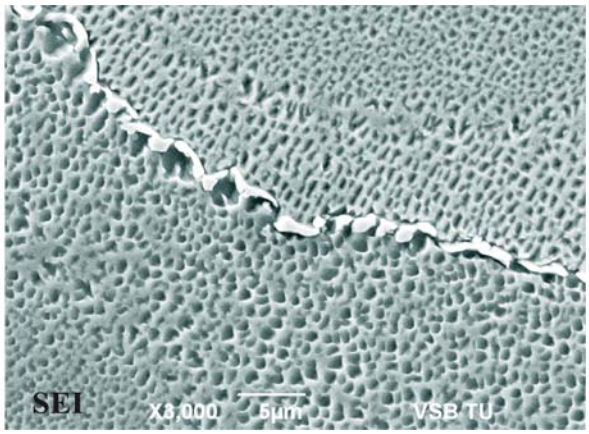

Fig. 6 Grain boundary decorated by particles $M_{23}C_6$ coated by γ′film

point of resistance to creep. Fig. 7 shows examples of structures after annealing of 2000 hours at the temperature of 850 °C.

With elongation of annealing duration at the temperature of 850 °C growth and coarsening of the phases which were present in a structure occurred already after annealing at 850 °C/100 hours. The phase rich in Zr was not anymore detected in the samples with duration of annealing since 2000 hours. After the longest duration of annealing (10 000 hours) morphology of γ′ phase particles has changed. Particles became rounder, the difference between their size inside dendrites and in interdendritic spaces diminishes. [3, 5]. Very important is the fact that no occurrence of TCP phases (for example σ phase, μ phase, R phase) was found in any of investigated samples.

5. Conclusions

The presented paper presents a carried out detailed phase analysis of the samples of refractory nickel superalloy IN 738 LC both in its initial state and after heat treatment to the required quality and after long-term annealing at the temperature of 850 °C with dwell in the interval from 10^2 to 10^4 hours.

It was possible to state on the basis of the obtained results that with increased duration of dwell at the temperature of 850 °C no precipitation of new minority phases occurred. Only processes of growth and coarsening of phases' particles which were present in the structure already after annealing at 850 °C/100 hours occurred. Morphology of particles of γ′ phase in the basic matrix γ also occurred as they coagulated and rounded off. This finding is in good correlation with the work [3].

Special attention was paid also to a possibility of undesirable TCP phases precipitation, particularly of the phase σ. Due to the value of concentration of vacancies on 3d sphere, which was determined as $\bar{N}_V \approx$ 2.36 max., precipitation of these undesirable phases appeared to be improbable. The microstructural analysis confirmed this assumption since these undesirable phases were not detected in any variant of a long term exposition at the temperature of 850 °C.

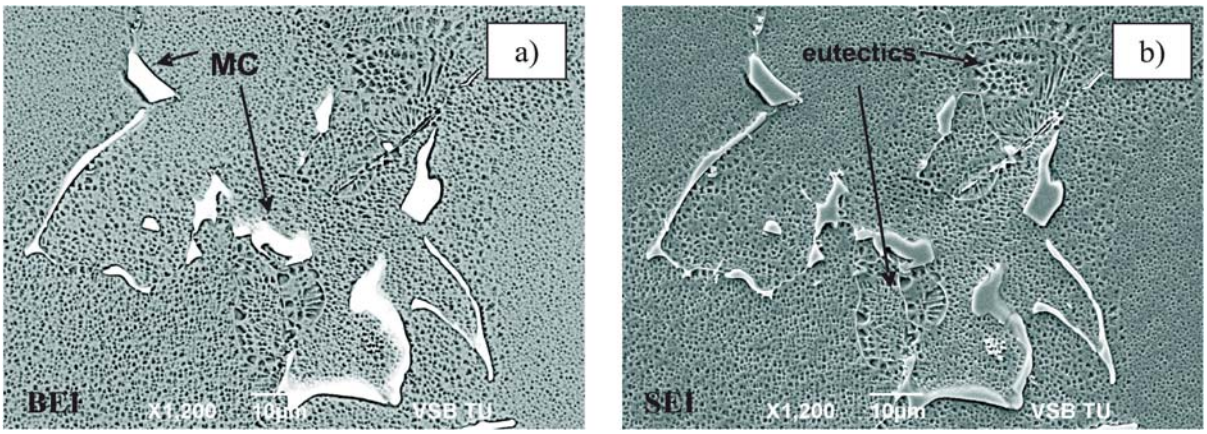

Fig. 7 Coarse MC carbides and indistinct eutectics

The realised microstructural analysis showed that structural changes at long term annealing at the temperature of 850 °C were not noticeably unfavourable and that they did not cause degradation of the investigated alloy at a long term high temperature exposition.

The obtained results extend the findings and knowledge about investigated superalloy from the viewpoint of ensuring its operational reliability and safety.

Acknowledgement

The paper was prepared thanks to the financial support of the MSMT MSM 6198910013 and RMTVC CZ.1.05/2.1.00/01.0040 projects.

References

[1] MOSHTAGHIN, R., S., ASGARI, S.: Growth Kinetics of γ′ Precipitates in Superalloy 738LC During Long Term Aging, In: *Materials & Design* [online], Vol. 24, 5/ 2003, pp. 325–330, ISSN 0261-3069.

[2] EL-BAGOURY, N., WALY, M.,.NOFAL, A.: Effect of Various Heat Treatment Conditions on Microstructure of Cast Polycrystalline IN738LC Alloy, In: *Materials Science and Engineering: A* [online], Vol. 487, Issues 1-2/2008, pp. 152–161, ISSN 0921-5093.

[3] HERNAS, A., JONSTA, Z., et. al.: *Refractory Steels and Alloys (in Czech)*, VSB-TU Ostrava, 2nd Edition, 2010, 340 pp, ISBN 80-968605-6-9.

[4] HRBACEK, K.: *Research and Development of Technology of Precise Casting of Blades for Stationary Gas Turbines Enabling Substitution of Forged Blades by Cast Blades (in Czech),* Research Report, Velka Bites, 2005, 40 pp.

[5] IDOWU, O., A., RICHARDS, N., L., CHATURVEDI, M., C.: Effect of Bonding Temperature on Isothermal Solidification Rate During Transient Liquid Phase Bonding of Inconel 738LC Superalloy, In: *Materials Science and Engineering: A* [online], Vol. 397, 1-2/ 2005, pp. 98–112, ISSN 0921-5093.

[6] WISNIEWSKI, A., BEDDOES, J.: Influence of Grain-Boundary Morphology on Creep of a Wrought Ni-base Superalloy, In: *Materials Science and Engineering: A* [online], Vol. 510-511, 2009, pp. 266–272, ISSN 0921-5093.

Eva Tillova – Maria Chalupova – Lenka Hurtalova *

EVOLUTION OF THE Fe-RICH PHASES IN RECYCLED AlSi9Cu3 CAST ALLOY DURING SOLUTION TREATMENT

Using recycled aluminium cast alloys is profitable in many aspects. Requiring only 5% of the energy to produce secondary metal as compared to primary metal and generates only 4% of the CO_2 emissions, the recycling of aluminium is therefore beneficial of both environmental and economical point of view. AlSi9Cu3 is a very frequently employed die-casting alloy. It is used in almost all fields of pressure die casting, especially in the fabrication various motor mounts, pistons, cylinder heads, heat exchangers, air conditioners or gearings. Al-Si-Cu alloys usually contain Cu and sometimes Mg as the main alloying elements, together with various impurities such as Fe, Mn or Cr. Presence of the Fe impurity enables the crystallization of brittles needles Al_5FeSi during solidification, even thought the Fe content is extremely low in a melt, and its presence severely lowers the dynamic fracture toughness of the alloy. Alloying elements such are Mn, Cr, Mo and Be have been used to change the morphology of the Al_5FeSi needles and Al(FeMnMg)Si skeleton (or "Chinese script") phases.

The present study is a part of larger research project, which was conducted to investigate and to provide a better understanding of the solution annealing on the morphology of Fe-rich intermetallic phases in cast Al-Si-Cu alloys. The Fe-rich changes of typical specimens under different solution heat treatment condition were examined using an optical and scanning electron microscope (SEM). The results show that optimal solution treatment causes increasing of mechanical properties, the change of Si-morphology and reduction iron rich phases.

Keywords: recycled Al-Si cast alloy, Fe-rich intermetallic phases, solution treatment

1. Introduction

Al-Si alloys are most universal materials, comprising 85% to 90% of the aluminium cast parts produced for the automotive industry (e.g. various motor mounts, engine parts, cylinder heads, pistons, valve retainer, compressor parts, etc.) [1, 2].

The application of Al-Si alloy castings in many mechanical components, especially for cars and rail vehicles, has gradually increased in the last years, thanks to the great potential of these materials as replacements for ferrous alloys. Today an increasing amount of the aluminium going into producing new aluminium alloy products is coming from recycled products. The increase in recycled metal becoming available is a positive trend, as secondary metal produced from recycled metal requires only about 2.8 kWh/kg of metal produced while primary aluminium production requires about 45 kWh/kg of metal produced. It is to the aluminium industry's advantage to maximize the amount of recycled metal, for both the energy-savings and the reduction of dependence upon overseas sources. Increasing the use of recycled metal is also quite important from the ecological standpoint, since producing aluminium by recycling creates only about 4% as much CO_2 as by primary production [3].

But it is recognized that these recycled Al-Si alloys are not likely to be suitable for fracture-critical components, where higher levels of Fe and Si have been shown to degrade fracture resistance. However the likelihood exists that they may perform quite satisfactorily in applications such as those listed where service life is determined by other factors [4].

The quality of recycled Al-Si casting alloys is considered to be a key factor in selecting an alloy casting for a particular engineering application. The microstructure of Al-Si-Cu cast alloy is composed of a certain amount of Fe, Mn and Mg that are present either accidentally, or they are added deliberately to provide special material properties. These elements partly go into solid solution in the matrix and partly form intermetallic particles during solidification. The size, volume and morphology of intermetallic phases are functions of chemistry, solidification conditions and heat treatment [1, 2, 5]. Fe is a common impurity in aluminium alloys that leads to the formation of complex Fe-rich intermetallic phases, and how these phases can adversely affect mechanical properties, especially ductility, and also lead to the formation of excessive shrinkage porosity defects in castings [6]. It is clear that the morphology of Fe-rich intermetallic phases influences harmfully also fatigue properties [7]. Much harmful effect proves the cast defects as porosity and microshrinkages because these defects have larger size than intermetallic phases.

The present study is a part of larger research project, which was conducted to investigate and to provide a better understand-

* **Eva Tillova, Maria Chalupova, Lenka Hurtalova**
Department of Material Engineering, Faculty of Mechanical Engineering, University of Zilina, Slovakia, E-mail: eva.tillova@fstroj.uniza.sk

ing of the influence of Fe on the structure and mechanical properties in recycled (secondary) AlSi9Cu3 cast alloy.

2. Experimental part

Recycled (secondary) AlSi9Cu3 cast alloy with chemical composition given in table 1 was used as an experimental material. The melt was not modified or refined. Experimental cast samples were given a heat treatment - solution treatment for 2, 4, 8, 16 or 32 hours at three temperatures (505, 515 and 525 °C); water quenching at 40 °C and natural aging for 24 hours at room temperature. After heat treatment the samples were subjected to a mechanical test. Hardness measurement was preformed by a Brinell hardness tester with a load of 62.5 Kp, 2.5 mm diameter ball and a dwell time of 15 s. The Brinell hardness value at each state was obtained by an average of at least six measurements.

Chemical composition of the alloy (wt. %) Table 1

Si	Cu	Mn	Fe	Mg	Ni	Pb	Zn	Ti	Al
10.7	2.4	0.22	< 0.8	0.47	0.08	0.11	1.1	0.03	rest

Metallographic samples were cut from selected tensile specimens (after testing) and hot mounted for metallographic preparation. The microstructures were studied using an optical microscope Neophot 32. Samples were prepared by standards metallographic procedures (wet ground on SiC papers, DP polished with 3 μm diamond pastes followed by Struers Op-S and etched by Dix-Keller, HNO_3, H_2SO_4 or MA). To determine the chemical composition of the intermetallic phases a scanning electron microscope (SEM) TESCAN VEGA LMU with EDX analyser BRUKER QUANTAX was employed.

3. Results and discussion

The structure of hypoeutectic AlSi9Cu3 cast alloy consists of dendrites α-phase (light grey), eutectic (dark grey) and intermetallic Fe- and Cu-rich phases. The formation of these phases should correspond to successive reaction during solidification Table 2 [1, 4, 8].

The effect of solution treatment on morphology of eutectic Si is demonstrated in Fig. 1. The changes in morphology of eutectic

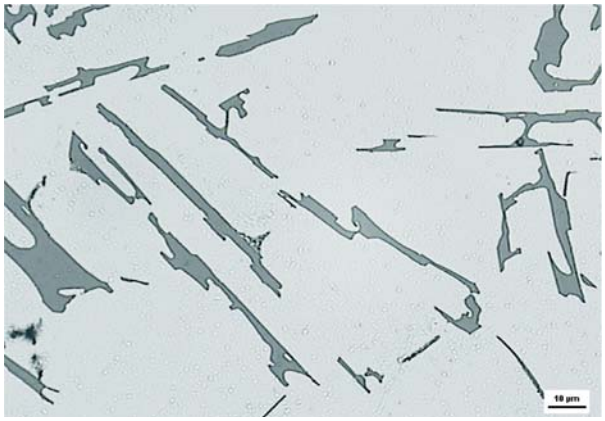

a) untreated state

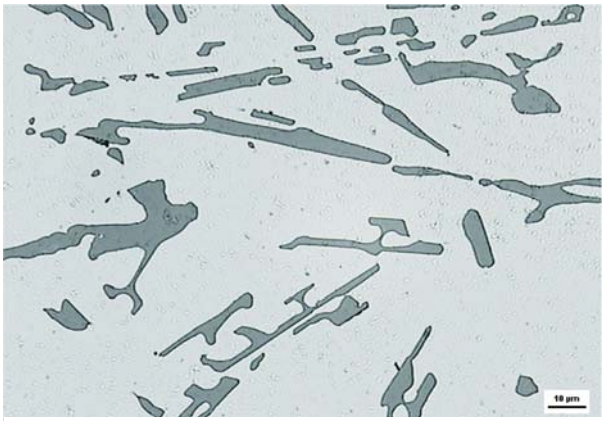

b) 505 °C, 4 hours

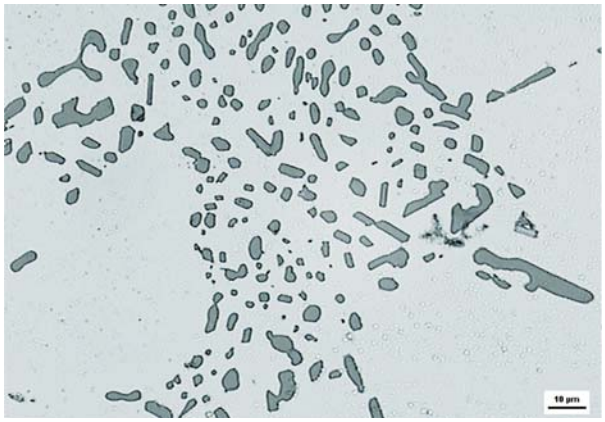

c) 515 °C, 4 hours

d) 525 °C, 4 hours

Fig. 1 Effect of solution treatment on morphology of eutectic Si, etch. Dix-Keller

Reactions occurring during solidification of Al-Si-Cu alloy Table 2

	Temperature, °C
α – dendritic network	609
Liq. → α - phase + $Al_{15}(FeMn)_3Si_2$ + Al_5FeSi	590
Liq. → α - phase + Si + Al_5FeSi	575
Liq. → α - phase + Si + Mg_2Si + $Al_8Mg_3FeSi_2$	554
Liq. → α - phase + Al_2Cu + Al_5FeSi + Si	525
Liq. → α - phase + Al_2Cu + Si + $Al_5Mg_8Si_6Cu_2$	507

Si observed after heat treatments are documented for holding time of 4 hours. Eutectic Si without heat treatment (untreated state) occurs in platelets form (Fig. 1a). After solution treatment by temperature of 505 °C we noted that the platelets were fragmentized into smaller platelets with spherical edges (Fig. 1b). The spheroidized process dominated at 515 °C. The smaller Si particles were spheroidized to rounded shape, see Fig. 1c. By solution treatment at 525 °C the spheroidized particles gradually grew larger (coarsening) (Fig. 1d).

For die casting, Fe is added to increase hot tear resistance and to reduce die sticking. In Al-Si-Cu type alloys, however, Fe showed to have the most detrimental effect on ductility of all of the common impurities. Iron impurities can either come from the original bauxite ore or be acquired during subsequent melting, remelting and casting, e.g. by contamination from the melting pot etc. Significant levels of Fe (e.g. > 0.5 %) can change the solidification characteristics of Al-Si alloys by forming pre- and post-eutectic Al_5FeSi (know as beta- or β- phase [4, 9, 10]).

Al_5FeSi phases precipitate in the interdendritic and intergranular regions as platelets (appearing as needles in the metallographic microscope – Fig. 2a). Long and brittle Al_5FeSi platelets (more than 500 ∝m) can adversely affect mechanical properties, especially ductility, and also lead to the formation of excessive shrinkage porosity defects in castings. It was also shown that the Al_5FeSi needles can act as nucleation sites for Cu-rich phases (Fig. 2b) [11].

The deleterious effect of Al_5FeSi can be reduced by increasing the cooling rate, superheating the molten metal, or by the addition of a suitable "neutralizer" like Mn, Co, Cr, Ni, V, Mo and Be. Mn was the most common addition. Mn excess may reduce Al_5FeSi phase and promote formation of Fe-rich phases $Al_{15}(FeMn)_3Si_2$ (known as alpha- or α-phase [4, 10-13]) in a "skeleton-like" form or in "Chinese script" form – Fig. 3a. This compact morphology "Chinese script" (skeleton – like) does not initiate cracks in the cast material to the same extent as Al_5FeSi does. If Mg is also present with Si, an alternative called pi- or π-phase can form, $Al_5Si_6Mg_8Fe_2$. $Al_5Si_6Mg_8Fe_2$ has a script-like morphology [4, 12].

Fe-rich phases (Al_5FeSi or $Al_{15}(FeMn)_3Si_2$) are completely brittle [1], since their particles break during polishing in slurry of alumina (Fig. 3b). It suggests that the intermetallic phases may act as stress raisers and crack initiation sites that reduce the strength and ductility of the recycled Al-Si-Cu alloys due to the lack of active slip systems in the intermetallic compounds.

Alloying with Mn and Cr, caution has to be taken in order to avoid the formation of hard complex intermetallic multi-component sludge, $Al_{15}(FeMnCr)_3Si_2$ – phase (Fig. 3c). These intermetallic compounds are hard and can adversely affect the overall properties of the casting. The formation of sludge phases [12] is a temperature dependent process in a combination with the concentrations of iron, manganese and chromium independent of the silicon content.

In recycled AlSi9Cu3 cast alloy that contains less than 0.8% of Fe and 0.22%Mn very short and little $A_{15}FeSi$ needles were present. Fe-phases precipitate first of all as skeleton-like $Al_{15}(FeMn)_3Si_2$ phase.

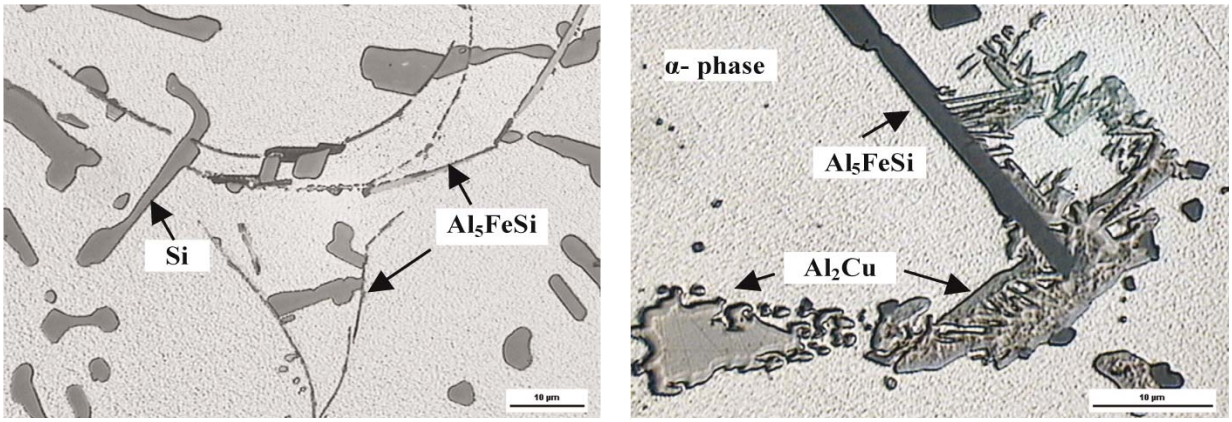

a) Al_5FeSi needles *b) Al_5FeSi needles as nucleation sites for Cu-rich phases*

Fig. 2 Morphology of Fe-rich needles in recycled AlSi9Cu3 cast alloy, etch. Dix-Keller

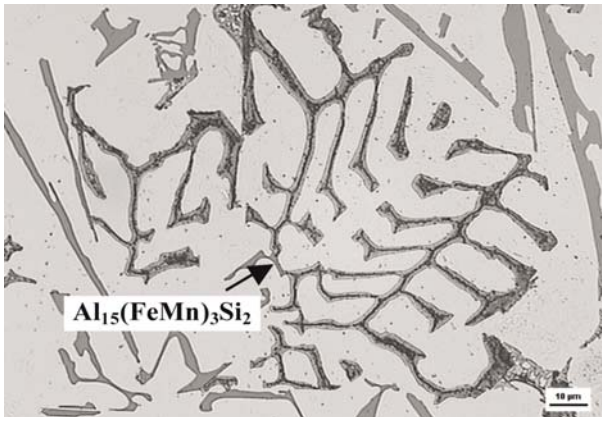

a) $Al_{15}(FeMn)_3Si_2$

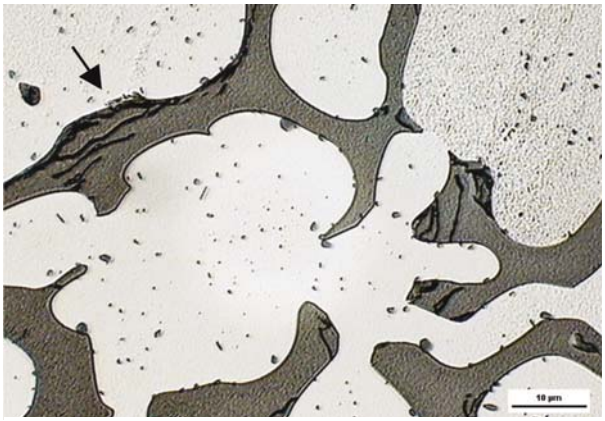

b) detail of brittle $Al_{15}(FeMn)_3Si_2$

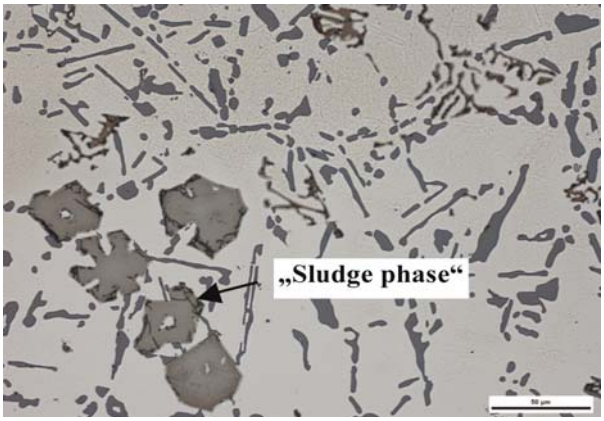

c) typical microstructure of "sludge"
(a coarse form of the $Al_{15}(FeMn)_3Si_2$ phase)

Fig. 3 Morphology of skeleton-like Fe-rich phases in recycled AlSi9Cu3 cast alloy, etch. Dix-Keller

3.1. The effect of solution treatment on mechanical properties

Mechanical properties of a cast component are determined largely by the shape and distribution of Si particles in the matrix. Optimum tensile, impact and fatigue properties are obtained with small, spherical and evenly distributed particles.

Heat treatment used to obtain the optimal combination of strength and ductility in casting involves: a) solutionizing to thermally prepare the material; b) quenching to retain the maximum concentration of hardening constituent (Al_2Cu) in solid solution and c) a combination of artificial and over-ageing to obtain the desired mechanical properties in the casting [5]. Solution treatment performs three roles: homogenization of as-cast structure; dissolution of certain intermetallic phases such as Al_2Cu; changes the morphology of eutectic Si phase by fragmentation, spheroidization and coarsening, thereby improving mechanical properties, particularly ductility. Most of the recommended heat treatment of alloys that contain cooper restricts the solution temperature below the final solidification point in order to avoid the melting of copper-rich phases.

Influence of solution treatment on mechanical properties (strength tensile – R_m and Brinell hardness - HBS) for recycled AlSi9Cu3 cast alloy is shown in Figs. 4 and 5. After solution treatment, tensile strength, ductility and hardness are remarkably improved, compared to the corresponding as-cast condition.

By increasing the solution holding time from 2 to 4 h, the tensile strength increased to 273 MPa for 515 °C. With further increase in solution temperature more than 515 °C and solution time more than 8 hours, tensile strength gently decreases during the whole solution period. This suggests that to enhance the tensile strength of this alloy by increasing the solution temperature more than 515 °C and by extending the solution time does not seem possible. Peak strength is reached after 4–8 h of natural ageing.

The results of hardness (Fig. 5) are comparable with results of tensile strength. The highest hardness was 124 HBS for 515 °C/4

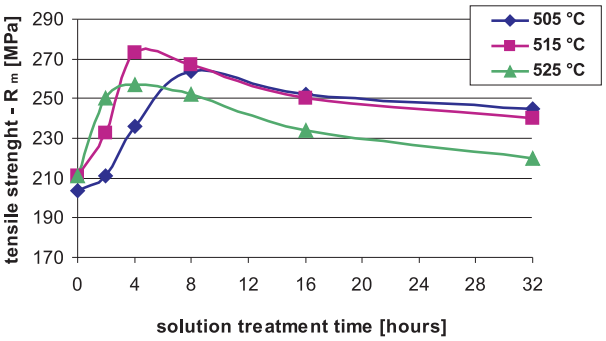

Fig. 4 Influence of solution treatment on strength tensile

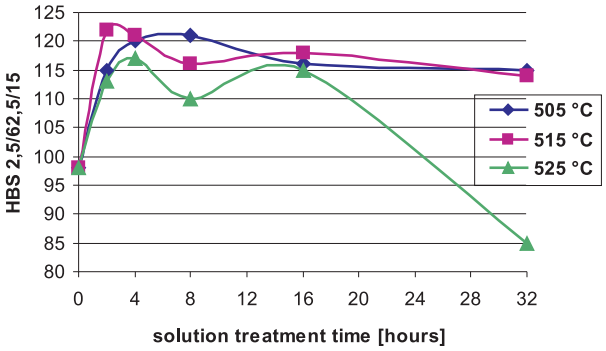

Fig. 5 Influence of solution treatment on hardness

hours. At 525 °C, test bars show hardness strong reduction due to the melting of the Al-Al_2Cu-Si phase [14–17].

3.2. The effect of solution treatment on the Fe-rich phases

The influence of iron on mechanical properties of aluminium alloys depends on the type, morphology and quantity of iron in the melt. Nevertheless, the shape of iron compounds is more influential than the quantity of those iron compounds.

The evolution of the Fe-rich phases during solution treatment is described in Fig. 6. Al_5FeSi phase is dissolved into very small needles (difficult to observe). The $Al_{15}(MnFe)_3Si_2$ phase was fragmented to smaller skeleton particles. In the untreated state $Al_{15}(FeMn)_3Si_2$ phase has a compact skeleton-like form (Fig. 6a). Solution treatment of this skeleton-like phase by 505°C tends to

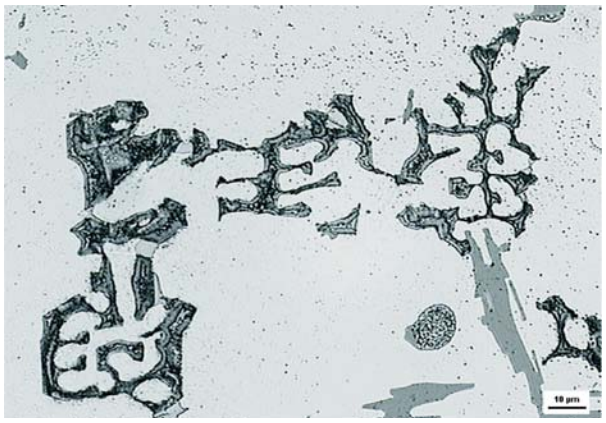

a) untreated state

b) 505 °C, 4 hours

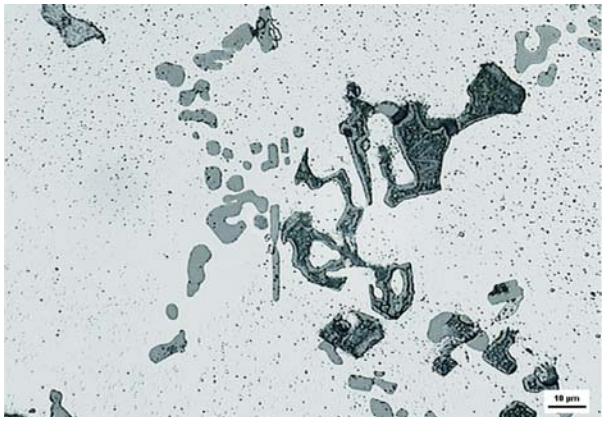

c) 515 °C, 4 hours

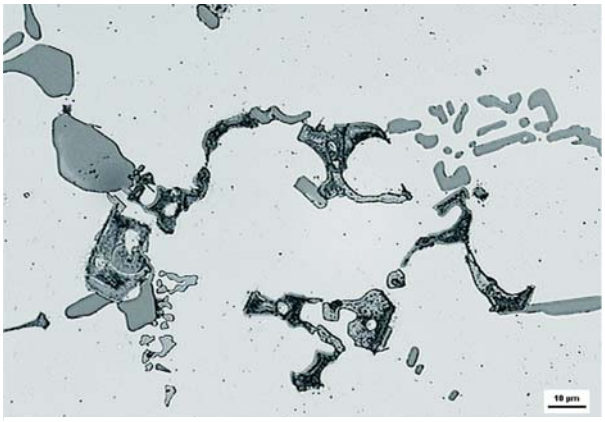

d) 525 °C, 4 hours

Fig. 6 Changes in morphology of $Al_{15}(FeMn)_3Si_2$ phases during solution treatment, etch. H_2SO_4

fragmentation (Fig. 6b) and by 515 or 525°C to spheroidization and segmentation (Fig. 6c, Fig. 6d).

It was established too that the temperature increase of solution treatment was attended not only by fragmentation of $Al_{15}(MnFe)_3Si_2$ phase, but also by decrease of area share of all Fe-rich phases in AlSi9Cu3 alloy. For the non-heat treated state the area share of Fe-rich phase was c. 4.5%, for temperature 515 °C c. 1.6% and for 525 °C only c. 1.3%. Solution treatment reduces its area rather than changes its morphology.

Quantitative metallography [18–19] was carried out on an Image Analyzer NIS – Elements to quantify Fe- rich phases (average area) morphology changes, during solution treatment. Fig. 7 shows the changes in the average area of Fe-rich phases during solution treatment. The maximum average area of Fe-rich phases was observed in as-cast samples (2 495 μm^2). By increasing the solution temperature the average area of Fe-phases dropped to 320 μm^2 for 515 °C. With a prolonged solution treatment time more than 8 h, the extent of dissolution of Fe-rich phases changed little.

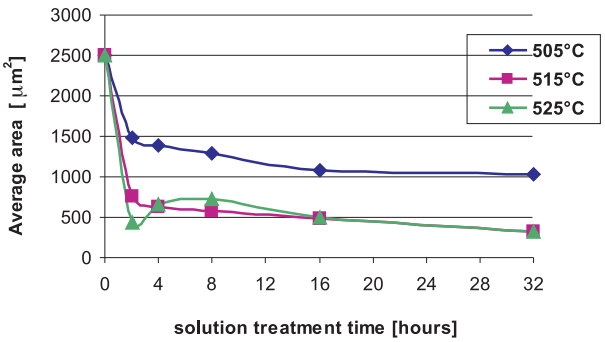

Fig. 7 Changes in average area of Fe-rich phases

4. Conclusions

In the present study, the evolution of the Fe-rich phases in recycled AlSi9Cu3 cast alloy during solution treatment was investigated. Microstructural characteristic and mechanical properties were studied. From the analysis of the results the following conclusions can be drawn:

- Two Fe-rich phases – Al_5FeSi needles and skeleton-like $Al_{15}(FeMn)_3Si_2$ were observed. $Al_{15}(FeMn)_3Si_2$ phase was dominant thanks to the presence of Mn.
- The morphology and size of iron phases are highly dependent on the solution treatment. Platelets Fe-rich phases (Al_5FeSi) are dissolved into very small needle phases. Skeleton-like Fe-rich phases ($Al_{15}(FeMn)_3Si_2$) are fragmented and dissolved (average area reduces from 2 495 to 320 μm^2).
- Optimal solution treatment (515 °C/4 hours) most improves mechanical properties. With further increases of solution treatment time (more than 4 hours) was tensile strength continuously dropped. Brinell hardness by increasis of solution treatment time dropped too. The temperature 525 °C is not suitable for secondary AlSi9Cu3 cast alloy solution treatment, because Cu-rich phases (Al-Al_2Cu-Si) are melt at this temperature [20].

Acknowledgement

This work has been supported by the Scientific Grant Agency of the Ministry of Education of the Slovak Republic and Slovak Academy of Sciences, N°1/0208/08 and No1/0249/09.

References

[1] RIOS, C. T. et al.: Intermetallic Compounds in the Al-Si-Cu system, In: *Acta Microscopia*, 12, 2003, 77–82.
[2] LI, R.: Solution Heat Treatment of 354 and 355 Cast Alloys, In: *AFS Transaction,* No. 26, 1996, pp. 777–783.
[3] DAS, S. K.: Designing Aluminium Alloys for a Recycling Friendly World, In: *Materials Science Forum,* Vol. 519–521, 2006, pp. 1239–1244.
[4] TAYLOR, J. A.: *The Effect of Iron in Al-Si Casting Alloys,* Proc. of 35th Australian Foundry Institute National Conference, Adelaide, South Australia, 2004, pp. 148-157.
[5] PARAY, F., GRUZLESKI, J. E.: Microstructure–mechanical Property Relationships in a 356 alloy – part I., In: *Microstructure, Cast Metals*, No. 7, 1994, pp. 29–40.
[6] CACERES, C. H., SVENSON, I. L., TAYLOR, J. A.: Strenght-ductility Behaviour of Al-Si-Cu-Mg Casting Alloys in T6 temper, In: *Int. J. Cast Metals Res.,* No. 15, 2003, pp. 531–543.
[7] WANG, Q. G., APELIAN, D., LADOS, D.A.: Fatigue Behavior of A356/357 Aluminum Cast Alloys - part II. Efect of Microstructural Constituents, In: *J. of Light Metals* 1/2001, pp. 85–97.
[8] TILLOVA, E., CHALUPOVA, M., PANUSKOVA, M.: Structural Analyses of the Al-Si-Cu Alloys, In: *Materials Engineering,* No. 13, 2006, pp. 25–30.
[9] SEIFEDINE, S., JOHANSSON, S., SVENSSON, I.: The Influence of Cooling Rate and Manganese Content on the β-Al_5FeSi Phase Formation and Mechanical Properties of Al-Si–based Alloys, In: *Materials Science and Engineering A,* No. 490, 2008, pp. 385–390.
[10] SAMUEL, A. M., SAMUEL, F. H., DOTY, H. W.: Observation on the Formation ß-Al_5FeSi Phase in 319 type Al-Si Alloys, In: *J. of Materials Science,* No. 31, 1996, pp. 5529–5539.

[11] MOUSTAFA, M. A.: Effect of Iron Content on the Formation of ß-Al5FeSi and Porosity in Al-Si Eutectic Alloys, In: *J. of Materials Processing Technology,* No. 209, 2009, pp. 605–610.
[12] SHABESTARI, S. G.: The Effect of Iron and Manganese on the Formation of Intermetallic Compounds in Aluminum–silicon Alloys, In: *Materials Science and Engineering A,* No. 383, 2004, pp. 289–298.
[13] ASHTARI, P., TEZUKA, H., SATO, T.: Modification of Fe-containing Intermetallic Compounds by K Addition to Fe-rich AA319 Aluminum Alloys, In: *Scripta Materialia* 53, 2005, pp. 937–942.
[14] SAMUEL, F. H.: Incipient Melting of $Al_5Mg_8Si_6Cu_2$ and Al_2Cu Intermetallics in Unmodified and Strontium-modified Al-Si-Cu-Mg (319) Alloys During Solution Heat Treatment, In: *J. of Materials Science,* No. 33, 1998, pp. 2283–2297.
[15] TILLOVA, E., PANUSKOVA, M.: Effect of Solution Treatment on Intermetallic Phase's Morphology in AlSi9Cu3 Cast Alloy,In: *Mettalurgija/METABK* No. 47, 2008, pp, 133–137, 1-4.
[16] TILLOVA, E., PANUSKOVA, M.: Effect of Solution Treatment on Intermetallic Phase's Morphology in AlSi9Cu3 Cast Alloy, In: *Materials Engineering,* No. 14, 2007, pp. 73–76.
[17] PANUSKOVA, M., TILLOVA, E., CHALUPOVA, M.: Relation Between Mechanical Properties and Microstructure of Cast Aluminum Alloy AlSi9Cu3, In: *Strength of Materials,* Vol. 40, 1/2008, pp. 98–101.
[18] SKOCOVSKY, P., VASKO, A.: *Quantitative Evaluation of Structure in Cast Iron,* EDIS, Zilina, 2007.
[19] VASKO, A., BELAN J.: Comparison of Methods of Quantitative Metallography, In. *Improvement of Quality Regarding processes and Materials* (ed(s): Borkowski, S. and Tillova, E.), PTM, Warszawa, PL, 2007, pp. 53–58.
[20] HURTALOVA, L., TILLOVA, E.: Evolution of the Structure in Recycled AlSi9Cu3 Cast Alloy During Solution Treatment, In: *J. of Machine Manufacturing,* XLIX, E3-E5, 2009, pp. 6–13.

COMMUNICATIONS – Scientific Letters of the University of Zilina
Writer's Guidelines

1. Submissions for publication must be unpublished and not be a multiple submission.
2. Manuscripts written **in English language** must include **abstract** also written in English. The submission should not exceed **10 pages** with figures and tables (format A4, Times Roman size 12). The **abstract** should not exceed 10 lines.
3. Submissions should be sent: **by e-mail** (as attachment in application MS WORD) to one of the following addresses: *komunikacie@uniza.sk* or *holesa@uniza.sk* or *vrablova@uniza.sk* or *polednak@fsi.uniza.sk* **with a hard copy** (to be assessed by the editorial board) **or on a CD** with a hard copy to the following address: Zilinska univerzita, OVaV, Univerzitná 1, SK-010 26 Zilina, Slovakia.
4. Abbreviations, which are not common, must be used in full when mentioned for the first time.
5. Figures, graphs and diagrams, if not processed by Microsoft WORD, must be sent in electronic form (as GIF, JPG, TIFF, BMP files) or drawn in contrast on white paper, one copy enclosed. Photographs for publication must be either contrastive or on a slide.
6. References are to be marked either in the text or as footnotes numbered respectively. Numbers must be in square brackets. The list of references should follow the paper (according to **ISO 690**).
7. The author's exact **mailing address of the organisation where the author works, full names, e-mail address or fax or telephone number,** must be enclosed.
8. The editorial board will assess the submission in its following session. In the case that the article is accepted for future volumes, the board submits the manuscript to the editors for review and language correction. After reviewing and incorporating the editor's remarks, the final draft (before printing) will be sent to authors for final review and adjustment.
9. The deadlines for submissions are as follows: September 30, December 31, March 31 and June 30.

COMMUNICATIONS

SCIENTIFIC LETTERS OF THE UNIVERSITY OF ZILINA
VOLUME 12

Address of the editorial office:
Zilinská univerzita
Office for Science and Research
(OVaV)
Univerzitna 1
SK 010 26 Zilina
Slovakia
E-mail: komunikacie@nic.uniza.sk,
pavel.polednak@fsi.uniza.sk

Each paper was reviewed by two reviewers.

Journal is excerpted in Compendex and Scopus

It is published by the University of Zilina in
EDIS – Publishing Institution of Zilina University
Registered No: EV 3672/09
ISSN 1335-4205

Published quarterly

Single issues of the journal can be found on:
http://www.uniza.sk/komunikacie